Illuminating seismic and aseismic fault slip from satellite geodesy: focus on continental creeping faults

By

Yuexin Li

A dissertation submitted in partial satisfaction of the

requirements for the degree of

Doctor of Philosophy

in

Earth and Planetary Science

in the

Graduate Division

of the

University of California, Berkeley

Committee in charge:

Professor Roland Bürgmann, Chair
Professor Douglas Dreger
Professor James Rector

Fall 2022

Illuminating seismic and aseismic fault slip from satellite geodesy: focus on continental creeping faults

Copyright 2022

by

Yuexin Li

Abstract

Illuminating seismic and aseismic fault slip from satellite geodesy: focus on continental creeping faults

by

Yuexin Li

Doctor of Philosophy in Earth and Planetary Science

University of California, Berkeley

Professor Roland Bürgmann, Chair

Earthquakes on major continental faults and subduction zones can be catastrophic, leading to severe damage, injuries, and casualties. Seismic and geodetic evidence shows that faults have heterogeneous degrees of locking, where earthquakes tend to occur on locked asperities and creeping patches do not accumulate interseismic strain. Accurately delineating the seismic and aseismic slip behavior on continental faults over the earthquake cycle is crucial for seismic hazard evaluation. In this dissertation, I use the space-geodetic Interferometric Synthetic Aperture Radar (InSAR) to study the crustal deformation during the co-, post- and interseismic period on faults in the Tibetan Plateau and San Francisco Bay Area. The first chapter introduces the context and gives an overview of the dissertation. In Chapter 2, I present the study of the co- and postseismic deformation of the 2017 Jiuzhaigou earthquake at the eastern boundary of the Tibetan Plateau. The Jiuzhaigou earthquake exhibits a strong shallow slip deficit (SSD) and has one of the lowest afterslip signals of recorded earthquakes (1%-3%). Such observations provide important implications for accommodations of fault strain in the shallow part of the crust and fault frictional properties. Ultimately, the SSD should be recovered through one or more earthquake cycles to maintain the conservation of the long-term slip. In Chapter 3, I show the analysis of the high-resolution interseismic deformation on the creeping Xianshuihe Fault at the eastern boundary of the Tibetan Plateau. A coupling model that characterizes the distribution of creep with depth is derived from the interseismic velocity map. The seismic potential of apparent rupture asperities along the Xianshuihe Fault is further refined by considering fault-crossing baseline data and the distribution of historical ruptures and microseismicity. In Chapter 4, I determine the interseismic deformation over the southern San Francisco Bay Area. I constrain the surface creep

rates on Bay Area creeping faults (San Andreas, Calaveras, Sargent, and Quien Sabe Faults) using cross-fault InSAR timeseries differences. I examine the spatiotemporal distribution of fault creep and identify a multi-annual fault coupling increase 2016-2018 on the San Andreas and Calaveras Fault. Finally in Chapter 5, I explore a deep learning approach to mitigate the atmospheric noise contributions and better detect the transient fault creep signals in the InSAR timeseries. The deep learning method is a promising approach to stretch the limit of InSAR on crustal deformation observation, with higher temporal resolution and better accuracy.

To my parents, for their unconditional love, support, and encouragement.

Contents

Contents **ii**

List of Figures **v**

List of Tables **x**

1 Introduction **1**

2 Evidence of Fault Immaturity from Shallow Slip Deficit and Lack of Postseismic Deformation of the 2017 Mw 6.5 Jiuzhaigou Earthquake **4**
2.1 Abstract . . . 4
2.2 Introduction . . . 5
2.3 Tectonic Setting . . . 6
2.4 Data and Methods . . . 8
2.4.1 InSAR data processing . . . 8
2.4.2 Inversion for Kinematic Rupture Parameters . . . 8
2.4.3 Akaike Information Criterion and Bayesian Information Criterion . . . 10
2.5 Results . . . 10
2.5.1 Coseismic deformation field . . . 10
2.5.2 Coseismic slip distribution . . . 12
2.5.3 Postseismic deformation and afterslip inversion . . . 12
2.6 Discussion . . . 16
2.6.1 Seismogenic fault geometry of the Jiuzhaigou earthquake . . . 16
2.6.2 Implications of shallow slip deficit (SSD) and lack of afterslip . . . 17
2.6.3 Effects of the Wenchuan earthquake on the 2017 Jiuzhaigou event . . . 19
2.7 Conclusion . . . 20

3 Partial Coupling and Earthquake Potential along the Xianshuihe Fault, China **21**
3.1 Abstract . . . 21
3.2 Introduction . . . 22
3.3 Data and Methods . . . 24

3.3.1 InSAR data and processing . . . 24
3.3.2 Kinematic inversion for the seismic and aseismic fault slip . . . 27
3.4 Results . . . 28
3.4.1 Average interseismic velocity map along the XSF . . . 28
3.4.2 Along-strike variation of the creep rate . . . 30
3.4.3 Coupling model along the XSF inverted from 2014-2019 deformation 32
3.4.4 The 2014 Kangding earthquake sequence and its coseismic slip model 37
3.4.5 Temporal characteristics of the postseismic deformation in the Kangding region . . . 40
3.5 Discussion . . . 42
3.5.1 Implications and limitations of the interseismic velocity map and coupling model . . . 42
3.5.2 Implications for the seismic potential on the XSF . . . 44
3.5.3 Possible mechanisms of the substantial afterslip in the Kangding region 46
3.6 Conclusion . . . 50

4 Spatiotemporal Variations of Surface Deformation, Shallow Creep Rate, and Slip Partitioning between the San Andreas and Southern Calaveras Fault 51
4.1 Abstract . . . 51
4.2 Introduction . . . 52
4.3 Data and Methods . . . 55
4.3.1 InSAR data and processing . . . 55
4.3.2 GPS timeseries and processing . . . 56
4.3.3 Creepmeter timeseries and alignment array data . . . 57
4.3.4 Seismicity, catalog declustering and b-value estimation . . . 57
4.3.5 Aseismic fault slip inferred from characteristic repeating earthquakes 58
4.4 Results . . . 59
4.4.1 Average InSAR LOS velocity, timeseries, and validations . . . 59
4.4.2 Spatial distribution of average creep rates along South Bay Area faults 64
4.4.3 Spatiotemporal variation of the short-term creep rates along the SAF and CF . . . 67
4.4.4 Spatiotemporal variation of the b-value at the SAF-CF junction . . . 70
4.5 Discussion . . . 70
4.5.1 Shallow fault creep on the SF and QSF . . . 71
4.5.2 Partitioning of the shallow fault creep among the SAF and CF . . . 72
4.5.3 Long-term coupling changes along the SAF and CF . . . 76
4.6 Conclusion . . . 79

5 Detecting Creep Transients in InSAR Timeseries Using Deep Neural Networks 80
5.1 Abstract . . . 80

5.2 Introduction . . . 80
5.3 Neural Network Structure . . . 82
5.4 Preparation of the Synthetic Training Set . . . 82
5.4.1 Synthetic atmospheric noise generation . . . 82
5.4.2 Synthetic InSAR timeseries generation . . . 84
5.5 Results . . . 85
5.5.1 Neural network training . . . 85
5.5.2 Evaluation on synthetic timeseries . . . 86
5.5.3 Evaluation on real timeseries . . . 87
5.6 Discussion . . . 91
5.6.1 Evaluation on different temporal patterns . . . 91
5.6.2 Evaluation on timeseries reconstruction with creep episodes . . . 93
5.6.3 Limitations of the synthetic training sets . . . 94
5.7 Conclusion . . . 95

Bibliography **96**

A Supporting information for: Evidence of Fault Immaturity from Shallow Slip Deficit and Lack of Postseismic Deformation of the 2017 Mw 6.5 Jiuzhaigou Earthquake **113**

B Supporting information for: Partial Coupling and Earthquake Potential along the Xianshuihe Fault, China **131**
B.1 Uncertainty quantification for the velocity maps . . . 131
B.2 The influence of profile length and fitting method choices for surface creep rate estimation . . . 132

C Supporting information for: Spatiotemporal variations of surface deformation, shallow creep rate, and slip partitioning between the San Andreas and southern Calaveras Fault **157**

D Supporting information for: Detecting Creep Transients in InSAR Timeseries Using Deep Neural Networks **187**

List of Figures

2.1 Background tectonics of the Tibetan Plateau and a close-up map of the eastern boundary of the Bayan Har Block. 7
2.2 Surface displacement of the Jiuzhaigou earthquake observed by InSAR. 11
2.3 Co- and postseismic slip distribution of the 2017 Mw6.5 Jiuzhaigou earthquake derived from Sentinel-1A InSAR data. 13
2.4 Comparison of observed and modeled LOS displacements from both ascending and descending Sentinel-1A tracks. 14
2.5 Cumulative LOS displacement field generated by SBAS method for ascending and descending tracks. 15

3.1 Overview map of active crustal deformation across the Tibetan Plateau and a zoom-in map of the Xianshuihe Fault region. 23
3.2 Examples of selected good and bad interferograms from descending track T135F3. 25
3.3 Coseismic deformation for the 2014 Kangding earthquake sequence. 27
3.4 Average LOS velocity maps for ascending track 26 and descending tracks 33 and 135 in the Xianshuihe Fault region. 29
3.5 Close-up view of the fault-parallel velocity field and fault-perpendicular velocity profiles. 31
3.6 The inverted interseismic shallow slip model and uncertainties using the average velocity map between 2014.12-2019.7 in the Xianshuihe Region. 34
3.7 Comparison of downsampled observed and modeled short-wavelength LOS velocities from both ascending and descending Sentinel-1 geometries. 35
3.8 Spatio-temporal distribution of the historical earthquake ruptures, surface creep rate variations, cross-section of microseismicity and comparisons of identified asperities, and 2D view of the fault coupling distribution between 2014.12-2019.7 along the XSF. 36
3.9 The best-fitting coseismic slip model of the Kangding earthquake sequence. . . . 38
3.10 Comparison of observed and modeled coseismic deformation of Kangding earthquake from both ascending and descending Sentinel-1 geometries. 39
3.11 Average LOS velocity map and cross-fault time series of the cumulative LOS displacement differences along the SE section of the XSF for descending track 135. 41
3.12 Cumulative 2014-2019 fault slip along the SE segment of the XSF derived from kinematic inversions and the coseismic-stress-driven afterslip model. 47

3.13 Schematic plots for three possible explanations of the rapid aseismic slip north of the rupture zone. 49

4.1 Overview map of the study region. 54
4.2 InSAR average 2015-2020 LOS velocity map for descending track 42 and validation with GPS velocities. 60
4.3 Close-up view of the InSAR LOS velocity field in the SAF-CF junction and comparison of InSAR timeseries with 3D continuous GPS timeseries. 61
4.4 Evaluation of the timing of peak seasonal uplift (phase) from InSAR and LOS GPS timeseries in a North American reference frame. 62
4.5 Cross-fault InSAR LOS timeseries differences along the SAF and CF. 65
4.6 Spatial distribution of average right-lateral creep rate derived from cross-fault timeseries differences along the SAF, CF, SF and QSF. 66
4.7 Spatiotemporal variation of the residual InSAR LOS cross-fault timeseries after the removal of a linear trend across the SAF and CF. 68
4.8 Spatio-temporal distribution of the b-values in the study region derived from the double-difference relocated and declustered seismicity catalog. 71
4.9 Map view of the spatial distribution of creep rates, unit normal-, and shear stress loading rate on SAF and CF. 74
4.10 Spatial distribution of normalized dextral creep rate, normal and shear stress loading on the SAF and CF arranged by latitude. 75
4.11 Along-fault (N45°W) distribution of creep rates on the SAF, CF, SF and QSF. . 76
4.12 Temporal variation of b-value, residual shallow slip timeseries inferred from InSAR and repeating earthquakes that are binned by latitude along the SAF and CF. 77

5.1 The neural network structure of the denoising autoencoder that is adapted from Rouet-Leduc et al. (2021) 83
5.2 An example of fractal analysis on the real-world DEM and synthetic DEM. . . . 85
5.3 An example of the synthetic InSAR timeseries generated for the training set. . . 86
5.4 Training curve of the denoising neural network model. 87
5.5 Performance of the denoising neural network model. 88
5.6 Examples of synthetic and DAE-recovered InSAR cumulative displacement with SNR of 0.1, 0.01 and 0.001. 89
5.7 Performance of the DAE neural network model on the NAF 90
5.8 Performance of the DAE neural network model on the Chaman Fault. 90
5.9 Examples of the DAE recovered InSAR cumulative displacement on timeseries with pure noise. 92
5.10 Examples of the DAE recovered InSAR cumulative displacement on timeseries with steady-rate deformation. 92
5.11 Examples of the DAE recovered InSAR cumulative displacement on 50 time steps with single and multiple creep transient episodes. 94

A.1 Example demonstrating the correction of topography-correlated troposphere delay through linear regression. . . . 116
A.2 Baseline plot for the co- and postseismic analysis of Sentinel-1 data from ascending track T128 and descending track T62. . . . 117
A.3 The trade-off curve between InSAR residuals and GPS residuals with different weight. . . . 118
A.4 A close-up view of wrapped, unwrapped and unwrapped masked interferograms used in the coseismic modeling. . . . 119
A.5 Coherence maps of the preseismic, coseismic, and coherence loss for ascending orbit T128. . . . 120
A.6 The trade-off curve between smoothing parameter (λ) and InSAR and GPS combined RMS=RMS^2_{gps}+RMS^2_{sar}. . . . 121
A.7 Example of an overly-rough and an overly-smooth slip model. . . . 122
A.8 Comparison of observed and modeled coseismic re-wrapped LOS displacements from both ascending and descending Sentinel-1A tracks. . . . 123
A.9 Atmospheric phase delay estimates of each selected scene from ascending and descending orbit acquisitions. . . . 124
A.10 Comparison of observed and modeled postseismic LOS displacements from both ascending and descending Sentinel-1A tracks. . . . 125
A.11 Inverted co- and postseismic slip based on both InSAR and GPS data. . . . 126
A.12 Comparison of observed and modeled co+postseismic LOS displacements from both ascending and descending Sentinel-1A tracks and GPS offsets. . . . 127
A.13 The inverted slip model with a secondary fault. . . . 128
A.14 Comparison of observed and modeled LOS displacements from both ascending and descending Sentinel-1A tracks with GPS for a secondary fault. . . . 129
A.15 Calculated Coulomb stress change and postseismic viscoelastic stress change caused by the 2008 Wenchuan earthquake at the time of the 2017 Jiuzhaigou earthquake. . . . 130

B.1 Estimated uncertainties for ascending track 26, descending tracks 33 and 135, fault-parallel, and vertical velocity fields along the XSF region. . . . 137
B.2 Comparison of the velocity maps in the overlapping region of descending tracks 33 and 135. . . . 138
B.3 Comparisons of surface creep rates along the XSF estimated by multiple profile settings. . . . 139
B.4 Interferogram network for tracks D33, D135 and A26 for co- and postseismic deformation used in this study. . . . 140
B.5 Examples of selected and rejected interferograms for descending track T135F2, descending track T33, and ascending track T26. . . . 141
B.6 Histogram of the standard deviation (STD) of selected and rejected unwrapped interferograms for D135F2. . . . 142
B.7 Histogram of hypocenter depths of M≥1.5 earthquakes within 10 km of the XSF. 143

B.8 Geometry of the deep dislocation model. 144
B.9 Comparison of downsampled observed and modeled long-wavelength LOS velocities from ascending and descending Sentinel-1 viewing geometries. 145
B.10 The observed, modeled, and residual of the long-wavelength LOS velocities from ascending track 26 and descending track 135. 146
B.11 Comparisons of observed and modeled GPS velocities using the derived deep dislocation model. 147
B.12 Trade-off curve for smoothing parameters of the shallow slip inversion. 148
B.13 Checkerboard tests for the model resolution using the preferred smoothing parameter of 0.005. 149
B.14 Comparisons of surface creep rate derived from the distributed-creep model by varying the smoothing parameters in the inversion. 150
B.15 Residual (RMS) plot for the coseismic slip model for ranges of locations of the surface trace and variable dip angles of the Mw5.9 rupture plane. 150
B.16 Stacked averaged LOS time series and the cross-fault time series differences for descending track 135 along the northern, central and southern fault sections. . . 151
B.17 Stacked averaged LOS cross-fault time series differences along the northern, central and southern fault sections with the linear and log-decay fittings. 152
B.18 The normalized weight of time-spans that are used in the average velocity map formation for descending track 135, descending track 33, and ascending track 26. 153
B.19 A zoom-in map of the average velocity map of descending track 135. 154
B.20 Simplified coseismic slip model using the fault geometry of the SE section of the coupling model. 155
B.21 Comparison of observed and modeled coseismic deformation of Kangding earthquake from both ascending and descending Sentinel-1 geometries using the fault geometry of the SE section of the coupling model. 156

C.1 SBAS network used in this study. 164
C.2 Coherence mask applied in unwrapping process with an average (temporal) coherence threshold of 0.2. 166
C.3 Histogram of the variance of the sequential interferograms (standard deviation in radians) before and after ERA5 correction. 167
C.4 Creepmeter timeseries measurements on the SAF and CF, respectively. 168
C.5 Distribution of nearest-neighbor distances, rescaled-time and rescaled-distance plot for all events in the NCEDC catalog. 169
C.6 Time-latitude plot of the original and declustered catalog using nearest-neighbor approach with $\eta = 1.25 \times 10^{-6}$. 170
C.7 Standard deviation of the InSAR LOS velocity when solving for a linear trend of the InSAR timeseries. 171
C.8 Comparison of the InSAR LOS velocity with 3D and 2D GPS velocities projected into LOS, respectively. 172

C.9 Comparison of GPS and InSAR timeseries at GPS sites relative to LUTZ (Central Valley stations excluded). . . . 173
C.10 Comparison of the amplitudes of seasonal deformation from InSAR and GPS timeseries. . . . 174
C.11 Seasonal effects of the atmospheric phase delay estimated from ERA5 weather model timeseries. . . . 175
C.12 Uncertainty of the amplitude and timing of peak seasonal uplift (phase) from InSAR and GPS timeseries. . . . 176
C.13 Uncertainty of the InSAR LOS cross-fault timeseries along the SAF and CF. . . 177
C.14 Comparison of spatial distributions of average right-lateral creep rates along the SAF and CF with topographic differencing measurements. . . . 178
C.15 InSAR LOS cross-fault timeseries differences along the Sargent Fault and Quien Sabe Fault. . . . 179
C.16 Uncertainty of the InSAR LOS cross-fault timeseries along the Sargent Fault and the Quien Sabe Fault. . . . 180
C.17 Simplified geologic map of the SAF-CF junction. . . . 181
C.18 Sedimentary thickness map with basin outline over the study region. . . . 182
C.19 Spatial distribution of the b-value, M_c, a-value and b-value uncertainties in each grid cell with grid size of 0.05°, 0.1°, and 0.025°. . . . 183
C.20 Spatial distribution of the microseismicity and b-values using the original and declustered catalogs. . . . 184
C.21 Spatiotemporal variation of the residual CRE-inferred slip timeseries after the removal of a linear trend along the SAF that are binned by latitude. . . . 185
C.22 Spatiotemporal variation of the residual CRE-inferred slip timeseries after the removal of a linear trend along the SAF that are binned by latitude. . . . 186

D.1 Histogram of the power-law exponent calculated from 500 randomly sampled land-based DEMs. . . . 188
D.2 Demonstration of the log-transformation and histogram of the LOS displacements from synthetic InSAR timeseries before and after log-transformation. . . . 189
D.3 Cumulative displacement of the noisy, DAE recovered, and clean InSAR time-series with a single creep transient episode. . . . 190
D.4 Cumulative displacement of the noisy, DAE recovered, and clean InSAR time-series with multiple creep transient episodes. . . . 191

List of Tables

3.1 Sentinel-1 InSAR data after the 2014 Kangding earthquake sequence generated in this study. 25

A.1 Focal mechanisms of the Jiuzhaigou earthquake determined by different institutes. 113
A.2 Comparison of RMS, AIC and BIC for inversions using different coseismic model geometry. 114
A.3 Interferograms generated for coseismic study. 114
A.4 Observed and modeled GPS displacements for coseismic study. 114
A.5 Observed and modeled GPS displacements for co- and postseismic study. 115

B.1 Selected interferograms used to form the average velocity maps. 134
B.2 Best-fitting characteristic decay times for time series differences taken from multiple swaths at variable distances from the fault. 135
B.3 List of historical (M>6) and recent (M>5 since 2010) earthquakes along the XSF. 135
B.4 List of identified asperities along the XSF. 136

C.3 Fault creep rates derived from Sentinel-1 InSAR timeseries (2015-2020). 161
C.4 Creep rates derived from alignment array and creepmeter measurements. 164
C.1 Effect of the selection of temporal-baseline networks on the statistics of InSAR velocity products. 165
C.2 List of GPS stations that are excluded in the InSAR-GPS rate comparison. . . . 165

Acknowledgments

I feel immensely fortunate to have the opportunity to travel halfway across the world and pursue my PhD degree in the US. I am grateful for the help received from many people here at UC Berkeley.

First of all, I would like to thank my advisor Prof. Roland Bürgmann, for his patience, guidance, and support over the past 5 years. He sets an exceptional example on how to be a good advisor, researcher, and scientist. He is always responsive to my questions and available for discussions. I benefit so much from his endless passion and rigorous attitude to scientific questions. I am thankful to him for giving me the maximum freedom to explore every research topic that I would like to pursue during my PhD.

I would like to thank my thesis and qualifying committee, Prof. Douglas Dreger, Prof. James Rector, and Prof. Michael Manga. I am grateful for all the inspiration and discussions all along the way. I would also like to thank the faculties and researchers at the Berkeley Seismological Lab, Prof. Richard Allen, Prof. Barbara Romanowicz, Prof. Harriet Lau and Dr. Taka'aki Taira. Thank you all for sharing your insight and showing me what a good scientist looks like over the years.

My special thanks to current and former members of the Active Tectonics group, Nam Maneerat, Kathryn Materna, Dani Lindsay, Zach Smith, Isis Lemus, Chris Johnson, Brent Delbridge, Kang Wang, Lian Xue, Xie Hu, Baptiste Rousset, Yuankun Xu, Heather Shaddox, Curtis Baden, and Kelian Dascher-Cousineau. I enjoyed spending time with the group and learned a lot from everyone both in research and life.

I would like to shout out to my officemates Kathryn Materna, William Hawley, Runze Miao, Dani Lindsay, Claire Doody, and Mrinal Durson. Many encouraging conversions happened in the office we share. Thank you all for always being a good listener, a cheerleader, and a good friend! I also wish to thank the current and former graduate students and postdocs in the Berkeley Seismological Lab, Nate Lindsey, Alex Robson, Robert Martin-Short, Sarina Patel, Sevan Adourian, Yuancong Gou, Li-Wei Chen and Yifang Cheng. I would not have gone that far without their accompany.

Finally, I would like to thank my parents for their unconditional love, support, and encouragement over the past 28 years. Thanks to them, I have the courage and strength to take on my journey. I owe a special thanks to Yijian, who is always a good listener and is always accompanying me through the emotional highs and lows. This degree would not have been possible without him.

Chapter 1

Introduction

Large earthquakes on plate boundaries and major faults can be catastrophic, leading to severe damages, injuries, and casualties. Over an earthquake cycle, the crustal strain gradually builds up over the interseismic period and is released by sudden coseismic ruptures. The effect of an earthquake can last for years to decades attributed to postseismic deformation processes. Characterizing the fault slip behaviors during the co-, post- and interseismic period allows us to better assess the seismogenic structure and regional seismic hazard. Unlike most faults that are locked in the shallow crust and release the accumulated elastic strain through seismic radiations, there are some special faults in particular locations that exhibit different slip behavior (Harris, 2017). Those creeping faults slip slowly in their upper few kilometers, accommodating the interseismic loading through aseismic fault slip. Even though there is little interseismic strain accumulation along the uppermost part of rapidly creeping faults, destructive earthquakes can still occur on the coupled sections of the fault to compensate for the slip deficit that are accumulated over time. In the context of regional seismic hazard evaluation, a better characterization of seismic and aseismic fault slip helps map out the distribution of locked and creeping patches on the fault, which can be incorporated into rupture and ground motion modeling (Field et al., 2015).

Seismic and aseismic slip on faults produce crustal deformation on the Earth's surface that can be measured by space geodetic tools. The amount of slip can be inverted from the measured ground deformation (e.g., Okada, 1985). To characterize fault slip at and below the Earth's surface, dense and accurate measurements of crustal deformation in both the near field and far field are crucial. The advent of modern space-geodetic techniques over the past decades provides an unprecedented opportunity for such large-scale observations. The Interferometric Synthetic Aperture Radar (InSAR) is a powerful geodetic tool that is capable of measuring large-scale ground deformation at high spatial resolution (<100 m) with sub-centimeter accuracy. The dense sampling of InSAR and its global coverage also make it a unique geodetic tool that can be leveraged in areas that lack dense GPS coverage. In this dissertation, I utilize the InSAR data acquired by the Sentinel-1A, B constellation

that was launched in 2014 and 2016, operated by ESA for the European Union Copernicus program throughout the analysis. The Sentinel-1 satellites have a regular recurrence interval of 6-24 days around the world, making it possible to delineate both spatial and temporal behaviors of seismic and aseismic fault creep.

Nonetheless, there are still substantial challenges for InSAR observations on creeping faults, given that the interseismic signals tend to be relatively subtle ($\sim$mm/yr) and are often contaminated by atmospheric noise. The tropospheric delay is a major error source for C-band interferometry and can introduce up to a few cm delays in a single Sentinel-1 InSAR interferogram. In this dissertation, I demonstrate different approaches to mitigate the effects of atmospheric noise in InSAR, including using an empirical linear relationship between the atmospheric delay and topography (Chapter 2), manually selecting long-term interferograms with minimal atmospheric perturbations (Chapter 3), modeling the atmospheric delay using external auxiliary weather models (Chapter 4), and deep-learning based neural network to remove the atmospheric perturbations in the InSAR timeseries (Chapter 5). With the atmospheric noise mitigation strategies, the chapters of this dissertation present case studies using space-geodetic tools InSAR to characterize co-, post-, and interseismic processes on faults in the Tibetan Plateau and San Francisco Bay Area.

In Chapter 2, I present the study of the co- and postseismic deformation of the 2017 Mw6.5 Jiuzhaigou earthquake that occurred at the northeastern boundary of the Tibetan Plateau using InSAR and GPS measurements. The inverted coseismic slip model indicates peak slip of up to $\sim$1 m at around 5 km depth accompanied by a strong shallow slip deficit (SSD). The earthquake has one of the lowest afterslip signals of recorded earthquakes (1%-3% of coseismic moment release). We argue that the observation of a pronounced SSD and lack of early afterslip of the 2017 Mw6.5 Jiuzhaigou earthquake is a representative feature of immature faults, in which case the phenomenon of SSD is a stage that all incipient young strike-slip faults go through. Ultimately, the SSD should be recovered through one or more earthquake cycles to maintain the conservation of the long-term slip. We would expect more distributed fault zone damage, rapid shallow afterslip, earthquakes that rupture the shallow layer, or future larger events to make up the existing slip deficits.

In Chapter 3, I determine high-resolution interseismic velocity maps along the 350-km-long central Xianshuihe Fault located at the eastern boundary of the Tibetan Plateau using Sentinel-1 InSAR data from 2014-2019. The InSAR data reveal multiple creeping sections and the estimated surface creep rates show high along-strike variability. A coupling model characterizes the distribution of creep at depth. The seismic potential of apparent rupture asperities along the Xianshuihe Fault is further refined by considering fault-crossing baseline data and the distribution of historical ruptures and microseismicity. In addition to the aseismic fault creep, we performed InSAR timeseries analysis on the SE section of the Xianshuihe Fault to study the co- and postseismic deformation of the 2014 Kangding earthquake sequence. Similar to the 2017 Jiuzhaigou earthquake, the 2014 Kangding earthquake

did not rupture to the surface and the coseismic slip model exhibits a clear SSD. However, a substantial afterslip was observed updip of the rupture, releasing the interseismic strain accumulation in the shallow crust. Although the Kangding earthquake and its afterslip released part of the accumulated strain on a previously identified 'seismic gap', the remaining slip deficit is still capable of generating a M7 event. Our work further addressed the locking status and seismic potential on the fault by adding evidence from geodetic observations and quantitative estimates of moment released by aseismic fault creep.

In Chapter 4, I show the interseismic deformation over the southern San Francisco Bay Area by performing a timeseries analysis using 5 years of Sentinel-1 InSAR data from May 2015 to October 2020. I derive the surface creep rates from cross-fault InSAR timeseries differences along the San Andreas Fault and Calaveras Fault, including adjacent Sargent and Quien Sabe Faults. The InSAR constrained fault creep rates on the SAF decrease from ∼18 mm/yr at Pinnacles to fully locked ∼10 km north of San Juan Bautista. The inferred strike-slip creep rate on the CF increases from ∼10 mm/yr in the south and reaches its peak rate ∼20 mm/yr at 36.9°N. We provide upper-bound estimates of surface creep of 4.2±3.1 mm/yr for the Sargent Fault and 3.5±2.6 mm/yr for the Quien Sabe Fault. I show that the distribution of fault creep is to first order controlled by the angle between fault strike and the background stress orientation. I further examine the spatiotemporal variation of creep rates along the SAF and CF and find a multi-annual coupling increase during 2016-2018 along the subparallel sections of both faults, with the CF coupling change lagging behind the SAF by 3 to 6 months. Similar temporal variations are also observed in both b-values inferred from declustered seismicity and aseismic slip rates inferred from characteristic repeating earthquakes.

Finally in Chapter 5, I explore a deep learning approach to eliminate the atmospheric noises and detect the transient fault creep signals in the InSAR timeseries. A deep neural network model, called denoising autoencoder, is trained with 10^6 synthetic InSAR timeseries to specifically target transient creep detection. The approach takes into account the different spatial-temporal characteristics between the tectonic deformation and atmospheric noises. I evaluate the trained neural network on synthetic InSAR timeseries with variable temporal behavior of creep transient episodes. The neural network performance is strongly dependent on the signal to noise ratio of the input InSAR timeseries. I further assess the performance of the neural network on the creeping North Anatolian and Chaman Fault. The neural network model is able to effectively remove the atmospheric noise in the InSAR timeseries as well as recover a creep transient episode on the North Anatolian Fault. The deep learning method is a promising approach to stretch the limit of InSAR for crustal deformation observation, with higher temporal resolution and better accuracy.

Chapter 2

Evidence of Fault Immaturity from Shallow Slip Deficit and Lack of Postseismic Deformation of the 2017 Mw 6.5 Jiuzhaigou Earthquake

The chapter was adapted from: Y. Li, R. Bürgmann, and B. Zhao (Jan. 2020). "Evidence of Fault Immaturity from Shallow Slip Deficit and Lack of Postseismic Deformation of the 2017 Mw 6.5 Jiuzhaigou Earthquake". *Bulletin of the Seismological Society of America* 110.1, pp. 154–165. ISSN: 0037-1106. DOI: 10.1785/0120190162

2.1 Abstract

The Mw 6.5 Jiuzhaigou earthquake occurred on 8 August 2017 36 km WSW of Yongle, Sichuan, China. We use both ascending and descending interferometric synthetic aperture radar (InSAR) data from Sentinel-1 and coseismic offsets of four GPS sites to obtain the coseismic surface deformation field and invert for the fault geometry and slip distribution. Most slip of the left-lateral strike-slip earthquake occurred in the 3-10 km depth interval with a maximum slip of about 1 m and a large shallow slip deficit (SSD). An 8-month InSAR time series analysis documents a lack of resolvable postseismic deformation and inversions for the distribution of postseismic slip demonstrate the lack of shallow afterslip. We argue that the observations of a pronounced SSD and no early afterslip of the Jiuzhaigou earthquake are indicative of an immature fault and that all incipient young strike-slip faults likely feature a SSD. We would expect a complex rupture geometry with distributed coseismic failure in the uppermost part of the brittle crust during the fault zone development. As faults mature, they straighten out, develop a localized fault zone core, and the SSD diminishes. By calculating the static Coulomb stress change and 9-year viscoelastic stress change caused

by the Wenchuan earthquake, we also show that the 2008 Wenchuan earthquake did not significantly affect the time of occurrence of the 2017 Jiuzhaigou earthquake.

2.2 Introduction

On 8 August 2017 (UTC 13:19:49), an Mw 6.5 earthquake shook Jiuzhaigou County in Sichuan Province, southwestern China. The location and source parameters determined by different institutes are listed in Table A.1. The earthquake occurred in the Jiuzhaigou Valley Scenic and Historic Interest Area, which is listed as a UNESCO world heritage site. It is famous for its beautiful mountains, multi-level waterfalls and colorful lakes; however, the landscape was damaged by more than 1800 triggered rock avalanches and landslides and the earthquake led to about 25 casualties (see Data and Resources Section). The shaking intensity reached VII according to the U.S. Geological Survey. Field investigations conducted after the mainshock found no surface ruptures and inferred that the fault hosting this earthquake represents an unmapped northern segment of the Huya Fault, which lies near the easternmost end of the eastern Kunlun fault zone (Yi et al., 2017).

The Jiuzhaigou region has an average altitude of about 3000 meters. Due to the high elevation and mountainous terrain of this area, few GPS stations have been set up near the recent rupture. InSAR satellites are able to provide dense and wide coverage of the deformation field, but the rough topography and vegetation present some challenges for the data processing. The Sentinel-1A mission was launched by the European Space Agency (ESA) in 2014 and Sentinel-1B followed in 2016. Sentinel-1 data serves as an important source for researchers studying crustal deformation due to its wide coverage, short repeat time and open-data policy.

Previous studies of the earthquake, using GPS, InSAR and/or teleseismic data, found a similar geometry of the seismogenic fault and similar patterns of slip distribution. Sun et al. (2018) proposed the existence of a secondary fault and a third rupture patch with the help of teleseismic waveforms. All previous studies agree on the earthquake rupturing a left-lateral, sub-vertical, and NNW striking strike-slip fault, with little or no slip in the upper ∼3km of the crust (Ji et al., 2017; Sun et al., 2018; Zhao et al., 2018; Zhang et al., 2018c).

Inversion of coseismic deformation of the InSAR deformation field for a kinematic model of the rupture allows us to better understand the seismogenic mechanism and earthquake source parameters, which helps us to improve the understanding and assessment of seismogenic structures and regional hazard. Examination of postseismic surface displacements provides additional information about fault and rock deformation processes and their mechanical properties. Here, we used Sentinel-1A SAR observations to obtain the coseismic and postseismic deformation of the 2017 Jiuzhaigou earthquake. We derived a distributed coseismic slip model of the rupture constrained by the InSAR and GPS data to document a strong shallow slip deficit (SSD). The observed postseismic deformation of the first 8 months

after the earthquake suggests little or no afterslip, and the SSD persists through the postseismic period. The results suggest that this event occurred on a young and discontinuous fault zone whose shallow deformation is broadly distributed across a zone of coseismic damage. Given the relatively short separation in space and time between the catastrophic May 12th, 2008, Mw7.9 Wenchuan earthquake and the 2017 Jiuzhaigou earthquake, we also examine the Coulomb stress change and viscoelastic stress change of the Wenchuan earthquake on the Jiuzhaigou fault plane. The result shows that the Jiuzhaigou earthquake is ultimately a result of the long-term collision of Indian Plate and Eurasian Plate, and the eastward extrusion of the Tibetan Plateau and its timing nearly a decade after the Wenchuan earthquake may not reflect a direct triggering relationship.

2.3 Tectonic Setting

The Bayan Har block is located near the northeastern edge of the Tibetan Plateau and extends from west to east across much of the plateau. The northern boundary of the Bayan Har Block is the Kunlun Fault Zone, and the Longmenshan thrust system represents its eastern margin. Here, the eastward extrusion of the Tibetan Plateau encounters a mechanically strong rigid lithospheric block underlying the Sichuan Basin and the adjoining south China Block (Zhang et al., 2012), and the differential motion is accommodated by strike-slip and thrust faulting along the eastern margin of the Tibetan Plateau (Avouac and Tapponnier, 1993; Burchfiel et al., 2008). In recent decades, the eastern boundary of the Bayan Har block has experienced several strong and moderate earthquakes, including the 1976 Mw 7.2 Songpan earthquake sequence, the 2008 Wenchuan Mw 7.9 earthquake and its aftershocks, the 2013 Lushan Mw 6.6 earthquake, and the 2017 Mw6.5 Jiuzhaigou earthquake (Figure 2.1).

The 8 August 2017 Mw 6.5 (Ms7.0) Jiuzhaigou earthquake was a left-lateral strike-slip rupture. Event focal mechanism parameters are shown in Table A.1. The earthquake is located near the extension of the easternmost Kunlun fault zone. Major recognized fault zones in the epicentral region include the Kunlun, Minjiang, Xueshan and Huya faults (Yi et al., 2017) (Figure 2.1). South of the rupture area, the left-lateral Huya Fault dips 80° to the southwest (Wilson et al., 2004). A buried fault strand of the unmapped northern extension of the Huya fault may have hosted the earthquake (e.g., Zhao et al., 2018), which may reflect the growth of an incipient fault (e.g., Thomas et al., 2013). Investigations of the detailed kinematics of the coseismic rupture and its postseismic deformation are crucial for understanding the characteristics of an evolving young fault zone like the northern Huya fault and may provide new insight on the tectonic evolution of the eastern Tibetan Plateau.

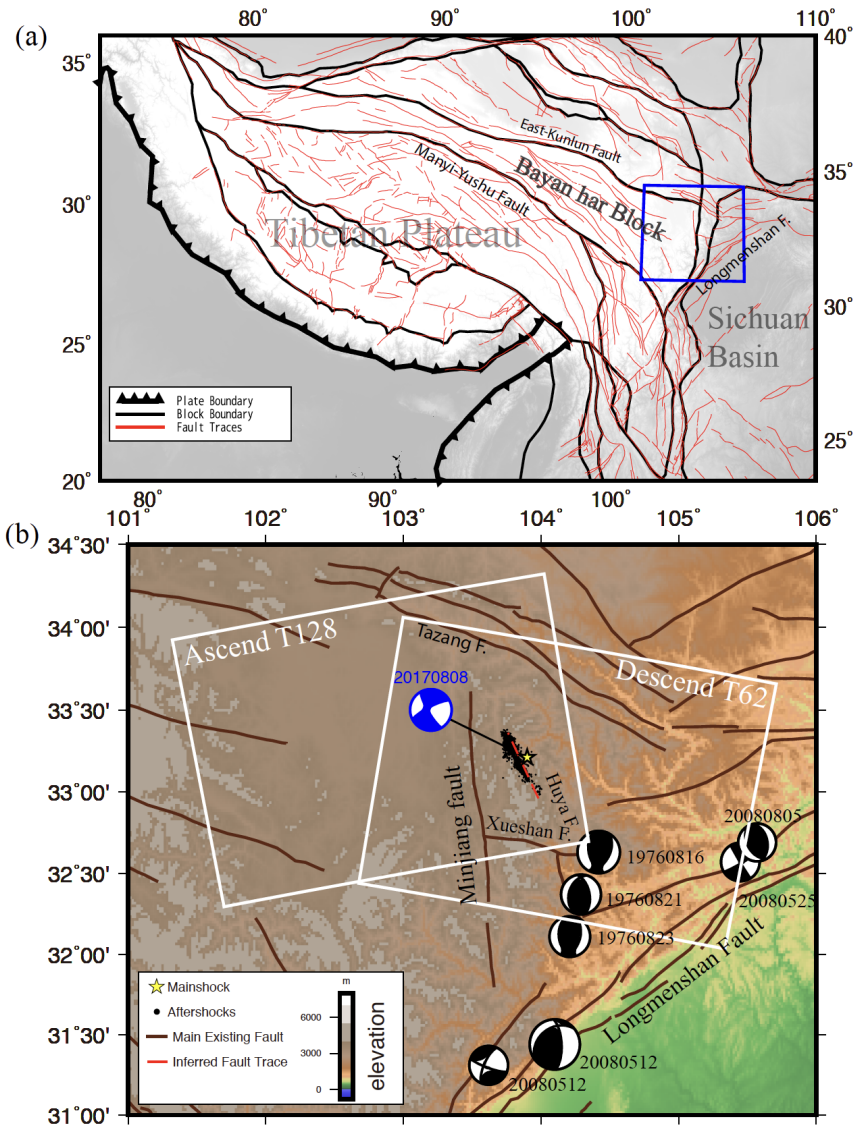


Figure 2.1: **(a)** Fault map and tectonic blocks of the Tibetan Plateau. **(b)** Close-up map of the eastern boundary of the Bayan Har Block shown by blue rectangle in **(a)**. Recent large (Mw $\geq$ 6.0) earthquakes in this region are shown with black global CMT focal mechanisms. The yellow star indicates the epicenter of the 2017 Jiuzhaigou earthquake and its GCMT focal mechanism is shown in blue. Mapped active fault traces are shown in brown ("Basic characteristics of active tectonics of China" 2003) and the inferred rupture zone of the Jiuzhaigou earthquake is indicated by a red dashed line. Aftershocks are shown as black dots (Fang et al., 2018), and align with the inferred northern extension of Huya Fault. White frames indicate the coverage of the ascending track 128 and descending track 62 of Sentinel-1A, respectively.

2.4 Data and Methods

2.4.1 InSAR data processing

Sentinel-1 data are processed using the GMTSAR software (Sandwell et al., 2011b; Sandwell et al., 2011a). For the coseismic deformation field, we use both ascending and descending orbit tracks to determine the radar line of sight (LOS) displacements, which provide constraints on both horizontal (mainly east-west) and vertical surface displacements. Considering that the phase change caused by atmospheric delay can be comparable to the signal of the earthquake itself, the tropospheric noise is mitigated by a linear regression between the phase and topography with the assumption that the troposphere is vertically stratified to first order (Figure A.1). After the correction of the atmospheric delay correlated with topography, random turbulent noise from the atmosphere remains. To further minimize its effect on our results, we consider all possible coseismic image pairs within 48 days of the event and choose one best interferogram with the clearest fringes for both flying directions, both 12-day pairs (Figure A.2). Information of all possible interferograms are listed in Table A.3. The selected ascending and descending interferograms have post-earthquake acquisitions taken 3 and 11 days following the mainshock, respectively.

To quantify any postseismic transient deformation following the mainshock, we obtained the first eight months of Sentinel-1A images for ascending track 128 and descending track 62. 82 interferograms using 23 ascending SAR scenes and 86 interferograms using 25 descending SAR scenes are produced based on a 60-day temporal baseline threshold and 200-meter perpendicular orbit baseline threshold. The selected interferogram pairs and A.2, all images are geometrically co-registered with one supermaster (i.e., the image that has the shortest temporal and spatial baselines as well as Doppler difference with respect to the rest of the data set) shown with red dots for each track. A coherence-based version of the Small Baseline Subset method (SBAS; Berardino et al., 2002; Schmidt and Bürgmann, 2003) is used for the time series processing. The InSAR data are corrected for atmospheric delay using an iterative common point stacking method (Tymofyeyeva and Fialko, 2015). Assuming that the atmospheric noise is random and temporally uncorrelated, we stack interferograms with a common scene in order to magnify and extract the atmosphere delay on that day. This method works well for capturing the spatially correlated but temporally uncorrelated noise. We also correct for topography-correlated delay in each iteration.

2.4.2 Inversion for Kinematic Rupture Parameters

The initial model fault geometry parameters of the coseismic rupture are constrained by the focal mechanism and the locations of early aftershocks (Fang et al., 2018). The kinematic slip inversion is conducted by superimposing the offsets of many rectangular dislocations in a homogeneous elastic half-space (Okada, 1992). Laplacian smoothing is applied to avoid abrupt slip variations between adjoining patches. As the resolution for slip distribution

decreases with depth, a depth-dependent fault meshing scheme is applied and dislocation patch sizes get larger with depth corresponding to the loss of resolution (Fialko, 2004). Each patch is allowed to have dip slip and left-lateral strike slip of up to 10 m. We also add constraints to the slip along the lower, left and right boundaries of the model rupture to be zero. No slip constraint was applied at the upper edge of the model fault surface.

Both ascending and descending tracks are used for the slip inversion. Horizontal coseismic GPS offsets of four sites (Zhao et al., 2018; Li et al., 2018a) are also used in the inversion. Relative InSAR and GPS weights are determined by a trade-off curve that balances InSAR and GPS RMSs (Figure A.3). Given the high resolution of each SAR image and the high spatial correlation of the data points, a quad-tree algorithm (Simons et al., 2002; Wang and Fialko, 2015) is used to downsample the data to improve the calculation efficiency. The inverse problem can be described as:

$$\begin{pmatrix} d_{\mathrm{sar}} \\ d_{gps} \\ 0 \end{pmatrix} = \begin{pmatrix} G_{sar} \\ G_{gps} \\ \lambda H^2 \end{pmatrix} \boldsymbol{m} \tag{2.1}$$

where d_{sar} represents the downsampled LOS displacement vectors from ascending and descending orbits, d_{gps} contains the GPS-measured horizontal coseismic offsets, G is the Green's function matrix, H is the Laplacian smoothing matrix weighted by smoothing factor, and m is the vector of fault slip components that is being inverted for using the constrained least squares method. We also solve for a ramp and offset in the inversion, that is, m not only contains the slip vector of each patch, but also the parameters for a plane $Ax + By + C = 0$ for both ascending and descending track data. Solving for a ramp mitigates the effect of gradients in the interferograms due to orbital errors or long-wavelength atmospheric delay.

To avoid local spurious noise being oversampled by the quad-tree algorithm, an iterative downsampling method is used (Wang and Fialko, 2015). After having an initial slip model, we use the synthetic LOS deformation of the slip model to refine the downsampling, which excludes the effect of random noise. After several iterations, the final grids are determined and data with low coherence (<0.1) is masked out.

We calculate InSAR and GPS RMS values between our model and observations using

$$RMS_{sar} = \sqrt{\frac{1}{n_1}\left([d_{sar} - d_{sar}{}']^2\right)}, d_{sar} = [d_{ascend}, d_{descend}] \tag{2.2}$$

$$RMS_{gps} = \sqrt{\frac{1}{n_2}\left([d_{gps} - d_{gps}{}']^2\right)}, d_{gps} = [d_e, d_n] \tag{2.3}$$

$n_1 = 1252$ is the total number of downsampled InSAR data points from both ascending and descending tracks. $n_2 = 8$ is the total number of horizontal GPS displacement components. ${d_{sar}}'$ and ${d_{gps}}'$ the modeled LOS and horizontal displacements. The relative weight of InSAR to GPS is 10, which is determined by the trade-off L-curve shown in Figure A.3.

2.4.3 Akaike Information Criterion and Bayesian Information Criterion

To quantify the performance of the two fault models presented in Section 2.6.1, the Akaike information criterion (AIC) and Bayesian information criterion (BIC) are determined. AIC and BIC are calculated through the following equations, where k is the total number of model parameters used, n is the number of data points.

$$AIC = 2k + n \cdot \ln\left(\frac{RMS}{\sqrt{n}}\right) \tag{2.4}$$

$$BIC = k \cdot \ln(n) + n \cdot \ln\left(\frac{RMS}{\sqrt{n}}\right) \tag{2.5}$$

$$RMS = \sqrt{\frac{1}{n}\left([d - d']^2\right)}, d = [d_{sar}, d_{gps}] \tag{2.6}$$

2.5 Results

2.5.1 Coseismic deformation field

Figure 2.2 shows the coseismic deformation derived from the selected Sentinel-1 interferograms. Close up views of wrapped ascending and descending interferograms are shown in Figure A.4, revealing that the near-fault data are mostly decorrelated and could introduce unwrapping error. Hence, areas with low coherence (<0.1) are masked out. In Figure 2.2(a), we can see an area with maximum displacements of around 16 cm away from the satellite in ascending orbit. The pattern of the deformation field roughly follows a butterfly pattern, which is indicative of strike-slip motion. Similarly, in 2.2(b) the deformation field of the descending-orbit interferogram has two prominent features: in the southeast displacements towards the satellite reach up to 12 cm and in the northeast motions away from the satellite amount to up to 6 cm. The opposite pattern of LOS displacements obtained from the ascending and descending orbits indicates the surface deformation is mainly horizontal, which is evident in 2.2 (c)(d) showing the derived vertical and E-W motions, respectively. The InSAR deformation field is consistent with the general features of a typical left-lateral strike-slip earthquake with a small dip-slip component. The denser fringes in the SW could be an indication of the dipping direction of the seismogenic fault.

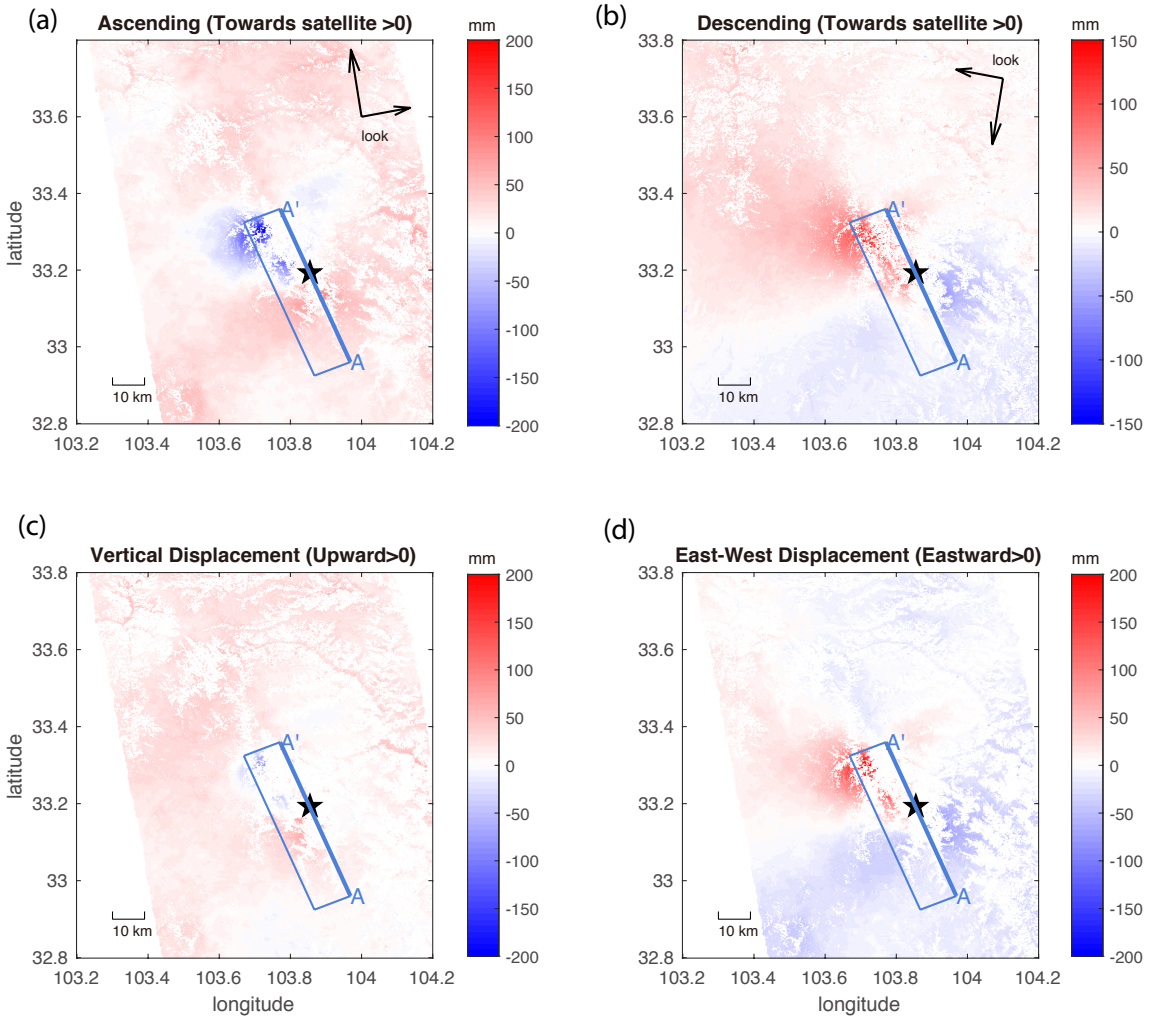


Figure 2.2: **(a)** Ascending LOS displacement, **(b)** descending LOS displacement obtained from selected 12-day interferograms spanning the time of the earthquake. Satellite flight and look directions are shown by arrows. Displacements towards the satellite are positive. **(c)** vertical and **(d)** E-W displacement derived from **(a)** and **(b)**. Uplift and eastward displacements are positive. USGS epicenter of Jiuzhaigou earthquake is shown with black star.

2.5.2 Coseismic slip distribution

The rupture geometry is determined by a combination of relocated aftershocks (Fang et al., 2018) and the location of InSAR near-field decorrelation (Figure A.5). Our fault model has a strike of 158° and dips 70° to the southwest, which is similar to the focal mechanism result from USGS (Table A.1) and consistent with the denser fringes to the southwest. The model fault has a length of 48 km and a width of 30 km, extending beyond the aftershock zone. We set fault patch sizes to increase with depth to compensate for the decreasing model resolution (Fialko, 2004). The smoothing parameter λ of 0.0005 is based on examination of the tradeoff of model misfit and roughness shown in Figure A.6. Examples of overly smooth and overly rough distributed slip models are shown in Figure A.7.

Our preferred coseismic slip model is shown in Figure 2.3. The slip pattern is dominated by left-lateral strike slip with a small dip-slip component (rake ∼10°). Slip is concentrated in a single patch, with peak slip of about 1.2 m in a depth range from 3-10 km. Early aftershocks appear to wrap around the high-slip area of the rupture. The moment magnitude calculated from the geodetically-constrained finite slip model, M_w6.5, is the same as the moment magnitude derived from seismic data. The observed and modeled LOS and GPS displacements are shown in Figure 2.4. The RMS values between observed and modeled InSAR and GPS are 1.028 cm and 0.262 cm, respectively. We also show the re-wrapped LOS displacements and their model predictions in Figure A.8.

2.5.3 Postseismic deformation and afterslip inversion

To see if there is any postseismic transient deformation following the mainshock and to test if afterslip acts to compensate the SSD, we obtained the first eight months of Sentinel-1A images for ascending track T128 and descending track 62 and determine the cumulative displacement field over the Jiuzhaigou earthquake region.

Figure A.9 shows the estimated atmospheric phase delay using the iterative common point stacking method including removal of elevation-correlated phase (Tymofyeyeva and Fialko, 2015). The atmospheric delay is removed before doing SBAS time series analysis. Figure 2.5 shows the cumulative displacement field at each epoch after the 2017 Jiuzhaigou earthquake. No clear postseismic signal near the coseismic rupture zone is seen in either the ascending or descending observations with a noise level of ∼5 mm (RMS).

To further quantify the amount of afterslip allowed for by the data, we attempt to invert the cumulative postseismic LOS displacement field for a slip model (Figure 2.3b). The fault geometry remains the same as in the coseismic slip inversion. We apply the same left-lateral constraint on the afterslip direction as in the coseismic slip inversion. The maximum obtained slip is 4.2 cm, which is less than 3.5% of the maximum coseismic rupture and the inferred geodetic moment of the afterslip is 3.6% of the coseismic value. Visual comparison of observed and model-predicted LOS displacements (Figure A.10) suggests that this model

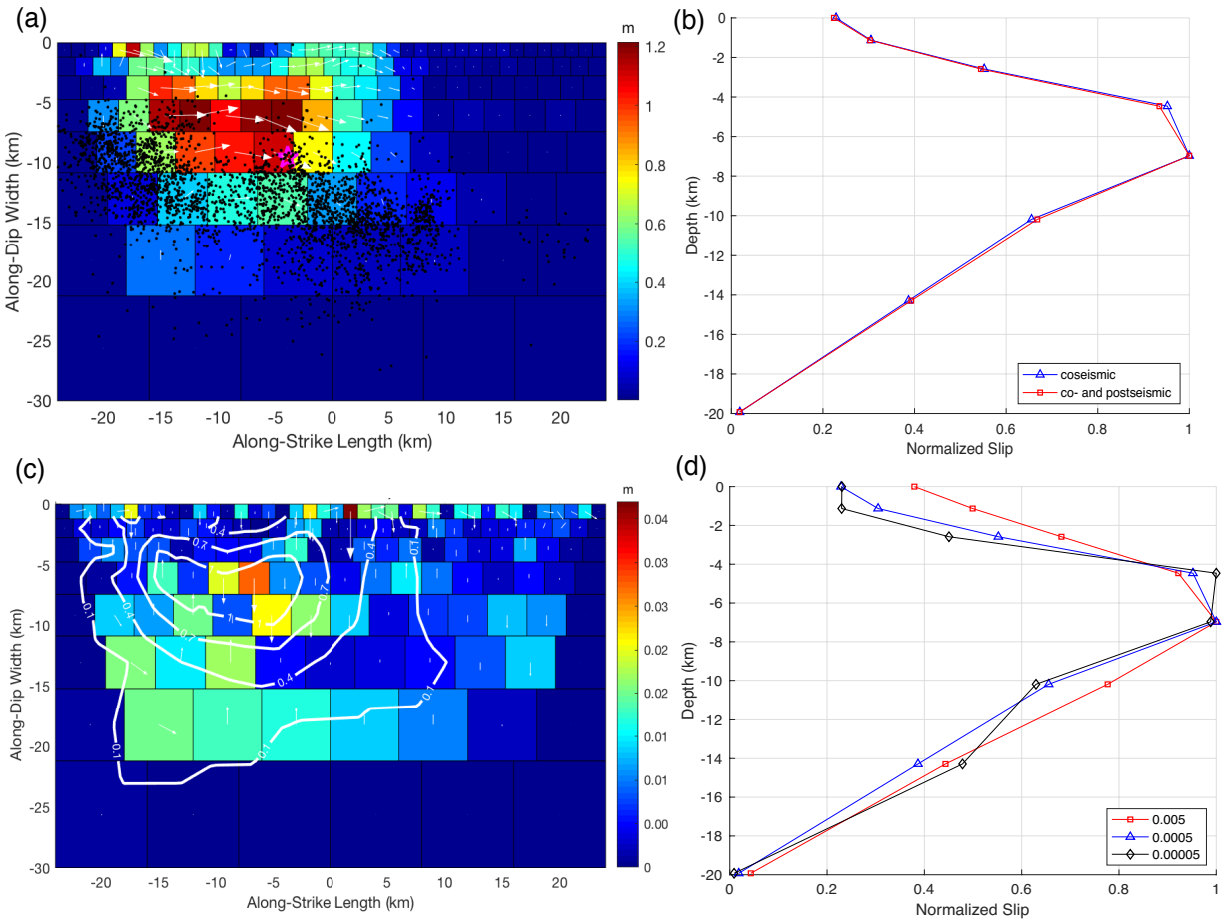


Figure 2.3: **(a)** Coseismic slip distribution of the 2017 Mw6.5 Jiuzhaigou earthquake derived from Sentinel-1A InSAR data. Color shows the slip in meters. The origin corresponds to the center of the fault's upper edge, which is at 103.82°E, 33.15°N. Pink star denotes the hypocenter from USGS. Black dots represent relocated aftershocks within 30 days after the Jiuzhaigou earthquake (Fang et al., 2018). **(b)** Distribution of normalized average coseismic, and of co- plus postseismic slip versus depth, both showing a clear SSD. **(c)** Inverted afterslip based on the cumulative displacement field of both ascending and descending orbit data (RMS_{sar}=0.35 cm). The coseismic slip is shown in white contour. **(d)** Distribution of normalized coseismic slip versus depth given different smoothing parameters. The SSD is slightly reduced when more smoothing is applied.

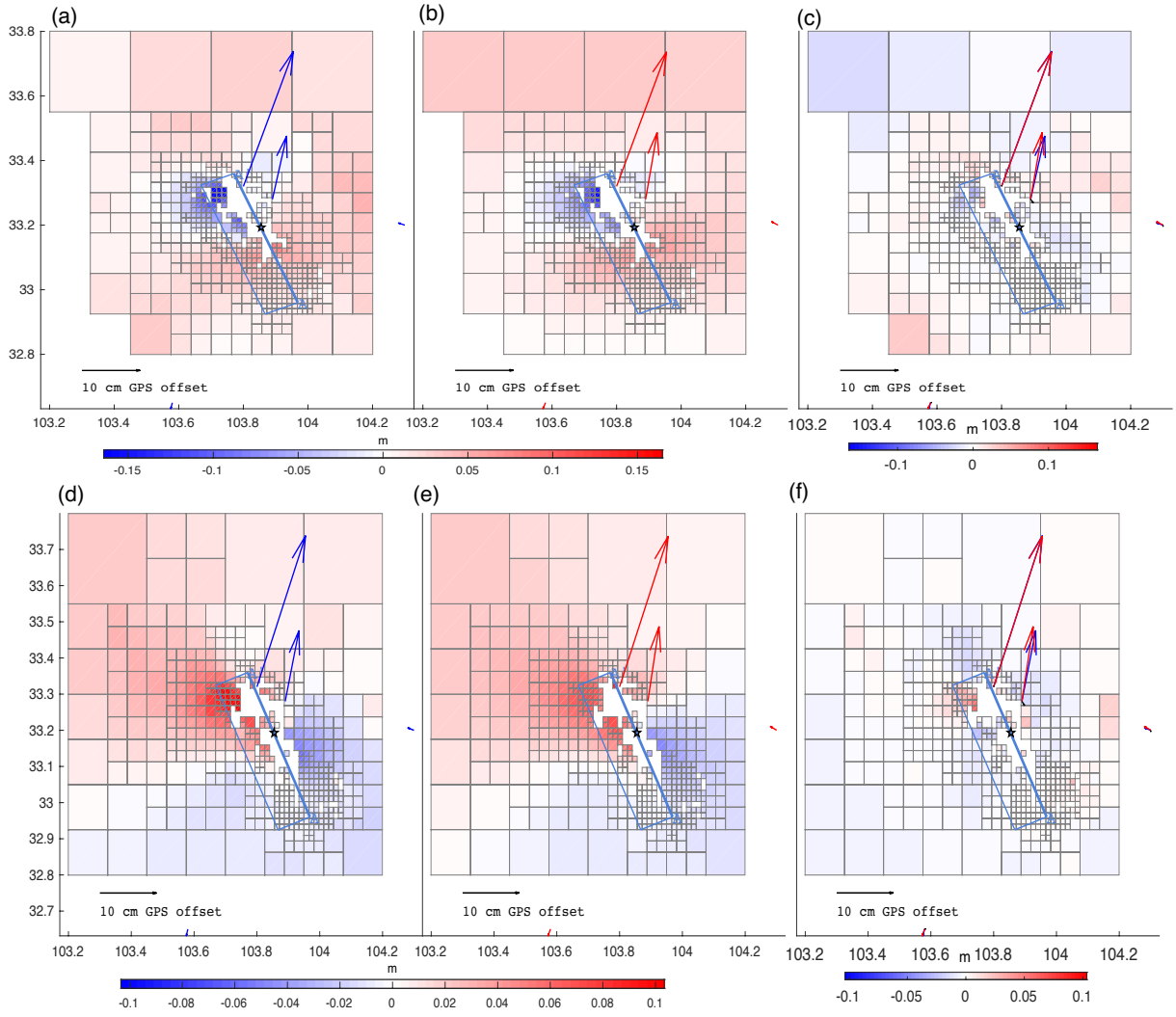


Figure 2.4: Comparison of observed and modeled LOS displacements from both ascending and descending Sentinel-1A tracks. **(a-c)** are observation, model and observed minus modeled residuals for ascending orbit T128. **(d-f)** are corresponding maps for descending orbit T62. Blue and red arrows show observed (Zhao et al., 2018) and modeled GPS offsets at two near-field stations. The model fault plane is drawn for reference and the upper edge is marked with AA'.

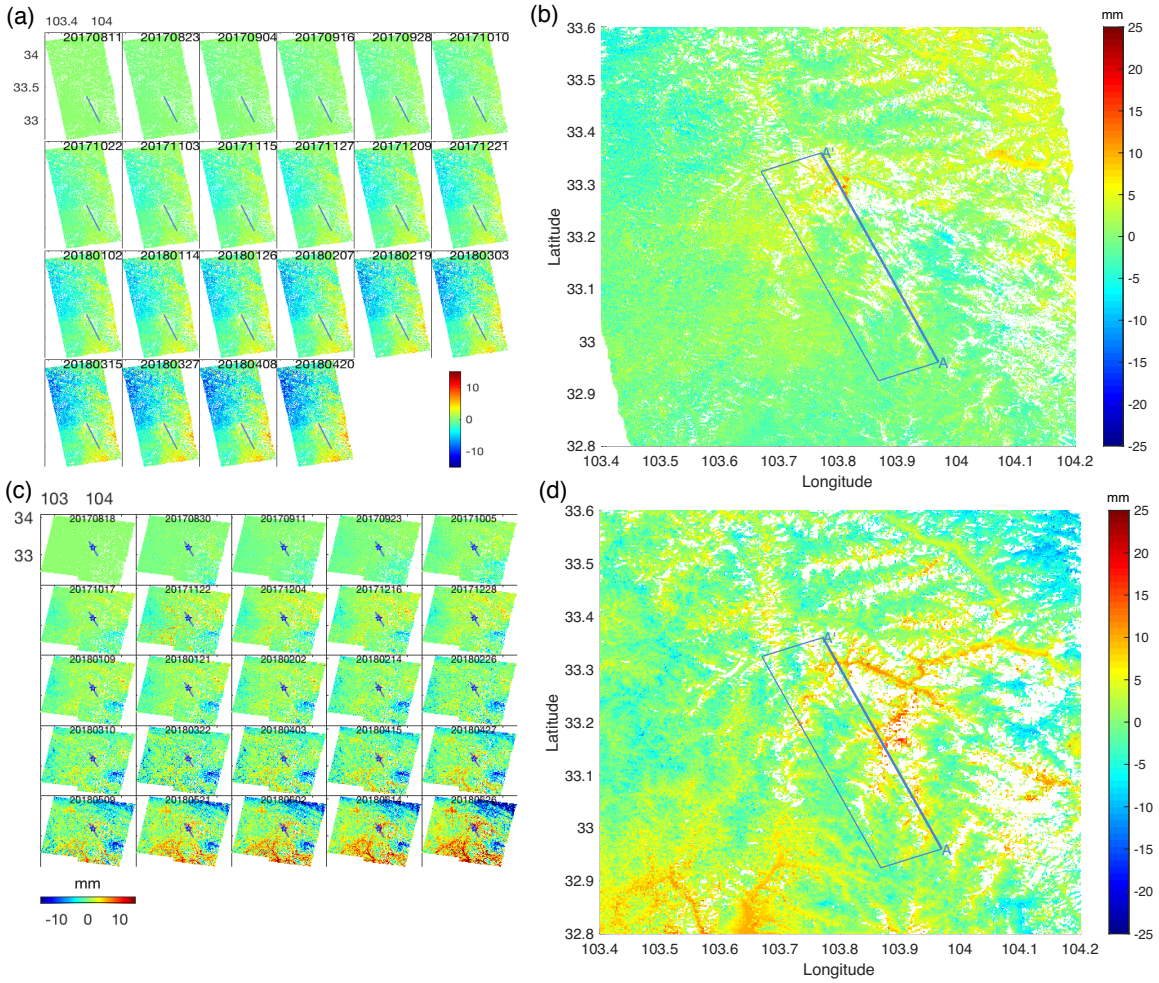


Figure 2.5: **(a)** Cumulative LOS displacement field generated by SBAS method for ascending orbit track T128. The scale for all images is in mm. **(b)** A zoom-in figure of cumulative displacement field by April 20, 2018. A ramp is removed from the total cumulative displacement before calculating RMS. **(c)** **(d)**. Similar to **(a)** and **(b)**, but for descending orbit. The RMS values of the ascending and descending cumulative displacement fields are 4.82 mm and 5.48 mm, respectively.

is not capturing meaningful systematic features in the data and the inverted afterslip could be mostly noise. We also combined the co- and postseismic displacement field to obtain an 8-month co- plus postseismic slip model (Figure A.11, Figure A.12). In this model, we also include GPS measurements spanning the earthquake and up to more than 10 months of postseismic deformation. The distribution of normalized average slip versus depth are shown in Figure 2.2b, which does not differ much from the coseismic model. The seismic moment discrepancy between the two models is less than 0.5% of the coseismic value.

Hence, no clearly resolvable afterslip is indicated by InSAR for the first 8 months after the 2017 Jiuzhaigou earthquake at the confidence level of 4.2 cm. In the depth interval of the shallow coseismic slip deficit (0-3 km), no more than 1 cm of slip could plausibly have occurred. The shallow slip deficit is not compensated by the early afterslip.

2.6 Discussion

2.6.1 Seismogenic fault geometry of the Jiuzhaigou earthquake

So far, slip models proposed for the 2017 Jiuzhaigou earthquake share similar overall geometries but differ in strike, dip and number of fault segments. Single-fault-segment models deduced from the location of early aftershocks share a similar strike angle around 150° (Ji et al., 2017; Zhao et al., 2018) and a preferred dip angle around 70°-85°, which is similar to our study. However, Zhang et al. (2018c) proposed a dip angle of 50° to optimally fit their GPS and InSAR observation. Despite of the different fault geometries, all slip models share a similar overall coseismic rupture pattern (Ji et al., 2017; Sun et al., 2018; Zhang et al., 2018c; Zhao et al., 2018). In all models, the slip is concentrated in the 3-10 km depth interval with a maximum slip of around 1 m.

Sun et al. (2018) suggest a multi-fault scenario with two main fault segments based on constraints from teleseismic data and the interferograms. The deformation field is not strictly quadrantal, with the largest displacements on the northwest (Figure 2.2). Both a second branch to the west or different elastic properties may help to address this asymmetry. To test Sun et al. (2018)'s proposal, we conduct an inversion with a secondary rupture segment based on their results. The inverted slip model is shown in Figure A.13. Adding a second fault does not change the general slip pattern of the main patch. Slip on the secondary fault is mostly left-lateral strike slip with a maximum slip of 0.5 m and geodetic moment equivalent to an Mw = 6.11. Figure A.14 shows the comparison of LOS deformation and the modeled deformation field. However, the LOS displacement residuals for the 2-fault-segment model and RMS misfit do not improve much (RMS = 0.85 cm) compared to the single-fault model (RMS = 1.06 cm) despite the significant number of additional model parameters. AIC and BIC values also do not show a significant improvement (Table A.2).

If the northern extension of the Huya fault is a young fault with limited slip history, it is

likely that the fault is made up of multiple discontinuous fault branches. Long et al. (2019) relocated the Jiuzhaigou earthquake aftershock sequence and their cross-sections reveal a complex seismogenic fault geometry with wide aftershock zone and varying dip angles especially in the northern part of the rupture. The secondary fault proposed by Sun et al. (2018), and the diversity of mechanisms in their multi-point source moment tensor inversion of the event, lend additional support to such an immature fault zone structure. Clearly, the planar fault structure in our model is an idealized representation, where in reality finer-scale strike and dip variations exist along discontinuous fault segments. While a single planar fault model may not perfectly recover the coseismic displacement field, the buried nature of the slip, poor near-field coherence and atmospheric noise in the InSAR data prevent us from resolving the detailed geometry. With the aim of capturing the general pattern of the kinematic behavior, a single planar fault model with homogeneous crustal properties adequately characterizes this event. The immaturity of this fault segment and lack of a well-developed and weakened gouge zone may play a key role in the observed SSD and minimal afterslip following the Jiuzhaigou earthquake.

2.6.2 Implications of shallow slip deficit (SSD) and lack of afterslip

The Jiuzhaigou earthquake exhibits a strong SSD and lacks afterslip exceeding 3-4% of the coseismic moment. The coseismic slip model in this study features two short patches of surface slip of about 0.5 meter. However, field investigations did not find a surface rupture (Ji et al., 2017; Sun et al., 2018), and an abrupt discontinuity only exists in the modeled LOS displacement field but not in the observed interferograms (Figure A.4). We consider the surface slip features to be spurious due to the loss of InSAR correlation near the fault and GPS station J416 being so close to the modeled fault trace. Independent of whether this event is a fully blind rupture or not, the slip model clearly shows a SSD (Figure 2.3). The slip peaks at 5 km depth with about 1.2 m maximum slip, but diminishes with a large slip gradient to near zero at the surface.

The inferred sharp slip gradient and SSD have important implications for the accommodation of fault strain in the shallow part of the crust and fault frictional properties. Ultimately, the SSD should be recovered through one or more earthquake cycles to maintain the conservation of the long-term slip. For example, rapid shallow afterslip (e.g., Floyd et al., 2016; Johanson et al., 2006) or an eventual earthquake that ruptures only the shallowest layer (Elliott et al., 2011) could catch up with the coseismic slip at depth. It is also possible to have a larger event that making up slip deficits built up in previous incomplete fault ruptures (e.g., Shen et al., 2009). The slip budget could also be partially compensated by interseismic shallow fault creep (e.g., Langbein et al., 2006). Alternatively, the inferred SSD could be due to distributed coseismic brittle damage in the uppermost section of this young and incipient fault (e.g., Fialko et al., 2005; Kaneko and Fialko, 2011). Moreover, such distributed fault zone damage may also be evident during the postseismic and interseismic periods. For example, shallow

creep was only observed along a 10-km-long fault segment after the Izmit earthquake whereas other parts of the fault may have experienced distributed creep or inelastic deformation (Çakir et al., 2012). Lindsey et al. (2014a) also found that enhanced interseismic strain rates could reduce yield strength in the fault zone and thus lead to unrecoverable distributed fault zone failure, which was also proposed as one possible source for SSD.

In addition to the 2017 Mw6.5 Jiuzhaigou earthquake, there are several major strike-slip earthquakes exhibiting the phenomenon of the SSD, including the 1992 Mw7.3 Landers earthquake, 1999 Mw7.1 Hector Mine earthquake and 2003 Mw6.5 Bam earthquake (e.g., Fialko et al., 2005; Kaneko and Fialko, 2011; Xu et al., 2016). The 2003 Bam earthquake was of comparable magnitude as the 2017 Jiuzhaigou event and its slip concentrated mostly at seismogenic depth (4-10 km) with minor slip in the uppermost crust (Fialko et al., 2005). Insignificant afterslip was found along the surface rupture in 10 months after the 2003 Bam earthquake (Fialko et al., 2005). Fielding et al. (2009) used postseismic data spanning 3.5 years and explained a zone of near-fault subsidence along the rupture as being due to dilatancy recovery in the shallow fault zone: the compaction of cracks and damaged zones is inferred to slowly recover coseismic dilatation. This is consistent with the distributed-failure hypothesis of Fialko et al. (2005). Therefore, in the case of the Jiuzhaigou earthquake that ruptured the buried Huya fault, the lack of resolvable afterslip in the first 10 months' postseismic time series supports the scenario of distributed coseismic damage across the shallow and immature fault zone. It is possible that a recovery of dilatancy could be resolved in several years, as was found in the case of the Bam earthquake. Wimpenny et al. (2017) compiled a series of geodetically derived co- and postseismic slip models and compared the postseismic to the coseismic moment release. Similar to the Bam earthquake, whose afterslip amounts to only 1% of the coseismic moment, the Jiuzhaigou earthquake has one of the lowest afterslip signals of recorded earthquakes (1%−3%). In contrast, mature faults with a well-developed shallow gouge zone may feature a temporary SSD that gets compensated by rapid shallow afterslip, as was observed for the 2004 Parkfield (Johanson et al., 2006) and the 2014 West Napa (Floyd et al., 2016).

Alternatively, Xu et al. (2016) showed that for some events at least part of the SSD can be an artifact due to incomplete data near the rupture, suggesting that more than 60% of the overall SSD could be recovered if immediate near-fault data are considered. Huang et al. (2017) also found that the SSD is affected by the size of shallow patches as well as the smoothing parameter in their model inversions. The SSD could be partly recovered if a finer fault patch size and a rougher model is applied if better near-fault data were available. Detailed field investigations and near-field observations using new techniques such as optical imaging or differential terrestrial lidar (e.g., Milliner et al., 2015; Scott et al., 2018) could provide additional data constraints to better assess evidence for or against distributed coseismic fault-zone shearing.

Based on the evidence available so far, even though some of the SSD we found could be

explained by lack of near field deformation data, we argue that the SSD is a real feature for the Jiuzhaigou earthquake as well as for most, if not all, strike-slip earthquakes on young faults with a cumulative slip history of less than ∼25 km (Dolan and Haravitch, 2014). Dolan and Haravitch (2014) examined the extent of SSDs of major strike-slip earthquakes and found a striking correlation with fault cumulative displacement, where structurally less mature young faults (cumulative slip history <25km) feature a larger SSD. The fault hosting the Jiuzhaigou earthquake is most likely an incipient fault that is going through a process of fault zone development, where the fault geometry has complex variation and a substantial portion of shallow coseismic deformation may have been broadly distributed. The immature shallow deformation zone apparently lacks faults with velocity strengthening properties, explaining the absence of resolvable afterslip in the zone of coseismic stress increase up dip of the rupture. If the SSD is a characteristic of immature strike-slip faults, slip histories of young strike slip faults may be systematically underestimated. Thus, better understanding of the nature of the slip deficit is also important for paleoseismic and seismic hazard studies. To assess the earthquake hazard implications of the Jiuzhaigou earthquake and its SSD, detailed field studies focused on finding active fault strands and paleoseismic evidence of ground rupture from previous events are warranted.

2.6.3 Effects of the Wenchuan earthquake on the 2017 Jiuzhaigou event

The relatively short separation in space and time from the catastrophic May 12th, 2008, Mw7.9 Wenchuan earthquake suggests the possibility of the Jiuzhaigou earthquake having been triggered by co- and postseismic stresses of the Wenchuan event. The Wenchuan earthquake was the largest earthquake during the past 50 years in China and caused more than 60,000 casualties. Located at the eastern boundary of the Tibetan Plateau, it ruptured the Beichuan Fault and the Pengguan Fault of the Longmenshan fault zone (Shen et al., 2009). Nine years later, the 2017 Jiuzhaigou earthquake struck the northeast boundary of the Tibetan Plateau around 370 km NNW of the 2008 epicenter.

In previous studies, the static Coulomb stress changes were calculated from different coseismic Wenchuan slip models by Han et al. (2018), Li et al. (2018a), and Zhao et al. (2018). The epicenter of the Jiuzhaigou earthquake falls into a region of increased static Coulomb failure stress change of 5-10 kPa, suggesting the Wenchuan earthquake accelerated its occurrence. However, Jia et al. (2018) find a decreased seismicity rate in the Jiuzhaigou region after the Wenchuan earthquake and also inferred a negative Coulomb stress change from their model, suggesting the occurrence of the Jiuzhaigou earthquake was in fact delayed by the 2008 Wenchuan earthquake.

However, considering the large magnitude of the Wenchuan earthquake, one cannot ignore the impact of its postseismic viscoelastic relaxation (e.g., Diao et al., 2018; Huang et al., 2014). Here, we obtained both negative Coulomb stress change and negative stress change

caused by the 9-year-viscoelastic-relaxation, even though the absolute value of stress change is rather small ∼1 kPa (Figure A.15). We used the coseismic slip model from Tong et al. (2010) and rheology properties from Diao et al. (2018) for the calculation using RELAX software (Barbot and Fialko, 2010). Stress change is projected onto the average slip vector on the Jiuzhaigou earthquake plane obtained in our model.

Even though the calculated stress change pattern differs between different coseismic slip models, receiver fault geometry and rheology properties, the common feature among the results above is their relatively small stress change no matter if it is negative or positive. Dynamic stress transients of teleseismic large earthquake could produce substantially larger transient stress changes depending on the magnitude of the teleseismic event and the distance from the receiver. However, given the long timespan between the two events, it is difficult to assert that this is a case of delayed dynamic triggering. We conclude that the 2008 Wenchuan earthquake did not significantly affect the time of occurrence of the Jiuzhaigou earthquake. The 2017 Jiuzhaigou earthquake is ultimately a result of the long-term collision of Indian Plate and Eurasian Plate, and the eastward extrusion of the Tibetan Plateau and its timing nearly a decade after the Wenchuan earthquake may not reflect a direct triggering relationship.

2.7 Conclusion

We obtained the coseismic and early postseismic deformation field of the 2017 Jiuzhaigou earthquake using both ascending and descending Sentinel-1A InSAR and GPS data. The inverted coseismic slip model indicates peak slip of up to ∼1 m at around 5 km depth accompanied by a strong SSD. A single-fault dislocation model does not capture all the observed deformation features, suggesting the rupture occurred along a young fault system with a complex shallow rupture process. The complex rupture geometry and distributed failure are further supported by the relocated aftershock distribution. No significant early afterslip was observed in the first 8 months after the earthquake. We argue that the observation of a pronounced SSD and lack of early afterslip of the Jiuzhaigou earthquake is a representative feature of immature faults, in which case the phenomenon of SSD is a stage that all incipient young strike-slip faults go through. We would expect that distributed coseismic failure in the uppermost part of the brittle crust accommodates the shallow slip budget on such young faults. Even though the 2017 Jiuzhaigou earthquake occurred within only 7 years and 370 km from the M 7.8 2008 Wenchuan earthquake, both coseismic and postseismic stress changes from the 2008 event were too small to produce a substantial clock advance of the later event.

Chapter 3

Partial Coupling and Earthquake Potential along the Xianshuihe Fault, China

The chapter was adapted from: Y. Li and R. Bürgmann (2021). "Partial Coupling and Earthquake Potential Along the Xianshuihe Fault, China". *Journal of Geophysical Research: Solid Earth* 126.7. ISSN: 2169-9313. DOI: 10.1029/2020jb021406

3.1 Abstract

The left-lateral Xianshuihe Fault is located at the eastern boundary of the Tibetan Plateau and is one of the most active faults in China. It is associated with substantial seismic potential, with more than 20 Mw>6 earthquakes since 1700. The fault has been documented to be creeping at the surface for decades; however, the spatial and temporal distributions of shallow creep along the fault are not well resolved. In this study, we obtain high-resolution interseismic velocity maps along the 350-km-long central Xianshuihe Fault and Interferometric Synthetic Aperture Radar (InSAR) time series along the Kangding segment using ascending and descending Sentinel-1 data. The InSAR data reveal multiple creeping sections and the estimated surface creep rates show high along-strike variability. A coupling model characterizes the distribution of creep with depth. The seismic potential of apparent rupture asperities along the Xianshuihe Fault is further refined by considering fault-crossing baseline data and the distribution of historical ruptures and microseismicity. Moreover, a stress-driven afterslip model of the observed accelerated creep around the Mw 5.9 2014 Kangding rupture indicates substantial shallow afterslip, which provides further constraints on the distribution of locked and creeping patches along this section of the Xianshuihe Fault.

3.2 Introduction

Creeping faults slip aseismically in their upper few kilometers and have been observed in various kinds of tectonic settings and environments around the world (Harris, 2017; Bürgmann, 2018). Continental strike-slip creeping faults represent an important portion of the slow slip family. In addition to field deployed creepmeters, alignment arrays and near-field GPS measurements, the dense spatial sampling of InSAR has proved to be particularly valuable for studies of creeping strike-slip faults, such as the San Andreas Fault (e.g., Ryder and Bürgmann, 2008; Tong et al., 2013; Khoshmanesh et al., 2015), the Hayward-Calaveras fault zone (e.g., Shirzaei and Bürgmann, 2013; Chaussard et al., 2015), and the Rodgers Creek Fault (e.g., Funning et al., 2007) in California, the Haiyuan Fault (e.g., Jolivet et al., 2012; Jolivet et al., 2013) in China, the North Anatolian Fault (e.g., Cakir et al., 2005; Kaneko et al., 2013; Cetin et al., 2014; Rousset et al., 2016; Aslan et al., 2019) in Turkey, the El Pilar fault in Venezuela (e.g., Pousse Beltran et al., 2016), and the Chaman Fault in Afghanistan and Pakistan (e.g., Fattahi and Amelung, 2016; Barnhart, 2017). Spatiotemporal variations of fault creep rates can be linked to the spatial distribution of locked fault sections and the occurrence of nearby earthquakes (e.g., Jolivet et al., 2012; Shirzaei and Bürgmann, 2013; Khoshmanesh et al., 2015).

Even though there is little interseismic strain accumulation along the uppermost part of rapidly creeping faults, destructive earthquakes can still occur on these faults to compensate for the slip deficit accumulating on coupled portions of the fault at greater depth over time. However, due to limited observations available, the mechanisms and dynamics of fault creep still remain unclear. Regarding what makes a fault creep, several possible explanations have been proposed, including specific fault zone materials that have low frictional resistance and rate-strengthening properties (e.g., talc-bearing serpentinite found near creeping faults in California, Moore and Rymer, 2007; Lockner et al., 2011), elevated pore pressure in the fault zone that reduces the effective normal stress (e.g., Superstition Hills Fault in California Wei et al., 2009), and the response to static and/or dynamic stress changes from nearby earthquakes (e.g., the North Anatolian Fault, Çakir et al., 2012). In the context of regional seismic hazard evaluation, a better characterization of creeping faults can also help map out the distribution of locked and creeping patches on the fault that can be incorporated into rupture and ground motion modeling (e.g., Aagaard et al., 2012).

The left-lateral Xianshuihe Fault (XSF) is located at the eastern boundary of the Tibetan Plateau (Figure 3.1), which is one of the bounding faults that accommodates the distributed convergence of the Indian and Eurasian plates (e.g., Allen et al., 1991; Xu and Kamp, 2000; Zhang, 2013). Being one of the most active faults in China, the Xianshuihe Fault is associated with substantial seismic potential. Since 1700, more than 20 Mw>6 earthquakes occurred along the Xianshuihe Fault (e.g., Allen et al., 1991; Wang et al., 2009; Bai et al., 2018), including the 1973 Ms 7.4 Luhuo earthquake (e.g., Wen et al., 2008), the 1981 Ms 6.8 Daofu earthquake (e.g., Wen et al., 2008), and the most recent 2014 Mw5.9 Kangding earthquake

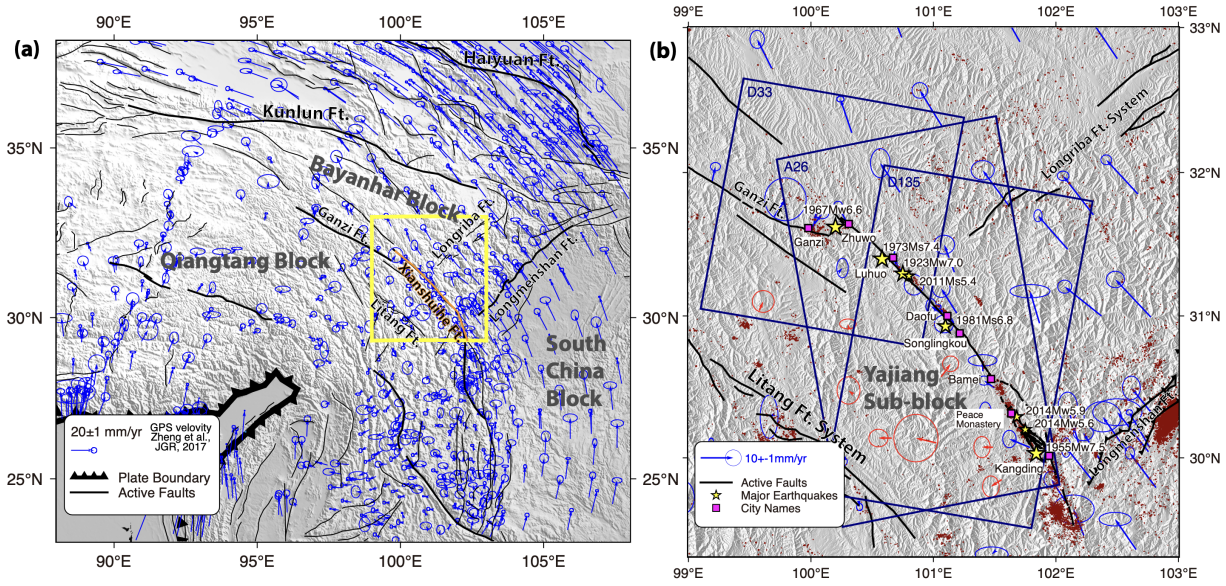


Figure 3.1: **(a)** Overview map of active crustal deformation across the Tibetan Plateau. The study region is indicated by the yellow rectangle. Blue arrows show GPS velocities tipped with 95% confidence ellipses measured during 1991–2015 (Zheng et al., 2017) referenced to the Yajiang sub-block. The Euler pole of the Yajiang block (angular rotation of lon/lat/w= [94.38°E, 22.38°N, -1.07°/Myr] with respect to Eurasia) is determined from velocities of GPS stations inside the Yajiang block. Velocities of GPS stations that were used to calculate the Euler pole are shown in red arrows. **(b)** A zoom-in map of the Xianshuihe Fault region. Navy blue boxes show the Sentinel-1 SAR coverage for ascending track 26 and descending tracks 33 and 135. Major earthquakes since 1923 are shown in yellow stars. Dark red circles show regional M $\geq$ 1.5 seismicity from China Seismic Experiment Site (2009-2019; Wu et al., 2019). Active fault lines are modified from Taylor and Yin (2009), Chevalier et al. (2017), and Bai et al. (2018).

doublet (e.g., Jiang et al., 2015b) (Figure 3.1).

Geological studies found its late Quaternary slip rates to be ∼10 mm/yr (e.g., Bai et al., 2018) consistent with the geodetic slip rate inferred from 25 years (1991–2015) of GPS measurements (e.g., Zheng et al., 2017). Regarding recent InSAR studies, Wang et al. (2009) first obtained a velocity map using data from the ERS-1/2 and Envisat satellites acquired between 1996 and 2008, and inverted for a 9∼12 mm/yr slip rate on a buried screw dislocation with a shallow 3-6 km locking depth along the northwestern XSF. Zhang et al. (2019) obtained a velocity map using Sentinel-1A data between December 2014 and November 2016 showing evidence of creep on the fault. Ji et al. (2020) further presented a velocity map using Sentinel-1 data covering a longer period from October 2014 to March 2018 and confirmed the existence of surface creep along the XSF. Moreover, Zhang et al.

(2018b) used more than 30 years of fault-crossing short-baseline and short-leveling surveys since 1976 to show the surface creep and slip behavior at seven sites along the XSF. The largest surface creep occurred near the 1973 Luhuo earthquake rupture, reflecting decaying surface slip rates following this event. However, details of the distribution of creep in space and time have not yet been resolved.

To characterize fault creep at and below the Earth's surface, dense and accurate measurements of crustal deformation in both the near field and far field are crucial. The dense sampling of InSAR and its global coverage make it a unique geodetic tool that we can leverage in areas that lack dense GPS coverage. The launches of Sentinel-1A in 2014 and Sentinel-1B in 2016 effectively reduced the satellites' recurrence intervals to as little as 6 days in some areas (e.g., Europe) and 12 days in China, making interseismic deformation and its temporal variation possible to resolve in a relatively short time period. However, there are still substantial challenges for InSAR observations of creeping faults, given that the interseismic signals tend to be relatively subtle (∼mm/yr) and are often contaminated by atmospheric noise.

Therefore, in this study, we aim to find optimal InSAR processing schemes that focus on retrieving the subtle interseismic signals as well as characteristics of surface creep along the XSF. As the recent Kangding earthquake occurred just after the launch of Sentinel-1, we also seek to quantify the aseismic fault slip response to the seismic event, and to assess how such seismic events interact with the interseismic fault creep.

3.3 Data and Methods

3.3.1 InSAR data and processing

The InSAR data are processed using the GMTSAR software (Sandwell et al., 2011b; Sandwell et al., 2011a). We use data from two Sentinel-1 descending tracks (135, 33) and one ascending track (26) covering the study region. The spatial coverage of the Sentinel-1 data is shown in Figure 3.1(b). All available (254) images from December 2014 to August 2019 are considered to estimate interseismic velocities and time series, excluding scenes collected before the 2014 Mw5.9 Kangding earthquake to separate out the coseismic offsets. More detailed information about the available interferograms can be found in Table 3.1.

Usually, the correlation between two SAR acquisitions will decrease with increasing time span due to the growth of vegetation, sediment transport, and extreme weather conditions. However, in some cases, interferograms spanning several years with small perpendicular baselines may have better performance than a much shorter-duration interferogram with an image contaminated by substantial atmospheric noise (e.g., wet or snowy season acquisitions). Therefore, to explore the optimal selection and combination of interferogram pairs for the velocity map formation, interferograms are produced based on a 2000-day temporal

Tracks	Orbit	# Scenes	# Intf	Time span	# Intf selected
T135	Descending	57	340	20141213-20190720	13
T33	Descending	95	1090	20141218-20190713	14
T26	Ascending	102	1174	20141206-20190713	21

Table 3.1: Sentinel-1 InSAR data after the 2014 Kangding earthquake sequence generated in this study. (# Intf: the number of all available interferograms generated in this study # Intf selected: the number of interferograms that are selected to form the average velocity map.)

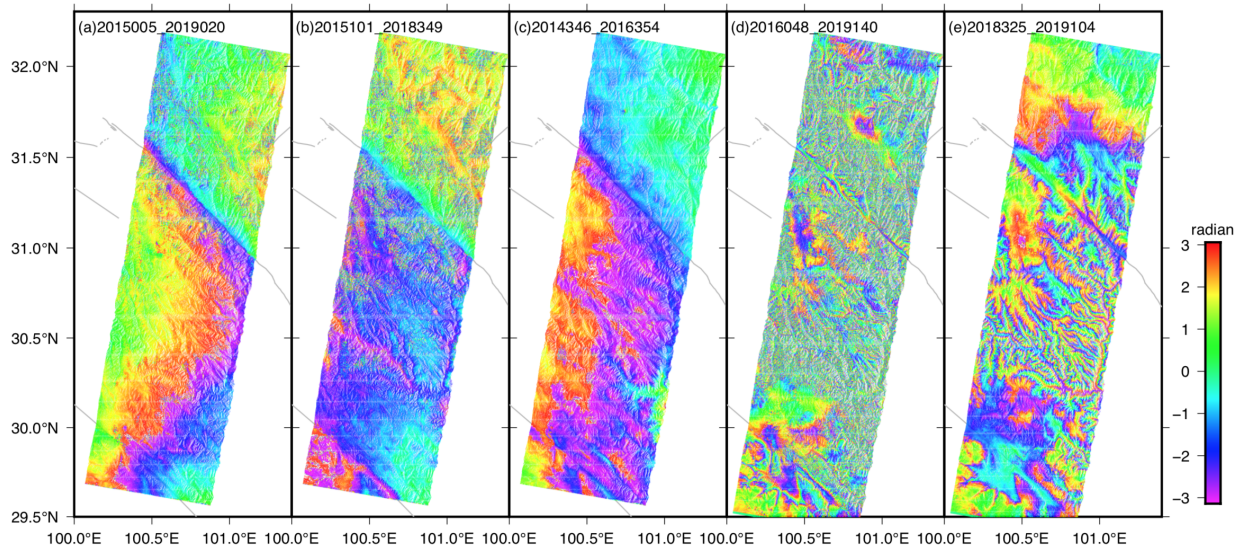


Figure 3.2: **(a)-(c)** Examples of selected good interferograms from descending track T135F3. **(d)-(e)** Examples of bad interferograms that are contaminated by decorrelation and topography-correlated atmospheric noise, respectively. Dates used to form the interferograms are shown at the top of each panel. See Figure B.5 for additional examples.

baseline threshold and 20-meter perpendicular orbit baseline threshold criteria. Baseline plots for all interferograms can be found in Figure B.4. We decimate the interferograms to be 1 in every 16 pixels in range and 1 in 4 pixels in azimuth direction, resulting in an image resolution of about 60×80 m. All interferograms are filtered using a 200-m Gaussian filter as well as an adaptive Goldstein filter (Goldstein and Werner, 1998). We calculated the average coherence of all manually selected interferograms that were used for stacking, then masked all pixels with an average coherence lower than 0.09. Then, the masked interferograms are interpolated to assist in phase unwrapping using the Statistical-cost, Network-flow Algorithm for Phase Unwrapping software (SNAPHU, Chen and Zebker, 2002). Finally, the unwrapped interferograms are geocoded with 150 m pixel spacing.

We found that average velocity maps generated from manually selected long-term inter-

ferograms with good signal-to-noise ratio work best for obtaining high-quality deformation observations in the XSF region compared with only using relatively short-term pairs. Therefore, we chose interferograms that are used to form the average velocity maps by visual inspection. The selected interferograms are listed in Table B.1 with the corresponding average coherence and standard deviation of unwrapped LOS change (STD) for the whole image. Note that the selected interferograms (Table B.1) are not necessarily independent, and the noise is mostly suppressed by visual selection of high-quality interferograms rather than the stacking of many independent pairs. Examples of selected interferograms that were used in the velocity map formation for each track, as well as some that were rejected, are shown in Figure 3.2 and Figure B.5.

Coseismic interferograms for the 2014 Kangding earthquake sequence

We use both ascending and descending Sentinel-1 interferograms to characterize the deformation field of the Kangding earthquake sequence. The coseismic interferograms used are 20141019-20141206 for track A26 and 20141026-20141213 for track D135. Baseline plots for the coseismic pairs are shown in Figure B.4. The earthquake occurred ∼7 months after the Sentinel-1A satellite launched. Luckily, the first available scenes covering the Kangding region along track A26 and D135 were acquired just before the earthquake. However, only one pre-earthquake scene is available and thus the atmospheric noise on that day contributing to the coseismic interferogram could not be suppressed by averaging multiple coseismic interferograms formed with different pre-earthquake scenes. We only applied a linear topography-correlated correction from the original unwrapped interferograms to mitigate the effects of tropospheric delays. The original, unwrapped, and corrected interferograms for ascending and descending tracks are shown in Figure 3.3.

Time series analysis using a subset of interferograms

To characterize the temporal behavior of fault creep along the XSF, more frequent temporal sampling of the SAR acquisitions is needed. We analyzed multiple properties of interferograms generated in Section 3.3.1 and found the manually selected interferograms used in the velocity map all have a relatively small standard deviation of unwrapped LOS change (STD) for the whole image (Figure B.6). Accordingly, we selected from the generated interferograms with STD<3 to include a larger subset of interferograms (202) in the time series analysis. Due to the limited signal to noise ratio in the interferograms, we focus on the Kangding region in the time series analysis using descending track 135. The ascending track 26 are not used because the derived time series has a very low signal-to-noise ratio and no meaningful signal can be extracted. The interferograms that are used in the time series analysis are shown in Figure B.4. Note that the interferograms used to produce the average velocity map in descending track 135 (Figure 3.3b) represent a subset of the ones that were used in the time series analysis. More interferograms are included to ensure denser temporal sampling. The time series analysis is conducted using Small Baseline Subset method (SBAS;

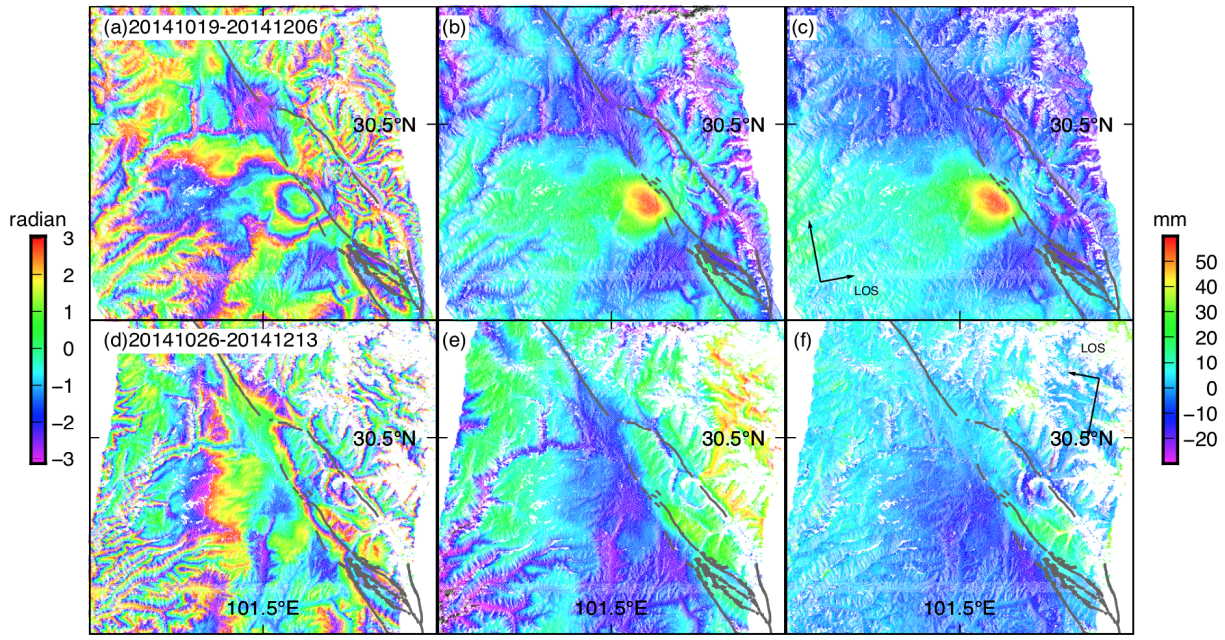


Figure 3.3: Coseismic deformation for the 2014 Kangding earthquake sequence. **(a)** Coseismic wrapped interferogram, **(b)** unwrapped interferogram and **(c)** interferogram after a linear topo-correlated atmospheric noise correction from ascending track 26. **(d-f)** Corresponding maps for descending track 135. Note that in **(f)**, we also manually corrected for a clear unwrapping error ($2pi$) in the NE corner of the image. Fault traces are from Bai et al. (2018) and Pan et al. (2020).

Berardino et al., 2002; Schmidt and Bürgmann, 2003). A linear regression between phase and topography was removed in each interferogram to reduce the effect of topography-correlated atmospheric noise.

3.3.2 Kinematic inversion for the seismic and aseismic fault slip

Kinematic inversions for both the coseismic and aseismic slip are conducted using the constrained least square methods. Green's functions relating unit slip on rectangular dislocations to range change or range change rate are calculated assuming a homogeneous elastic half-space (Okada, 1985). Laplacian smoothing is applied to avoid abrupt slip variations between neighboring patches. The inversion problem can be described as:

$$\begin{pmatrix} los \\ 0 \end{pmatrix} = \begin{pmatrix} G \\ \lambda H^2 \end{pmatrix} m \tag{3.1}$$

where *los* represents the line of sight (LOS) range change measurements from the ascending and descending tracks, G is the Green's function matrix, H is the Laplacian smoothing matrix, *lambda* is the smoothing factor and m is the slip vector for each fault patch that is being solved in the inversion. In this study, we only allow left-lateral strike slip for the slip vector m.

3.4 Results

3.4.1 Average interseismic velocity map along the XSF

We form the average velocity map by summing the total LOS range change and dividing by the total time interval of all selected interferograms (Eq 3.2, Wright et al., 2001, Wright et al., 2004). By stacking the manually selected interferograms listed in Table B.1, we form average velocity maps for both ascending and descending tracks (Figure 3.4 a, b). The LOS velocities measured in the two SAR geometries have opposite signs across the XSF, indicating that the signal is dominated by horizontal strike-slip fault motion. The uncertainty quantification of the stacked velocity maps using bootstrapping is described in Text B.1 and the resulting maps of estimated pixel-by-pixel uncertainties are shown in Figure B.1.

$$V_{los} = \frac{\lambda \sum \phi_i}{4\pi \sum t_i} \tag{3.2}$$

If we assume all horizontal motions to be fault parallel, the LOS velocity maps from ascending and descending looking geometries can be decomposed into fault-parallel velocities u and vertical velocities w, where θ is the average fault strike of the patch, and $(look_E, look_N, look_Z)$ are look vectors for each flight direction, respectively (Eq 3.2).

$$\begin{pmatrix} V_{los\_asc} \\ V_{los\_des} \end{pmatrix} = \begin{pmatrix} look_{E\_asc} \sin\theta + look_{N\_asc} \cos\theta & look_{Z\_asc} \\ look_{E\_des} \sin\theta + look_{N\_des} \cos\theta & look_{Z\_des} \end{pmatrix} \begin{pmatrix} u \\ w \end{pmatrix} \tag{3.3}$$

However, the strike of the XSF increases from ∼125° in the NW to ∼160 ° in the SE. Due to such a significant change in strike, assuming a uniform strike for the velocity decomposition would bias the result. Thus, we divide the LOS velocity maps into three swaths shown in Figure 3.4 a, b. From NW to SE, the patch lengths are 80, 120 and 120 km, respectively. The average strike of each patch is 129°, 131° and 145°. All patches have 100 km widths, extending for 50 km on either side of the fault.

This allows us to obtain velocity maps of fault-parallel and vertical components using the average strike of the corresponding patch, assuming that all horizontal motions are parallel to the corresponding fault segment (Figure 3.4 c, d). The inferred fault-parallel velocity

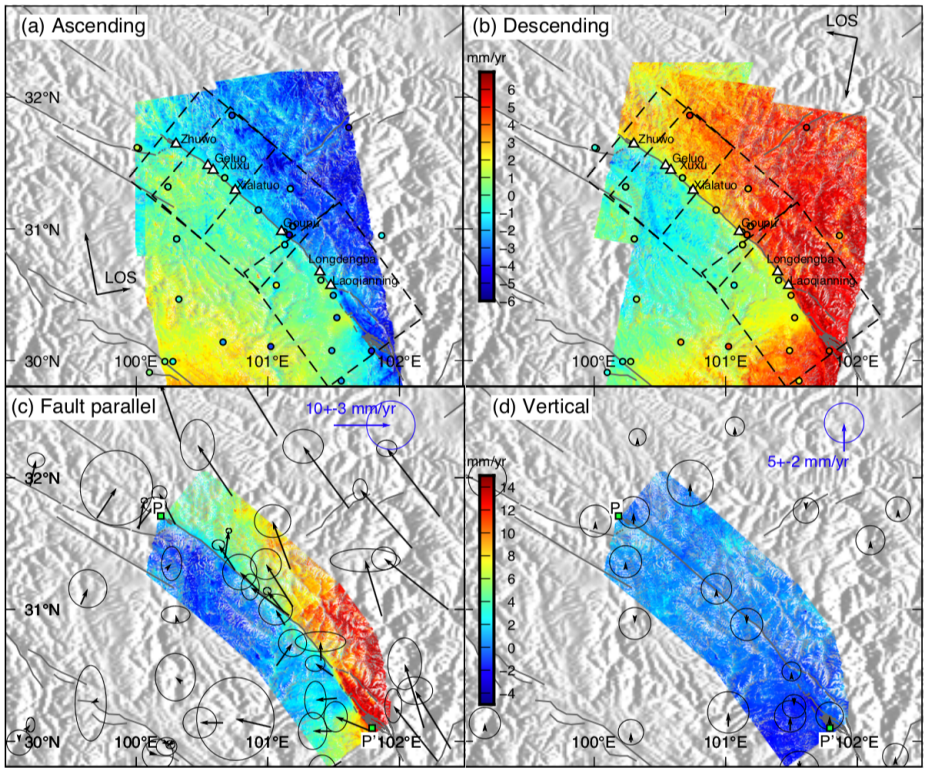


Figure 3.4: **(a), (b)**: Average LOS velocity maps for **(a)** ascending track 26 and **(b)** descending tracks 33 and 135 in the Xianshuihe Fault region. In both **(a)** and **(b)**, red color represents radar range increase and blue color represents range decrease. Fault-crossing baseline survey sites from Zhang et al. (2018b) are denoted with yellow triangles labeled with their station names. Co-registered and projected LOS velocities from GPS measured horizontal velocities from Zheng et al. (2017)) are shown with circles using the same color scale. InSAR and GPS velocities are referenced to the Yajiang sub-block (Figure 3.1). **(c), (d)**: Decomposed velocity maps of **(c)** fault-parallel and **(d)** vertical components. In **(c)**, red coloring represents NW motion and blue indicates SE motion. Different fault strikes are used along three segments of the fault, introducing linear discontinuities in the inferred fault-parallel velocity field. GPS vectors are horizontal GPS velocities from Zheng et al. (2017)) referenced to the regional Yajiang sub-block. In **(d)**, positive values represent uplift . GPS vectors are vertical GPS velocities from Liang et al. (2013). We subtract 1.41 mm/yr of uplift from the original GPS velocities in the ITRF2008 reference frame to highlight local uplift-rate variations (Liang et al., 2013). Active fault lines are modified from Taylor and Yin (2009), Chevalier et al. (2017), Bai et al. (2018), and Pan et al. (2020).

difference across the fault of 10-12 mm/yr between areas ∼50 km away from the fault trace is generally consistent with GPS measurements (Figure 3.4c) and geologic slip-rate studies (Zheng et al., 2017; Bai et al., 2018; Wang and Shen, 2020). No significant vertical motion was observed. The decomposed vertical velocities range from 0-2 mm/yr, which is consistent with the vertical GPS solution by Liang et al. (2013) (Figure 3.4d).

3.4.2 Along-strike variation of the creep rate

With the high-resolution average velocity map along the XSF, we first manually mapped the active fault trace of the XSF within the SAR coverage by finding the maximum InSAR velocity gradient and considering published fault trace maps and the regional morphology in Google Earth (Figure 3.5). The InSAR-derived fault traces match well with previously published fault traces (Chevalier et al., 2017; Bai et al., 2018; Pan et al., 2020)). Then, we estimate surface creep rates along the fault trace by drawing fault-normal velocity profiles every 2 km along the fault, where each profile includes data from a 2-km wide zone. We explored multiple choices of profile lengths on either side of the fault that are used to estimate surface creep and compared results using alternative estimation methods (Text B.2). In our preferred approach, the profiles extend for 1.5 km on either side of the fault. The pixels within 0.5 km of the fault trace are masked out to allow for uncertainties of the assumed fault location and potential filtering effects of the InSAR products. Thus, only the velocity of pixels between 0.5-1.5 km from the fault on each side are used in the creep rate estimation. For each profile, we did a linear regression to fit a straight line on each side of the fault. Then, we calculate the modeled velocity at the points closest to the fault (x=±0.5km). The surface creep rate is estimated by differencing the modeled fault-parallel velocities across the fault (Eq 3.4). The standard deviation of the surface creep rate is estimated through the misfit of the linear regression and error propagation (Eq 3.5). Example diagrams of surface creep rate estimation for selected profiles are shown in Figure 3.5.

$$cr = v_{model}(x = 0.5 \text{ km}) - v_{\text{model}}\,(x = -0.5 \text{ km}) \tag{3.4}$$

$$std_{cr} = \sqrt{\frac{1}{n}\sum_{i=1}^{n}\left(v_{obs+} - v_{model+}\right)^2 + \frac{1}{m}\sum_{i=1}^{m}\left(v_{obs-} - v_{model-}\right)^2} \tag{3.5}$$

The InSAR-derived surface creep-rate distribution is variable along the fault (Figure 3.8b) and matches the fault crossing baseline surveys from Zhang et al. (2018b)) at their site locations. To first order, the distribution of surface creep rate also appears correlated with nearby recent ruptures: 1) average creep rates of ∼2.5 mm/yr near the 1981 Daofu earthquake rupture and 2) surface creep of up to ∼5 mm/yr around the 2014 Kangding earthquake sequence, indicating that the surface creep is possibly linked to afterslip from these seismic

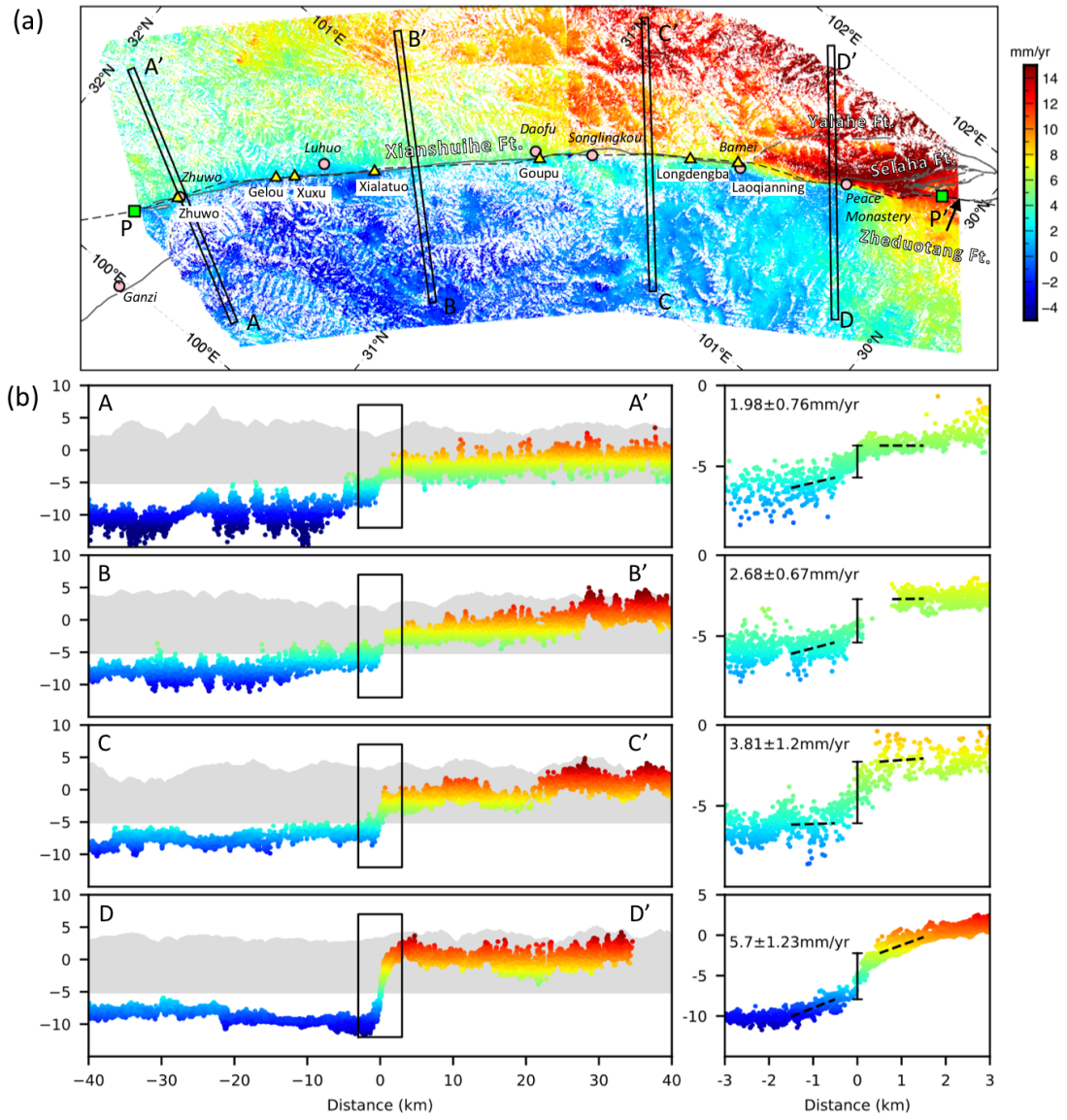


Figure 3.5: **(a)** Close-up view of the fault-parallel velocity field in Figure 3.4**(c)**. Green squares on fault are the same as those shown in Figure 3.4**(c)**. Black dashed line shows the InSAR-derived surface fault trace, and dark gray lines show the fault traces mapped by Chevalier et al. (2017), Bai et al. (2018), and Pan et al. (2020). **(b)** Fault-perpendicular velocity profiles (AA', BB', CC' and DD') with their locations shown in **(a)**. Gray shaded areas represent the topography along the corresponding profiles. Right panels show the near-fault zoom of the left panels. The linear fit of the velocity trends at each side of the fault (0.5-1.5km) are labeled in dashed lines. The estimated surface creep rates are labeled in each profile.

events. In Section 3.4.4, we will investigate the SE segment of the XSF in more detail, given the coverage of Sentinel-1 data starting just before and continuing after the 2014 Kangding earthquake.

3.4.3 Coupling model along the XSF inverted from 2014-2019 deformation

To capture the subsurface slip distribution along the XSF using InSAR data from both the near and far field, we conduct a two-step inversion following Chaussard et al. (2015). The model geometry is set up following the InSAR-derived surface trace (black dashed line in Figure 3.5a). Note that at SE end, the XSF splays into three branches, namely the Yalahe fault, Selaha fault, and Zheduotang fault (Figure 3.5a). Our model simplified the complex fault geometry at the SE end and only includes the northern Selaha branch and northwestern extension of the Zheduotang branch. While it is likely that the deep slip rate and locking depth change along fault strike, there is also some trade-off between the locking depth and deep slip rate, where higher slip rates are obtained when using deeper locking depths. Therefore, here we assume a constant locking depth and only solve for a uniform deep slip rate along the XSF. As the locking depth is not well constrained, we tested the model over a range of locking depths, and chose 12 km as it corresponds to a reasonable cutoff depth of seismicity (87%, Figure B.7) and results in a slip rate close to prior geologic and geodetic studies.

We first invert for the long-term slip rate using a 1000-km-wide (effectively semi-infinite) vertical deep extension of the surface fault trace below 12 km. We also extend the deep model dislocation far beyond the lateral edges of our model domain to prevent spurious far-field deformation gradients associated with the fault terminations. The geometry of the deep dislocation model is shown in Figure B.8. The InSAR LOS velocities (Figure 3.4 a, b) are downsampled for denser sampling near fault and a sparser grid away from the fault trace. Pixels within one locking depth away from the fault trace are masked out given that the near field data may include contributions from shallow creep. The inverted deep slip rate is 12.1 mm/yr with RMS residuals of 0.7 mm/yr (64% reduction of RMS). The resampled observed, modeled and residual long-wavelength LOS velocities for ascending and descending tracks are shown in Figure B.9, while Figure B.10 shows the full-resolution results. The predicted GPS velocities using our derived deep dislocation model match the GPS observations as well (RMS_{GPS} 2.1 mm/yr, Figure B.11). We also tested the inversion results for different locking depths and the data fit equally well, where 10 km locking depth would lead to a deep slip rate of 11.2 mm/yr (RMS_{SAR} 0.7 mm/yr, RMS_{GPS} 2.1 mm/yr) and 14 km would lead to 13.1 mm/yr (RMS_{SAR} 0.7 mm/yr, RMS_{GPS} 2.1 mm/yr). As discussed, the results show a trade-off between the resolved locking depth and deep slip rate. This confirms the limitations of InSAR and GPS to constrain the locking depth (Segall, 2002; Smith-Konter et al., 2011).

For the inversion of shallow fault creep, we use the residual velocity maps from the deep dislocation model (Figure B.10 c, f). We downsample the InSAR data iteratively using a curvature-based quadtree algorithm (Simons et al., 2002; Wang and Fialko, 2015) to ensure more data points in areas with high velocity gradients near the fault trace. We discard pixels with standard deviation larger than 1 mm/yr before downsampling, which leads to removing 13% and 8% of the total pixels in the ascending and descending velocity maps. Pixels within 0.5 km of the fault trace are masked out to avoid averaging across the fault and smearing out the sharp velocity gradient through downsampling. We assume a vertical fault geometry due to the lack of evidence of variations in the along-strike fault dip. The model fault is 20 km wide, allowed to extend below the 12 km locking depth to accommodate potential deep afterslip of the 2014 Kangding earthquake. The inverted slip below 12 km will add to the previously determined interseismic deep slip rate. We discretized the fault into 1×1 km patches at the surface, and the patch size increases with depth to compensate for the loss of resolution (Fialko, 2004). We choose the smoothing parameter (λ in Eq 3.1) to be 0.005, relying on the trade-off curve between the smoothing parameter and RMS of the residuals shown in Figure B.12. In the shallow slip inversion, we only allow left-lateral strike slip and fix the dip-slip component to zero. The model resolution is evaluated through checkerboard tests with patterns of varying length scales (Figure B.13).

The preferred distributed creep-rate model and corresponding uncertainties are shown in Figure 3.6. The model uncertainties are calculated through bootstrapping the downsampled InSAR data with replacement (i.e., data points can be drawn multiple times), for 1000 times. Each time, we take N downsampled InSAR data with replacement and invert for a slip model, where N is the total number of downsampled InSAR data points. The model uncertainty is estimated by calculating the standard deviation of the slip rates of the 1000 inverted slip models. The observed and modeled LOS velocity maps are shown in Figure 3.7, and the residual map has an RMS misfit of 0.6 mm/yr (38% RMS reduction). Some apparent misfits exist in the NW of the ascending track (Figure 3.7c), we attribute this to the residual atmospheric noise and simplification of the model geometry, where the Ganzi fault northwest of the XSF is omitted in our model. In the model, patches with slip rate lower than 1.5 mm/yr are colored in white and are considered to be locked (Figure 3.6). The surface creep rates from the distributed creep model match generally well with those from the fault-perpendicular velocity profiles (Figure 3.8b). Southeast of the XSF near the 2014 Kangding earthquake sequence, creep rates from the distributed creep model exceed the profile estimation (220-250 km distance in Figure 3.8b). This discrepancy can be attributed to slip at depth being smoothed to the surface, or the slip is distributed over a larger length scale, which cannot be fully captured by the profile estimation. We show surface creep rate derived from the distributed creep model with a series of smoothing parameters in Figure B.14, showing that the creep-rate discrepancy near 220∼250 km distance does not persist when reducing the smoothing parameter.

We show the coupling model, which is directly derived from the distributed creep-rate model,

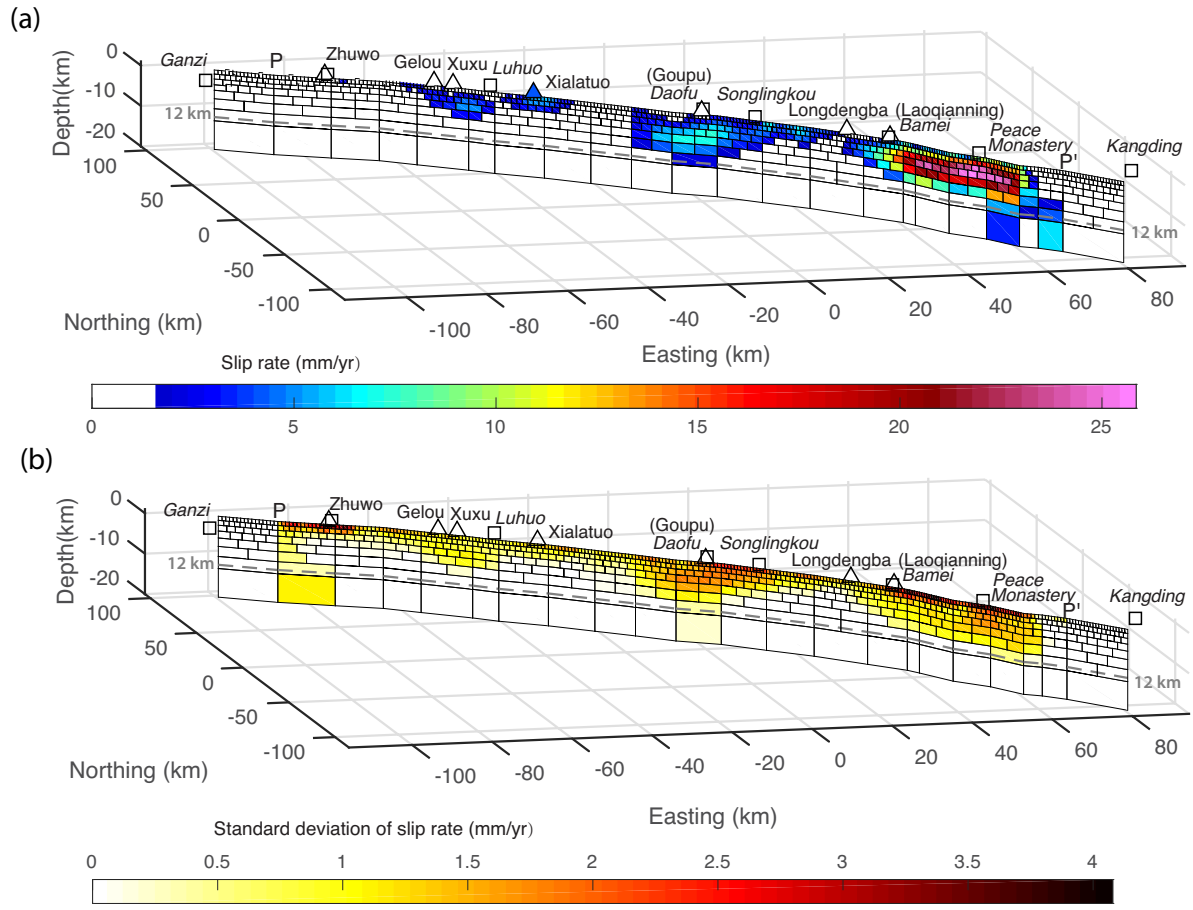


Figure 3.6: **(a)** The inverted interseismic shallow slip model using the average velocity map between 2014.12-2019.7 in the Xianshuihe Region. Fault patches are colored by their sinistral slip rates (mm/yr). Patches with slip rate lower than 1.5 mm/yr are colored in white to assist visualization. The model also includes 1000-km-wide deep dislocations below 12 km slipping at 12.1 mm/yr with lateral extensions that go far beyond the fault tips to account for the long-wavelength interseismic strain accumulation (see Figure B.8). The inverted slip below 12 km adds to the interseismic deep slip rate, possibly reflecting lower-crustal afterslip following the Kangding earthquake. The locations of P and P' are marked in Figure 3.4. Fault crossing baselines from Zhang et al. (2018b) are shown as triangles colored by the reported along-strike slip rates (all but one below 1.5 mm/yr). Locations of major cities along the XSF are labeled with squares. **(b)** Standard deviations of the shallow slip model in **(a)**. The uncertainties are determined by bootstrapping the downsampled InSAR data with replacement for 1000 times and calculating the standard deviation of the slip rates for the 1000 inversions.

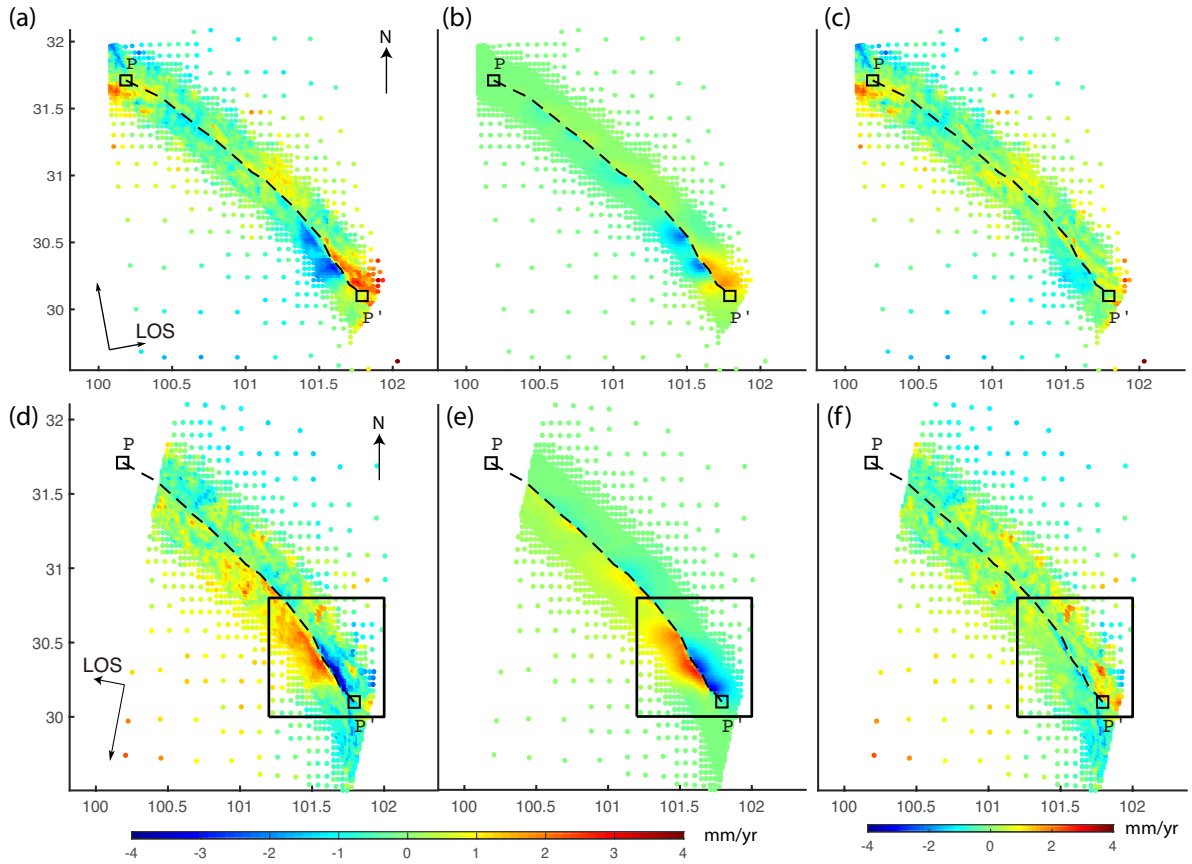


Figure 3.7: Comparison of downsampled observed and modeled short-wavelength LOS velocities from both ascending and descending Sentinel-1 geometries. Positive velocities indicate LOS motion towards the satellite, and vice versa. **(a-c)** are observed, modeled, and observed-minus-modeled residuals for ascending track 26. **(d-f)** are corresponding maps for descending orbit 135. Descending LOS velocities inside the black box are used in the Kangding afterslip study, a zoom-in map of the sub-region is shown in Figure B.19. Note that in (a) and (d), we have already subtracted the velocity field due to 12.1 mm/yr of slip on a buried dislocation below 12 km.

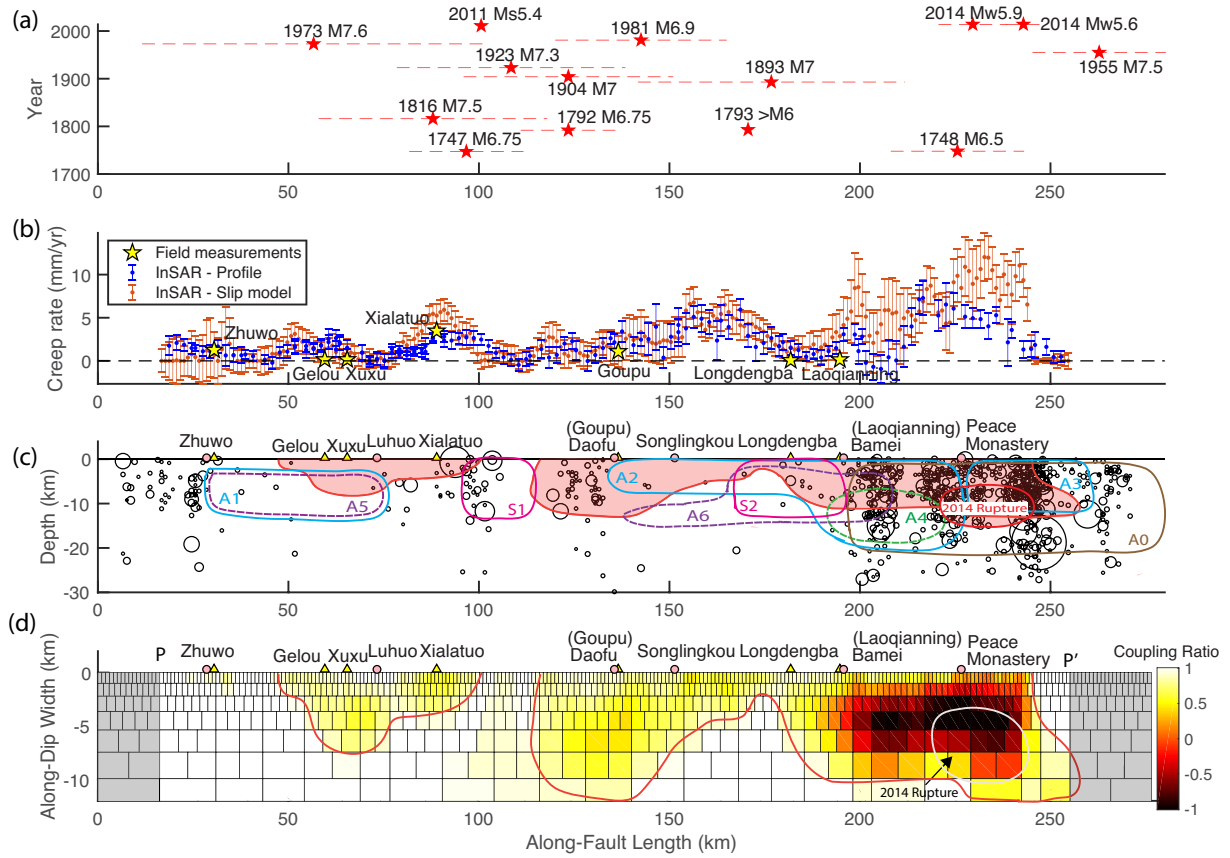


Figure 3.8: **(a)** Spatio-temporal distribution of the historical earthquake ruptures along the XSF. **(b)** Creep rate variation along the XSF estimated from fault-perpendicular velocity profiles and the distributed creep model. The averaged surface creep-rate measurements (1970s-2010s) from Zhang et al. (2018b) are shown with yellow stars. **(c)** Cross-section of microseismicity and comparisons of identified asperities along the XSF. Black circles show M≥1.5 seismicity within 10 km of the XSF from China Seismic Experiment (2009-2019; Wu et al., 2019). A0: seismicity gap identified by Wen et al. (2008). A1-A3: asperities suggested by Jiang et al. (2015a). A4: asperity proposed by Yi (2005). A5-A6: asperities from Zhang et al. (2018b). S1-S2: potential locked asperities identified by this study. The shallow creeping area outlined from the shallow slip model is filled in red. **(d)** 2D view of the fault coupling distribution between 2014.12-2019.7 with outlined shallow creeping area. The coupling ratio is defined to be one when the fault is fully locked and zero when it is slipping at a tectonic loading rate of 12.1 mm/yr. Negative values indicate creep rates in excess of long-term values. Patches outside of our model domain (PP') are shaded in gray. We assume fault patches below 12 km are fully uncoupled.

in Figure 3.8 (d). The XSF represents a partially coupled fault with asperities, and we identify several areas with shallow creep of up to ∼4-15 mm/yr (e.g., patches near Xialatuo site, Goupu site, etc). The high slip rates exceeding the tectonic loading rate on the SE part of the fault is likely associated with postseismic processes of the 2014 Kangding earthquake. If we assume a 12.1 mm/yr long-term slip rate and a locking depth of 12 km, 30% of the interseismic strain is released through aseismic slip along this 270-km-long section of the XSF, during the time period of December 2014 to July 2019. The inferred interseismic moment deficit rate along a fault decreases with decreasing slip rate and locking depth. Thus, the percentage of the moment budget being released will be higher for a lower long-term slip rate and/or a shallower locking depth.

3.4.4 The 2014 Kangding earthquake sequence and its coseismic slip model

Unlike the rather simple central segment, the southeastern part of the Xianshuihe Fault zone is more complex, where the fault splits into three branches, the Yalahe fault, the Selaha fault and the Zheduotang fault (e.g., Fang et al., 2015; Bai et al., 2018). The November 22, 2014 Mw5.9 Kangding earthquake was the most recent moderate earthquake along the XSF. The earthquake triggered more than 1000 aftershocks, including a Mw5.6 earthquake on November 25, 2014 (Jiang et al., 2015b). No surface ruptures were found in field investigations following the two events (Jiang et al., 2015b). The Mw5.9 event was inferred to have occurred on the Selaha branch, whereas the Mw5.6 event likely occurred on the northern extension of the Zheduotang branch of the XSF (Jiang et al., 2015b).

We use the relocated aftershocks from Fang et al. (2015) to determine the fault geometry of the coseismic slip model. The aftershocks are divided into two clusters representing aftershocks of the Mw5.9 and Mw5.6 event, respectively. Based on the spatial extent of the aftershocks, we set the fault lengths to be 20 km and 10 km for the two events and their downdip widths to 20 km. For each aftershock cluster, we use the principal component analysis (PCA) to find the fault strike that minimizes the residuals of the distances between the aftershock locations and the fault plane. The optimal strikes of the Mw5.9 and Mw5.6 fault planes are 141° and 153°, respectively. As the dips derived from PCA are near vertical (89° and 84°) and the aftershocks are quite scattered at depth, we did not use the inverted dip angles from the PCA. For the smaller Mw5.6 event, we assume the fault to be vertical. For the Mw5.9 event, the fault location was originally determined by the aftershocks assuming a vertical fault plane. We then added the fault dip and eastward shift of the surface fault trace location as a free parameter to account for the location ambiguity. We found a dip angle of 80° to the southwest and a 1500 m eastward shift that minimize the RMS residual from the grid search analysis for the Mw5.9 fault plane (Figure B.15). After this adjustment, the fault centers for the Mw5.9 and Mw5.6 events are (101.66°, 30.30°) and (101.72°, 30.19°), respectively.

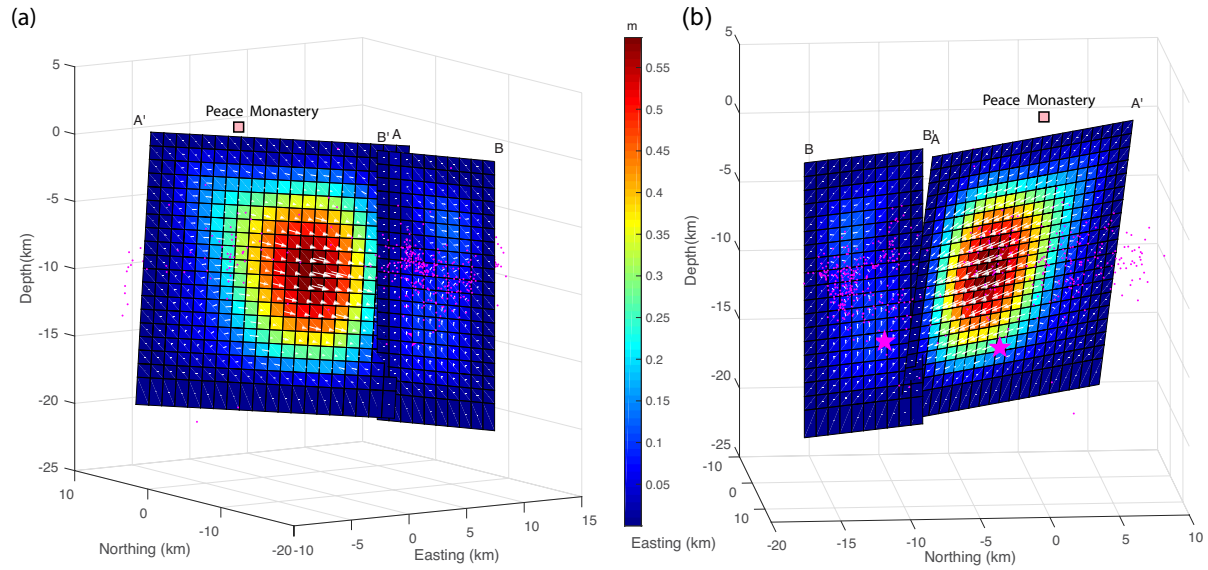


Figure 3.9: The best-fitting coseismic slip model of the Kangding earthquake sequence. **(a)** and **(b)** show the slip model from opposite viewing geometries. The magenta stars show the hypocenters of the Mw5.9 and Mw5.6 events. Magenta dots show the first 24 days of relocated aftershocks of the 2014 Kangding earthquake sequence (Fang et al., 2015). We use 0.008 as our preferred smoothing parameter in the inversion. The location of Peace Monastery is 101.64°E, 30.31°N.

Next, we solve for the distributed coseismic slip on the two fault planes using the down-sampled ascending and descending interferograms. We impose a left-lateral-only constraint on the strike-slip component, and do not apply any constraint on the dip-slip component in the inversion. Our preferred model is shown in Figure 3.9, where the coseismic slip concentrates between 8-12 km depth with a maximum slip of about 0.6 m. The slip diminishes to near zero at ∼5km depth and no slip was found in the shallowest 3-4 km, representing a blind rupture model with a substantial shallow slip deficit. The observed and modeled coseismic deformation is shown in Figure 3.10. The geodetic derived seismic moment is Mw6.15, which is far more than the Mw5.9 moment magnitude derived from the seismic data (Mw5.99 including all aftershocks). Previously published slip models also documented a similar discrepancy, where Jiang et al. (2015b) found the geodetic derived seismic moment magnitude to be Mw6.2 from ALOS-2 data. Xie et al. (2017) discuss the possible factors that could lead to such discrepancies, such as the choice of regional shear modulus, the inclusion of early afterslip in the coseismic interferograms, and various assumptions made in either estimate. In section 3.5.3, a stress-driven afterslip forward model is used to address the possible contribution of early afterslip during the 14 and 21 days between the mainshock and acquisitions of the post-event ascending and descending image, respectively.

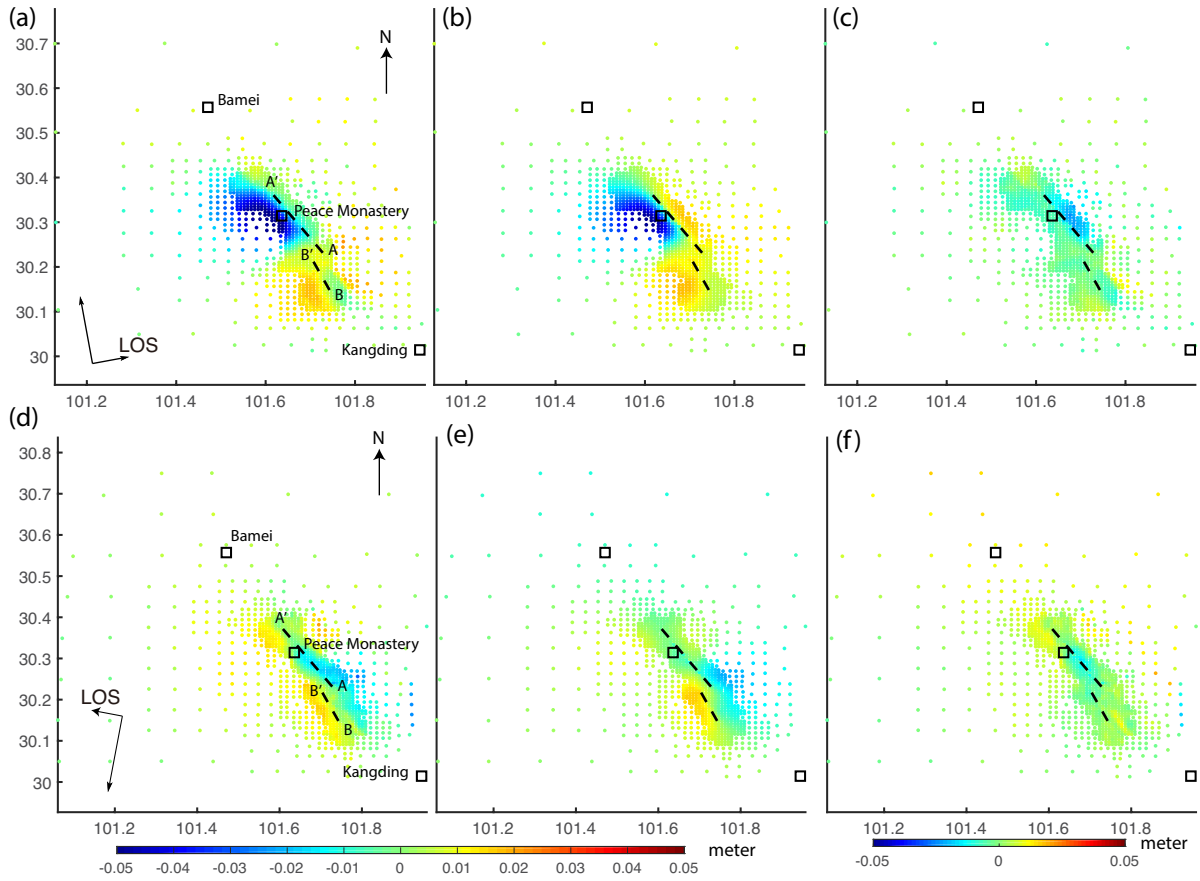


Figure 3.10: Comparison of observed and modeled coseismic deformation of Kangding earthquake from both ascending and descending Sentinel-1 geometries. Positive values indicate LOS motions towards the satellite, and vice versa. **(a-c)** are the downsampled observed, modeled, and observed-minus-modeled residuals for ascending track 26. **d-f** are corresponding maps for descending orbit 135. Black squares indicate major landmarks. Black dashed lines show surface traces of the fault rupture model in Figure 3.9, where letters AA' and BB' mark the fault tips.

3.4.5 Temporal characteristics of the postseismic deformation in the Kangding region

After the removal of deformation from the deep interseismic dislocation model, the largest fault offsets are observed along the southeast section of the XSF (Figure 3.7), near the rupture of the 2014 Kangding earthquake sequence. A corresponding pattern of high slip rates is also found in the inverted creep-rate model (Figure 3.6) and patches with inferred negative coupling (excess slip) in the coupling model (Figure 3.8d). The modeled fault slip rate of up to 25 mm/yr in the Kangding region exceeds the interseismic loading rate (∼12 mm/yr). Considering the InSAR data spans the postseismic period of the 2014 Kangding earthquake sequence, such high slip is probably related to postseismic afterslip. Given the Kangding earthquake did not rupture to the surface and its coseismic slip model shows a clear shallow slip deficit (Figure 3.9), we infer that the earthquake ruptured a locked asperity at depth and the rapid creep represents afterslip in the shallow portions of the fault up dip of the rupture.

Therefore, a time series analysis is carried out using 189 additional interferograms from track 135 to assess the time dependence of the afterslip (data described in section 3.3.1). The LOS velocity map from the time series analysis (Figure 3.11a) is noisier but otherwise comparable to that formed from the manually selected interferograms (Figure 3.4b). Given the limited signal to noise ratio of the cumulative displacements solved by SBAS, we take three pairs of 1∼2-km-wide and ∼15-km-long swaths on each side of the fault and focus on the average cross-fault time series differences between each pair of swaths. Multiple time series differences are taken from subswaths ranging from 0-1 km, 1-2 km, 2-3 km, 1-3km, and 3-5 km away from the fault trace on each side of the fault.

The averaged cumulative LOS displacement differences across the fault at 1-3 km in the northern, central and southern swaths are shown in Figure 3.11b. For reference, the stacked averaged time series of patches west and east of the fault prior to differencing are shown in Figure B.16. The cumulative displacement shows a temporal decay and can be fitted with a logarithmic function, consistent with the assumption that the deformation is associated with transient creep or afterslip (e.g., Savage et al., 2005; Savage and Svarc, 2009). Therefore, we fit the time series using Eq 3.6, where c_1 and c_2 are constants, t is the days after the earthquake, and τ is the characteristic decay time. We first fit the time series for each swath separately and find the characteristic decay times τ that minimize the RMS misfit for the northern, central and southern swath to be 2500 days, 200 days and 150 days, respectively (Figure 3.11b, Figure B.17). We repeated the process and found the best-fitting characteristic decay times for all swath pairs at varying distances away from the fault (Table B.2). The northern swath has a distinctly longer characteristic decay time than the other two swaths and the linear model fits equally well compared with the log-decay model. This indicates the slip in the northern swath is less likely to be afterslip. The characteristic decay time is reduced from >6000 days to 1500 days for swath pairs further away from the fault, indicating

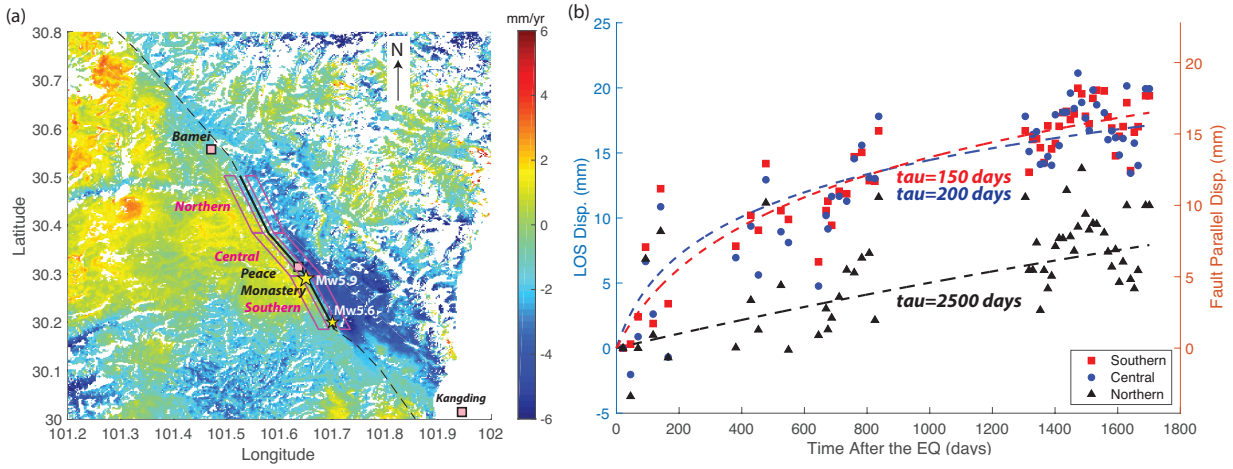


Figure 3.11: **(a)** Average LOS velocity map of the SE section of the XSF for descending track 135 derived from the time series analysis (December 2014-July 2019). Red color represents LOS motion towards the satellite and blue color represents LOS motion away from the satellite. Epicenters of the 2014 Kangding earthquake and its largest aftershock are labeled and shown as yellow stars. The InSAR-derived fault geometry that is used in the distributed shallow slip model is shown by the dashed line. Magenta boxes outline the near-fault patches that are used for differencing cross-fault time series for the northern, central and southern Kangding fault sections, respectively. **(b)** Averaged cross-fault time series of the cumulative LOS displacement differences along the northern, central, and southern fault sections shown in **(a)**. Dashed lines show the fitting curves on each fault sections assuming a logarithmic afterslip decay time with characteristic decay times labeled on the curve. Blue y-axis shows the LOS displacements whereas the orange axis on the right shows the corresponding fault parallel displacement assuming all motions are fault parallel.

some decaying slip at depth, regardless of it having small contribution overall. As for the central and southern swaths, the characteristic decay times are the shortest near the fault trace (100 days at 0-1 km) and become longer (500 and 200 days at 3-5 km) when moving away from the fault trace. Such a pattern could possibly be due to a shallow decaying afterslip. As the resolved characteristic decay time changes with distance from the fault, we select τ=200 days as the characteristic decay time for the whole section in the afterslip analysis as an approximation, which is the characteristic decay time for the central segment at 1-3 km swaths and southern segment at 3-5 km swaths.

$$disp(t) = c_1 + c_2 \log\left(1 + \frac{t}{\tau}\right) \tag{3.6}$$

$$\Delta disp(t_1, t_2) = disp(t_1) - disp(t_2) = c_2 \left[\log\left(1 + \frac{t_1}{\tau}\right) - \log\left(1 + \frac{t_2}{\tau}\right) \right] \tag{3.7}$$

$$S = \sum \frac{\Delta disp(t_1, t_2)}{\Delta disp(0, t_{max})} \tag{3.8}$$

Based on this relationship and assuming τ=200 days, only 3.0% and 4.5% of the postseismic moment is released in the first 14 and 21 days. Thus, the ascending and descending coseismic interferogram spanning 14 and 21 days after the earthquake will include 3.0% and 4.5% of the afterslip deformation. For reference, the moment release would be 1.2% and 1.9% if we assume τ=1500 days, and 4.6% and 6.7% if we assume 100 days.

Using the relationship in Eq 3.6, we can reconstruct the cumulative displacement map from the average velocity map for the Kangding section of the XSF that will be further discussed in Section 3.5.3. For each interferogram, the displacement in the corresponding time span can be calculated using Eq 3.7. When t_2=t_{max} (end of the observation period) and t_1=0, the displacement corresponds to the total cumulative postseismic displacement. Combined with the weight of each time span in the formation of the average velocity map (Figure B.18), a cumulative displacement map can be reconstructed by applying a scaling factor S to the average velocity map obtained through stacking (Eq 3.8, Figure B.19). The scaling factor is S=5.20 when τ=200. If we assume a steady-slip scenario, S=4.49 and is equivalent to the total time span (in years) used in the stacking. Note that we did not use the cumulative displacement derived from SBAS given its high uncertainties introduced by the low signal and high atmospheric noise levels. Therefore, the spatial pattern of the reconstructed deformation is the same as the average velocity map. We also ignore the possible contribution of other postseismic mechanisms such as viscoelastic relaxation and poroelastic rebound. The reconstructed cumulative displacement map relies on the assumption of a spatially uniform logarithmic decay of the signal.

3.5 Discussion

3.5.1 Implications and limitations of the interseismic velocity map and coupling model

We have to admit that the substantial vegetation cover, the high atmospheric noise content and the relatively low tectonic signal (∼12 mm/yr) along the XSF make the extraction of the interseismic deformation signal through InSAR challenging. In this study, we use InSAR data spanning December 2014 to August 2019 to form interseismic average velocity maps from a selected subset of high-quality interferograms that show a clear offset along the fault and have relatively modest atmospheric artifacts. The signal-to-noise ratio in a single interferogram

spanning a year or longer can be significantly improved since the long-term interferogram will capture more deformation assuming the same noise level (Figure 3.2). Therefore, we obtained a regional high-resolution interseismic velocity field in the XSF region by using manually selected long-term interferograms. As some of the manually selected interferograms share the same scene, the interferograms used in stacking are not independent. We acknowledge the potential noise enhancement through stacking such dependent interferograms. However, to assess the noise contributions we also examined the overlapping areas of descending tracks 135 and 33 and the histogram of the velocity differences between the two tracks suggests the potential bias is limited (see Figure B.2, Text B.1). Furthermore, we acknowledge the existence of remaining atmospheric noise in the stacked average velocity maps, as is evident in both the observations (Figure 3.4) and the residual maps for the coupling model (Figure 3.7). As we use the averaged velocity maps for the coupling model inversion, this model does not address temporal variation of the deformation field and slip distribution. The interferograms are unevenly distributed in time, and the weight of each time period in the mean rate estimate is unbalanced (Figure B.18). Such unbalanced sampling in time will not affect our coupling model if the slip behavior along the fault is temporally invariant. We were not able to extract the temporal evolution of the slip behavior due to data limitations, except for the SE section of the XSF near the location of the 2014 Kangding earthquake sequence, where a decaying pattern is captured. Hence, we chose to keep the steady slip-rate assumption and use the averaged velocity map to derive the coupling model, regardless of the potential underestimation of slip rate in the SE section ($\sim$12%).

Due to the inherent limitations of the SAR observations, multiple simplifications and constraints were applied when inverting for our preferred coupling model. First of all, we used a single fault-trace geometry for the model, where we omitted the effect of the Ganzi fault to the NW and simplified the three southern branches of the XSF into a single trace. We masked the near field data, fixed the locking depth at 12 km and inverted for the long-term deep dislocation slip rate. We do not allow the slip rate and locking depth to vary along strike, despite of geologic studies reporting a southeastward decrease in slip rate along the XSF from 10-15 mm/yr to 5-10 mm/yr (e.g., Allen et al., 1991; Xu et al., 2003) or a southeastward increase from 6-8 to 10 mm/yr (e.g., Zhang, 2013; Chevalier et al., 2017; Wang et al., 2017b; Wang et al., 2017a; Bai et al., 2018; Wang et al., 2021). In the inversion for shallow creep, we only allow for left-lateral strike slip, despite of the possible contribution of minor dip slip. While this model comes with a number of inherent uncertainties, the inferred coupling distribution can provide valuable observational constraints of variable fault behavior along the XSF. Previous models focused on the coupling status and strain accumulation along sections of the XSF (e.g., Jiang et al., 2015a; Li et al., 2018b). However, those studies mainly depend on GPS to constrain their analysis and do not have sufficient spatial resolution. Our up-to-date, high-resolution geodetic observations provide additional data constraints that should be of value for future investigations of the XSF.

3.5.2 Implications for the seismic potential on the XSF

The XSF is one of the most seismically active regions in China. Being one of the major faults that accommodates the partitioning of regional deformation at the eastern boundary of the Tibetan Plateau (Figure 3.1), all segments of the XSF appear to have ruptured at least once since 1700. Wen et al. (2008) investigated the modern and historical records of the seismic intensity, rupture extent and geological investigations, and compiled a detailed rupture history along the XSF. Recent ruptures since 1747 are shown in Figure 3.8a and listed in Table B.3. The spatiotemporal pattern of historical ruptures along the XSF does not seem characteristic, that is, the fault slip appears to be neither slip nor time predictable. However, the historical rupture records on a fault segment are still valuable as one can calculate the slip deficit since the latest earthquake and infer the seismic potential on the fault assuming all accumulated seismic moment will be released by future seismic events. In this section, we estimate the equivalent seismic moment deficit along corresponding fault segments based on a locking depth of 12 km and deep slip rate of 12.1 mm/yr, consistent with the values used for deriving our coupling model (Figure 3.6, 3.8). If the slip rate is decreased to 10 mm/yr, the estimated cumulative moment deficit will decrease by ∼Mw0.05. Likewise, if the locking depth is increased to 14 km, the estimated equivalent cumulative seismic moment will rise by ∼Mw0.05.

A seismic gap was identified along a fault segment between the Bamei and Kangding area (A0 in Figure 3.6c), where the most recent rupture being the 1748 M6.5, 1955 Mw7.5 and 1925 Mw7 events from north to south along the segment (Wen et al., 2008). The 2014 Kangding earthquake sequence occurred within this proposed seismic gap. However, the spatial extent of the rupture and the total seismic moment release (Mw5.99 including aftershocks) does not compensate for the slip deficit that has accumulated. Bai et al. (2018) estimated the seismic moment accumulation on the entire Selaha-Kangding segment (∼60 km long) since the 1955 Mw7.5 event, which found to be capable of generating a Mw6.5∼6.8 earthquake. If we account for the moment accumulation separately on the section of the fault since the 1748 and 1955 events (>70∼80 km, Figure 3.8a), this seismic gap is capable of generating a Mw>7.1. The moment release of the 2014 Kangding earthquake sequence only equals ∼10 years of strain accumulation on the estimated 1748 rupture asperity, less than 4% of the total. In addition to the A0 seismic gap, we note two segments along the XSF that have not ruptured for about a century. One of them is a ∼20-km-long segment SE of the Xialatuo area (S1 in Figure 3.8c), where the latest recorded rupture was a M 7.3 event in 1923. No surface creep is identified on that segment, indicating the fault segment is probably a fully locked asperity and accumulating strain interseismically. The slip deficit on segment S1 since 1923 is capable of generating a Mw6.55. The second identified segment with high seismic potential is located between NW of Longdengba and Laoqianning/Bamei (S2 in Figure 3.8c). The latest rupture on the corresponding segment S2 occurred in 1893 and the cumulative slip deficit since that M ∼7 event is capable of generating a Mw6.74 event. If we combine the surrounding areas with substantial slip deficit accumulated since their latest rupture from

Longdengba to Kangding (A0+S2), the combined segment has a seismic potential of up to ∼Mw7.18.

Our work further addresses the locking status and seismic potential on the fault by adding evidence from geodetic observations and quantitative estimates of moment released by aseismic fault slip. From the coupling model derived from InSAR observations (Figure 3.6,3.8), we mapped the detailed distribution of the shallow creeping sections of the fault (Figure 3.8c), where a total of 32% of the interseismic strain is released through aseismic slip during the observation period. If the slip rate is decreased to 10 mm/yr or the locking depth changed to 10 km, ∼37-39% of the interseismic strain will be released through aseismic slip. Moreover, if we assume all creeping patches do not contribute to interseismic strain accumulation and their slip budget is fully accommodated by aseismic slip, including both steady creep and afterslip following nearby ruptures, there will be a ∼46% reduction of seismic potential.

In addition to the historical earthquake records that document the longer-term seismic slip history along the XSF, modern microseismicity provides additional evidence of the locking status along the fault. Yi (2005) consider the spatial distribution of b-values and propose a probable asperity between Bamei and Selaha (A4 in Figure 3.8c) due to its unusually low b-value (0.66-0.73). Zhang et al. (2018b) also identified a locked asperity between Zhuwo and Luhuo (A5) and another one between Goupu/Daofu and Laoqianning (A6), evidenced by the sparsity of microseismicity on the fault along these sections in the past decade. The asperity locations derived from microseismicity are generally consistent with our aseismic slip model, where the proposed locked patches are also free of or have limited shallow aseismic slip. Information and references on proposed asperities mentioned above are listed in Table B.4.

The primary discrepancy occurs on the segment between Bamei and Selaha, the northern extension of the fault plane of the 2014 Kangding earthquake sequence (hereinafter referred to as N-Selaha segment), where we find substantial aseismic slip and the segment appears fully uncoupled (Figure 3.6 and 3.6d) in our model. In contrast, the N-Selaha segment has been identified as a potential asperity by Yi (2005) because of low b-values as well as by Jiang et al. (2015a) from their joint inversion of InSAR and GPS data using a viscoelastic model. This could indicate that the coupling status on the N-Selaha segment changed from locked to fully uncoupled after the 2014 Kangding earthquake. One interpretation for this could be that after the 2014 Kangding earthquake ruptured the locked asperity, slip on this segment occurred postseismically. In summary, though the Kangding earthquake and its afterslip released part of the accumulated strain on a previously identified "seismic gap", the remaining slip deficit is still capable of generating a ∼M7 event. Enhanced seismic and geodetic monitoring will be crucial to further improve the seismic hazard evaluation and quantification of earthquake potential along the XSF.

3.5.3 Possible mechanisms of the substantial afterslip in the Kangding region

Substantial near fault deformation is observed near the location of the 2014 Kangding earthquake sequence since the event. The inverted fault slip on the corresponding fault patches far exceeds the tectonic loading rate and the temporal evolution of the deformation can be characterized by a logarithmic decay function, indicating that such deformation is probably due to postseismic afterslip. One common explanation for the origin of afterslip is that it is directly driven by the coseismic stress change (Bürgmann, 2018). To test if the kinematically inverted slip model makes physical sense, we use a stress-driven forward model to simulate the possible afterslip induced by the coseismic stress changes.

The stress-driven afterslip modeling is conducted using Unicycle (Barbot et al., 2017; Barbot, 2018). We assume a steady-state, rate-strengthening friction law without healing and slip weakening effects. In this simplification, the slip evolution can be represented by Eq 3.9 (Barbot et al., 2009; Wang and Bürgmann, 2020). All fault patches are set to be velocity strengthening except for the coseismic rupture area, where patches with negative stress change are pinned and not allowed to slip. As the temporal evolution of the slip behavior is not well constrained, we do not seek to find the best-fitting frictional properties of the fault interface, that is, the exact values of $a\sigma$ and V_0 are not discussed. We only focus on the slip value at full relaxation, which indicates the maximum possible afterslip that could be induced by the coseismic rupture.

$$V = 2V_0 \sinh \frac{\Delta\tau}{a\sigma} \tag{3.9}$$

To simplify the simulation process, we use the fault geometry of the SE section of the coupling model for the coseismic slip inversion, rather than using the best-fitting coseismic slip model with two segments shown in Figure 3.9. The simplified slip model is shown in Figure B.20 with the data fitting shown in Figure B.21. The same fault geometry is then used for the stress-driven afterslip modeling, and the kinematic slip inversion and the stress-driven afterslip can be compared more directly. We consider two kinematic slip models. The first kinematic model is taken from the average slip rate in Figure 3.7d converted to cumulative slip by the scaling factor S=5.20, as described in Section 3.4.5. For the second slip inversion, we do not allow afterslip to occur on patches with negative coseismic stress change (same constraint as the stress-driven model). The inverted kinematic slip models and simulated stress-driven afterslip model are shown in Figure 3.12, with the modeled LOS displacements and their residuals. The deformation produced by the fully relaxed, coseismic-stress-driven afterslip captures the observed cumulative deformation to first order, but somewhat overpredicts the near-field deformation. The moment release from the afterslip is equivalent to Mw5.96 for the kinematic inversion (Figure 3.12a), Mw5.91 for the constrained kinematic inversion (Figure 3.12b), and Mw5.80 (Figure 3.12c) for the stress-driven forward model.

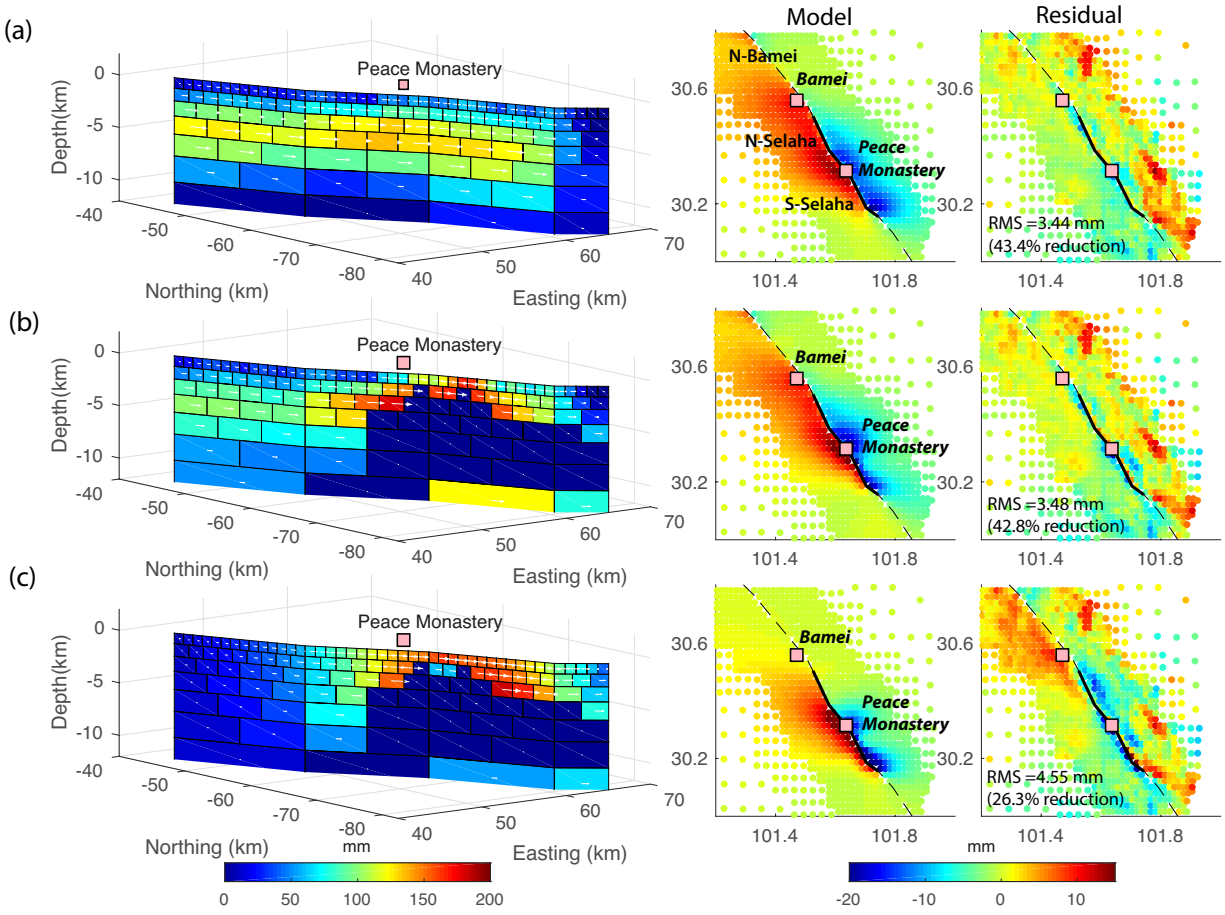


Figure 3.12: Cumulative 2014-2019 fault slip along the SE segment of the XSF derived from **(a)** kinematic inversion from Figure 3.6, **(b)** kinematic inversion imposing zero slip on patches that have coseismic slip >0.1m, and **(c)** coseismic-stress-driven afterslip model. Right panels show the modeled and observed-minus-modeled residual cumulative LOS displacements. Positive values indicate LOS motions towards the satellite, and vice versa. RMS misfits and the percentage of RMS reduction for each afterslip model are labeled in the residual map. The RMS misfit of the original data is 6.09 mm. The location of Peace Monastery is 101.64°E, 30.31°N.

The maximum amplitude for the stress-driven model prediction is ∼0.18 m, exceeding the maximum slip in the kinematic model ∼0.1 m. However, if we apply the locked-asperity constraint in the kinematic inversion, the maximum amplitude of the constrained kinematic model is about the same as in the stress-driven model (Figure 3.12b). The misfits of the two kinematic inversions are comparable, with RMS values of 3.44 mm (43.4% RMS reduction) and 3.48 mm (42.8% RMS reduction). The fully-relaxed stress-driven model has a higher misfit (RMS = 4.55 mm, 25.3% RMS reduction), which appears mainly due to a modest over-estimate of the shallow afterslip and lack of slip further NW where significant displacements are observed (Figure 3.12c).

There is a substantial difference between the kinematic and stress-driven models NW of the Kangding rupture along the N-Selaha and N-Bamei segments. The stress-driven afterslip model is only capable of producing afterslip in the vicinity of the coseismic rupture and does not predict slip along those segments located more than 20 km from the coseismic rupture (Figure 3.12c), whereas the kinematic inversions suggest more than 0.1 m of slip in N-Selaha and N-Bamei (Figure 3.12a, b). That is, the inverted slip at depth along the N-Selaha and N-Bamei segments (Figure 3.12a) cannot be explained by the coseismic stress change, and it also exceeds the long-term slip rate (Figures 3.6 and 3.8d). The excess deformation north of Selaha is quite clear from the residual map (Figure 3.12c), and is unlikely to represent an artifact.

Three possible explanations of the rapid aseismic slip beyond the immediate afterslip zone are proposed (Figure 3.12). One possibility is that the N-Selaha and N-Bamei segments exhibit steady creep interseismically and the observed shallow aseismic slip is independent of the earthquake (Figure 3.13a). This would be consistent with the near-linear evolution of the cross-fault LOS difference shown in Figure B.17a, but not with the slip at depth apparently exceeding the long-term rate (Figures 3.6, 3.8d). Another scenario is that fault patches on those segments were originally velocity weakening and locked. The dynamic shaking of the 2014 Kangding earthquake may have perturbed the fault zone frictional properties and altered the corresponding patch from velocity weakening to velocity strengthening, allowing it to release ambient stress via aseismic slip (Figure 3.13b). The dynamic stress perturbation may have led to fault-zone compaction and associated pore pressure increase, thus temporally decreasing its fault strength. Finally, if the N-Selaha and N-Bamei segments of the XSF are only slightly velocity weakening at depth, the dynamic stress of the earthquake could also trigger a slow slip event, though no clear pattern of acceleration or deceleration is observed (Figure 3.13c).

Slow slip events have been widely observed on continental strike-slip faults (e.g., Bilham, 1989; Linde et al., 1996; Bokelmann and Kovach, 2003). More recent studies also observed slow slip events triggered by nearby and remote earthquakes (e.g., Taira et al., 2014; Tymofyeyeva et al., 2019). Using characteristically repeating earthquake activity to track slow slip, Taira et al. (2014) observed substantial afterslip after the 1998 San Juan Bautista earthquake

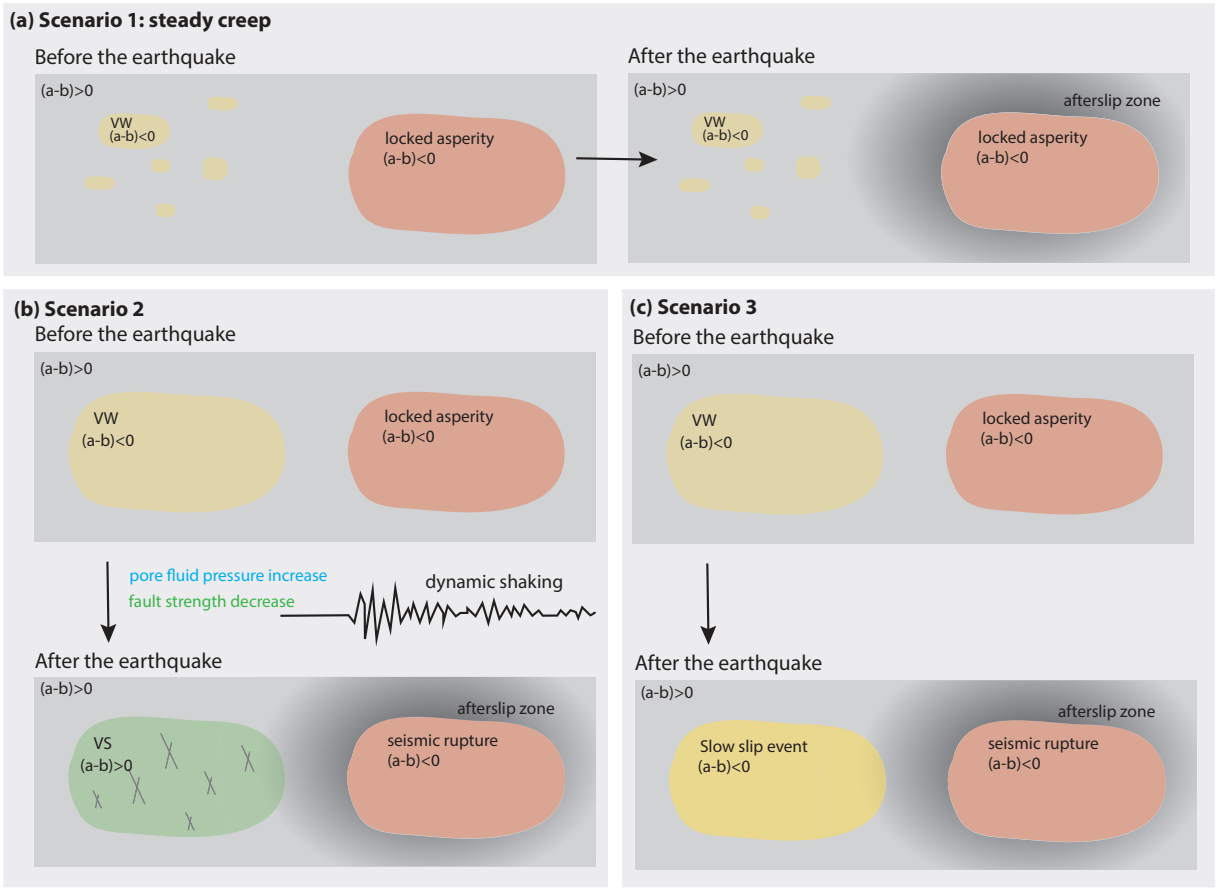


Figure 3.13: Schematic plots for three possible explanations of the rapid aseismic slip north of the rupture zone. **(a)** Scenario 1: steady creep independent of the seismic rupture. **(b)** Scenario 2: dynamic shaking of the seismic waves altered the northern patch from velocity weakening to velocity strengthening properties, allowing it to release ambient stress via aseismic slip. **(c)** Scenario 3: enduring triggered slow slip event on modestly velocity weakening fault patch.

that cannot be explained by the coseismic stress change, and attributed this to a triggered slow slip event. Moreover, Tymofyeyeva et al. (2019) observed a slow slip event with the aid of InSAR and creepmeter data on the southern San Andreas Fault that was remotely triggered by the distant 2018 Mw8.2 Chiapas, Mexico earthquake. Detailed assessment of the temporal behavior of the slip evolution is crucial for distinguishing such triggered slow slip events associated with shaking from earthquakes. However, lacking near-field data to confirm the creep rate prior to the 2014 earthquake sequence, we cannot confirm or rule out either of the possible mechanisms.

3.6 Conclusion

We present a high-resolution interseismic velocity map along the XSF using ascending and descending Sentinel-1 InSAR data spanning from Dec 2014 to July 2019. The decomposed fault parallel velocity map reveals heterogeneous surface creep rates ranging from 0-6 mm/yr along the fault. We further derived distributed shallow slip and coupling models along the XSF. Several creeping patches are identified along the fault, including near Xialatuo, Goupu-Songlingkou and Bamei-Selaha-Kangding. The creeping sections release 32±6% of the interseismic moment budget during the observation period. Considering the most recent rupture history on each segment since 1748, we can identify two patches with high seismic potential 1) a ∼20-km-long segment SE of the Xialatuo area, and 2) a section between NW of Longdengba and Laoqianning/Bamei. The former is capable of generating a Mw6.54 event since an M 7.3 event in 1923, whereas the latter is capable of generating a Mw6.73 event since an M 7 earthquake in 1893 and ∼Mw7.18 if including surrounding locked areas. Along the SE section of the XSF, the inverted slip rate exceeds the tectonic loading rate. We performed a time series analysis of near-surface slip in the Kangding earthquake rupture region and the time series shows a logarithmic decay pattern of the cumulative displacement. The observed postseismic deformation along the rupture segment is consistent with the deformation produced by a coseismic-stress-driven afterslip model, indicating a velocity strengthening section of the fault up dip of the buried mainshock rupture. However, the shallow creep observed along the N-Selaha and N-Bamei segments is located outside of the coseismic static stress-change zone, suggesting this is a zone of rapid steady fault creep or represents the occurrence of an enduring triggered slow slip event.

Chapter 4

Spatiotemporal Variations of Surface Deformation, Shallow Creep Rate, and Slip Partitioning between the San Andreas and Southern Calaveras Fault

The chapter was adapted from: Y.Li, R. Bürgmann and T. Taira (2022). "Spatiotemporal variations of surface deformation, shallow creep rate, and slip partitioning between the San Andreas and southern Calaveras Fault". doi: https://doi.org/10.1002/essoar.10512336.1. *(Under review at Journal of Geophysical Research: Solid Earth)*

4.1 Abstract

The Calaveras Fault (CF) branches from the San Andreas Fault (SAF) near San Benito, extending sub-parallel to the SAF for about 50 km with only 2-6 km separation and diverging northeastward. Both the SAF and CF are partially coupled, exhibit spatially variable aseismic creep and have hosted moderate to large earthquakes in recent decades. Understanding how slip partitions among the main fault strands of the SAF system and establishing their degree of coupling is crucial for seismic hazard evaluation. We perform a timeseries analysis using more than 5 years of Sentinel-1 data covering the Bay Area (May 2015-October 2020), specifically targeting the spatiotemporal variations of creep rates around the SAF-CF junction. We derive the surface creep rates from cross-fault InSAR timeseries differences along the SAF and CF including adjacent Sargent and Quien Sabe Faults. We show that the variable creep rates (0-20 mm/yr) at the SAF-CF junction are to first order controlled by the angle between the fault strike and the background stress orientation. We further

examine the spatiotemporal variation of creep rates along the SAF and CF and find a multi-annual coupling increase during 2016-2018 the subparallel sections of both faults, with the CF coupling change lagging behind the SAF by 3 to 6 months. Similar temporal variations are also observed in both b-values inferred from declustered seismicity and aseismic slip rates inferred from characteristic repeating earthquakes.

4.2 Introduction

The 1100-km-long San Andreas Fault (SAF) system extends from the Gulf of California in the southeast to the Mendocino triple junction in the northwest (Wallace, 1990). Between Parkfield and San Juan Bautista lies the 150-km-long central creeping section, where the majority of the 38 mm/yr right-lateral plate motion between the Sierra-Nevada Great-Valley block and Pacific plate (D'Alessio et al., 2005) is accommodated through aseismic slip (Savage and Burford, 1973; Ryder and Bürgmann, 2008; Michele et al., 2011; Jolivet et al., 2015a; Khoshmanesh et al., 2015). The Calaveras Fault (CF) branches from the SAF at its northern transition zone between creeping and locked segments, extends sub-parallel to the SAF for about 50 km, with only 2-6 km separation from San Benito to Paicines (Figure 4.1), and diverges away from the SAF further north (Watt et al., 2014). At the SAF-CF junction where the two faults are sub-parallel, the distribution of microseismicity indicates that the SAF is nearly vertical, the CF is dipping to the southwest, and the two faults are possibly connected at depth (Watt et al., 2014). The two faults take up the majority of the plate motion, and both faults exhibit shallow creep (e.g., Burford and Harsh, 1980; Galehouse and Lienkaemper, 2003; Johanson and Bürgmann, 2005; Tong et al., 2013; Scott et al., 2020). Additionally, a modest part of the slip budget is partitioned onto the Sargent Fault (SF) and Quien Sabe Fault (QSF) (Prescott and Burford, 1976; Templeton et al., 2008; Mongovin and Philibosian, 2021).

Both the SAF and CF are partially coupled at the SAF-CF junction and have hosted moderate to large earthquakes in the past decades (Johanson and Bürgmann, 2005; Oppenheimer et al., 1990). Creep rates on the SAF taper off to zero along the northern transition zone, and the fault remains fully locked to the north, where it hosted the 1989 M6.9 Loma Prieta and 1906 M7.9 San Francisco earthquakes (Thatcher et al., 1997; Zhang et al., 2018a). Being one of the most seismically active branches of the SAF system, the CF hosted a sequence of four northward progressing earthquakes, including the 1979 M5.9 Coyote Lake earthquake, the 1984 M6.2 Morgan Hill earthquake, the 1988 M5.1 Alum Rock earthquake, and the 2007 M5.6 Alum Rock earthquake (Oppenheimer et al., 1990; Du and Aydin, 1993; Toppozada et al., 2002; Murray-Moraleda and Simpson, 2009).

Spatiotemporally variable creep on the SAF and CF has been documented by alignment array (Burford and Harsh, 1980; Lisowski and Prescott, 1981; Lienkaemper and Prescott, 1989) and creepmeter measurements (Schulz, 1989; Bokelmann and Kovach, 2003; Bilham et al., 2004)

since the 1960s. While alignment-array and creepmeter measurements provide decades of accurate records of shallow fault creep, the spatial extent of creep mapping is largely limited by the sparsely distributed locations of these geodetic sites. A detailed assessment of the spatiotemporal distribution of fault creep along the SAF system, especially at the transition zone, is relevant for seismic hazard evaluation in the densely populated San Francisco Bay Area (e.g., Field et al., 2014; Harris, 2017).

Interferometric Synthetic Aperture Radar (InSAR) is a powerful geodetic tool capable of measuring large-scale ground deformation at high spatial resolution (<100 m) with sub-centimeter accuracy. In recent decades, interseismic deformation at the SAF-CF junction has been measured through the ERS (1992-2001, e.g., Johanson and Bürgmann, 2005; Ryder and Bürgmann, 2008) and Envisat (2003-2010, e.g. Turner et al., 2015) satellites launched by the European Space Agency (ESA), as well as the ALOS mission (2006-2010, e.g., Tong et al., 2013; Jolivet et al., 2015a launched by the Japan Aerospace Exploration Agency. The minimum image acquisition intervals of these systems ranged from 35-46 days, but there were often longer gaps in data collection. Due to the limited number of radar acquisitions, only rate information of fault slip around the SAF-CF junction had been previously extracted through stacking (e.g., Ryder and Bürgmann, 2008) and timeseries analysis (e.g., Jolivet et al., 2015a). With the launch of the Sentinel-1A, B constellation in 2014 and 2016, operated by ESA for the European Union Copernicus program, the recurrence interval in the study region is reduced to 12 days, making it possible to delineate both spatial and temporal behaviors of fault creep.

Various factors have been proposed to control fault creep (Harris, 2017; Bürgmann, 2018). Serpentinite has been found along several California creeping faults (Harris, 2017), and laboratory experiments show that the mineral talc in serpentine significantly reduces the fault strength due to its special frictional properties (Moore and Rymer, 2007). Other creeping faults contain mixtures of clays and other velocity-strengthening and low-friction minerals, and high fluid pressure, or low effective normal stress, is also understood to favor aseismic fault slip (Bürgmann, 2018 and references cited therein).

Nearby earthquakes can accelerate or suppress creep on Bay Area faults due to static stress changes (Lienkaemper et al., 1997; Bokelmann and Kovach, 2003). In terms of the temporal variability of fault creep, episodic slip rate changes on the Central SAF have been proposed to be driven by pore pressure variations (Khoshmanesh and Shirzaei, 2018) and modulated by rainfall as well as other seasonal effects (Roeloffs, 2001). Shallow aseismic slip transients can be dynamically triggered by remote earthquakes (Tymofyeyeva et al., 2019), and the presence of shallow accelerated creep can be a lingering effect of decaying postseismic deformation from nearby large earthquakes (Bokelmann and Kovach, 2003).

In addition to geodetic datasets, seismological observations can also provide a unique perspective of fault creep at depth. Spatiotemporal variability of aseismic fault creep can be inferred

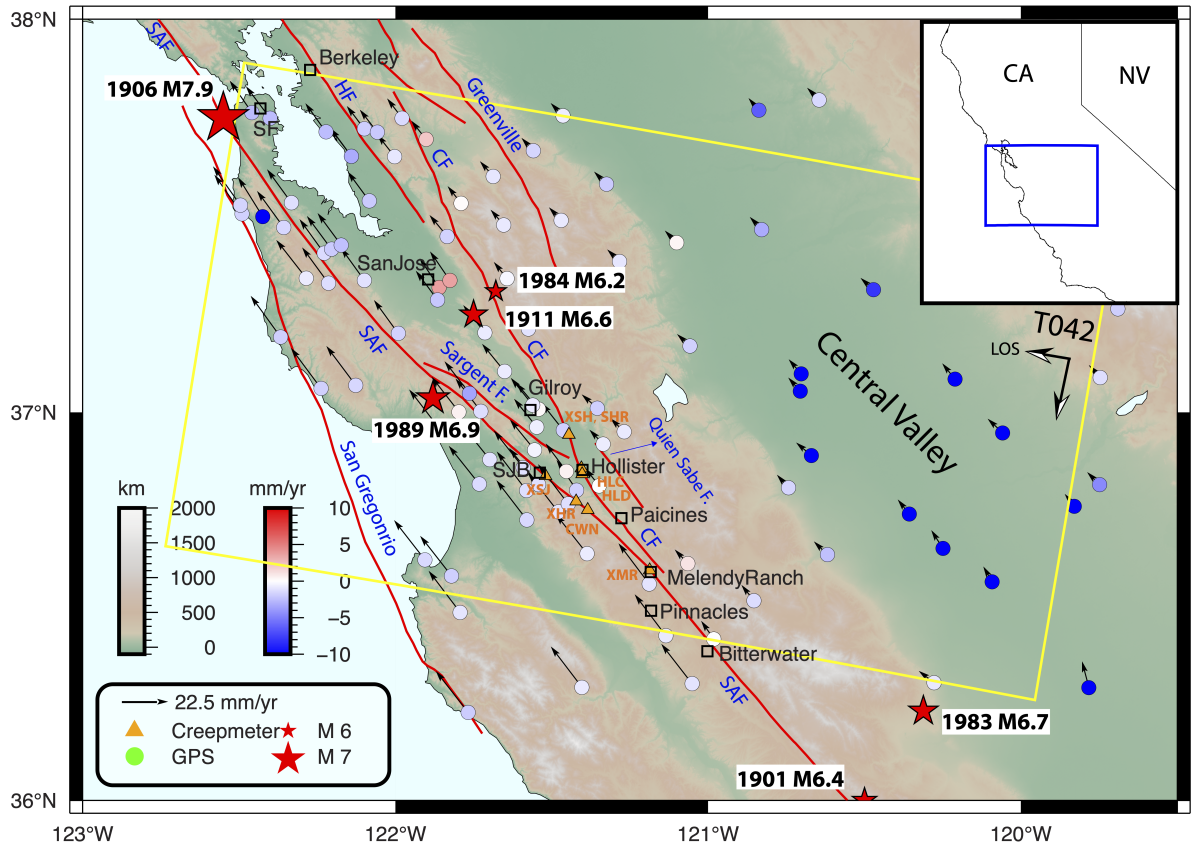


Figure 4.1: Overview map of the study region. The yellow rectangle shows the spatial footprint of the Sentinel-1 InSAR coverage. Black arrows show the horizontal velocity field in the North American reference frame, derived from GPS timeseries spanning the InSAR observation period from the Nevada Geodetic Laboratory (Kreemer et al., 2014; Blewitt et al., 2018). Vertical rates at GPS sites are shown by colored circles. Note that the color for stations in the Central Valley is saturated due to rapid subsidence in excess of 10 mm/yr. Major faults are shown in red lines. SAF: San Andreas Fault, CF: Calaveras Fault, HF: Hayward Fault; SF: San Francisco, SJB: San Juan Bautista. Epicenters of historical M>6 earthquakes since 1900 from USGS are shown as red stars. Locations of creepmeters on the SAF and CF at the SAF-CF junction are shown as orange triangles.

from characteristic repeating earthquakes (CREs, Nadeau and Johnson, 1998; Nadeau and McEvilly, 2004; Uchida and Bürgmann, 2019). Moreover, a recent study by Liu et al. (2022) shows that the distribution of fault creep rates can be directly linked to spatial variations in the fraction of non-clustered seismicity and in b-values.

In this study, we aim to update the interseismic velocity map over the southern San Francisco Bay Area using more than 5 years of Sentinel-1 data through systematic InSAR timeseries analysis. We benchmark our InSAR results with multiple complementary datasets, including alignment arrays, creepmeters, and Global Positioning System (GPS) timeseries. We assess the spatiotemporal behavior of the tectonic and non-tectonic deformation and discuss the slip partitioning between major faults in the SAF-CF junction. Then, we obtain up-to-date creep rate estimates along the SAF and CF at the CF-SAF junction and obtain a detailed mapping of creep behaviors in space and time through the transition zone. We evaluate temporal variations of creep rates on multi-annual time scales. The multi-annual changes of surface creep rates are further compared with temporal changes of seismicity, CREs, and b-values.

4.3 Data and Methods

4.3.1 InSAR data and processing

We use all available Sentinel-1 SAR data collected from descending track 42 covering the study region. We only use descending track data because the ascending geometry is not well-oriented for capturing Bay Area fault motion and is acquired at dusk with substantially greater ionospheric noise (Zhang et al., 2022). The spatial footprint of the SAR coverage is shown in Figure 4.1. A total of 133 images were acquired between May 2015 and October 2020. The InSAR data are processed using the GMTSAR software (Sandwell et al., 2011b; Sandwell et al., 2011a). We use both short-term and 1-year interferograms to form the interferogram network (Figure C.1). For each SAR acquisition, we form interferograms with its five nearest scenes before and after the acquisition; that is, a total of 10 links for each acquisition. No perpendicular-baseline restriction is set when forming the short-term interferograms. To limit the potential phase bias in short-term interferograms (fading signal, Ansari et al., 2021), we add 1-year pairs (350-380 days temporal baseline) with <50 m perpendicular orbit baseline to the network. This leads to a total of 739 interferograms for short- (650) and long-term (89) temporal baselines. All interferograms are geometrically aligned with the reference acquisition acquired on April 26^{th}, 2018. We select the reference acquisition that is at the center of the SBAS network in terms of both the spatial and temporal baselines (Figure C.1). We remove topographic phase contributions using the 30 m SRTM-1 digital elevation model (Farr et al., 2007). We decimate the interferograms 16 and 4 times in range and azimuth direction, respectively, leading to a ∼60 by 80 m pixel resolution. A 200 m Gaussian filter and adaptive Goldstein filter (Goldstein and Werner, 1998) are

applied on the interferograms. The interferograms are unwrapped using the Statistical-cost, Network-flow Algorithm for Phase Unwrapping software (SNAPHU, Chen and Zebker, 2002 with an average coherence mask of 0.2 (Figure C.2). Then, all interferograms are geocoded with a pixel spacing of 60 m.

Tropospheric delay is a major error source for C-band interferometry, and its contribution can be estimated and mitigated through auxiliary information from weather models (e.g., Berrada Baby et al., 1988; Jolivet et al., 2011; Bekaert et al., 2015a). The new generation of the ERA5 weather model (Hersbach et al., 2020) delivered by the European Center for Medium-Range Weather Forecasts (ECMWF) provides hourly solutions of temperature and relatively humidity in 137 vertical pressure levels with 31-km spatial resolution. Here we follow the method described in Jolivet et al. (2011) to correct for the atmospheric delay in each interferogram using the ERA5 weather model products. The ERA5 correction effectively reduces 37% of the variance in the interferograms after ramp removal (Figure C.3). All interferograms are referenced to a 10-by-10 pixel area near GPS station LUTZ, located on a central bedrock exposure in the southern Santa Clara Valley (Figure 4.1). We perform timeseries analysis on interferograms after ERA5 correction using the Small BAseline Subset method (SBAS; Berardino et al., 2002; Schmidt and Bürgmann, 2003. The timeseries product is further cleaned using the Common Scene Stacking method (CSS, Tymofyeyeva and Fialko, 2015 for the removal of remaining, temporally uncorrelated atmospheric noise. Finally, we estimate the average velocity and corresponding uncertainties from the timeseries using linear least squares regression. Note that the CSS method may smooth out the seasonal cycles on the InSAR timeseries (e.g., Figure C.9, station P242), therefore, to better quantify and preserve the temporal behaviors along the faults, we use timeseries results before applying the CSS method in Section 4.4.1 and Section 4.4.3.

4.3.2 GPS timeseries and processing

We download GPS daily solution timeseries from the Nevada Geodetic Laboratory (Blewitt et al., 2018) in the North American plate reference frame (Kreemer et al., 2014). A total of 75 stations that collected continuous data during the InSAR observation period (May 2015 – October 2020) within the InSAR footprint are selected. For the comparison with InSAR, we reference the 3-component displacement timeseries of all stations to GPS station LUTZ. Next, we estimate their secular velocities and corresponding uncertainty in the east, north, and vertical direction, respectively. Then, the 3-component velocities, timeseries, and corresponding uncertainties are projected into the InSAR line of sight (LOS) direction, based on the local look vector at each GPS station. Note that we keep the GPS timeseries in the North American reference frame when modeling seasonal loading parameters in Section 4.4.1.

4.3.3 Creepmeter timeseries and alignment array data

To validate the InSAR average rate and temporal behavior of fault creep, we download creepmeter timeseries from USGS (https://earthquake.usgs.gov/monitoring/deformation/data/download.php). For the SAF, daily solution timeseries from three stations (XSJ2, XHR2, CWC3) and 10-minute solution timeseries from 4 stations (XSJ3, XHR3, CWN1, XMR1) are available for 1985-2020. On the other hand, for the four stations on the CF (XSH1, SHR1, HLC1, HLD1), only manual measurements that were surveyed several times a year are available for the period spanning 1985-2015. Long-term creepmeter timeseries on the SAF and CF used in this study are shown in Figure C.4. Creep rates on the SAF increased immediately after the 1989 Loma Prieta earthquake, whereas fault creep on the CF was suppressed for ∼10 years following the event. Considering the time-dependent nature of the creepmeter records, we divide the creepmeter data into four time periods (1985-1989, 1989-2000, 2000-2015, 2015-2020) and estimate the rates separately (Table C.4). Note that creepmeter measurements are not available on the CF for the InSAR period (2015-2020). Therefore, we only compare creepmeter timeseries on the SAF with our InSAR timeseries in Figure 4.3.

In addition to creepmeter timeseries, we collected published creep rates from alignment array measurements at the SAF-CF junction (e.g., Burford and Harsh, 1980; Lisowski and Prescott, 1981; Galehouse and Lienkaemper, 2003; Titus et al., 2006; McFarland et al., 2017). A complete summary and references of the data sources can be found in Table C.4.

4.3.4 Seismicity, catalog declustering and b-value estimation

We download the double-difference seismic catalog from the Northern California Earthquake Data Center (NCEDC) from 1984 to 2021 (Waldhauser and Schaff, 2008; Waldhauser, 2009). To investigate the spatiotemporal variation of the background seismicity rate, we use the nearest-neighbor approach (Zaliapin and Ben-Zion, 2013; Johnson et al., 2017) to decluster the seismic catalog and exclude the effect of dependent aftershocks on the b-value estimation. We calculate the nearest distance η_{ij} between event pairs (Eq 4.1) from the rescaled time T_{ij} and distance R_{ij} to identify clustered events in the catalog.

$$\eta_{ij} = T_{ij} R_{ij} \tag{4.1}$$

$$T_{ij} = t_{ij} 10^{-qbm_i} \tag{4.2}$$

$$R_{ij} = (r_{ij})^{d_f}\, 10^{-(1-q)bm_i} \tag{4.3}$$

For each event pair, the rescaled time T_{ij} is a function of interevent time t_{ij}, b-value b, event magnitude m_i, and scaling factor q (Eq 4.2). The rescaled distance is a function of event distance r_{ij}, b-value b, event magnitude m_i, scaling factor q and distance scaling factor d_f

(Eq 4.3). Here, we use b=1, q=0.5, d_f=1.6 for the nearest-neighbor distance calculation (Johnson et al., 2017).

We calculate the nearest distance η_{ij} for event pairs of all magnitudes. The distribution of nearest-neighbor distances, and the nearest-neighbor rescaled time and distance plot are shown in Figure C.5. We observe a bimodal distribution of the clustered and background seismicity. The clustered events are close in space and time, therefore have smaller nearest-neighbor distances than the background seismicity. We eliminate the clustered seismicity by removing all events with $\eta < 1.25 \times 10^{-6}$. The comparison between the original (96148 events) and declustered (51324 events) catalogs is shown in Figure C.6.

We estimate b-values using the original and declustered catalogs. The frequency-magnitude distribution of the seismicity can be described by the Gutenberg-Richter law (Eq 4.4, Gutenberg and Richter, 1944), where N is the cumulative number of events larger than a given magnitude M. The constants a and b are the a-value and b-value, where the a-value is a representation of the overall seismicity level, and the b-value is the slope of the distribution, reflecting the relative number of larger- and smaller-magnitude events. The magnitude of completeness M_c is estimated using the maximum curvature method (MAXC) (Wiemer and Wyss, 2000), where we define M_c as the magnitude that has the maximum non-cumulative number of events.

$$\log_{10} N = a - bM, M \geq M_c \tag{4.4}$$

4.3.5 Aseismic fault slip inferred from characteristic repeating earthquakes

We use the Northern California Seismic System (NCSS) waveform catalog to search for CREs. The CREs have nearly identical seismic waveforms and locations, and are believed to repeatedly rupture the same asperity on a fault (Uchida and Bürgmann, 2019). Following our previous studies (Shirzaei et al., 2013; Taira et al., 2014), a waveform coherency analysis was performed to identify CREs. As M_c in our target region is around 1.0 (Tormann et al., 2014), we used earthquakes with M $\geq$ 1.0 from the NCSS catalog during 1984-2019. A total of 70,335 earthquakes were analyzed. For each earthquake, we download seismic records from stations that are located within 35-km from the epicenter. Our analysis used vertical-component data from either broadband sensors or short-period geophones. The waveform coherence was measured with a 10.24-sec data window from the direct P-wave in the frequency band 8-24 Hz. This 10.24-sec window includes S waves and coda waves, and the frequency band was selected to suppress false detections of CREs with M $\geq \sim$1.0 following (Uchida, 2019). As the horizontal location errors for the majority of earthquakes in our target area is less than 3 km, our coherency analysis was applied only for pairs of earthquakes where catalog event separations (horizontally) are less than 3 km. Following previous work (e.g., Materna et al., 2018), CREs were identified if two or more stations meet a coherency threshold to ensure waveform similarity. We used four different coherency

thresholds: 0.95, 0.96, 0.965, and 0.97. In this study, we used the CRE detections with our highest threshold (0.97) to minimize false detection. A total of 21961 CREs in 3667 sequences are detected during 1984-2019.

For each CRE sequence, we can infer the slip from the event magnitude using the empirical relation proposed by Nadeau and Johnson (1998) (Eq 4.5), where d is the slip in the event and inferred aseismic slip driving the CRE recurrence, M_0 is the seismic moment of the CREs, a and b are the scaling factors. We adopt the calibration constants a=-2.36±0.2 and b=0.17±0.001 (Nadeau and Johnson, 1998; Turner et al., 2013) in our study. The seismic moment M_0 is calibrated from the moment-magnitude relationship (Eq 4.6, Hanks and Kanamori, 1979). We estimated the slip on a given fault section by averaging the slip among all sequences within the section, and reconstructed the cumulative slip history from CREs following the procedures described in Nadeau and McEvilly (2004).

$$\log_{10}(d) = a + b \log_{10}(M_0) \tag{4.5}$$

$$\log_{10}(M_0) = 16.1 + 1.5 M_w \tag{4.6}$$

4.4 Results

4.4.1 Average InSAR LOS velocity, timeseries, and validations

The InSAR LOS velocity map derived from the timeseries analysis is shown in Figure 4.2a, and its corresponding uncertainty map is shown in Figure C.7. Our Sentinel-1 velocity map reveals similar ground deformation features as have been identified in previous InSAR studies, including the tectonic fault motion of the San Andreas Fault system (e.g., Johanson and Bürgmann, 2005; Ryder and Bürgmann, 2008; Tong et al., 2013), elastic aquifer deformation due to groundwater-level changes in the Santa Clara Valley (e.g., Schmidt and Bürgmann, 2003; Chaussard et al., 2014; Chaussard et al., 2017), and rapid subsidence in the Central Valley due to unsustainable agricultural pumping (e.g., Ojha et al., 2018; Liu et al., 2019). The InSAR LOS velocities agree well with the projected 3D GPS velocities (Figure 4.2a) with a 1.39 mm/yr standard deviation of the LOS rate differences (Figure 4.2b, c). A complimentary comparison between InSAR and 2D (horizontal only) GPS LOS velocities leads to a 1.46 mm/yr standard deviation of the velocity differences (Figure C.8). Note that nine stations are excluded from the analysis, including seven stations experiencing severe subsidence within the Central Valley and two stations in coastal areas that have extremely poor InSAR coherence (Table C.2).

$$CR_{\text{right-lateral}} = \frac{CR_{LOS}}{[l_e, l_n] \cdot [\sin\theta, \cos\theta]} \tag{4.7}$$

The InSAR timeseries are further validated with creepmeter and GPS timeseries. For comparison with creepmeter measurements, we use InSAR timeseries averaged from 0.5-by-1.5km

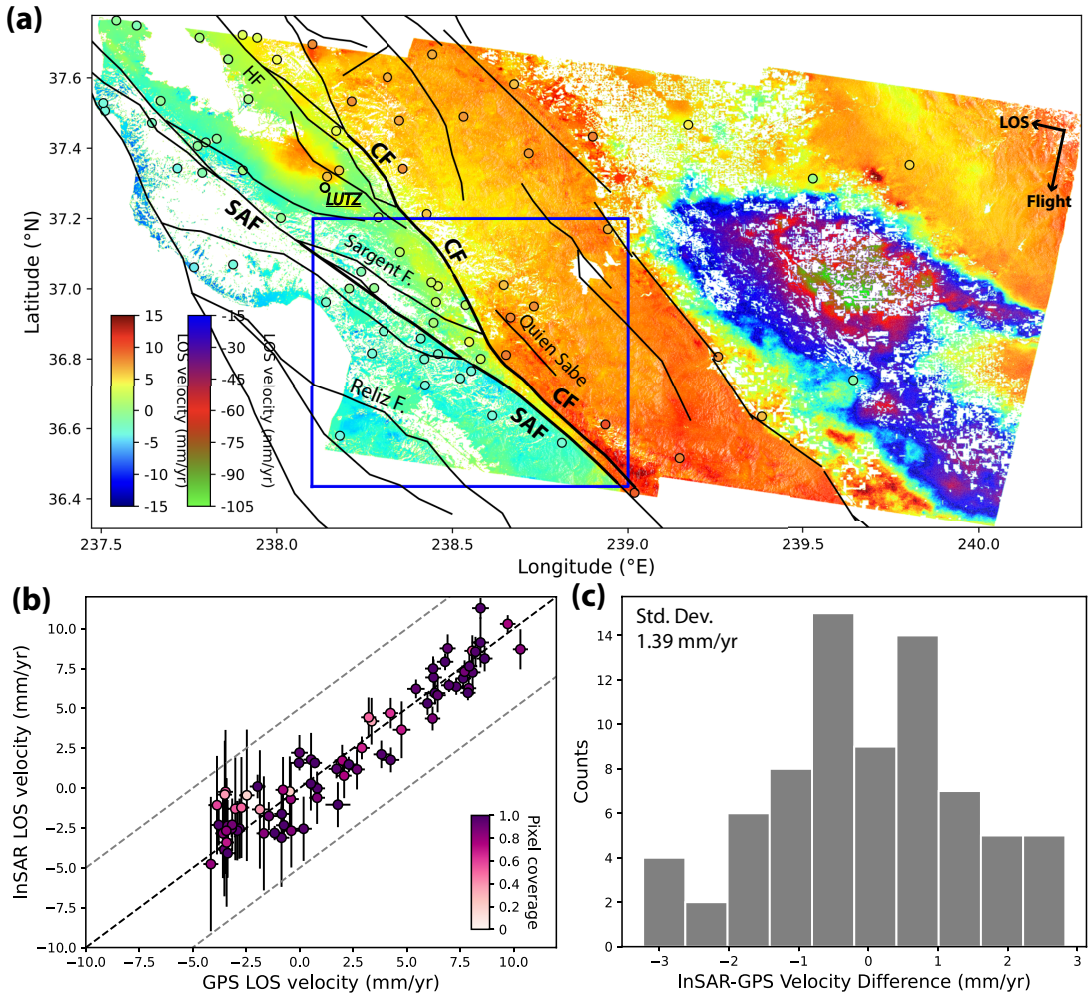


Figure 4.2: InSAR results and validation with GPS velocities. **(a)** Average 2015-2020 LOS velocity map for descending track 42. Red color indicates motion towards the satellite and blue color indicates motion away from the satellite with respect to GPS station LUTZ. Colored circles show GPS LOS velocities projected from 3D velocities estimated from the GPS timeseries during the same time period. InSAR and GPS LOS velocities are in the same color scale. Blue rectangle outlines the SAF-CF junction shown in Figure 4.3a. **(b)** Comparison of the InSAR and GPS LOS velocities colored by pixel coverage, defined as the proportion of valid InSAR pixels within the 10-by-10 box near each GPS station. The InSAR uncertainty at each GPS station is defined by the standard deviation of the InSAR velocities within the 10-by-10 box. Stations within the Central Valley are excluded (Table C.2). **(c)** Histogram of the InSAR-GPS velocity differences with a standard deviation of 1.39 mm/yr.

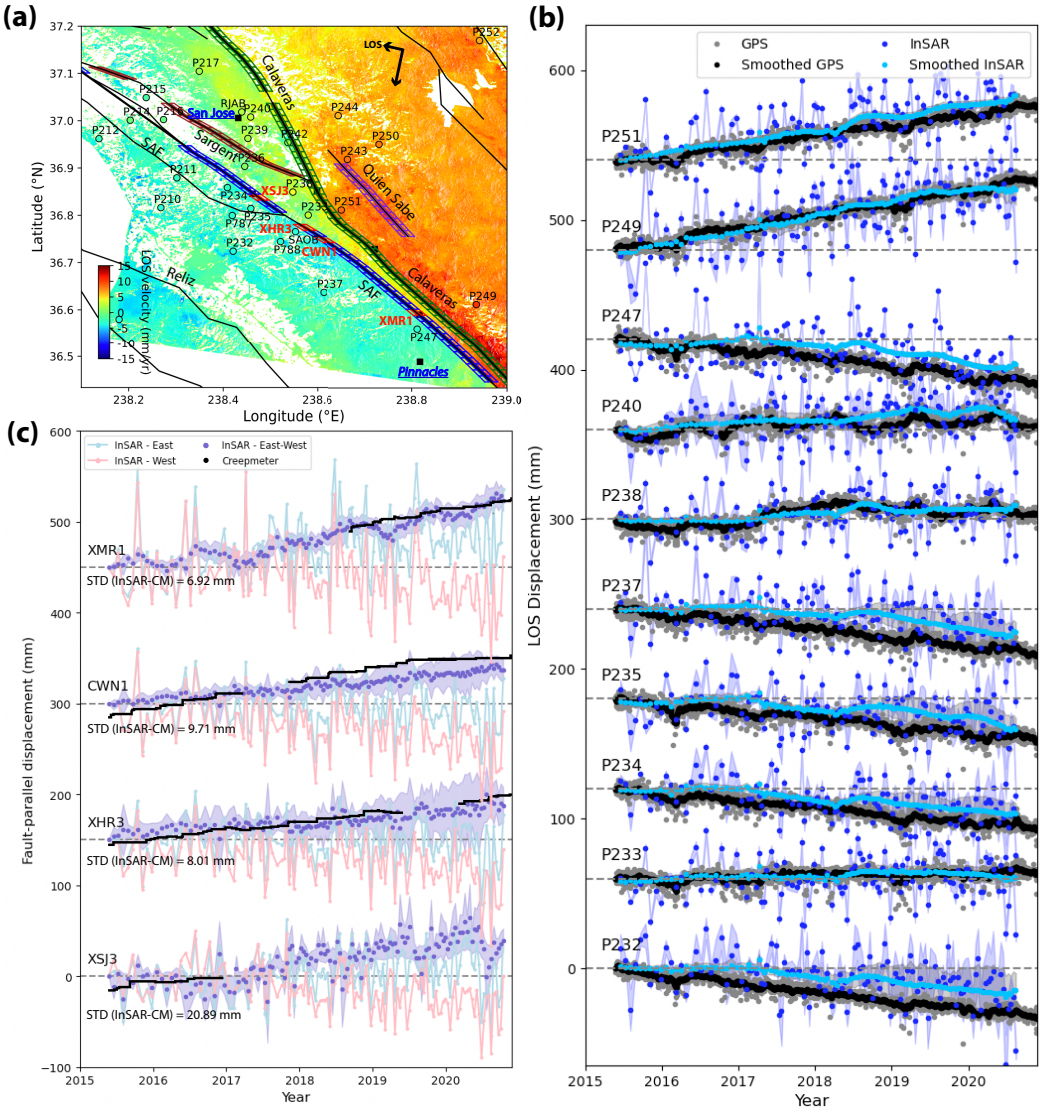


Figure 4.3: InSAR time series and validation. **(a)** Close-up view of the secular velocity field in the SAF-CF junction outlined in Figure 4.2a. Locations of near-fault profiles on each side of the SAF, CF, SF and QSF are shown in blue, green, brown, and purple boxes. **(b)** Comparison of InSAR timeseries with 3D continuous GPS timeseries relative to station LUTZ. Locations of selected stations are shown in (a). Gray dots show the raw GPS timeseries, black dots show the smoothed GPS timeseries using a 14-day moving average, blue dots show the InSAR timeseries, and cyan dots show the InSAR timeseries with common scene stacking method applied (Tymofyeyeva and Fialko, 2015). **(c)** Comparison of cumulative fault creep inferred from cross-fault InSAR timeseries (purple) with creepmeter data (black). Locations of cross-fault boxes are shown as red boxes in (a). InSAR timeseries east and west of the fault are shown in light blue and light pink, respectively.

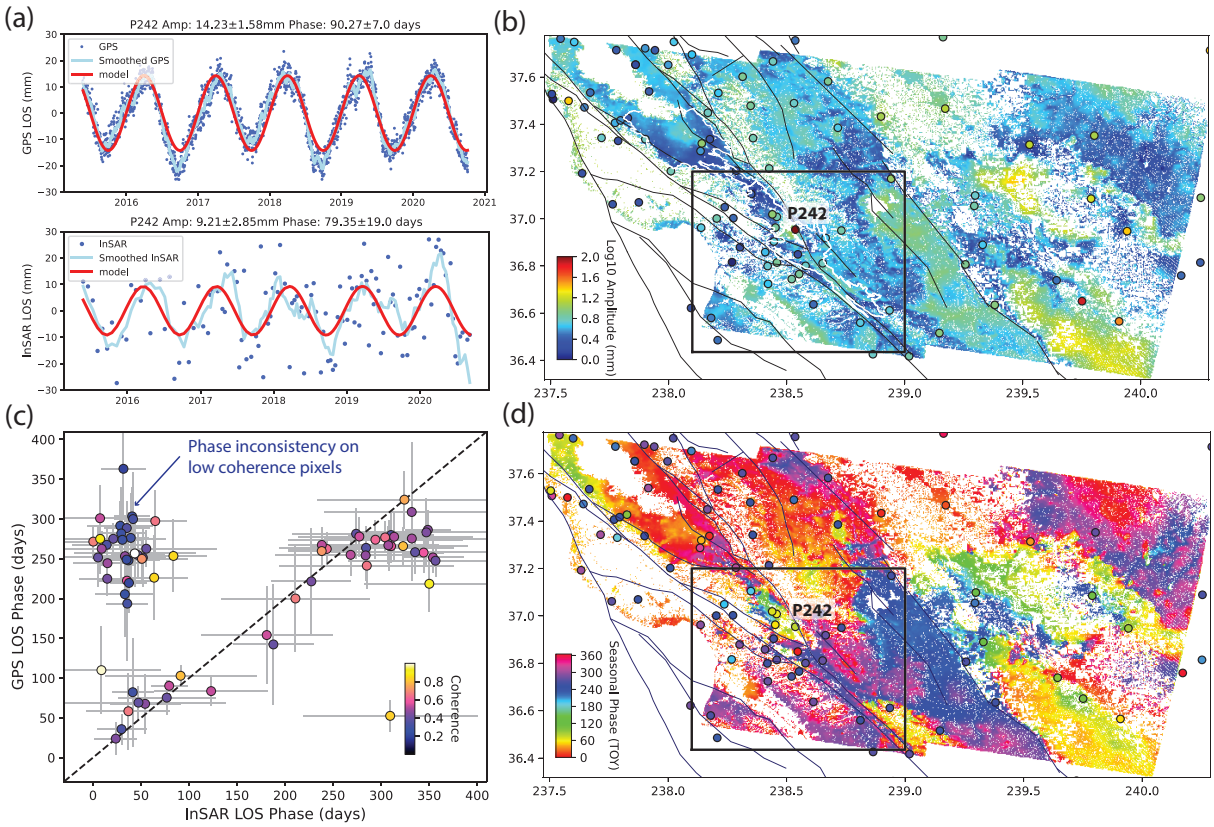


Figure 4.4: Evaluation of the timing of peak seasonal uplift (phase) from InSAR and LOS GPS timeseries in a North American reference frame. **(a)** Example of InSAR and GPS timeseries at station P242. Best-fitting seasonal sinusoidal functions are shown in red curves. **(b)** Amplitude and **(d)** timing of peak seasonal uplift (phase) map obtained from InSAR timeseries. The seasonal amplitude is shown in log scale. Amplitude and phase values derived from GPS timeseries are shown in colored circles. Black rectangle outlines the SAF-CF junction, and white lines in (b) delineate young sedimentary basins in the vicinity of the SAF and CF faults (see Figure C.18 for basin depths across the area). **(c)** Comparison of timing of seasonal uplift from InSAR and GPS timeseries. Each dot is colored with the average coherence from InSAR.

boxes on each side of the fault and compare the cross-fault InSAR-timeseries differences that projected onto the LOS direction (Figure 4.3a, b). Assuming insignificant vertical fault displacements in the region (<2 mm/yr, Figure 4.1), the LOS creep rate can be converted to the right-lateral fault-parallel rate using Eq 4.7, where $[l_e, l_n]$ are the horizontal components of the look vector and θ is the fault strike. The cross-fault InSAR timeseries agree with the creepmeter data with standard deviations of 6.92 mm, 9.71 mm, 8.01 mm and 20.89 mm for station XMR1, CWN1, XHR3, XSJ3, respectively. For comparison with the GPS timeseries, we average the InSAR timeseries from 10-by-10 pixel areas that are collocated with the GPS sites. In the comparison, both InSAR and GPS are referenced to GPS station LUTZ. Examples of InSAR and GPS timeseries collocated at GPS sites around the SAF-CF junction (Figure 4.3a) are shown in Figure 4.3c. Comparisons of InSAR and GPS timeseries at all GPS sites are shown in Figure C.9. The InSAR timeseries agrees with GPS timeseries with average standard deviation of 4.1 mm (with CSS) and 13.5 mm (without CSS), respectively.

As mentioned above, the InSAR timeseries include contributions from multiple sources, including tectonic fault motion and non-tectonic hydrological deformation processes (including elastic surface loading and poroelastic aquifer deformation) that often have a seasonal pattern. To better evaluate the temporal behaviors of non-tectonic deformation and its effect on the assessment of fault behavior, we model the InSAR and GPS displacement timeseries using Eq 4.8, after realizing a North American reference frame (Amos et al., 2014; Materna et al., 2021), where A-F are coefficients of the loading terms, and ω is the angular frequency of the annual seasonal loading. We put our InSAR timeseries into a North American reference frame by finding the best-fitting model parameters (Eq 4.8) for the reference GPS station LUTZ and adding the modeled seasonal cycle to all InSAR timeseries. This assists in the visualization of regional hydrological loading signals in seasonal amplitude and phase maps (e.g., Amos et al., 2014). Then, the amplitude and timing (phase) of the maximum seasonal uplift can be estimated from Eq 4.9, 4.10 (Figure 4.4a).

Figure 4.4b and d show the seasonal amplitude and phase maps derived from the InSAR and GPS timeseries in the North American reference frame. A phase of peak uplift in early spring is consistent with the poroelastic response to aquifer recharge at local groundwater basins (e.g. San Benito-Hollister Basin), whereas a peak in late summer and autumn suggests contributions of the elastic unloading response to the reduction in total water storage in the dry season (e.g., Amos et al., 2014).

$$disp = A\sin(\omega t) + B\cos(\omega t) + C\sin(2\omega t) + D\cos(2\omega t) + Et + F \tag{4.8}$$

$$\text{annual amplitude } = \sqrt{A^2 + B^2} \tag{4.9}$$

$$\text{annual phase } = \tan^{-1}\frac{A}{B} \tag{4.10}$$

The phase derived from InSAR and GPS timeseries agrees well, especially for pixels with coherence >0.2 (Figure 4.4c). The phase inconsistency mainly occurs for low-coherence pixels, and the InSAR phase clustered at ∼50 days is likely due to unmodeled residual atmospheric noise (Figure C.11). If we eliminate the InSAR points clustered ∼50 days, the Pearson correlation coefficient (r) between InSAR and GPS measured phase is 0.87. Figure C.10 shows the comparison of seasonal amplitude between InSAR and GPS timeseries. We see systematic higher seasonal amplitude from InSAR timeseries. This is probably because InSAR is more sensitive to shallow surface processes than GPS sites, which are established on stable bedrocks. Figure C.12 shows the uncertainty of estimated seasonal amplitude and phase from InSAR and GPS timeseries. Here we estimate the phase uncertainty by shifting the phase from the best-fitting model parameters and determining the phase shift producing a 5% residual increase. Similarly, we adjust the amplitude until reaching 5% residual increase to determine the amplitude uncertainty.

4.4.2 Spatial distribution of average creep rates along South Bay Area faults

We measure the spatial distribution of surface creep rates along the South Bay Area faults (the SAF, CF, SF and QSF). To achieve this, we take InSAR timeseries averaged from 1-km-wide, 1-km-long boxes extending from 0.5 km to 1.5 km on each side of the fault and use the cross-fault timeseries differences to obtain the LOS-displacement timeseries of shallow fault creep. The surface fault traces are taken from the latest version of the National Seismic Hazard Model (NSHM, Hatem et al., 2021and resampled it into ∼2-km-long sections. The chosen 2-km interval is comparable to the scale of undulations and corrugations on the SAF (∼2.77 km, Manighetti et al., 2021. Locations of the cross-fault boxes are shown in Figure 4.3a. The profile length is selected to be 0.5-1.5 km on each side of the fault following our previous work (Li and Bürgmann, 2021), and more detailed discussion on the effect of profile length on creep rate estimation can be found in Li and Bürgmann (2021). Given that atmospheric noise is dominantly a long-wavelength signal in space (Bekaert et al., 2015b), nearby pixels share common atmospheric noise features and the majority of atmospheric noise can be canceled out by taking the cross-fault differences. The atmospheric perturbation is significantly reduced after differencing the timeseries (Figure 4.3c). Figure 4.5 shows the LOS displacement timeseries along the two faults arranged by latitude. We define the uncertainty of the cross-fault displacements as the root sum square of the standard deviations of displacements on each side of the fault (Figure C.13). For each InSAR cross-fault displacement timeseries, we estimate the average creep rate through linear regression, and evaluate the residual displacement timeseries as a representation of short-term creep rate variation (Figure 4.5c). In this section, we only discuss the spatial distribution of average fault creep rates along those faults and will consider the residual timeseries (Figure 4.7) in Section 4.4.3.

The spatial distribution of the average surface creep rate along the SAF and CF is shown

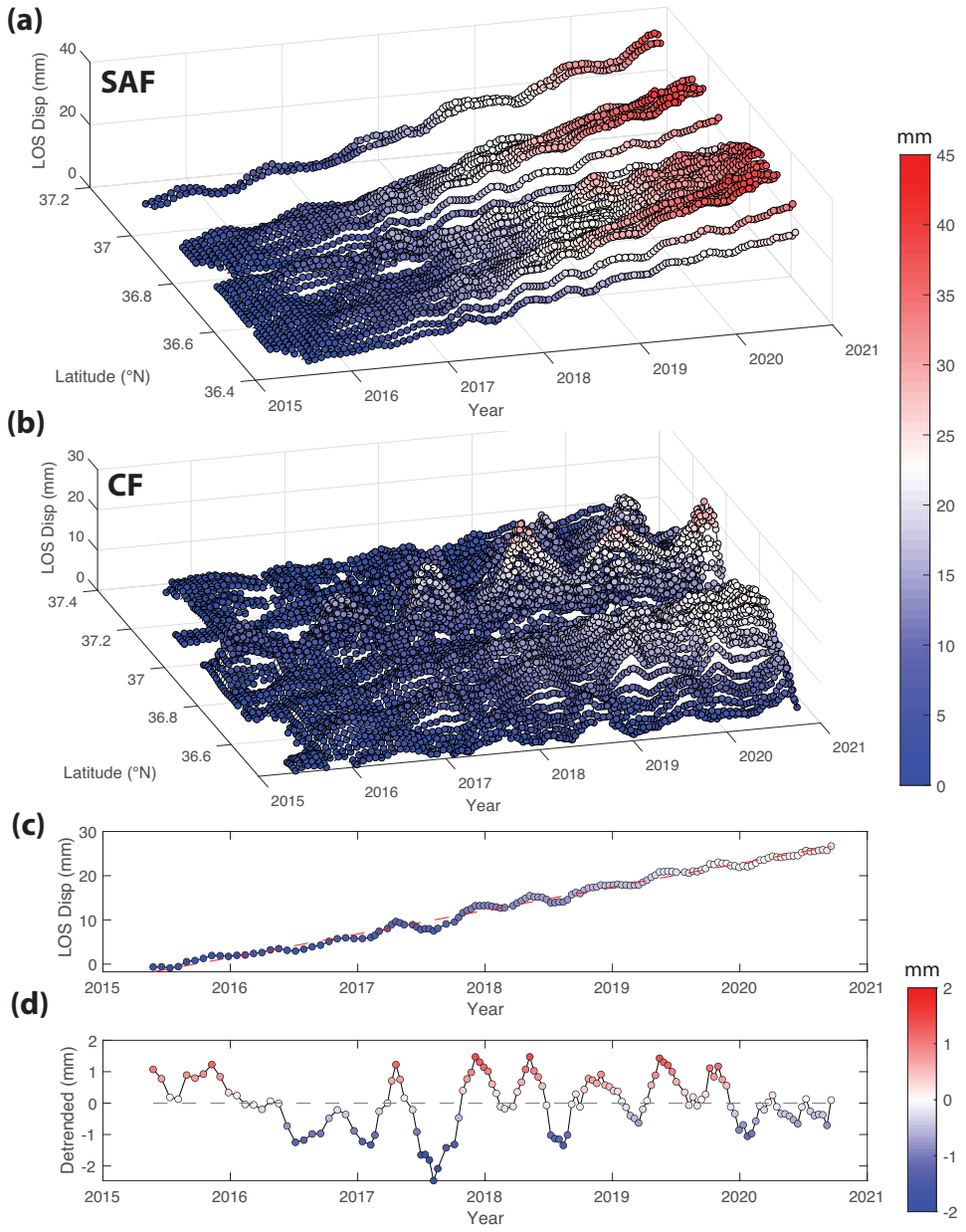


Figure 4.5: Cross-fault InSAR LOS timeseries differences along the **(a)** SAF and **(b)** CF. The cross-fault timeseries are calculated by differencing the InSAR timeseries averaged from 1-km-wide, 1-km-long boxes 0.5-1.5 km on each side of the faults (Figure 4.3). **(c)** Example of cross-fault timeseries on the SAF at latitude 36.45°N. The average InSAR LOS rate due to fault creep is estimated by linear regression (red dashed line). **(d)** We subtract the average creep rate from the original timeseries to highlight the short-term rate variations in the LOS direction. Short-term rate variations after removing the average rate on all profiles are shown in Figure 4.7.

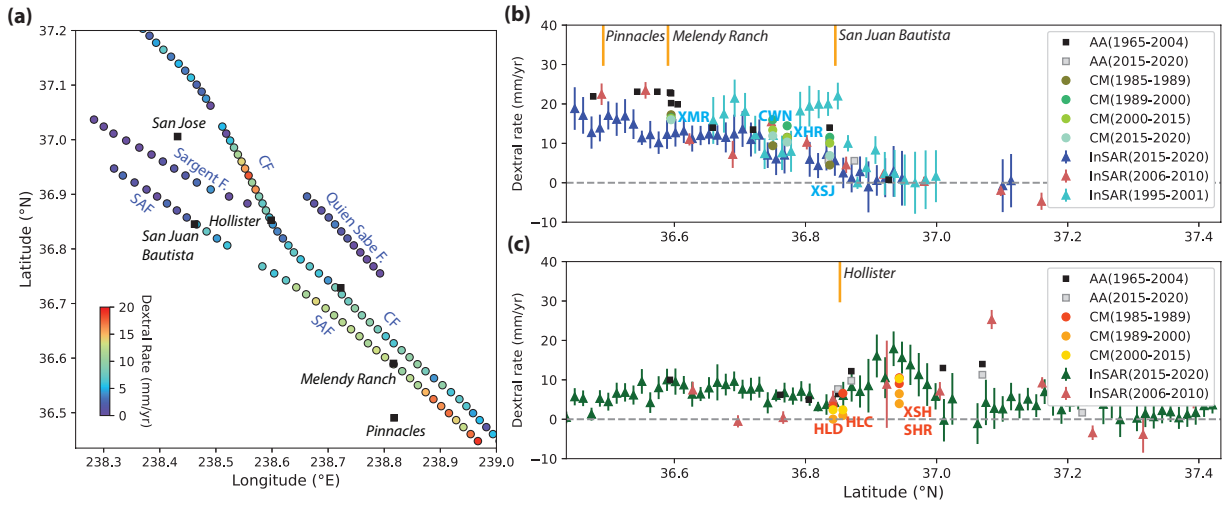


Figure 4.6: **(a)** Spatial distribution of average right-lateral creep rate derived from cross-fault timeseries differences along the SAF, CF, SF and QSF (Table C.3) in map view. Spatial distributions of average right-lateral creep rates along the **(b)** SAF and **(c)** CF arranged by latitude. Blue and green triangles show the creep rates derived in this study (2015-2020) on the SAF and CF, respectively. Cyan and pink triangles show the results from InSAR during 1995-2001 (Johanson and Bürgmann, 2005) and 2006-2010 (Tong et al., 2013), respectively. Green and orange dots with different shades show the rates from creepmeter measurements during 1985-1989 (pre-Loma Prieta earthquake), 1989-2000 (post-earthquake), 2000-2015, 2015-2020, respectively. Black and gray squares show measurements from alignment arrays from multiple sources spanning 1965-2004 and 2015-2020 (McFarland et al., 2017) (Table C.4).

in Figure 4.6, with the LOS rate is converted to right-lateral rate using Eq 4.7. A detailed list of the derived creep rates is shown in Table C.3. At the SAF-CF junction, the SAF is transitioning from its central creeping section to the locked Santa Cruz Mountain segment that hosted the 1989 Loma Prieta earthquake. The creep signal is clearly defined by sharp LOS velocity discontinuities along both the SAF and CF (Figure 4.2a). Our InSAR observations clearly document the existence of shallow fault creep on the subparallel sections of the SAF and CF, where the faults extend for about 50 km with only <5 km separation. Our results capture the decrease in surface creep rate along the SAF from ∼18 mm/yr near Pinnacles/Dry Lake Valley to ∼0 mm/yr (fully locked) north of San Juan Bautista. The CF steps from the SAF at ∼36.4°N, accommodates a portion of the tectonic motion of the San Andreas Fault system and also exhibits fault creep. The inferred strike-slip creep rate on the CF increases from ∼10 mm/yr in the south and reaches its peak rate of ∼20 mm/yr at 36.9°N. Along the subparallel section (36.4°N-36.7°N), the northward decrease of the SAF creep rates is accompanied by an increase of CF creep rates. This anticorrelated distribution of creep rates possibly indicates shallow slip partitioning between the two faults (Figure

4.6a).

We cross-validate our Sentinel-1 InSAR derived creep rates (2015-2020) on the SAF and CF with existing geodetic measurements, including previous InSAR (ERS, 1995-2001, Johanson and Bürgmann, 2005; ALOS, 2006-2010, Tong et al., 2013), alignment arrays (1965-2004, e.g., Burford and Harsh, 1980; Lisowski and Prescott, 1981; Galehouse and Lienkaemper, 2003; Titus et al., 2006) and creepmeter measurements (1985-2020, e.g., Bokelmann and Kovach, 2003; Bilham et al., 2004) (Figure 4.6b, c). A detailed record of the derived creep rates from other sources is listed in Table C.4. Overall, our InSAR-derived creep rates are consistent with the previous datasets. However, we find the surface creep rate derived from ERS InSAR (1995-2001) is significantly higher along a 10-km-long section just south of San Juan Bautista (∼36.8°N), compared to that derived from ALOS (2006-2010) and Sentinel-1 (2015-2020) data (Figure 4.6b). Behr et al. (1990) and Bokelmann and Kovach (2003) observed accelerated surface creep rates on the San Juan Bautista section of the SAF in response to the 1989 Loma Prieta earthquake, and such accelerated creep is also indicated by repeating earthquakes in the region (Turner et al., 2013). The higher creep rates during 1995-2001 may be due to the lingering effect of the fault's response to the 1989 Loma Prieta earthquake and its enduring, deep seated viscoelastic relaxation (Huang et al., 2016). The overall consistency between pre-1989 measurements and present-day InSAR measurements indicates the creep activity has mostly returned to pre-earthquake levels. We also compare our InSAR derived creep rates with topographic differencing measurements (2007-2018, Scott et al., 2020), where we observe systematically higher creep rates from topographic differencing than measurements from other sources (Figure C.14).

We also estimate the shallow creep along the SF and QSF with the same approach we applied to the SAF and CF (Figure 4.6a). The InSAR cross-fault timeseries differences and their associated uncertainties are shown in Figure C.15, C.16 for the SF and QSF, respectively. We identify a section that creeps at up to 4.2±3.1 mm/yr on the SF, while the other section of the fault appears fully locked (Figure 4.6a). Additionally, surface creep up to 3.5±2.6 mm/yr is identified along the QSF. Regardless of the substantial uncertainties on the creep rate estimation, we can at least provide an upper bound of surface creep rates along the SF and QSF from the noisy InSAR timeseries. A detailed documentation of the InSAR-derived creep rates on all faults is provided in Table C.3.

4.4.3 Spatiotemporal variation of the short-term creep rates along the SAF and CF

To capture the time-dependent characteristics of the deformation, we subtract the 2015-2020 linear trend from the InSAR timeseries and focus on the residual InSAR timeseries as representing the displacement history that deviates from the long-term trend (Figure 4.5c). Figure 4.7a, b shows the spatiotemporal variation of the residual InSAR timeseries, representing short-term LOS displacement deviations along the SAF and CF. The InSAR

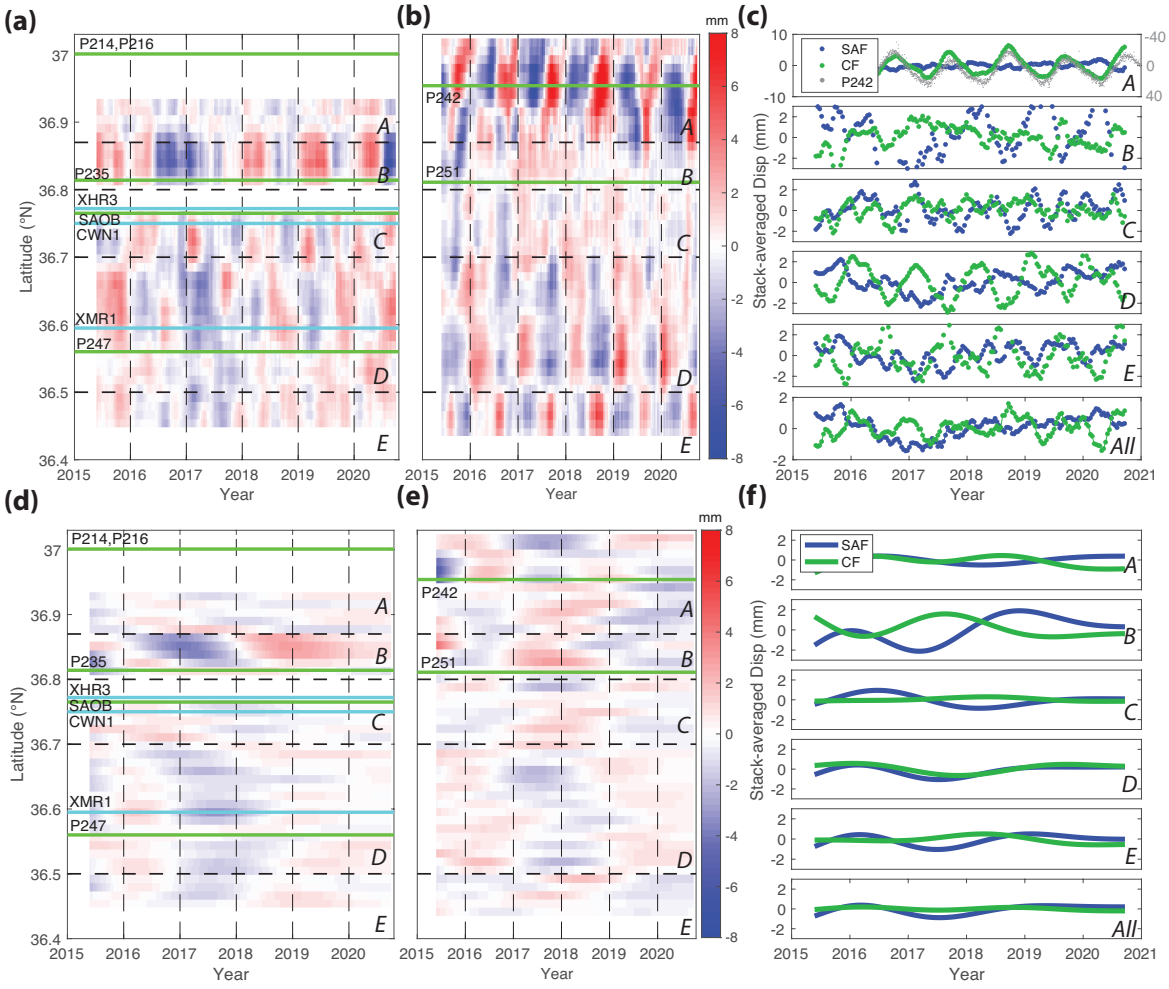


Figure 4.7: Spatiotemporal variation of the residual InSAR LOS cross-fault timeseries after the removal of a linear trend across the **(a)** SAF and **(b)** CF. The red color indicates periods when the short-term displacement exceeds the long-term trend, whereas the blue color indicates short-term displacement below the long-term trend (see Figure 4.5). The locations of near-fault GPS and creepmeter sites are shown with labeled green and cyan lines, respectively. **(c)** Stack-averaged residual InSAR LOS timeseries for the corresponding fault segments A through E arranged by latitude for both SAF (blue) and CF (green). The fault segmentation is indicated with black dashed lines in (a) and (b). LOS timeseries of GPS station P242 are shown in gray dots with y-axis on the right in segment A. **(d)** Multi-annual variation of the residual InSAR timeseries on the SAF after applying an 18-month low-pass filter on (a). **(e)** Multi-annual variation of the residual InSAR timeseries on the CF after applying an 18-month low-pass filter on (b). **(f)** Stack-averaged residual InSAR timeseries on each fault segment after 18-month low-pass filtering. The blue and green lines show the timeseries on the SAF and CF, respectively.

timeseries are resampled into 12-day intervals to accommodate less frequent radar acquisition before the launch of Sentinel-1B in 2016. We also use a 60-day by 10-km-distance moving average window to smooth the spatiotemporal timeseries. Seasonal deformation, mostly contributed by vertical hydrological loading, dominates some of the residual timeseries (e.g., Figure 4.7c-A). The segmentation of the seasonal variations may be related to variations of near-fault lithology (see geologic map in Figure C.17). We divide the cross-fault timeseries into segments, defined by their dominant timing of maximum seasonal LOS variations, and stack-averaged the residual timeseries in each segment (Figure 4.7c). Between 36.4°N-36.7°N, we see phase-shifted timing of the seasonal cycles along the SAF and CF. Further north of 36.9°N, the InSAR timeseries with strong seasonal displacements matches well with the LOS timeseries from a nearby GPS station, P242.

Variable timing of maximum seasonal uplift inferred from the InSAR timeseries has been discussed in Section 4.4.1 (Figure 4.4), where the phase representing the seasonal trough in the LOS timeseries (consistent with peak uplift) in early Spring can be related to the poroelastic response of aquifer systems to groundwater-level rise, and the phase in late summer is consistent with the elastic response to California's water loading cycle. This could also explain the distinct seasonal cycles of the InSAR cross-fault timeseries along different segments, where the two sides of the fault may be exposed to different deformation processes (e.g., Figure 4.7c-D). According to the sediment thickness map from Shah and Boyd (2018) (Figure C.18) and our InSAR phase analysis (Figure 4.4), thick sediments in the Hollister-San Benito basin between the SAF and CF exhibit poroelastic deformation associated with groundwater-level changes in a confined aquifer. This is likely the main cause of the seasonal cycles in the cross-fault InSAR timeseries, leading to anticorrelated patterns in the cross-fault residual timeseries observed on the SAF and CF. Near GPS station P242, the CF serves as a boundary of the local aquifer system, with strong groundwater variations west of the fault that dominates the seasonal pattern of P242 and the cross-fault InSAR timeseries. Therefore, we attribute most, if not all of the short-term deformation observed in the cross-fault InSAR LOS timeseries to contributions from vertical hydrological deformation processes, rather than a tectonic source.

To minimize the effect of short-term seasonal contributions from hydrological deformation processes on the estimated fault creep, we apply an 18-month low pass filter to the residual InSAR timeseries. The low-pass filtered spatiotemporal distribution of fault creep is shown in Figure 4.7 d,e,f. The 18-month window is selected to ensure the seasonal signals are effectively removed. We observe multi-year long-term creep rate changes (deviating by up to 2-3 mm from the long-term average rates) along the SAF and CF from the low-passed filtered InSAR timeseries. We see a rate decrease around mid-2017 on both the SAF and CF, mostly between 36.5°N-37.5°N, where the two faults are sub-parallel to each other with $<$5 km separation. We will validate the observed subtle coupling change with information from seismicity and CREs in section 4.5.3.

4.4.4 Spatiotemporal variation of the b-value at the SAF-CF junction

We estimate the spatiotemporal distribution of the b-value at the SAF-CF junction using the declustered and relocated catalog from NCEDC (1984-2021) (Waldhauser and Schaff, 2008; Waldhauser, 2009). The spatial distribution of the seismicity and the resolved b-values calculated in 0.05° grid elements around the SAF-CF junction are shown in Figure 4.8a. For each grid cell, we extract all available events during 1984-2020 within the grid, and only estimate b-values for grid cells containing N>200 events. Then, we estimate the magnitude of completeness M_c, and obtain the a-value and b-value using Eq 4.4 on all valid grids. We also evaluated the spatial distribution of b-values on 0.025° and 0.1° grid elements. The spatial distribution of M_c, a-value, b-value and b-value uncertainties with grid size of 0.05°, 0.1° and 0.025° are shown in Figure C.19. To examine the effect of clustered seismicity on the b-value estimation, we compare the spatial distribution of seismicity and b-value before and after declustering, finding a very similar spatial pattern (Figure C.20). The SAF generally has a lower b-value (0.4-0.8) than the nearby CF (0.8-1.2) derived from both original and declustered catalogs.

We inspect the temporal variation of the b-value during 2015-2020, corresponding to the InSAR observation period in this study. Limited by the total number of available events in each time interval, we use a 1-year moving window (±0.5 year) window with 0.5-year step to ensure at least 100 events in each time step (Figure 4.8). We then separate the microseismicity into three groups, including the seismicity along the SAF and CF within 2.5 km of the fault traces, and off-fault events that are >2.5 km away from the two faults. The total number of events in each time step and the resolved b-values along the SAF, CF and off-fault areas are shown in Figure 4.8b,c,d. Monthly precipitation data from the North America Land Data Assimilation System (NLDAS, Xia et al., 2012) is shown in Figure 4.8e. The b-value fluctuation along the SAF and CF share similar patterns, whereas the off-fault regions show different temporal evolutions. The b-values decrease between 2016-2017 and recover between 2017-2018, leading to relatively low b-values in 2017 along the SAF and CF. The temporal fluctuation of the b-values between 2016-2018 have a similar pattern as the long-term decrease of creep rate from the residual InSAR timeseries. In addition, we do not see a significant seismicity rate change during the period of b-value changes (Figure 4.8c). The potential mechanisms underlying the b-value variations in 2016-2018 and their correlation with the InSAR long-term creep rate changes will be further discussed in Section 4.5.3.

4.5 Discussion

In this section, we will discuss the observed shallow fault creep on the SF and QSF (Section 4.5.1) and explore the partitioning of shallow fault creep between the SAF, CF, SF and QSF

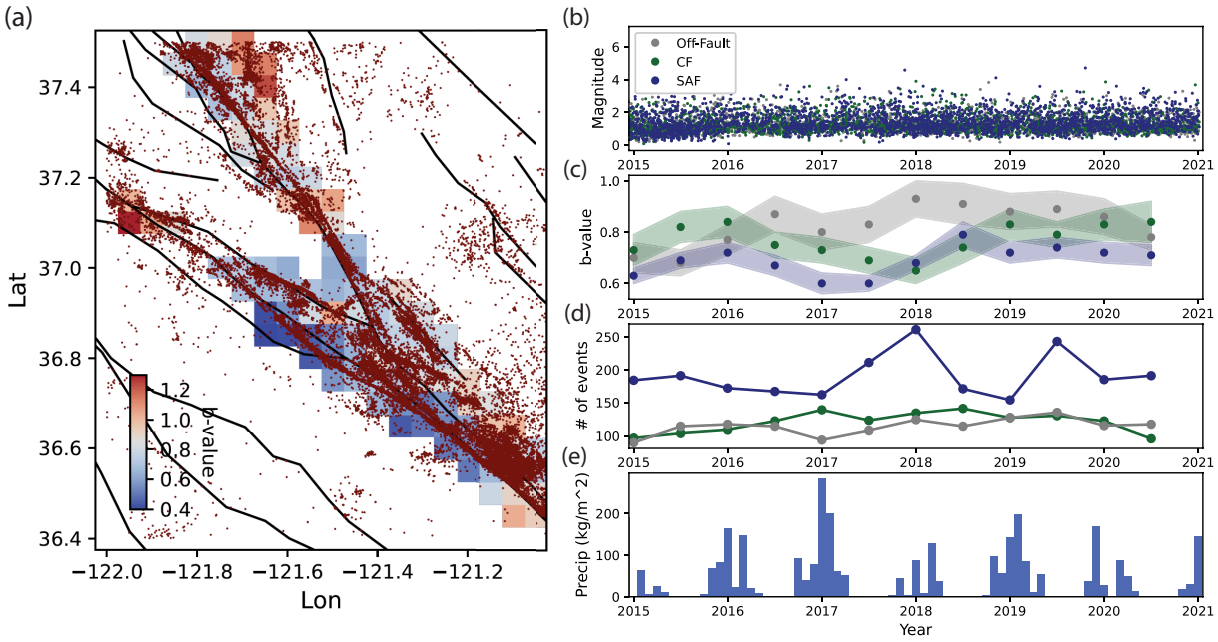


Figure 4.8: **(a)** Spatial distribution of the double-difference relocated and declustered seismicity from NCEDC (1984-2021) and b-values in the study region. **(b)** Magnitude-time plot of the declustered seismicity (2015-2020) along the SAF, CF and off-fault events. **(c)** Temporal evolution of b-values calculated with a 1-year moving window that steps by 0.5-year for each seismicity group (see (b) for color legend). **(d)** The total number of M>Mc events in each time interval for each seismicity group. **(e)** Monthly total precipitation in the study area retrieved from NLDAS (Xia et al., 2012).

(Section 4.5.2). In the last section (Section 4.5.3), we relate the observed multi-year coupling change from InSAR timeseries to variations in CREs and seismicity, and propose possible driving mechanisms underlying the observations.

4.5.1 Shallow fault creep on the SF and QSF

Being one of the main faults in the area between the SAF and CF at the SAF-CF junction, the 55-km-long SF appears to connect the locked section of the SAF in the Santa Cruz Mountains and the creeping CF near Hollister (Figure 4.1, Mongovin and Philibosian, 2021). The southern SF has been shown to creep at the surface at 2.9±0.7 mm/yr (Prescott and Burford, 1976). A recent study by Mongovin and Philibosian (2021) resurveyed the alignment array sites of Prescott and Burford (1976) and obtains a creep rate of 3.3±1.3 mm/yr and 1.7±0.8 mm/yr for the northern and southern arrays, which are 3.7 km apart from each other. Evidence from repeating earthquake sequences suggests a 1-2 mm/yr (Turner et al., 2013) or 5.3±2.0 mm/yr (Waldhauser and Schaff, 2021) fault creep rate at 2.5-7.5 km depth on the SF. Similar to the creeping sections of the SAF and CF, there are CREs along a 20-

km-long southern section of the SF (Turner et al., 2013; Waldhauser and Schaff, 2021; this study). The co-existence of InSAR-observed shallow creep (up to 4.2±3.1 mm/yr) and CREs indicates that shallow aseismic slip on the SF plays an important role in slip partitioning and strain transfer on the SAF system.

The 25-km-long QSF is located near the southeastern Hollister Valley, east of creeping sections of the SAF and CF. Unlike the localized seismicity observed along the SAF, CF, and SF, the seismicity is distributed across a 2-4 km wide zone (Watt et al., 2014). Based on CRE observations, the fault has been inferred to creep at depth at 2.2-11.4 mm/yr (Templeton et al., 2008) and 5.4±2.0 mm/yr (Waldhauser and Schaff, 2021). Recent geological mapping also found en-échelon cracks on a fault-crossing road surface in the southern Hollister Valley section of the fault (Baldwin and Bloszies, 2022), indicating possible evidence of aseismic slip on the fault. Our InSAR results also indicate surface creep at up to 3.5±2.6 mm/yr.

Our work provides the first InSAR observation of shallow creep (0-4 mm/yr) along the SF and QSF, and the information on fault coupling near the surface from the geodetic and repeating-earthquake data should be of value for rupture-scenario simulations and seismic hazard analysis for these faults. This indicates that secondary structures, including the creeping SF and QSF, participate in the complex shallow deformation along the SAF-CF junction, accommodate more distributed deformation away from the two primary fault strands, and relieve some of the tectonic loading by continuous creep.

4.5.2 Partitioning of the shallow fault creep among the SAF and CF

At the SAF-CF junction, the SAF is transitioning from rapidly creeping to fully locked at the surface, while the CF branches from the SAF and exhibits spatially variable creep rates. Understanding how shallow fault slip partitions among the main fault strands of the SAF system is crucial for seismic hazard evaluation (Field et al., 2014), especially in the densely populated Bay Area. A number of hypotheses have been proposed to explain the extent of fault creep, including the presence of frictionally weak and velocity-strengthening materials in the fault core (e.g., Lockner et al., 2011; Moore and Rymer, 2007), low effective normal stress due to elevated pore pressure (e.g., Wei et al., 2009) and faults that have high roughness and complex fault structure (Bürgmann, 2018). Fault geometry has also been proposed to be a key factor controlling the spatial distribution of fault creep, including the local fault strike with respect to the regional principal stress orientations (Jolivet et al., 2013), creep localization on transpressional segments (Bilham and Williams, 1985; Lindsey et al., 2014b), and fault roughness that possibly leads to a heterogeneous stress field and promotes creep (Jolivet et al., 2015b).

Here we explore the correlation of fault creep with the local fault geometry, specifically the angle between fault strike and background stress orientation (Jolivet et al., 2013). The

regional background stress orientation resolved from M>1.5 focal mechanisms (Johnson et al., 2017) is shown in Figure 4.9. We take N15°E as the maximum horizontal stress orientation (β in Eq 4.11), assuming a uniform background stress in the SAF-CF junction. We note that the horizontal stress field inferred from inversion of focal mechanisms varies modestly across the region and the uniform background stress is only a first-order approximation. We then calculate the proportion of the maximum principal stress that is projected onto the receiving fault geometry. That is, assuming a uniform background stress field and loading rate, the proportion of stress that is effectively acting in the fault-parallel (shear) and perpendicular (normal) directions on the local fault geometry. We refer to these measures as the unit shear- and normal-stress loading rates along the SAF and CF (Figure 4.9, Eq 4.11, 4.12), where θ is the local fault strike and β is the maximum horizontal stress orientation.

$$\dot{\sigma} = \cos(2(\theta - \beta)) \tag{4.11}$$

$$\dot{\tau} = \sin(2(\theta - \beta)) \tag{4.12}$$

The spatial distribution of creep rate and the unit shear- and normal-stress loading rates are shown in Figure 4.9. We further assess the variation of normalized creep rate and the normal- and shear-stress loading rates on the SAF and CF arranged by latitude (Figure 4.10). For the SAF, a striking correlation between the creep rate and relative shear stress loading (Pearson correlation coefficient r=0.74), and anticorrelation with normal-stress loading (clamping) are observed (r=-0.71) (Figure 4.10a). Even though the correlation for the CF is less clear (Figure 4.10b), the distribution of fault creep still matches the stress loading patterns to the first order. Particularly at ∼36.9°N on the CF, the peak creep rates match the location with high shear stress and low normal stress. This correlation suggests that the fault geometry, and thus the local shear- and normal-stress loading on the fault plane, play a role in controlling the first-order variation of surface creep rates.

Our results show that creep rate variations may be influenced by geometry and effective normal stress, where higher shear-stress and lower normal stress loading rates tend to promote aseismic fault creep at the SAF-CF junction. This is opposite to the observation on the southern SAF (Bilham and Williams, 1985; Lindsey et al., 2014b), where higher rates of localized creep are more evident on transpressional segments. The possible effect of fault-normal convergence rates on fault creep has also been discussed by Argus and Gordon (2001), who found that reduced fault-normal convergence rates can only partially explain the distribution of creeping faults along the SAF system. That is, even though there is overall support for the hypothesis that low fault-normal convergence rates and stress are associated with stable fault creep, there are also counter examples. What we observe at the SAF-CF junction and the observations along the southern SAF (Lindsey et al., 2014b), may represent end-member cases of the hypothesis discussed by Argus and Gordon (2001).

At the SAF-CF junction, the tectonic loading of the SAF system is mainly accommodated by the SAF and CF. Secondary structures like the SF and QSF also play a role in the

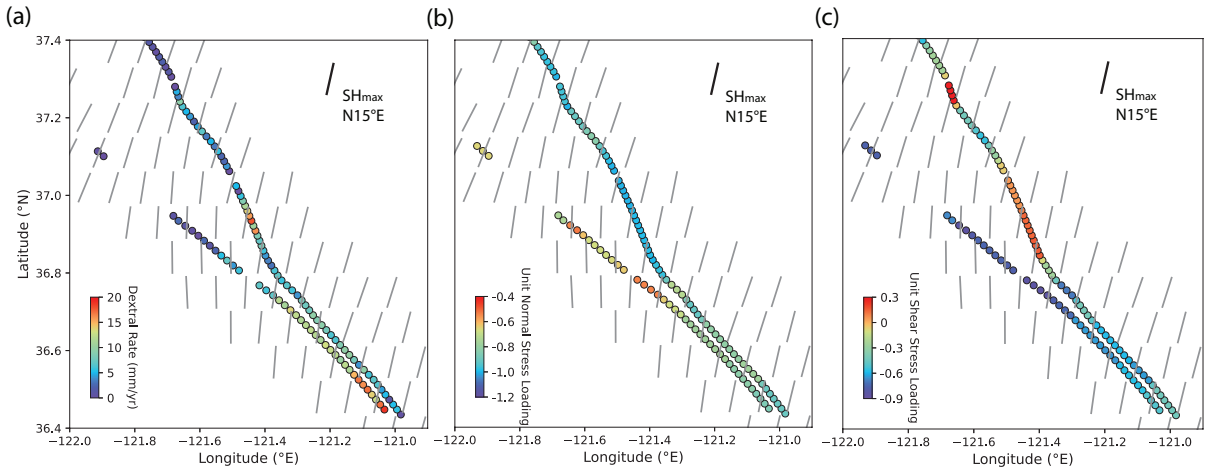


Figure 4.9: Map view of the spatial distribution of **(a)** creep rates, **(b)** unit normal-, and **(c)** shear stress loading rate on SAF and CF. The unit normal and shear stressing loading rates are calculated assuming an average N15°E maximum horizontal stress orientation. Background maximum-stress orientations in the study region are from Johnson et al. (2017). Positive unit normal stress loading rate indicates clamping while negative value indicates unclamping.

partitioning. If there are multiple faults that are weakly coupled, it is likely that creep gets distributed among them to continually relieve the tectonic loading. To explore the spatial partitioning of shallow fault creep among the SAF, CF, and secondary structures, we project the creep rates onto a profile parallel to the creeping section of the SAF (N45°W) and calculate the summed creep rates among all faults (Figure 4.11). The along-fault sum of right-lateral creep rates remains steady (∼20-25 mm/yr) from 0-60 km along-fault distance from Bitterwater (121°W, 36.4°N), where the SAF and southern CF are subparallel to each other. The summed creep rates gradually decrease northward (60-100 km distance), where the fault creep is partially partitioned onto the SF and QSF (Figure 4.11b). Further to the north, a further decrease of the summed creep rates is indicated, as most of the CF creep is transferred to the Hayward Fault (Chaussard et al., 2015).

We show that the shallow aseismic slip can be partitioned between nearby structures simply due to geometric constraints. Of course, other factors also affect the distribution of shallow creep rate, such as fault frictional properties (Jolivet et al., 2013) and the spatial distribution of locked asperities at depth (e.g., Savage and Lisowski, 1993; Bürgmann et al., 2000; Simpson et al., 2001). The absolute differences of the tectonic loading projected on fault sections due to variable fault strike are quite subtle. The modulation of fault creep by stress loading may thus indicate relatively low frictional resistance of the creeping faults in the SAF system, particularly for the SAF. Such low friction on the creeping section of the SAF has also been supported by stress orientations (Provost and Houston, 2001), heat flow measurements

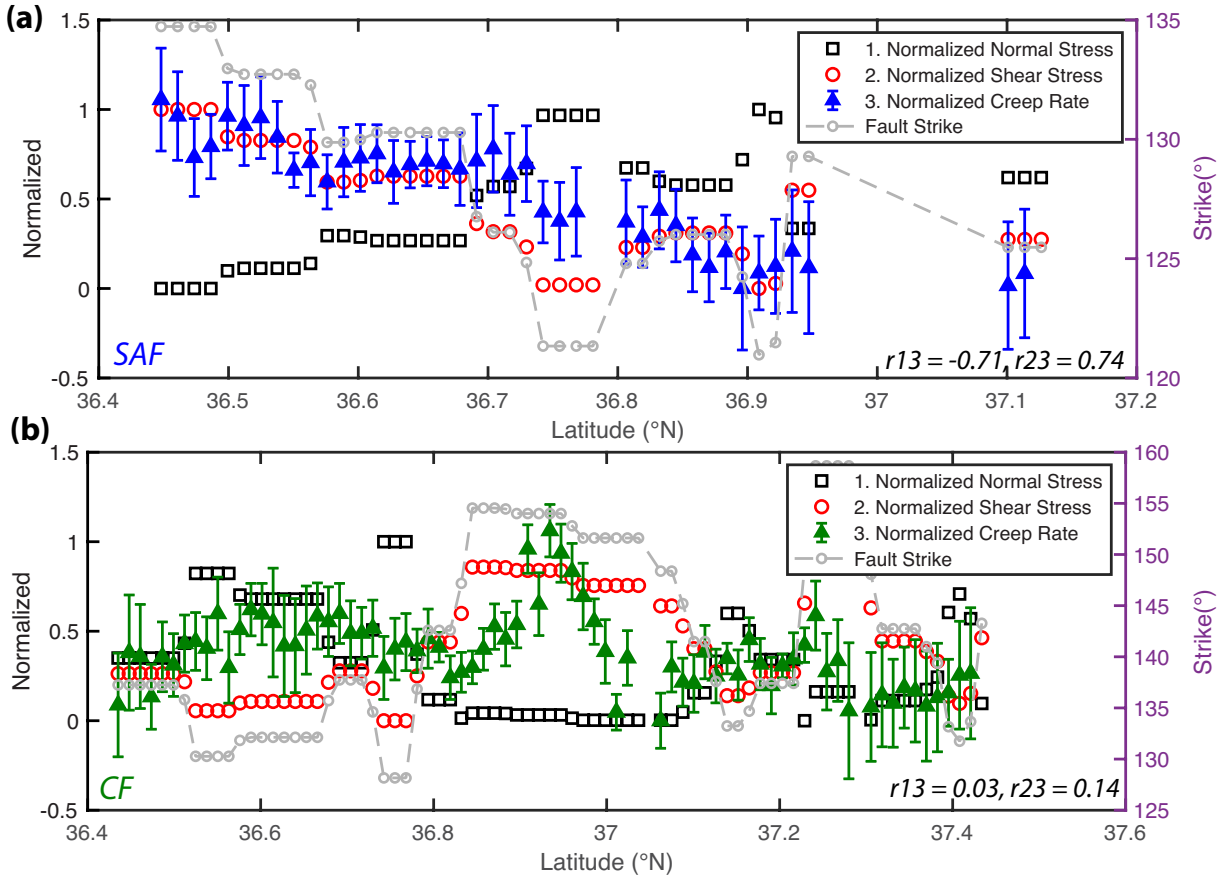


Figure 4.10: Spatial distribution of normalized dextral creep rate, normal and shear stress loading on the **(a)** SAF and **(b)** CF arranged by latitude. The background maximum horizontal stress orientation is assumed to be N15°E. Larger normal stress loading rate indicates more clamping while smaller indicates reduced clamping. The Pearson correlation coefficient between normalized stress components and creep rate are labeled in the plot (subscript number pairs refer to numbered values in legend), where $r = -1$ indicates anti-correlation and $r = 1$ indicates perfect correlation.

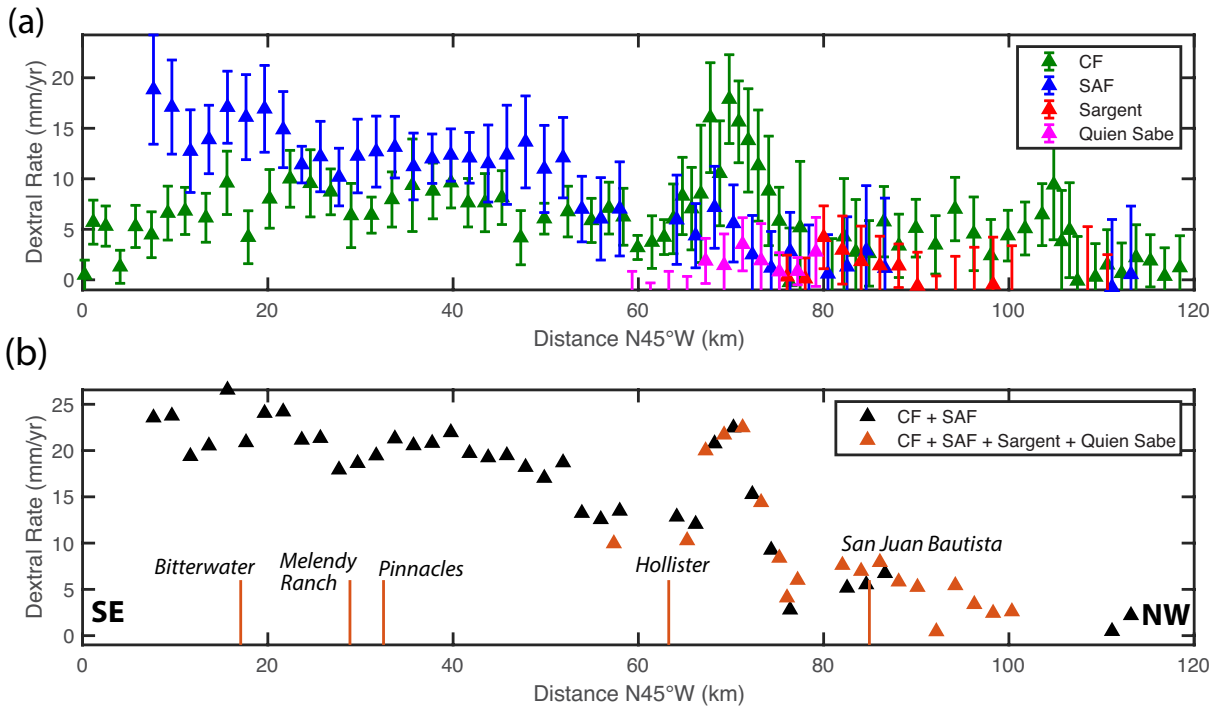


Figure 4.11: **(a)** Along-fault (N45°W) distribution of creep rates on the SAF, CF, SF and QSF. **(b)** Along-fault sum of right-lateral creep rates on the SAF, CF, SF and QSF. The along-fault distance is calculated with respect to Bitterwater (121°W, 36.4°N).

(D'Alessio et al., 2006), and laboratory experiments (Lockner et al., 2011).

4.5.3 Long-term coupling changes along the SAF and CF

As described in Section 4.4.3, we see a subtle, multi-year change of the long-term creep rate along the SAF and CF after applying an 18-month low-pass filter on the original detrended InSAR timeseries (Figure 4.7). To further investigate this feature, we compare the temporal variations of our InSAR-derived creep rates with slip inferred from CREs and changes in b-value derived from microseismicity in the study region during the same time period (2015-2020).

The spatial distribution of the CREs is shown in Figure 4.12a. Following the same procedure previously applied to the InSAR timeseries, we remove a linear trend from the cumulative slip timeseries inferred from the CREs along the SAF and focus on the residual timeseries. The spatiotemporal variation of the residual slip inferred from CREs, and the associated uncertainties are shown in Figure C.21, where the uncertainties are based on the uncertainties of the scaling parameters of the empirical relationship (Eq 4.5). We only calculate the CREs inferred slip on the SAF because there are very few CREs on the CF (Figure 4.12a). The

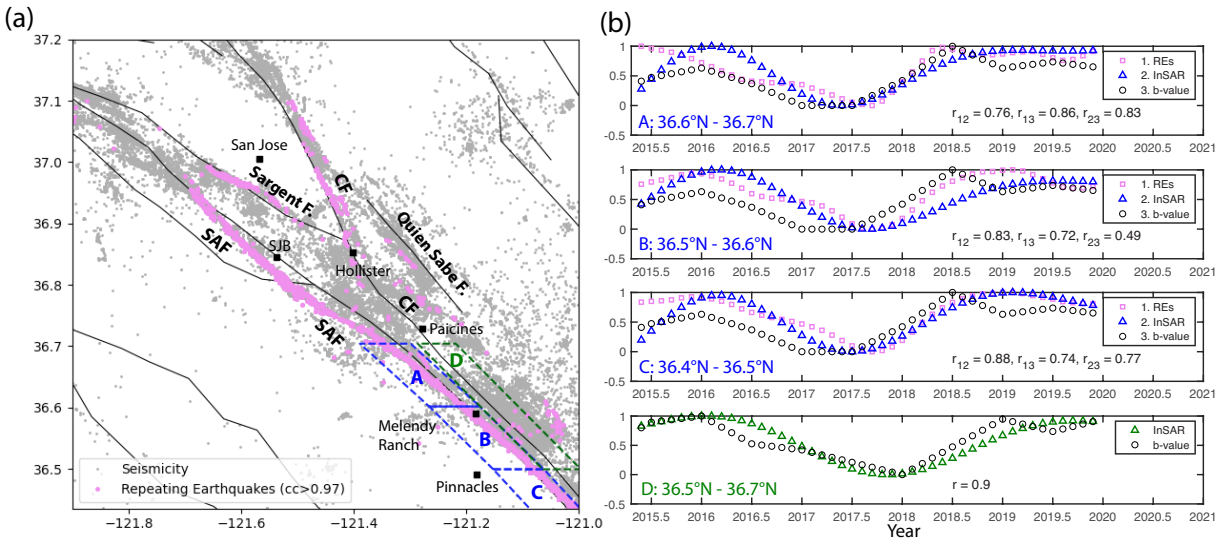


Figure 4.12: **(a)** Spatial distribution of the NCEDC seismicity (gray) and identified repeating earthquakes with cc>0.97 (pink) in this study. **(b)** Temporal variation of b-value, residual shallow slip timeseries inferred from InSAR and repeating earthquakes that are binned by latitude along the SAF and CF. Top three panels show analysis on the SAF (blue) and bottom panel shows analysis on the CF (green). The corresponding regions are outlined in (a) with blue and green boxes on the SAF and CF, respectively. The residual InSAR, CRE-inferred slip and b-value timeseries are normalized to [0, 1]. The Pearson correlation coefficients (r_{ij}) between scaled b-value, residual InSAR and CRE-inferred slip timeseries are labeled in the plot (subscript number pairs refer to numbered values in legend).

lack of CREs on portions of CF possibly indicates the fault is locked at depth with larger asperities, which is also inferred from coupling models (e.g., Manaker et al., 2003).

A direct comparison of the temporal evolution of b-value, InSAR, and CRE-inferred creep rate on the SAF along 36.4°-36.7° is shown in Figure 4.12b. The b-value, InSAR, and CRE-inferred residual timeseries are normalized by their maximum values, given these measures cannot be directly compared with an absolute scale. Note that we apply a 1-year moving window (±0.5 year) on the timeseries of both b-value and CREs inferred slip, while the InSAR timeseries is low-pass filtered to 18 months to eliminate potential seasonal hydrological effect. We only compare SAF fault sections with resolved variations in CRE-inferred slip (36.4°-36.7° in Figure 4.12). During 2015-2020, we find similar temporal behaviors in the residual timeseries from both InSAR and CREs, indicating a lower than average rise in cumulative fault slip, particularly during Jan-June 2017. The residual timeseries gradually recover to the average level after reaching a minimum in June 2017. The same temporal pattern is also observed in the b-value variations along the SAF. The high correlation coefficient between all curves (r=0.7-0.88) lends support to the temporal coupling changes inferred from the low-

pass filtered InSAR timeseries. Similar temporal behaviors are also observed in CRE-inferred timeseries with different moving windows (0.2, 0.6, 1.0, 1.5 years) (Figure C.22), indicating the observed feature is independent of the choice of smoothing. In 2015, we do not see a similar initial increase in the CRE and b-value data. Therefore, we think this initial increase may be an artifact introduced by the filtering of InSAR timeseries. Along 36.8°-36.9°, we attribute the InSAR-measured variations to hydrological processes, given the contrast in sediment thickness across the fault (Figure C.18), as well as the lack of CRE-derived slip variations along that section (Figure C.21).

For the CF, we can compare the temporal evolution of b-value and residual InSAR (Figure 4.12b, bottom panel) due to the lack of repeating earthquake sequences on the CF. A high correlation coefficient (0.90) between the b-value and residual InSAR timeseries shows a lower than average rise in creep rate accompanied by a decrease in b-value, during 2017-2018. The temporal behavior of the b-values and residual InSAR timeseries on the SAF precede the CF by three to six months, indicating a possible transfer of shallow slip at the SAF-CF with a time-lag. Considering the close separation (2-6 km) of the two faults along the subparallel section, it is possible that accelerated fault slip on one fault imposes a stress shadow on the other fault, and the two faults interact by static stress transfer. Further modeling is required to validate this reference.

A link between temporal b-value and creep rate changes has been discussed in Schorlemmer et al. (2004), where they find significant correlation between b-value change and a creep episode along the Parkfield section of the SAF in 1993. Our analysis suggests the correlation between long-term changes of b-value and fault slip inferred from CREs and InSAR timeseries for the SAF and CF fault section between 36.4°N-36.7°N. While InSAR observations show shallow fault coupling change near the surface, CREs inferred slip variations show the coupling change at seismogenic depth (5-10 km). Assuming the tectonic loading remains constant over a longer period, a slight decrease of fault creep at the seismogenic depth indicates temporal coupling increase, suggesting that temporarily less stress is accommodated through seismic and aseismic slip, leading to increased stress levels, possibly reflected in lower b-values, which may indicate relatively higher seismic potential. The origin of such short-term, transient coupling changes could be due to the static stress interactions between the two faults, temporal changes of fault frictional properties, variations of pore fluid pressure, fault zone damage, and dilatancy changes. It is worth mentioning that the 2016-2017 wet season had extensive precipitation (Figure 4.8e), and the coupling change between 2016-2018 was possibly affected by the rainfall. Overall, all observations provide evidence of resolvable coupling changes between 2016-2018. The correlation of b-value and shallow creep rate changes may indicate that the SAF and CF are sensitive to small stress perturbations. This also indicates that InSAR could be a promising tool for monitoring subtle spatiotemporal changes of coupling and stress conditions.

4.6 Conclusion

We perform a timeseries analysis using 5 years of Sentinel-1 InSAR data from May 2015 to October 2020 covering the southern San Francisco Bay Area. The derived InSAR velocities agree with the GPS LOS velocities with 1.39 mm/yr standard deviation for 66 stations, and the InSAR timeseries agree with GPS and creepmeter timeseries with 4.1 mm and 11.3 mm standard deviation, respectively. Fault creep rates on the SAF decrease from ∼18 mm/yr at Pinnacles to fully locked ∼10 km north of San Juan Bautista. The inferred strike-slip creep rate on the CF increases from ∼10 mm/yr in the south and reaches its peak rate ∼20 mm/yr at 36.9°N. Our InSAR observations clearly document shallow fault creep on the subparallel sections of the SAF and CF, where the faults extend for about 50 km with only <5 km separation. Along the subparallel section (36.4°N-36.7°N), the northward decrease of the SAF creep rates is accompanied by an increase of CF creep rates, suggesting a transfer of shallow slip. We provide upper-bound estimates of surface creep of 4.2±3.1 mm/yr for the SF and 3.5±2.6 mm/yr for the QSF. We show that the distribution of fault creep is to first order controlled by the angle between fault strike and the background stress orientation. We further examine the spatiotemporal variation of the long-term creep rates and find a long-term coupling increase during 2016-2018 along the SAF and CF. A striking correlation (0.72-0.88) between long-term changes of b-values and residual aseismic slip timeseries inferred from CREs and InSAR timeseries is found along the sub-parallel sections of the SAF and CF between 36.4°N and 36.7°N. The temporal behavior of the b-values and residual InSAR timeseries on the SAF proceed the CF by three to six months, indicating the possible transfer of slip between the SAF-CF with a time-lag. These observations indicate that InSAR is a promising tool for monitoring subtle changes of fault coupling and creeping faults are extremely sensitive to small stress perturbations.

Chapter 5

Detecting Creep Transients in InSAR Timeseries Using Deep Neural Networks

5.1 Abstract

Interferometric Synthetic Aperture Radar (InSAR) is a powerful tool to monitor tectonic fault creep in high spatial resolution and large spatial coverage with a regular temporal basis from days to months. However, the detectability of low amplitude transient creep signals from InSAR timeseries is still largely limited by the contamination of atmospheric noises in SAR acquisitions. In this study, we adopt the neural network structure from (Rouet-Leduc et al., 2021) and train it with 10^6 synthetic InSAR timeseries to specifically targeting transient creep detection. We evaluate the trained denoising autoencoder (DAE) on synthetic InSAR timeseries and find the performance is strongly dependent on the SNR of the input timeseries. Additionally, we test the performance of the DAE on InSAR timeseries with pure noise and steady-rate signal, and validate the DAE's applicability on reconstruction of InSAR timeseries with multiple creep episodes. We further assess the performance of the DAE on the timeseries of the creeping North Anatolian and Chaman Fault.

5.2 Introduction

Creeping faults in California exhibit both steady and episodic behaviors, including slow slip events (Wei et al., 2013). Growing evidence indicates that shallow fault creep can be triggered by nearby (e.g., Linde et al., 1996; Wei et al., 2011; Li and Bürgmann, 2021) or remote earthquakes (e.g., Tymofyeyeva et al., 2019), modulated by elevated pore pressure (Khoshmanesh and Shirzaei, 2018), and composed of aseismic slip transients in addition to the background steady creep (e.g., Bilham and Behr, 1992; Rousset et al., 2016). Variable

creep behaviors contribute to regional strain and stress variations, and accelerations of creep rates may produce stress perturbations on faults and even trigger earthquakes. Due to limited observations of such low-amplitude near-fault signals, the governing factors for variable creep behaviors are still not well understood. Better quantification of the spatiotemporal fault creep will not only reveal its underlying mechanisms but may also provide insight for seismic hazard assessment.

Interferometric Synthetic Aperture Radar (InSAR) measures high-resolution large-scale ground deformation on a routine basis. With the launch of Sentinel-1, the satellite recurrence interval was reduced to 6-12 days globally, making it possible to monitor short-term transient deformation, such as afterslip (Wang and Bürgmann, 2020), remotely triggered slow slip events (Tymofyeyeva et al., 2019), and shallow aseismic slip transients (Rousset et al., 2016). Theoretically, InSAR timeseries can reach sub-centimeter accuracy if the SBAS network is properly designed and atmospheric noise contributions are minimized (Ferretti et al., 2007). However, the detectability of low-amplitude transient signals is still largely limited by the contamination of atmospheric noises in SAR acquisitions.

Traditional atmospheric correction methods include applying an empirical model between topography and atmospheric delay (e.g., linear, Elliott et al., 2008; quadratic, Wright et al., 2004; power-law, Bekaert et al., 2015a), using an external auxiliary dataset to estimate the atmospheric delay (e.g., Moderate Resolution Imaging Spectroradiometer, MODIS, Li et al., 2005; European Centre for Medium-Range Weather Forecasts, ECMWF, Jolivet et al., 2011; Generic Atmospheric Correction Online Service, GACOS, Yu et al., 2018), and applying stacking or temporal smoothing methods (e.g., common scene stacking, Tymofyeyeva and Fialko, 2015; Kalman filter, Dalaison and Jolivet, 2020). Even though the aforementioned methods have proven effective for long-term interseismic rate estimation, it is still challenging to extract low-amplitude short-duration signals from InSAR timeseries. Enabled by the increasing volume of SAR acquisitions, deep learning algorithms have been applied to automatically identify earthquake and volcano deformations in InSAR images (e.g., Anantrasirichai et al., 2018; Anantrasirichai et al., 2019; Sun et al., 2020; Brengman and Barnhart, 2021). Moreover, Rouet-Leduc et al. (2021) developed an encoder-decoder neural network and showed its effectiveness in denoising InSAR timeseries.

In this study, we aim to develop a neural network structure that is well designed for detecting shallow creep transients, based on the encoder-decoder structure proposed by Rouet-Leduc et al. (2021). Specifically, we aim to evaluate a series of neural network structures trained with synthetic timeseries incorporating synthetic and real noise features, and finally apply the denoising method on the creeping North Anatolian Fault and Chaman Fault to identify transient creep signals. The development of a successful InSAR denoising method will refine our understanding of how strain and stress evolve on continental creeping faults over time. This work also benefits past (e.g. ERS, Envisat, ALOS) and planned future SAR missions (e.g. NISAR) by mitigating the atmospheric delay in radar measurements.

5.3 Neural Network Structure

The autoencoder is a type of neural network that learns the key features of the input data and reconstructs the original input using its compressed representation. The denoising autoencoder (DAE) is one of its variations that adds noise into the original input and recovers the clean image through the encoder-decoder structure. The original introduction of DAE aimed to avoid overfitting and only learn robust features through deep neural networks. Currently, DAEs have been widely used in the image denoising community (e.g. applications in medical images, Gondara, 2016). We start with the autoencoder structure proposed by Rouet-Leduc et al. (2021), and modify the neural network design to optimize for the detection of transient fault creep events.

The detailed structure of the neural network adapted from Rouet-Leduc et al. (2021) is shown in Figure 5.1. The inputs of the DAE are a batch of InSAR timeseries consisting of 9 epochs. Through training, the DAE learns to differentiate between the spatiotemporal statistics of tectonic signal and atmospheric noise, and output the noise-free cumulative displacement of the input timeseries. The DAE consists of 5 convolutional layers and 2 pooling layers in the encoder. Each pooling layer is reducing feature maps in the time domain, while keeping the spatial dimension unchanged. At the bottleneck, the topography is added as an extra feature map accounting for the topography-correlated atmospheric noises. A batch normalization layer is followed by the bottleneck. The DAE is further decoded with 4 convolutional layers to reconstruct the cleaned output. We use the rectified linear unit (ReLU) activation function after each convolutional layer. Each convolutional layer contains 64 3x3x2 filter kernels in the encoder and 64 $3\times3\times1$ kernels in the decoder, respectively. In total, more than 400k trainable parameters are included.

5.4 Preparation of the Synthetic Training Set

As described in Section 5.3, the extraordinary amount of trainable parameters in the DAE requires substantial training datasets to sufficiently train the neural network. Given there is no ground-truth noise-free measurements from InSAR, we will use synthetic deformation timeseries with added noises as training sets.

5.4.1 Synthetic atmospheric noise generation

The atmospheric noises in the interferograms are composed of two major components, namely the spatially-correlated turbulence delay and topography-correlated stratified tropospheric delay. For the turbulent component, we simulate the spatially-correlated Gaussian noise using the model proposed by Lohman and Simons (2005), where the noise covariance matrix C_d is a function of distance L_{ij} and scale length Lc (Eq 5.1), and the correlated Gaussian noise matrix N_c can be simulated from the uncorrelated Gaussian noise matrix N_n, the eigenvalues

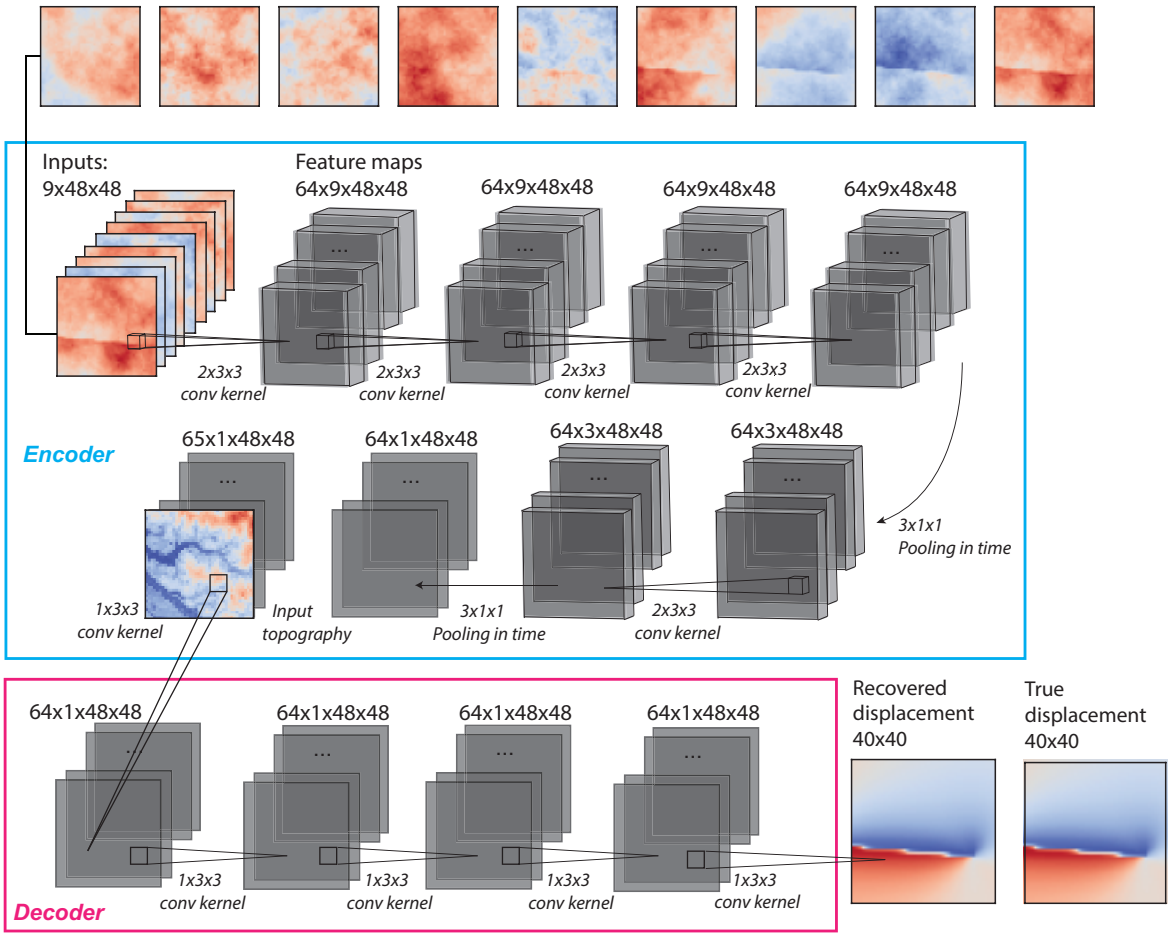


Figure 5.1: The neural network structure of the denoising autoencoder that is adapted from Rouet-Leduc et al. (2021). It takes a batch of InSAR timeseries as input and outputs cumulative displacement over the same time period. A DEM is fed into the model as secondary input at the bottleneck.

U and the eigenvectors V of the covariance matrix C_d (Eq 5.2). Here we randomly generate the uncorrelated Gaussian noise matrix N_n and randomly select the scale length Lc in the range of [5, 95] pixel size.

$$C_d = e^{-\frac{L_{ij}}{L_c}} \tag{5.1}$$

$$N_c = V\sqrt{U}N_n \tag{5.2}$$

For the topography-correlated tropospheric noise, we first create synthetic digital elevation models (DEMs) by generating isotropic 2D fractal surfaces with a power-law behavior (Hanssen, 2001). The power-law exponent (β) of the radially averaged 1D power profile in log-log scale is randomly taken from the continuous range of [1,3]. The range of β is determined from 500 real-world DEMs randomly sampled from the major continents around the world (Brengman and Barnhart, 2021) (Figure D.1). An example of the fractal analysis on the real-world and synthetic DEMs is shown in Figure 5.2. With the randomly generated synthetic DEMs, we simulate the topography-correlated atmospheric noise from the power-law model from Bekaert et al. (2015a) , where the tropospheric delay is a function of reference height h_0, local height h, power-law exponent α and a scaling factor K (Eq 5.3). Components of spatially-correlated and topographic-correlated noises are combined with a random weight to form the synthetic atmospheric noises.

$$\Delta\Phi_{\text{tropo}} = K\left(h_0 - h\right)^{\alpha} \tag{5.3}$$

5.4.2 Synthetic InSAR timeseries generation

For the spatial characteristics of the transient fault creep, we generate surface deformation through the Okada dislocation model (Okada, 1992), assuming an elastic homogeneous half-space. Fault parameters including location, length, width, depth, strike, dip and the amount of strike-slip are randomly drawn from a uniform distribution within a given range. Here we constrain the fault depth to be close to the surface and the fault plane to be near vertical (70°-90°), representing behaviors of continental creeping faults. The 3D displacements are further projected into the line of sight (LOS) direction using randomly generated heading and incidence angle that are reasonable for Sentinel-1 ascending and descending viewing geometries.

The synthetic InSAR timeseries is generated by projecting the spatial characteristics of the deformation into a sequence following particular temporal evolution pattern (Figure 5.3). That is, the deformation signals share the same spatial pattern over time with evolving amplitudes. We assume the temporal evolution of the shallow creep transients follows the cumulative distribution function of a Gaussian distribution (Rouet-Leduc et al., 2021). The onset and end times of the transients are randomly generated as well. Under the assumption

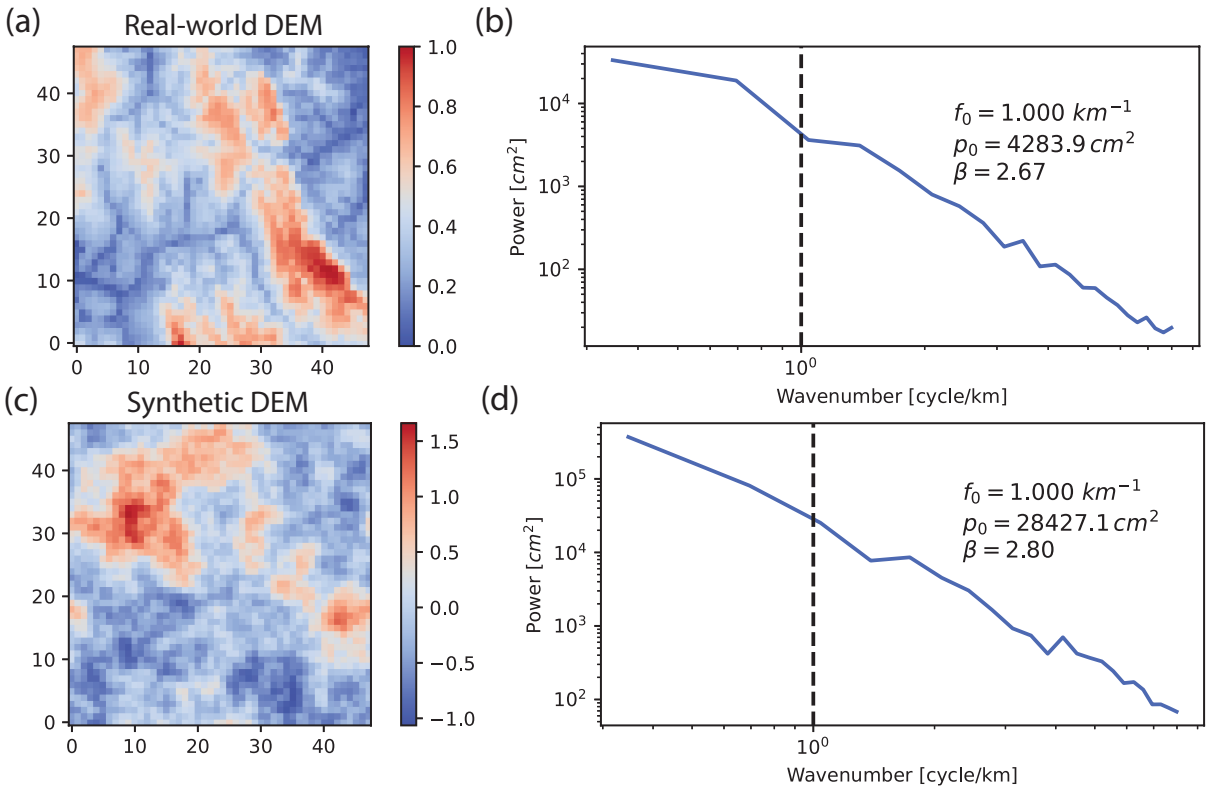


Figure 5.2: An example of fractal analysis on the **(a)** real-world DEM and **(b)** synthetic DEM.

that the atmospheric perturbations are random in time, we add the atmospheric noise components to each epoch of the InSAR timeseries with a random signal-to-noise ratio (SNR, Eq 5.1) ranging from 10^{-5} to 10^{3}. An example of the synthetic timeseries is shown in Figure 5.3.

$$\text{SNR} = \frac{P_{\text{signal}}}{P_{\text{noise}}} = \left(\frac{\text{RMSE}_{\text{signal}}}{\text{RMSE}_{\text{noise}}}\right)^2 \tag{5.4}$$

5.5 Results

5.5.1 Neural network training

The neural network structure is implemented in PyTorch (Paszke et al., 2019). We select the batch size and learning rate to be 64 and 0.001, respectively. We use the mean absolute error (MAE) as the loss function and Adam optimizer (Kingma and Ba, 2014) during the neural network training. We also apply a log-transformation on the input synthetic timeseries,

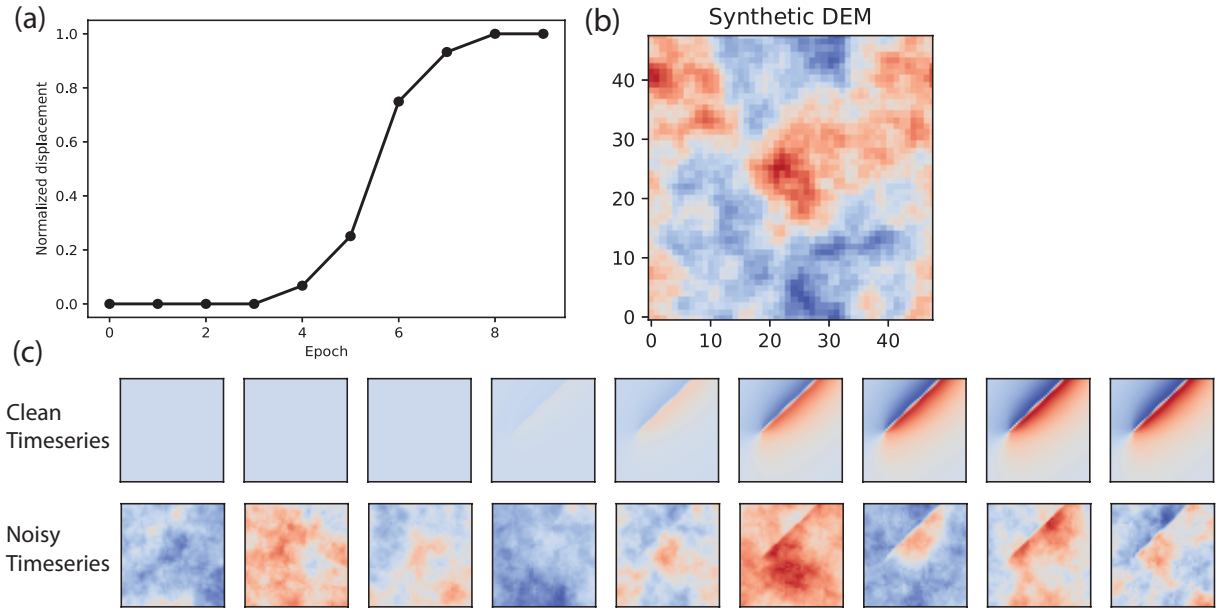


Figure 5.3: An example of the synthetic InSAR timeseries generated for the training set. **(a)** Temporal evolution of the transient signal following the cumulative distribution function of the Gaussian function. **(b)** Synthetic DEM. **(c)** Clean and noisy InSAR timeseries with randomly generated fault parameters. Both spatially-correlated and topography-correlated atmospheric noises are considered in the noisy timeseries.

where we keep the sign of the input signal and only convert the amplitude of the signal to preserve the deformation characteristics (Figure D.2). The log-transformation effectively suppresses the dynamic range of the data, and prevents the loss function being dominated by the near-fault pixels with large deformation signal. The DAE is trained using 10^6 synthetic InSAR timeseries and validated on 10^4 independent timeseries. The training curve is shown in Figure 5.4. After 15625 iterations, the training and validation loss is reduced to 0.14 and 0.13, respectively.

5.5.2 Evaluation on synthetic timeseries

The performance of the DAE strongly depends on the SNR of the input timeseries. We evaluate the performance of the trained DAE on synthetic InSAR timeseries with varying SNR (10^{-5}-10^3). We use the structural similarity index measure (SSIM), which is a matrix to evaluate similarity between images, as the accuracy of the neural network. SSIM=0 indicates a poor match between images, while SSIM=1 indicates a perfect match. An evaluation of the denoising accuracy (SSIM) with varying SNR is shown in Figure 5.5. The trained DAE significantly improves the detection accuracy compared with timeseries analysis without correction.

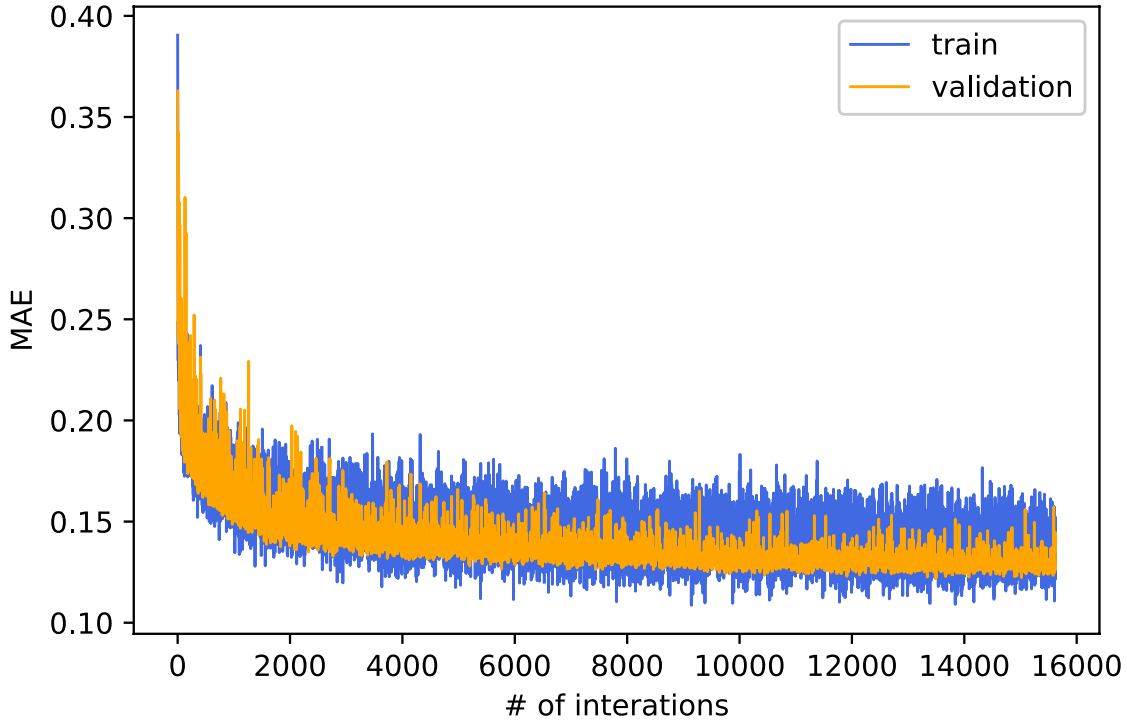


Figure 5.4: Training curve of the denoising neural network model. For each iteration, we calculate the averaged mean absolute error (MAE) over a batch of timeseries (batch size=64).

The DAE denoised timeseries show improved performance over a wide range of SNR (10^{-3}-10^{2}). The DAE denoised timeseries achieve decent accuracy (SSIM=0.4) until SNR=0.1 whereas the noisy timeseries without denoising have an SSIM close to 0 and only reached the same accuracy with SNR=1. In general, the DAE enhances the detectability of shallow fault creep transient signals by at least 10 times. Figure 5.6 shows examples of synthetic noisy and DAE recovered InSAR timeseries and cumulative displacement with SNR of 0.1, 0.01, and 0.001. For low SNR InSAR timeseries (SNR<0.01, Figure 5.6), more than 90% of the atmospheric noises are effectively removed regardless of the accuracy, suggesting the DAE's promising potential for both signal recovery and noise removal.

5.5.3 Evaluation on real timeseries

To further evaluate the performance of the DAE, we apply the trained neural network on InSAR timeseries on the North Anatolian Fault and the Chaman Fault. Both faults have segments exhibiting aseismic fault creep behaviors that are well-documented by InSAR observations (Cakir et al., 2005; Kaneko et al., 2013; Cetin et al., 2014; Fattahi and Amelung,

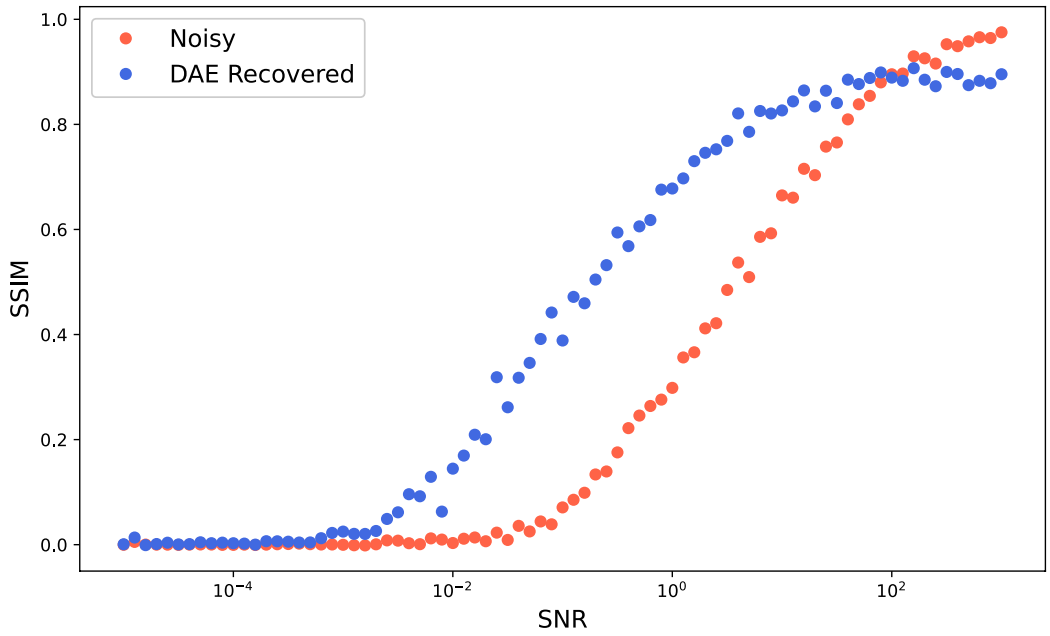


Figure 5.5: Performance of the denoising neural network model. Each point represents the average performance via the structural similarity index measure (SSIM) of a batch of InSAR timeseries for their corresponding SNR (batch size=64). The neural network model improves the detectability of timeseries analysis over a wide range of SNR ($10^{-3} - 10^{2}$).

2016; Rousset et al., 2016; Barnhart, 2017; Aslan et al., 2019; Dalaison et al., 2021).

The North Anatolian Fault

Located in northern Turkey, the 1200-km-long North Anatolian Fault (NAF) is the major active right-lateral fault accommodating the motion between the Anatolian and Eurasian plates at a rate of ∼25 mm/yr (McClusky et al., 2000; Şengör et al., 2005). Over the last decade, present-day deformation on the NAF has been well-documented by geodetic InSAR and GPS measurements (e.g., Cakir et al., 2005; Kaneko et al., 2013; Cetin et al., 2014; Rousset et al., 2016; Aslan et al., 2019; Weiss et al., 2020). At least two creeping sections have been identified on the NAF, including a 60-km-long section near the 1999 Mw7.6 Izmit earthquake rupture (Çakir et al., 2012) and the 80-km-long Ismetpasa segment that hosts the 1944 Mw7.3 and 1951 Mw6.9 earthquakes (Çakir et al., 2012; Rousset et al., 2016). At the Ismetpasa creeping segment, Rousset et al. (2016) observe an aseismic transient slip episode using the timeseries analysis of the Cosmo-SkyMed (CSK) InSAR data between August-September 2013. The transient episode has ∼2 cm of slip burst, which is equivalent to ∼1 year of the tectonic loading (Rousset et al., 2016).

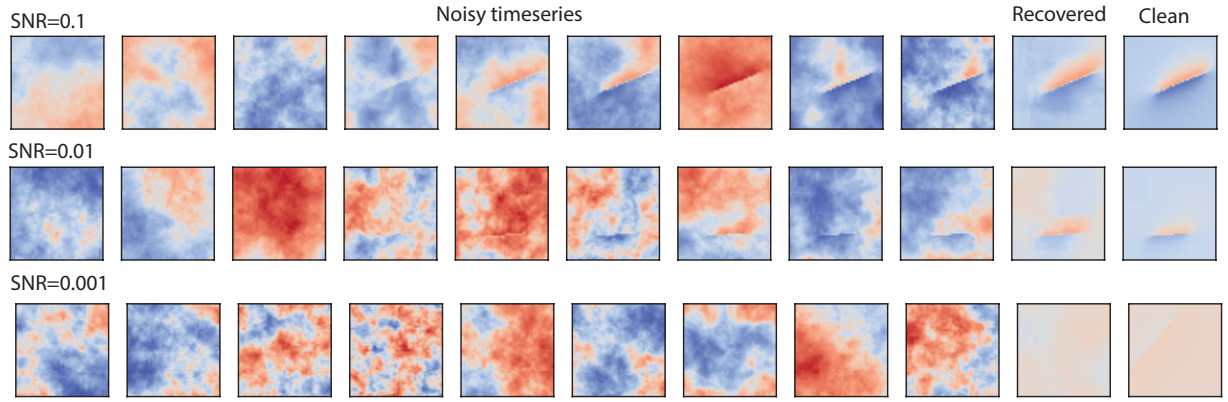


Figure 5.6: Examples of synthetic and DAE recovered InSAR cumulative displacement with SNR of 0.1, 0.01 and 0.001. The 1^{st}-9^{th} columns show the noisy InSAR timesereies, the 10^{th} column shows the DAE recovered cumulative displacement, and the last column shows the ground-truth noise-free displacement. The SSIM between recovered and noise-free cumulative displacements are 0.68, 0.16, and 0.03 for the timeseries with SNR of 0.1, 0.01, and 0.001, respectively.

We test our trained DAE on the CSK timeseries from Rousset et al. (2016) spanning the period of the transient creep episode in 2013. Figure 5.7 shows the performance of the DAE on the timeseries on the NAF from 2013-09-06 to 2013-10-23. The atmospheric noises are effectively removed on the recovered cumulative displacement (Figure 5.7). The comparisons between fault-perpendicular velocity profiles (Figure 5.7c) show that the DAE is capable of removing the atmopsheric noises over the region and enhancing the ability of InSAR to detect shallow fault creep.

The Chaman Fault

The ∼1000-km-long Chaman fault zone in Afghanistan and Pakistan is the western boundary between India and Eurasia plates. At the complex transpressional plate boundary region, the tectonic plate motion is accommodated by both 23-36 mm/yr left-lateral strike-slip motion and 0-18 mm/yr convergence (DeMets et al., 2010; Kreemer et al., 2014; Dalaison et al., 2021). The Chaman Fault takes up ∼30% of the strike-slip motion and slips at ∼ 12 mm/yr (Dalaison et al., 2021). Spatially variable shallow fault creep has been identified on the Chaman Fault ranging from 0-12 mm/yr from InSAR observations (e.g., Fattahi and Amelung, 2016; Barnhart, 2017; Dalaison et al., 2021), accompanied by moderate size (M5-6) earthquakes along the fault.

For the Chaman Fault, we use the Sentinel-1 InSAR timeseries spanning 2015-2021 (Kang Wang, *pers. commun.*). Figure 5.8 shows the performance of the DAE on the timeseries

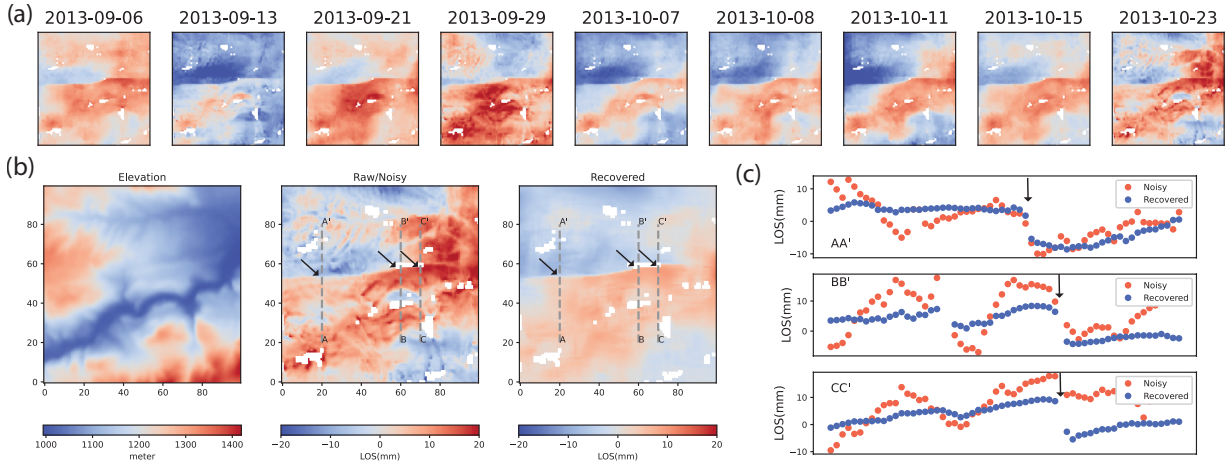


Figure 5.7: Performance of the DAE neural network model on the NAF. **(a)** Input CSK InSAR timeseries from Rousset et al. (2016). **(b)** Input DEM, original and DAE recovered cumulative displacement at the last scene (2013-10-23). **(c)** Comparisons of profiles between original and recovered displacement. Locations of profiles are labeled in (b).

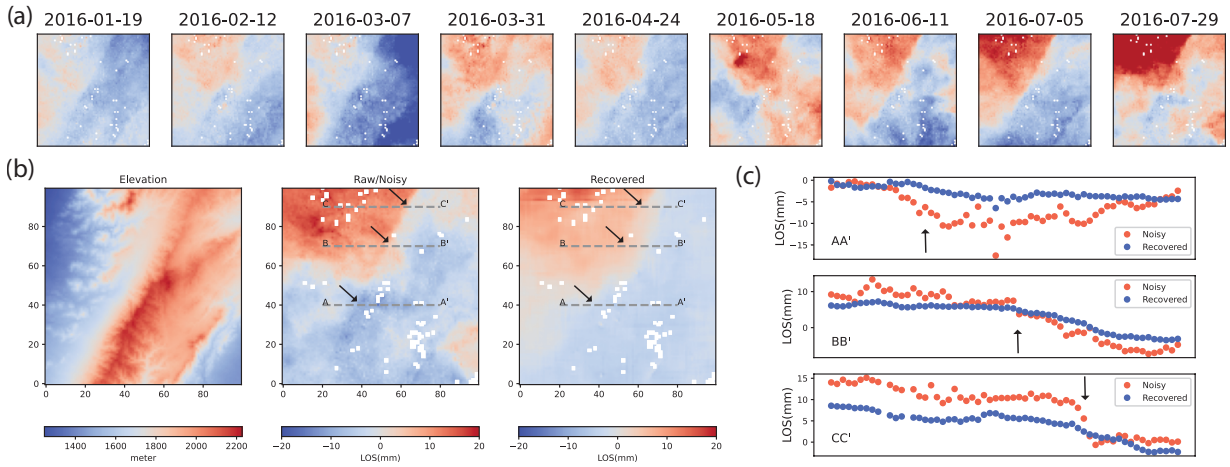


Figure 5.8: Performance of the DAE neural network model on the Chaman Fault. **(a)** Input Sentinel-1 InSAR timeseries from Kang Wang (*pers. commun.*). **(b)** Input DEM, original and DAE recovered cumulative displacement at the last scene (2016-07-29). **(c)** Comparisons of profiles between original and recovered displacement. Locations of profiles are labeled in (b).

on the Chaman Fault from 2016-01-19 to 2016-07-29. Again, the atmospheric noises are effectively removed from the cumulative displacement (Figure 5.8). However, we do not observe significant fault creep on the velocity profiles (Figure 5.8c). Note that the input Sentinel-1 timeseries are taken from a time period without known slow slip transients, and the approximately north-south geometry of the Chaman Fault also leads to only a small portion of the fault motion is being projected onto the InSAR LOS direction. It is possible that the SNR on the Chaman Fault is more than an order smaller than that observed on the east-west trending NAF during the transient episode. In addition, the steep topographic contrast along the Chaman Fault trace insert difficulties for the DAE to distinguish between fault creep signal and the topographic-correlated atmospheric noise.

5.6 Discussion

5.6.1 Evaluation on different temporal patterns

As described in Section 5.4.2, the DAE is trained with a particular temporal evolution pattern, where the displacement timeseries follow the characteristics of the Gaussian cumulative distribution function (Rouet-Leduc et al., 2021). Similar to observed slow slip events, the slip episodes have both acceleration and deceleration phases. However, in reality, different mechanisms lead to different temporal patterns of the creep behaviors. The temporal behaviors of postseismic afterslip and triggered creep generally have a logarithmic or exponential decay driven by the stress changes from an earthquake. In addition, the background creep rate response to tectonic loading may be nearly constant. Moreover, spatially variable shallow fault creep has been identified on creeping faults around the world (e.g., Tong et al., 2013; Fattahi and Amelung, 2016; Barnhart, 2017; Aslan et al., 2019; Dalaison et al., 2021; Li et al., 2021). Identifying and locating the spatial extent of the creeping segment is crucial for seismic hazard models. To further evaluate the applicability of the DAE on various deformation patterns, we test the trained DAE on timeseries with pure noise as well as steady-state constant creep rates.

We show the performance of the DAE on timeseries of pure noise in Figure 5.9. For the synthetic InSAR timeseries with pure noise, only random atmospheric noises are added into the timeseries and the ground-truth cumulative displacement is zero throughout the image. Because of this, the SSIM is not applicable on the pure noise scenario. We use an alternative evaluation matrix variance reduction (VR), the proportion of the variance that is reduced by the DAE, to evaluate the DAE performance. In all examples shown in Figure 5.9, the DAE leads to >0.9 VR on all InSAR timeseries, indicating its applicability on discriminating creeping and non-creeping segments on the fault. Even though we do not specifically train the DAE for the pure noise scenario, the synthetic training sets with a wide range of SNR (10^{-5}-10^{3}) sufficiently encompass the pure noise scenario, where the pure noise scenario resembles the endmember cases of signals with extremely low SNR.

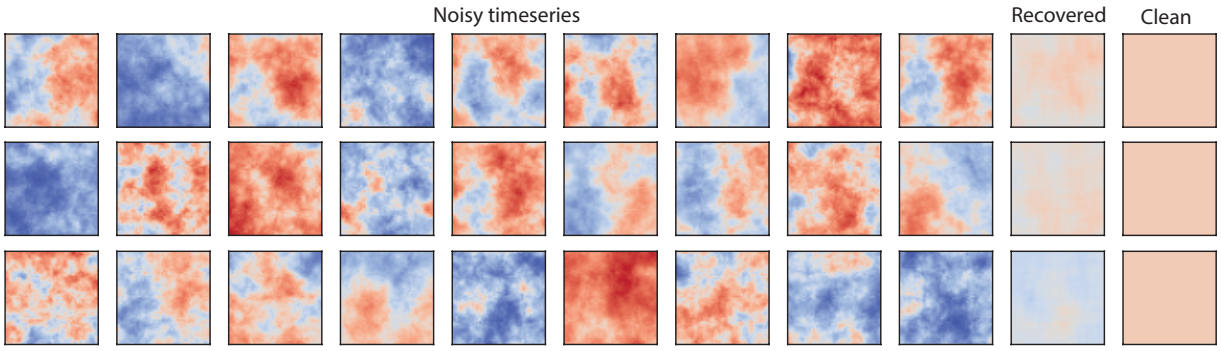


Figure 5.9: Examples of the DAE recovered InSAR cumulative displacement on timeseries with pure noise. The 1^{st}-9^{th} columns show the noisy InSAR timesereies, the 10^{th} column shows the DAE recovered cumulative displacement, and the last column shows the ground-truth signal with no displacement. The VR between the recovered and ground-truth cumulative displacements are 0.93, 0.92 and 0.90 for each row, respectively.

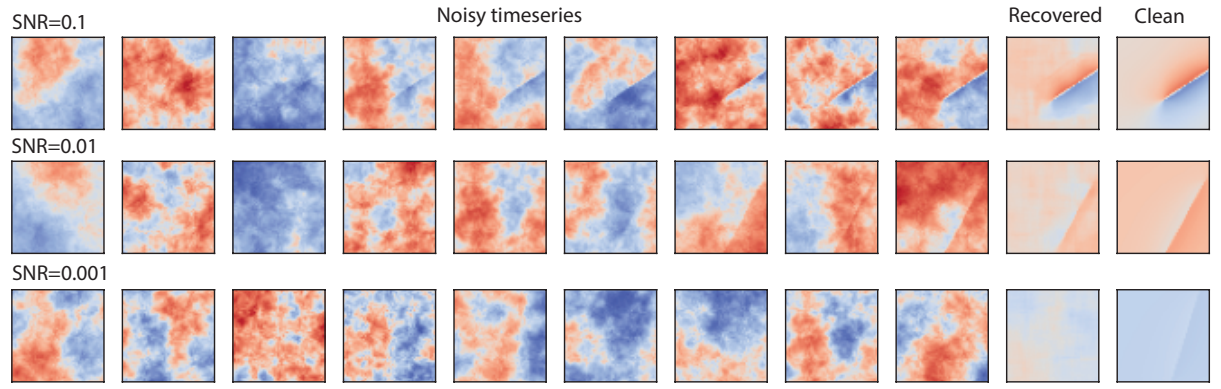


Figure 5.10: Examples of the DAE recovered InSAR cumulative displacement on timeseries with steady-rate deformation. The 1^{st}-9^{th} columns show the noisy InSAR timesereies, the 10^{th} column shows the DAE recovered cumulative displacement, and the last column shows the ground-truth noise-free displacement. The SSIM between recovered and noise-free cumulative displacements are 0.52, 0.04, and 0.02, and the VR are 0.94, 0.92 and 0.86 for the timeseries with SNR of 0.1, 0.01, and 0.001, respectively.

We present the results of the DAE on timeseries with steady-rate fault creep in Figure 5.10. For the steady-rate scenario, the deformation of fault creep is evolving linearly over time. From Figure 5.10 we see the accuracy (SSIM) is similar to the evaluation on timeseries with a Gaussian pulse signal. The good performance of the DAE on steady-rate timeseries indicates that we not only can apply the trained DAE to detect transient creep events, but also use it to detect signals with different temporal patterns.

5.6.2 Evaluation on timeseries reconstruction with creep episodes

In Section 5.5.2 and 5.5.3, we evaluate the performance of the DAE on synthetic and real-world InSAR timeseries by comparing the cumulative displacements at the last time step. Only the cumulative displacement of the input timeseries is reconstructed from the DAE. This is because the DAE is designed to discriminate the spatiotemporal pattern between the fault creep transient signal and atmospheric noises, which compromises the temporal resolution of the input timeseries. Current satellite constellations typically have SAR acquisitions with a regular recurrence interval over 5-7 years (e.g., Sentinel-1, ALOS-2). The length of the available InSAR timeseries (typically >100 epochs) will be much longer than the length of the input timeseries for the DAE (9 epochs). Therefore, it is possible to reconstruct a longer deformation timeseries with the DAE.

In this section, we show examples of the reconstructed InSAR with transient creep episodes. We simulate synthetic InSAR timeseries with 1-2 creep episodes over 50 time steps. Figure 5.11 shows the noisy, clean and DAE reconstructed timeseries at a selected pixel near the fault. Full cumulative displacement timeseries and locations of the selected pixels are shown in Figure D.3 and Figure D.4. From 5.11, the DAE is able to efficiently remove the atmospheric noises and reconstruct the creep transient episodes. The transient signal is otherwise obscured by the atmospheric noises without the DAE.

The successful reconstruction of the timeseries with creep transient episodes indicates the DAE is able to reveal transients signals on creeping faults that are otherwise below the detection threshold for the traditional atmospheric correction methods. It is also worth noting that the performance of the timeseries reconstruction is highly dependent on the SNR as previously discussed in Section 5.5.2. Moreover, the current timeseries reconstruction method assumes the creep episodes are separate events that do not overlap in time. If two creep episodes are close in time (separation<9 epochs), the DAE may not be able to distinguish the individual events and lead to ambiguities on the onset of the creep episodes. We also assume the deformation is steady on the first 9 time steps. Deformation occurs on those scenes will lead to deformation aliasing.

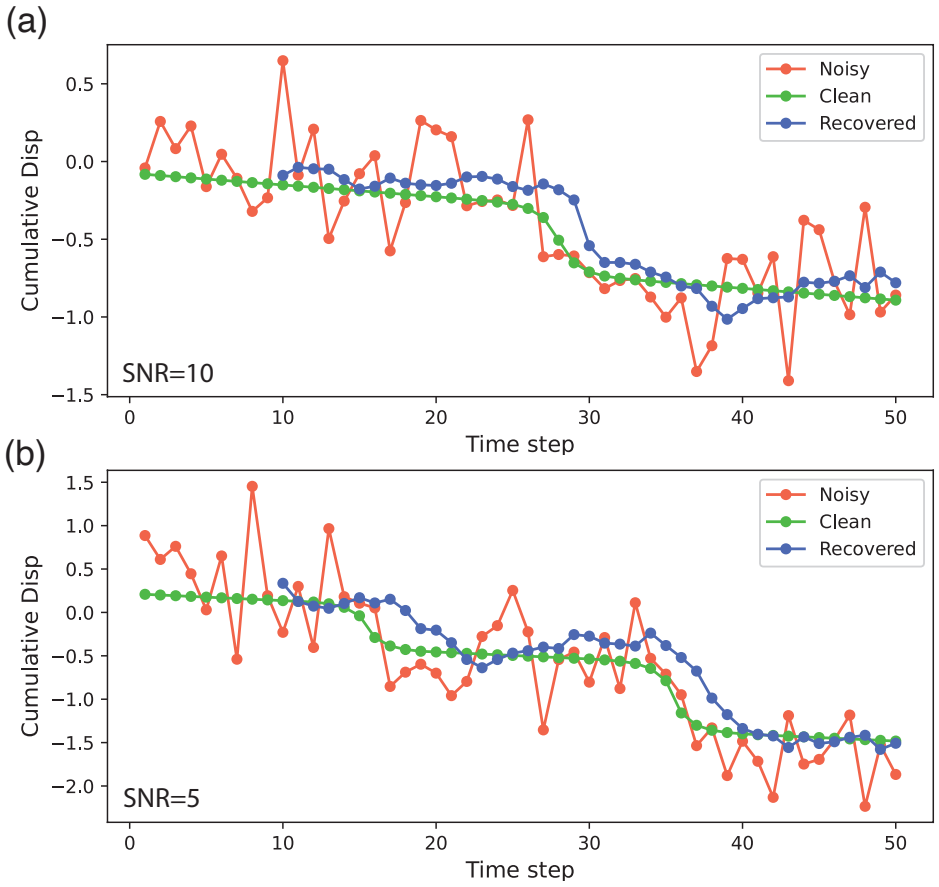


Figure 5.11: Examples of the DAE recovered InSAR cumulative displacement on 50 time steps with **(a)** single and **(b)** multiple creep transient episodes. Temporal patterns of the clean, the DAE recovered, and the noisy timeseries are shown in green, blue and red, respectively.

5.6.3 Limitations of the synthetic training sets

The DAE trained with 10^6 synthetic InSAR timeseries shows good performance on the synthetic timeseries and the NAF CSK timeseries. However, the DAE is not able to fully recover the creep signals on the Chaman Fault. It is possible to attribute the performance decrease to the low SNR on the Chaman Fault or the steep topographic contrast colocated with the fault trace. It can also be that the synthetic atmospheric noises are not representative of the real-world atmospheric noises. For future improvements, the performance of the DAE can be boosted by implementing a two stage transfer learning strategy. The DAE will be first trained by synthetic InSAR timeseries with modeled atmospheric noises. Then, we will use more than 10^4 short-term (6-12 days) interferograms acquired around the world to construct a realistic atmospheric noises database. The short-terms interferograms are selected

in regions without rapid deformations (e.g., earthquake, subsidence, volcano deformation). The DAE is fine-tuned using the synthetic deformation timeseries and noise taken from the short-term interferograms.

5.7 Conclusion

We adopt the deep neural network structure called denoising autoencoder (DAE) from (Rouet-Leduc et al., 2021) and train the DAE using 10^6 synthetic InSAR timeseries with simulated spatially-correlated and topographic-correlated atmospheric noises. The performance of the DAE is strongly dependent on the SNR of the input timeseries. The DAE show improved accuracy over a wide range of SNR (10^{-5}-10^3). We further evaluate the performance of the DAE on InSAR timeseries on the creeping North Anatolian Fault (NAF) and Chaman Fault. The DAE effectively removes atmospheric noises of the InSAR timeseries and recovers the creep transient episodes on the NAF. However, the creep signal on the Chaman Fault is not fully recovered. This is possibly due to the low SNR on the Chaman Fault creep and the steep topography co-located with the fault trace. Additionally, we test the performance of the DAE on InSAR timeseries with pure noise and steady-rate signal, and assess the DAE's applicability on reconstruction of InSAR timeseries with creep episodes. The results show that the DAE is capable of identifying not only the temporal deformation pattern that is being fed into the training process, but also patterns that are not seen before. The performance of the DAE can be further improved by incorporating InSAR timeseries with real-noise taken from short-term interferograms using the transfer learning strategy.

Bibliography

Aagaard, B. T., J. J. Lienkaemper, and D. P. Schwartz (2012). "Probabilistic estimates of surface coseismic slip and afterslip for Hayward fault earthquakes". *Bulletin of the Seismological Society of America*. ISSN: 00371106. DOI: 10.1785/0120110200.

Allen, C. R. et al. (1991). "Field study of a highly active fault zone : The Xianshuihe fault of southwestern China". *Geological Society of America Bulletin*.

Amos, C. B. et al. (2014). "Uplift and seismicity driven by groundwater depletion in central California". *Nature* 509.7501, pp. 483–486. ISSN: 1476-4687. DOI: 10.1038/nature13275.

Anantrasirichai, N. et al. (2018). "Application of Machine Learning to Classification of Volcanic Deformation in Routinely Generated InSAR Data". *Journal of Geophysical Research: Solid Earth* 123.8, pp. 6592–6606. DOI: https://doi.org/10.1029/2018JB015911. eprint: https://agupubs.onlinelibrary.wiley.com/doi/pdf/10.1029/2018JB015911.

Anantrasirichai, N. et al. (2019). "The Application of Convolutional Neural Networks to Detect Slow, Sustained Deformation in InSAR Time Series". *Geophysical Research Letters* 46.21, pp. 11850–11858. DOI: https://doi.org/10.1029/2019GL084993. eprint: https://agupubs.onlinelibrary.wiley.com/doi/pdf/10.1029/2019GL084993.

Ansari, H., F. D. Zan, and A. Parizzi (2021). "Study of Systematic Bias in Measuring Surface Deformation With SAR Interferometry". *IEEE Transactions on Geoscience and Remote Sensing* 59.2, pp. 1285–1301. ISSN: 0196-2892. DOI: 10.1109/tgrs.2020.3003421.

Argus, D. F. and R. G. Gordon (2001). "Present tectonic motion across the Coast Ranges and San Andreas fault system in central California". *GSA Bulletin* 113.12, pp. 1580–1592. ISSN: 0016-7606. DOI: 10.1130/0016-7606(2001)113<1580:PTMATC>2.0.CO;2.

Aslan, G. et al. (2019). "Shallow Creep Along the 1999 Izmit Earthquake Rupture (Turkey) From GPS and High Temporal Resolution Interferometric Synthetic Aperture Radar Data (2011–2017)". *Journal of Geophysical Research: Solid Earth* 124.2, pp. 2218–2236. ISSN: 21699356. DOI: 10.1029/2018JB017022.

Avouac, J. and P. Tapponnier (1993). "Kinematic model of active deformation in central Asia". *Geophysical Research Letters*. ISSN: 19448007. DOI: 10.1029/93GL00128.

Bai, M. et al. (2018). "Southeastward increase of the late Quaternary slip-rate of the Xianshuihe fault, eastern Tibet. Geodynamic and seismic hazard implications". *Earth and*

Planetary Science Letters 485, pp. 19–31. ISSN: 0012821X. DOI: 10.1016/j.epsl.2017.12.045.

Baldwin, J. and C. Bloszies (2022). "Tectonic Geomorphic and Quaternary Geologic Mapping of the Quien Sabe Fault, Santa Clara and San Benito Counties, California". *USGS Final Technical Report* G21AP10015. URL: https://earthquake.usgs.gov/cfusion/external_grants/reports/G21AP10015.pdf.

Barbot, S. (2018). *Asthenosphere Flow Modulated by Megathrust Earthquake Cycles*. DOI: 10.1029/2018GL078197.

Barbot, S. and Y. Fialko (2010). "A unified continuum representation of post-seismic relaxation mechanisms: Semi-analytic models of afterslip, poroelastic rebound and viscoelastic flow". *Geophysical Journal International*. ISSN: 0956540X. DOI: 10.1111/j.1365-246X.2010.04678.x.

Barbot, S., Y. Fialko, and Y. Bock (2009). "Postseismic deformation due to the Mw 6.0 2004 Parkfield earthquake: Stress-driven creep on a fault with spatially variable rate-and-state friction parameters". *Journal of Geophysical Research: Solid Earth*. ISSN: 21699356. DOI: 10.1029/2008JB005748.

Barbot, S., J. D. Moore, and V. Lambert (2017). "Displacement and stress associated with distributed anelastic deformation in a half-space". *Bulletin of the Seismological Society of America*. ISSN: 19433573. DOI: 10.1785/0120160237.

Barnhart, W. D. (2017). "Fault creep rates of the Chaman fault (Afghanistan and Pakistan) inferred from InSAR". *Journal of Geophysical Research: Solid Earth* 122.1, pp. 372–386. ISSN: 21699356. DOI: 10.1002/2016JB013656.

"Basic characteristics of active tectonics of China" (2003). *Science in China Series D: Earth Sciences* 46.4, pp. 356–372. ISSN: 1862-2801. DOI: 10.1360/03yd9032.

Behr, J et al. (1990). "Aseismic slip on the San Andreas Fault south of Loma Prieta". *Geophysical Research Letters* 17.9, pp. 1445–1448. ISSN: 0094-8276. DOI: https://doi.org/10.1029/GL017i009p01445.

Bekaert, D. P. S., A. Hooper, and T. J. Wright (2015a). "A spatially variable power law tropospheric correction technique for InSAR data". *Journal of Geophysical Research: Solid Earth* 120.2, pp. 1345–1356. DOI: https://doi.org/10.1002/2014JB011558. eprint: https://agupubs.onlinelibrary.wiley.com/doi/pdf/10.1002/2014JB011558.

Bekaert, D. P. S. et al. (2015b). "Statistical comparison of InSAR tropospheric correction techniques". *Remote Sensing of Environment* 170, pp. 40–47. ISSN: 0034-4257. DOI: https://doi.org/10.1016/j.rse.2015.08.035.

Berardino, P. et al. (2002). "A new algorithm for surface deformation monitoring based on small baseline differential SAR interferograms". *IEEE Transactions on Geoscience and Remote Sensing*. ISSN: 01962892. DOI: 10.1109/TGRS.2002.803792.

Berrada Baby, H, P Golé, and J Lavergnat (1988). "A model for the tropospheric excess path length of radio waves from surface meteorological measurements". *Radio Science* 23.6, pp. 1023–1038. ISSN: 0048-6604. DOI: https://doi.org/10.1029/RS023i006p01023.

Bilham, R. (1989). "Surface slip subsequent to the 24 November 1987 Superstition Hills, California, earthquake monitored by digital creepmeters". *Bulletin - Seismological Society of America*.

Bilham, R. and J. Behr (June 1992). "A two-layer model for aseismic slip on the Superstition Hills fault, California". *Bulletin of the Seismological Society of America* 82.3, pp. 1223–1235. ISSN: 0037-1106. DOI: 10.1785/BSSA0820031223. eprint: https://pubs.geoscienceworld.org/ssa/bssa/article-pdf/82/3/1223/5340801/bssa0820031223.pdf.

Bilham, R., N. Suszek, and S. Pinkney (2004). "California creepmeters". *Seismological Research Letters* 75.4, pp. 481–492. ISSN: 1938-2057.

Bilham, R. and P. Williams (1985). "Sawtooth segmentation and deformation processes on the southern San Andreas Fault, California". *Geophysical Research Letters* 12.9, pp. 557–560. ISSN: 0094-8276. DOI: https://doi.org/10.1029/GL012i009p00557.

Blewitt, G., W. C. Hammond, and C. Kreemer (2018). "Harnessing the GPS data explosion for interdisciplinary science". *Eos* 99.10.1029, p. 485.

Bokelmann, G. H. and R. L. Kovach (2003). "Long-term creep-rate changes and their causes". *Geophysical Research Letters*. ISSN: 00948276. DOI: 10.1029/2003GL017012.

Brengman, C. M. J. and W. D. Barnhart (2021). "Identification of Surface Deformation in InSAR Using Machine Learning". *Geochemistry, Geophysics, Geosystems* 22.3, e2020GC009204. DOI: https://doi.org/10.1029/2020GC009204.

Burchfiel, B. C. et al. (2008). "A geological and geophysical context for the Wenchuan earthquake of 12 May 2008, Sichuan, People's Republic of China". *GSA Today*. ISSN: 10525173. DOI: 10.1130/GSATG18A.1.

Burford, R. O. and P. W. Harsh (1980). "Results of alignment array surveys along the San Andreas fault in Central California in relation to contemporary seismicity". *Bull. Seism. Soc. Am.* 70, pp. 1233–1261.

Bürgmann, R. (2018). "The geophysics, geology and mechanics of slow fault slip". *Earth and Planetary Science Letters*. ISSN: 0012821X. DOI: 10.1016/j.epsl.2018.04.062.

Bürgmann, R. et al. (2000). "Earthquake Potential Along the Northern Hayward Fault, California". *Science* 289.5482, pp. 1178–1182. DOI: 10.1126/science.289.5482.1178.

Cakir, Z. et al. (2005). "Creeping along the Ismetpasa section of the North Anatolian fault (Western Turkey): Rate and extent from InSAR". *Earth and Planetary Science Letters*. ISSN: 0012821X. DOI: 10.1016/j.epsl.2005.06.044.

Çakir, Z. et al. (2012). "Onset of aseismic creep on major strike-slip faults". *Geology*. ISSN: 00917613. DOI: 10.1130/G33522.1.

Cetin, E. et al. (2014). "Extent and distribution of aseismic slip on the Ismetpaşa segment of the North Anatolian Fault (Turkey) from Persistent Scatterer InSAR". *Geochemistry, Geophysics, Geosystems*. ISSN: 15252027. DOI: 10.1002/2014GC005307.

Chaussard, E et al. (2014). "Predictability of hydraulic head changes and characterization of aquifer-system and fault properties from InSAR-derived ground deformation". *Journal of Geophysical Research: Solid Earth* 119.8, pp. 6572–6590. ISSN: 2169-9313. DOI: https://doi.org/10.1002/2014JB011266.

Chaussard, E. et al. (2015). "Interseismic coupling and refined earthquake potential on the Hayward-Calaveras fault zone". *Journal of Geophysical Research: Solid Earth*. ISSN: 21699356. DOI: 10.1002/2015JB012230.

Chaussard, E. et al. (2017). "Remote Sensing of Ground Deformation for Monitoring Groundwater Management Practices: Application to the Santa Clara Valley During the 2012–2015 California Drought". *Journal of Geophysical Research: Solid Earth* 122.10, pp. 8566–8582. ISSN: 2169-9313. DOI: https://doi.org/10.1002/2017JB014676.

Chen, C. W. and H. A. Zebker (2002). "Phase unwrapping for large SAR interferograms: Statistical segmentation and generalized network models". *IEEE Transactions on Geoscience and Remote Sensing*. ISSN: 01962892. DOI: 10.1109/TGRS.2002.802453.

Chevalier, M.-L. et al. (2017). "Temporally constant slip rate along the Ganzi fault, NW Xianshuihe fault system, eastern Tibet". *GSA Bulletin* 130.3-4, pp. 396–410. ISSN: 0016-7606. DOI: 10.1130/B31691.1.

Dalaison, M. and R. Jolivet (2020). "A Kalman Filter Time Series Analysis Method for InSAR". *Journal of Geophysical Research: Solid Earth* 125.7. e2019JB019150 10.1029/2019JB019150, e2019JB019150. DOI: https://doi.org/10.1029/2019JB019150. eprint: https://agupubs.onlinelibrary.wiley.com/doi/pdf/10.1029/2019JB019150.

Dalaison, M. et al. (2021). "The Interplay Between Seismic and Aseismic Slip Along the Chaman Fault Illuminated by InSAR". *Journal of Geophysical Research: Solid Earth* 126.12. e2021JB021935 2021JB021935, e2021JB021935. DOI: https://doi.org/10.1029/2021JB021935. eprint: https://agupubs.onlinelibrary.wiley.com/doi/pdf/10.1029/2021JB021935.

D'Alessio, M. A., C. F. Williams, and R Bürgmann (2006). "Frictional strength heterogeneity and surface heat flow: Implications for the strength of the creeping San Andreas fault". *Journal of Geophysical Research: Solid Earth* 111.B5. ISSN: 0148-0227. DOI: https://doi.org/10.1029/2005JB003780.

D'Alessio, M. A. et al. (2005). "Slicing up the San Francisco Bay Area: Block kinematics and fault slip rates from GPS-derived surface velocities". *Journal of Geophysical Research: Solid Earth* 110.B6. ISSN: 0148-0227. DOI: https://doi.org/10.1029/2004JB003496.

DeMets, C., R. G. Gordon, and D. F. Argus (2010). "Geologically current plate motions". *Geophysical journal international* 181.1, pp. 1–80. ISSN: 0956-540X.

Diao, F. et al. (2018). "Fault behavior and lower crustal rheology inferred from the first seven years of postseismic GPS data after the 2008 Wenchuan earthquake". *Earth and Planetary Science Letters*. ISSN: 0012821X. DOI: 10.1016/j.epsl.2018.05.020.

Dolan, J. F. and B. D. Haravitch (2014). "How well do surface slip measurements track slip at depth in large strike-slip earthquakes? The importance of fault structural maturity in controlling on-fault slip versus off-fault surface deformation". *Earth and Planetary Science Letters*. ISSN: 0012821X. DOI: 10.1016/j.epsl.2013.11.043.

Du, Y. and A. Aydin (1993). "Stress transfer during three sequential moderate earthquakes along the central Calaveras Fault, California". *Journal of Geophysical Research: Solid*

Earth 98.B6, pp. 9947–9962. ISSN: 0148-0227. DOI: https://doi.org/10.1029/93JB00154.

Elliott, J. R. et al. (2008). "InSAR slip rate determination on the Altyn Tagh Fault, northern Tibet, in the presence of topographically correlated atmospheric delays". *Geophysical Research Letters* 35.12, n/a–n/a. ISSN: 0094-8276. DOI: 10.1029/2008gl033659.

Elliott, J. R. et al. (2011). "Depth segmentation of the seismogenic continental crust: The 2008 and 2009 Qaidam earthquakes". *Geophysical Research Letters*. ISSN: 00948276. DOI: 10.1029/2011GL046897.

Fang, L. et al. (2015). "Preliminary report on the 22 November 2014 Mw 6:1/Ms 6:3 Kangding Earthquake, Western Sichuan, China". *Seismological Research Letters*. ISSN: 19382057. DOI: 10.1785/0220150006.

Fang, L. et al. (2018). "Relocation of mainshock and aftershock sequence of the M S 7.0 Sichuan Jiuzhaigou earthquake". *Chinese Science Bulletin* 63.7, pp. 649–662.

Farr, T. G. et al. (2007). "The Shuttle Radar Topography Mission". *Reviews of Geophysics* 45.2. ISSN: 8755-1209. DOI: https://doi.org/10.1029/2005RG000183.

Fattahi, H. and F. Amelung (2016). "InSAR observations of strain accumulation and fault creep along the Chaman Fault system, Pakistan and Afghanistan". *Geophysical Research Letters* 43.16, pp. 8399–8406. ISSN: 19448007. DOI: 10.1002/2016GL070121.

Ferretti, A. et al. (2007). "Submillimeter Accuracy of InSAR Time Series: Experimental Validation". *IEEE Transactions on Geoscience and Remote Sensing* 45.5, pp. 1142–1153. DOI: 10.1109/TGRS.2007.894440.

Fialko, Y. (2004). "Probing the mechanical properties of seismically active crust with space geodesy : Study of the coseismic deformation due to the 1992 M w 7 . 3 Landers (southern California) earthquake". 109, pp. 1–19. DOI: 10.1029/2003JB002756.

Fialko, Y. et al. (2005). "Three-dimensional deformation caused by the Bam, Iran, earthquake and the origin of shallow slip deficit". *Nature*. ISSN: 00280836. DOI: 10.1038/nature03425.

Field, E. H. et al. (2014). "Uniform California earthquake rupture forecast, version 3 (UCERF3)—The time-independent model". *Bulletin of the Seismological Society of America* 104.3, pp. 1122–1180. ISSN: 1943-3573.

Field, E. H. et al. (2015). "Long-term time-dependent probabilities for the third Uniform California Earthquake Rupture Forecast (UCERF3)". *Bulletin of the Seismological Society of America* 105.2A, pp. 511–543. ISSN: 1943-3573.

Fielding, E. J. et al. (2009). "Shallow fault-zone dilatancy recovery after the 2003 Bam earthquake in Iran". *Nature*. ISSN: 00280836. DOI: 10.1038/nature07817.

Floyd, M. A. et al. (2016). "Spatial variations in fault friction related to lithology from rupture and afterslip of the 2014 South Napa, California, earthquake". *Geophysical Research Letters*. ISSN: 19448007. DOI: 10.1002/2016GL069428.

Funning, G. J. et al. (2007). "Creep on the Rodgers Creek fault, northern San Francisco Bay area from a 10 year PS-InSAR dataset". *Geophysical Research Letters* 34.19, pp. 3–7. ISSN: 00948276. DOI: 10.1029/2007GL030836. arXiv: 1606.01587.

Galehouse, J. S. and J. J. Lienkaemper (2003). "Inferences drawn from two decades of alinement array measurements of creep on faults in the San Francisco Bay region". *Bulletin of the Seismological Society of America* 93.6, pp. 2415–2433. ISSN: 1943-3573.

Goldstein, R. M. and C. L. Werner (1998). "Radar interferogram filtering for geophysical applications". *Geophysical Research Letters*. ISSN: 00948276. DOI: 10.1029/1998GL900033.

Gondara, L. (2016). "Medical image denoising using convolutional denoising autoencoders". In: *2016 IEEE 16th international conference on data mining workshops (ICDMW)*. IEEE, pp. 241–246. DOI: doi:10.1109/ICDMW.2016.0041.

Gutenberg, B. and C. F. Richter (1944). "Frequency of earthquakes in California". *Bulletin of the Seismological society of America* 34.4, pp. 185–188. ISSN: 0037-1106.

Han, L. et al. (2018). "Preliminary Report on the 8 August 2017 Ms 7.0 Jiuzhaigou, Sichuan, China, Earthquake". *Seismological Research Letters*.

Hanks, T. C. and H. Kanamori (1979). "A moment magnitude scale". *Journal of Geophysical Research: Solid Earth* 84.B5, pp. 2348–2350. ISSN: 0148-0227. DOI: https://doi.org/10.1029/JB084iB05p02348.

Hanssen, R. F. (2001). *Radar interferometry: data interpretation and error analysis*. Vol. 2. Springer Science & Business Media.

Harris, R. A. (2017). *Large earthquakes and creeping faults*. DOI: 10.1002/2016RG000539.

Hatem, A. E. et al. (2021). *Earthquake geology inputs for the National Seismic Hazard Model (NSHM) 2023, version 1.0: US Geological Survey data release*.

Hersbach, H. et al. (2020). "The ERA5 global reanalysis". *Quarterly Journal of the Royal Meteorological Society* 146.730, pp. 1999–2049. ISSN: 0035-9009. DOI: https://doi.org/10.1002/qj.3803.

Huang, M. H., R. Bürgmann, and A. M. Freed (2014). "Probing the lithospheric rheology across the eastern margin of the Tibetan Plateau". *Earth and Planetary Science Letters*. ISSN: 0012821X. DOI: 10.1016/j.epsl.2014.04.003.

Huang, M. H., R. Bürgmann, and F. Pollitz (2016). "Lithospheric rheology constrained from twenty-five years of postseismic deformation following the 1989 Mw 6.9 Loma Prieta earthquake". *Earth and Planetary Science Letters* 435, pp. 147–158. ISSN: 0012821X. DOI: 10.1016/j.epsl.2015.12.018.

Huang, M. H. et al. (2017). "Fault geometry inversion and slip distribution of the 2010 Mw 7.2 El Mayor-Cucapah earthquake from geodetic data". *Journal of Geophysical Research: Solid Earth*. ISSN: 21699356. DOI: 10.1002/2016JB012858.

Ji, L.-Y. et al. (2017). "InSAR observation and inversion of the seismogenic fault for the 2017 Jiuzhaigou M¡inf¿S¡/inf¿7.0 earthquake in China". *Acta Geophysica Sinica*. ISSN: 00015733. DOI: 10.6038/cjg20171032.

Ji, L. et al. (2020). "Characterizing interseismic deformation of the Xianshuihe fault, eastern Tibetan Plateau, using Sentinel-1 SAR images". *Advances in Space Research* 66.2, pp. 378–394. ISSN: 18791948. DOI: 10.1016/j.asr.2020.03.043.

Jia, K. et al. (2018). "Did the 2008 Mw 7.9 Wenchuan Earthquake Trigger the Occurrence of the 2017 Mw 6.5 Jiuzhaigou Earthquake in Sichuan, China?" *Journal of Geophysical Research: Solid Earth*. ISSN: 21699356. DOI: 10.1002/2017JB015165.

Jiang, G. et al. (2015a). "Geodetic imaging of potential seismogenic asperities on the Xianshuihe-Anninghe-Zemuhe fault system, southwest China, with a new 3-D viscoelastic interseismic coupling model". *Journal of Geophysical Research: Solid Earth* 120.3, pp. 1855–1873. ISSN: 2169-9313. DOI: https://doi.org/10.1002/2014JB011492.

Jiang, G. et al. (2015b). "Joint analysis of the 2014 Kangding, southwest China, earthquake sequence with seismicity relocation and InSAR inversion". *Geophysical Research Letters* 42.9, pp. 3273–3281. ISSN: 19448007. DOI: 10.1002/2015GL063750.

Johanson, I. A. and R Bürgmann (2005). "Creep and quakes on the northern transition zone of the San Andreas fault from GPS and InSAR data". *Geophysical Research Letters* 32.14. ISSN: 0094-8276. DOI: https://doi.org/10.1029/2005GL023150.

Johanson, I. A. et al. (2006). "Coseismic and postseismic slip of the 2004 Parkfield earthquake from space-geodetic data". *Bulletin of the Seismological Society of America*. ISSN: 00371106. DOI: 10.1785/0120050818.

Johnson, C. W., Y. Fu, and R. Bürgmann (2017). "Stress Models of the Annual Hydrospheric, Atmospheric, Thermal, and Tidal Loading Cycles on California Faults: Perturbation of Background Stress and Changes in Seismicity". *Journal of Geophysical Research: Solid Earth* 122.12, pp. 10,605–610,625. ISSN: 2169-9313. DOI: 10.1002/2017jb014778.

Jolivet, R et al. (2011). "Systematic InSAR tropospheric phase delay corrections from global meteorological reanalysis data". *Geophysical Research Letters* 38.17. ISSN: 0094-8276. DOI: https://doi.org/10.1029/2011GL048757.

Jolivet, R. et al. (2012). "Shallow creep on the Haiyuan fault (Gansu, China) revealed by SAR interferometry". *Journal of Geophysical Research: Solid Earth*. ISSN: 21699356. DOI: 10.1029/2011JB008732.

Jolivet, R. et al. (2013). "Spatio-temporal evolution of aseismic slip along the Haiyuan fault, China: Implications for fault frictional properties". *Earth and Planetary Science Letters* 377-378, pp. 23–33. ISSN: 0012821X. DOI: 10.1016/j.epsl.2013.07.020.

Jolivet, R et al. (2015a). "Aseismic slip and seismogenic coupling along the central San Andreas Fault". *Geophysical Research Letters* 42.2, pp. 297–306. ISSN: 0094-8276. DOI: https://doi.org/10.1002/2014GL062222.

Jolivet, R. et al. (2015b). "The burst-like behavior of aseismic slip on a rough fault: The creeping section of the Haiyuan fault, China". *Bulletin of the Seismological Society of America* 105.1, pp. 480–488. ISSN: 19433573. DOI: 10.1785/0120140237.

Kaneko, Y. and Y. Fialko (2011). "Shallow slip deficit due to large strike-slip earthquakes in dynamic rupture simulations with elasto-plastic off-fault response". *Geophysical Journal International*. ISSN: 0956540X. DOI: 10.1111/j.1365-246X.2011.05117.x.

Kaneko, Y. et al. (2013). "Interseismic deformation and creep along the central section of the North Anatolian Fault (Turkey): InSAR observations and implications for rate-and-state friction properties". *Journal of Geophysical Research: Solid Earth* 118.1, pp. 316–331. ISSN: 21699356. DOI: 10.1029/2012JB009661.

Khoshmanesh, M., M. Shirzaei, and R. M. Nadeau (2015). "Time-dependent model of aseismic slip on the central San Andreas Fault from InSAR time series and repeating earth-

quakes". *Journal of Geophysical Research: Solid Earth*. ISSN: 21699356. DOI: 10.1002/2015JB012039.

Khoshmanesh, M. and M. Shirzaei (2018). "Episodic creep events on the San Andreas Fault caused by pore pressure variations". *Nature Geoscience* 11.8, pp. 610–614. ISSN: 17520908. DOI: 10.1038/s41561-018-0160-2.

Kingma, D. P. and J. Ba (2014). "Adam: A method for stochastic optimization". *arXiv preprint arXiv:1412.6980*.

Kreemer, C., G. Blewitt, and E. C. Klein (2014). "A geodetic plate motion and Global Strain Rate Model". *Geochemistry, Geophysics, Geosystems* 15.10, pp. 3849–3889. ISSN: 1525-2027. DOI: https://doi.org/10.1002/2014GC005407.

Langbein, J., J. R. Murray, and H. A. Snyder (2006). "Coseismic and initial postseismic deformation from the 2004 Parkfield, California, earthquake, observed by global positioning system, electronic distance meter, creepmeters, and borehole strainmeters". *Bulletin of the Seismological Society of America*. ISSN: 00371106. DOI: 10.1785/0120050823.

Li, Q. et al. (2018a). "Joint inversion of GNSS and teleseismic data for the rupture process of the 2017 Mw6.5 Jiuzhaigou, China, earthquake". *Journal of Seismology*. ISSN: 1573157X. DOI: 10.1007/s10950-018-9733-1.

Li, Y. et al. (2021). "Heterogeneous Interseismic Coupling Along the Xianshuihe-Xiaojiang Fault System, Eastern Tibet". *Journal of Geophysical Research: Solid Earth* 126.11, e2020JB021187. ISSN: 2169-9313. DOI: https://doi.org/10.1029/2020JB021187.

Li, Y. and R. Bürgmann (2021). "Partial Coupling and Earthquake Potential Along the Xianshuihe Fault, China". *Journal of Geophysical Research: Solid Earth* 126.7. ISSN: 2169-9313. DOI: 10.1029/2020jb021406.

Li, Y., R. Bürgmann, and B. Zhao (Jan. 2020). "Evidence of Fault Immaturity from Shallow Slip Deficit and Lack of Postseismic Deformation of the 2017 Mw 6.5 Jiuzhaigou Earthquake". *Bulletin of the Seismological Society of America* 110.1, pp. 154–165. ISSN: 0037-1106. DOI: 10.1785/0120190162.

Li, Y. et al. (2018b). "Present-day crustal deformation and strain transfer in northeastern Tibetan Plateau". *Earth and Planetary Science Letters* 487, pp. 179–189. ISSN: 0012821X. DOI: 10.1016/j.epsl.2018.01.024.

Li, Z. et al. (2005). "Interferometric synthetic aperture radar (InSAR) atmospheric correction: GPS, Moderate Resolution Imaging Spectroradiometer (MODIS), and InSAR integration". *Journal of Geophysical Research: Solid Earth* 110.B3. DOI: https://doi.org/10.1029/2004JB003446. eprint: https://agupubs.onlinelibrary.wiley.com/doi/pdf/10.1029/2004JB003446.

Liang, S. et al. (2013). "Three-dimensional velocity field of present-day crustal motion of the Tibetan Plateau derived from GPS measurements". *Journal of Geophysical Research: Solid Earth* 118.10, pp. 5722–5732. ISSN: 21699356. DOI: 10.1002/2013JB010503.

Lienkaemper, J. J. and W. H. Prescott (1989). "Historic surface slip along the San Andreas fault near Parkfield, California". *Journal of Geophysical Research: Solid Earth* 94.B12, pp. 17647–17670. ISSN: 0148-0227.

Lienkaemper, J. J., J. S. Galehouse, and R. W. Simpson (1997). "Creep Response of the Hayward Fault to Stress Changes Caused by the Loma Prieta Earthquake". *Science* 276.5321, pp. 2014–2016. ISSN: 0036-8075. DOI: 10.1126/science.276.5321.2014.

Linde, A. T. et al. (1996). "A slow earthquake sequence on the San Andreas fault". *Nature*. ISSN: 00280836. DOI: 10.1038/383065a0.

Lindsey, E. O. et al. (2014a). "Interseismic Strain Localization in the San Jacinto Fault Zone". *Pure and Applied Geophysics* 171.11, pp. 2937–2954. ISSN: 14209136. DOI: 10.1007/s00024-013-0753-z.

Lindsey, E. O. et al. (2014b). "Localized and distributed creep along the southern San Andreas Fault". *Journal of Geophysical Research: Solid Earth* 119.10, pp. 7909–7922. ISSN: 2169-9356. DOI: 10.1002/2014jb011275.

Lisowski, M. and W. H. Prescott (1981). "Short-range distance measurements along the San Andreas fault system in central California, 1975 to 1979". *Bulletin of the Seismological Society of America* 71.5, pp. 1607–1624. ISSN: 1943-3573.

Liu, Y.-K. et al. (2022). "A unified perspective of seismicity and fault coupling along the San Andreas Fault". *Science Advances* 8.8, eabk1167. DOI: 10.1126/sciadv.abk1167PMID-35196076.

Liu, Z. et al. (2019). *Monitoring Groundwater Change in California's Central Valley Using Sentinel-1 and GRACE Observations*. DOI: 10.3390/geosciences9100436.

Lockner, D. A. et al. (2011). "Low strength of deep San Andreas fault gouge from SAFOD core". *Nature* 472.7341, pp. 82–85. ISSN: 1476-4687. DOI: 10.1038/nature09927.

Lohman, R. B. and M. Simons (2005). "Some thoughts on the use of InSAR data to constrain models of surface deformation: Noise structure and data downsampling". *Geochemistry, Geophysics, Geosystems* 6.1.

Long, F. et al. (2019). "Geometry and tectonic deformation of the seismogenic structure for the 8 August 2017 ¡i¿M¡/i¿¡sub¿S¡/sub¿ 7.0 Jiuzhaigou earthquake sequence, northern Sichuan, China". *Earth and Planetary Physics* 3.3, pp. 253–267. ISSN: 2096-3955. DOI: 10.26464/epp2019027.

Manaker, D. M. et al. (2003). "Distribution of interseismic slip rates and the potential for significant earthquakes on the Calaveras fault, central California". *Journal of Geophysical Research: Solid Earth* 108.B6. ISSN: 0148-0227. DOI: https://doi.org/10.1029/2002JB001749.

Manighetti, I, A Mercier, and L De Barros (2021). "Fault Trace Corrugation and Segmentation as a Measure of Fault Structural Maturity". *Geophysical Research Letters* 48.20, e2021GL095372. ISSN: 0094-8276. DOI: https://doi.org/10.1029/2021GL095372.

Materna, K., T. Taira, and R. Bürgmann (2018). "Aseismic Transform Fault Slip at the Mendocino Triple Junction From Characteristically Repeating Earthquakes". *Geophysical Research Letters* 45.2, pp. 699–707. ISSN: 0094-8276. DOI: https://doi.org/10.1002/2017GL075899.

Materna, K. et al. (2021). "GNSS characterization of hydrological loading in South and Southeast Asia". *Geophysical Journal International* 224.3, pp. 1742–1752. ISSN: 0956-540X. DOI: 10.1093/gji/ggaa500.

McClusky, S. et al. (2000). "Global Positioning System constraints on plate kinematics and dynamics in the eastern Mediterranean and Caucasus". *Journal of Geophysical Research: Solid Earth* 105.B3, pp. 5695–5719. DOI: https://doi.org/10.1029/1999JB900351. eprint: https://agupubs.onlinelibrary.wiley.com/doi/pdf/10.1029/1999JB900351.

McFarland, F. et al. (2017). *Data from theodolite measurements of creep rates on San Francisco Bay region faults, California*. English. Tech. rep. DOI: 10.3133/ofr20091119.

Michele, M de et al. (2011). "Spatiotemporal evolution of surface creep in the Parkfield region of the San Andreas Fault (1993–2004) from synthetic aperture radar". *Earth and Planetary Science Letters* 308.1, pp. 141–150. ISSN: 0012-821X. DOI: https://doi.org/10.1016/j.epsl.2011.05.049.

Milliner, C. W. et al. (2015). "Quantifying near-field and off-fault deformation patterns of the 1992 Mw 7.3 Landers earthquake". *Geochemistry, Geophysics, Geosystems*. ISSN: 15252027. DOI: 10.1002/2014GC005693.

Mongovin, D. D. and B. Philibosian (2021). "Creep on the Sargent Fault over the Past 50 Yr from Alignment Arrays with Implications for Slip Transfer between the Calaveras and San Andreas Faults, California". *Bulletin of the Seismological Society of America* 111.6, pp. 3189–3203. ISSN: 0037-1106. DOI: 10.1785/0120210041.

Moore, D. E. and M. J. Rymer (2007). "Talc-bearing serpentinite and the creeping section of the San Andreas fault". *Nature*. ISSN: 14764687. DOI: 10.1038/nature06064.

Murray-Moraleda, J. R. and R. W. Simpson (2009). "Geodetically Inferred Coseismic and Postseismic Slip due to the M 5.4 31 October 2007 Alum Rock Earthquake". *Bulletin of the Seismological Society of America* 99.5, pp. 2784–2800. ISSN: 0037-1106. DOI: 10.1785/0120090017.

Nadeau, R. M. and L. R. Johnson (1998). "Seismological studies at Parkfield VI: Moment release rates and estimates of source parameters for small repeating earthquakes". *Bulletin of the Seismological Society of America* 88.3, pp. 790–814. ISSN: 0037-1106. DOI: 10.1785/BSSA0880030790.

Nadeau, R. M. and T. V. McEvilly (2004). "Periodic Pulsing of Characteristic Microearthquakes on the San Andreas Fault". *Science* 303.5655, pp. 220–222. ISSN: 0036-8075. DOI: 10.1126/science.1090353PMID-14716011.

Ojha, C. et al. (2018). "Sustained Groundwater Loss in California's Central Valley Exacerbated by Intense Drought Periods". *Water Resources Research* 54.7, pp. 4449–4460. ISSN: 0043-1397. DOI: https://doi.org/10.1029/2017WR022250.

Okada, Y. (1992). "Internal deformation due to shear and tensile faults in a half-space". *Bulletin - Seismological Society of America* 82.2, pp. 1018–1040.

Okada, Y. (1985). "Surface deformation due to shear and tensile faults in a half-space". *Bulletin of the seismological society of America* 75.4, pp. 1135–1154.

Oppenheimer, D. H., W. H. Bakun, and A. G. Lindh (1990). "Slip partitioning of the Calaveras Fault, California, and prospects for future earthquakes". *Journal of Geophysical Research: Solid Earth* 95.B6, pp. 8483–8498. ISSN: 0148-0227. DOI: https://doi.org/10.1029/JB095iB06p08483.

Pan, J. et al. (Nov. 2020). "A newly discovered active fault on the Selaha-Kangding segment along the SE Xianshuihe fault: the South Mugecuo fault". *Acta Geologica Sinica* 94.11, pp. 3178–3188. DOI: doi:10.19762/j.cnki.dizhixuebao.2020196.

Paszke, A. et al. (2019). "PyTorch: An Imperative Style, High-Performance Deep Learning Library". In: *Advances in Neural Information Processing Systems 32*. Curran Associates, Inc., pp. 8024–8035. URL: http://papers.neurips.cc/paper/9015-pytorch-an-imperative-style-high-performance-deep-learning-library.pdf.

Pousse Beltran, L. et al. (2016). "Spatial and temporal variations in creep rate along the El Pilar fault at the Caribbean-South American plate boundary (Venezuela), from InSAR". *Journal of Geophysical Research: Solid Earth*. ISSN: 21699356. DOI: 10.1002/2016JB013121.

Prescott, W. and R. Burford (1976). "Slip on the Sargent Fault". *Bulletin of the Seismological Society of America* 44.1, pp. 123–134. DOI: https://doi.org/10.1785/BSSA0660031013PMID-7823326.

Provost, A.-S. and H. Houston (2001). "Orientation of the stress field surrounding the creeping section of the San Andreas Fault: Evidence for a narrow mechanically weak fault zone". *Journal of Geophysical Research: Solid Earth* 106.B6, pp. 11373–11386. ISSN: 0148-0227. DOI: https://doi.org/10.1029/2001JB900007.

Roeloffs, E. A. (2001). "Creep rate changes at Parkfield, California 1966–1999: Seasonal, precipitation induced, and tectonic". *Journal of Geophysical Research: Solid Earth* 106.B8, pp. 16525–16547. ISSN: 0148-0227. DOI: https://doi.org/10.1029/2001JB000352.

Rouet-Leduc, B. et al. (2021). "Autonomous extraction of millimeter-scale deformation in InSAR time series using deep learning". *Nature Communications* 12.1, p. 6480. DOI: 10.1038/s41467-021-26254-3. eprint: 2012.13849.

Rousset, B. et al. (2016). "An aseismic slip transient on the North Anatolian Fault". *Geophysical Research Letters*. ISSN: 19448007. DOI: 10.1002/2016GL068250.

Ryder, I. and R. Bürgmann (2008). "Spatial variations in slip deficit on the central San Andreas Fault from InSAR". *Geophysical Journal International* 175.3, pp. 837–852. ISSN: 0956540X. DOI: 10.1111/j.1365-246X.2008.03938.x.

Sandwell, D. et al. (2011a). *GMTSAR: An InSAR Processing System Based on Generic Mapping Tools*.

— (2011b). "Open radar interferometry software for mapping surface Deformation". *Eos, Transactions American Geophysical Union*. ISSN: 0096-3941. DOI: 10.1029/2011eo280002.

Savage, J. C. and R. O. Burford (1973). "Geodetic determination of relative plate motion in central California". *Journal of Geophysical Research (1896-1977)* 78.5, pp. 832–845. ISSN: 0148-0227. DOI: https://doi.org/10.1029/JB078i005p00832.

Savage, J. C. and M. Lisowski (1993). "Inferred depth of creep on the Hayward Fault, central California". *Journal of Geophysical Research*. ISSN: 01480227. DOI: 10.1029/92JB01871.

Savage, J. C. and J. L. Svarc (2009). "Postseismic relaxation following the 1992 M7.3 Landers and 1999 M7.1 Hector Mine earthquakes, southern California". *Journal of Geophysical Research: Solid Earth*. ISSN: 21699356. DOI: 10.1029/2008JB005938.

Savage, J. C., J. L. Svarc, and S. B. Yu (2005). "Postseismic relaxation and transient creep". *Journal of Geophysical Research: Solid Earth*. ISSN: 21699356. DOI: 10.1029/2005JB003687.

Schmidt, D. A. and R. Bürgmann (2003). "Time-dependent land uplift and subsidence in the Santa Clara valley, California, from a large interferometric synthetic aperture radar data set". *Journal of Geophysical Research: Solid Earth*. ISSN: 01480227. DOI: 10.1029/2002jb002267.

Schorlemmer, D, S Wiemer, and M Wyss (2004). "Earthquake statistics at Parkfield: 1. Stationarity of b values". *Journal of Geophysical Research: Solid Earth* 109.B12. ISSN: 0148-0227. DOI: https://doi.org/10.1029/2004JB003234.

Schulz, S. S. (1989). *Catalog of creepmeter measurements in California from 1966 through 1988*. ENGLISH. Tech. rep. DOI: 10.3133/ofr89650.

Scott, C. P. et al. (2018). "The M7 2016 Kumamoto, Japan, Earthquake: 3-D Deformation Along the Fault and Within the Damage Zone Constrained From Differential Lidar Topography". *Journal of Geophysical Research: Solid Earth*. ISSN: 21699356. DOI: 10.1029/2018JB015581.

Scott, C. P., S. B. DeLong, and J. R. Arrowsmith (2020). "Distribution of Aseismic Deformation Along the Central San Andreas and Calaveras Faults From Differencing Repeat Airborne Lidar". *Geophysical Research Letters* 47.22. ISSN: 0094-8276. DOI: 10.1029/2020gl090628.

Segall, P. (2002). "Integrating Geologic and Geodetic Estimates of Slip Rate on the San Andreas Fault System". *International Geology Review* 44.1, pp. 62–82. ISSN: 0020-6814. DOI: 10.2747/0020-6814.44.1.62.

Şengör, A. et al. (2005). "The North Anatolian fault: A new look". *Annu. Rev. Earth Planet. Sci.* 33, pp. 37–112.

Shah, A. K. and O. S. Boyd (2018). *Depth to basement and thickness of unconsolidated sediments for the western United States—Initial estimates for layers of the U.S. Geological Survey National Crustal Model*. English. Tech. rep. Reston, VA. DOI: 10.3133/ofr20181115.

Shen, Z. K. et al. (2009). "Slip maxima at fault junctions and rupturing of barriers during the 2008 Wenchuan earthquake". *Nature Geoscience*. ISSN: 17520894. DOI: 10.1038/ngeo636.

Shirzaei, M. and R. Bürgmann (2013). "Time-dependent model of creep on the Hayward fault from joint inversion of 18 years of InSAR and surface creep data". *Journal of Geophysical Research: Solid Earth*. ISSN: 21699356. DOI: 10.1002/jgrb.50149.

Shirzaei, M., R. Bürgmann, and T. Taira (2013). "Implications of recent asperity failures and aseismic creep for time-dependent earthquake hazard on the Hayward fault". *Earth and Planetary Science Letters* 371, pp. 59–66. ISSN: 0012-821X.

Simons, M., Y. Fialko, and L. Rivera (2002). "Coseismic deformation from the 1999 Mw 7.1 Hector Mine, California, earthquake as inferred from InSAR and GPS observations". *Bulletin of the Seismological Society of America*. ISSN: 00371106. DOI: 10.1785/0120000933. arXiv: /www.jstor.org/stable/3700093 [http:].

Simpson, R. W., J. J. Lienkaemper, and J. S. Galehouse (2001). "Variations in creep rate along the Hayward Fault, California, interpreted as changes in depth of creep". *Geophysical Research Letters* 28.11, pp. 2269–2272. ISSN: 0094-8276. DOI: https://doi.org/10.1029/2001GL012979.

Smith-Konter, B. R., D. T. Sandwell, and P. Shearer (2011). "Locking depths estimated from geodesy and seismology along the San Andreas Fault System: Implications for seismic moment release". *Journal of Geophysical Research: Solid Earth* 116.B6. ISSN: 0148-0227. DOI: https://doi.org/10.1029/2010JB008117.

Sun, J. et al. (2020). "Automatic detection of volcanic surface deformation using deep learning". *Journal of Geophysical Research: Solid Earth* 125.9, e2020JB019840.

Sun, J. et al. (2018). "The 2017 Jiuzhaigou Earthquake: A Complicated Event Occurred in a Young Fault System". *Geophysical Research Letters*. ISSN: 19448007. DOI: 10.1002/2017GL076421.

Taira, T. et al. (2014). "Variability of fault slip behavior along the San Andreas Fault in the San Juan Bautista Region". *Journal of Geophysical Research: Solid Earth*. ISSN: 21699356. DOI: 10.1002/2014JB011427.

Taylor, M. and A. Yin (2009). "Active structures of the Himalayan-Tibetan orogen and their relationships to earthquake distribution, contemporary strain field, and Cenozoic volcanism". *Geosphere* 5.3, pp. 199–214. ISSN: 1553-040X. DOI: 10.1130/GES00217.1.

Templeton, D. C., R. M. Nadeau, and R. Bürgmann (2008). "Behavior of Repeating Earthquake Sequences in Central California and the Implications for Subsurface Fault Creep". *Bulletin of the Seismological Society of America* 98.1, pp. 52–65. ISSN: 0037-1106. DOI: 10.1785/0120070026.

Thatcher, W, G Marshall, and M Lisowski (1997). "Resolution of fault slip along the 470-km-long rupture of the great 1906 San Francisco earthquake and its implications". *Journal of Geophysical Research B: Solid Earth* 102.B3, pp. 5353–5367. URL: http://pubs.er.usgs.gov/publication/70019238.

Thomas, A. M., R. Bürgmann, and D. S. Dreger (2013). "Incipient faulting near lake pillsbury, california, and the role of: Accessory faults in plate boundary evolution". *Geology* 41.10, pp. 1119–1122. ISSN: 00917613. DOI: 10.1130/G34588.1.

Titus, S. J., C. DeMets, and B. Tikoff (2006). "Thirty-five-year creep rates for the creeping segment of the San Andreas fault and the effects of the 2004 Parkfield earthquake: Constraints from alignment arrays, continuous global positioning system, and creepmeters". *Bulletin of the Seismological Society of America* 96.4B, S250–S268. ISSN: 1943-3573.

Tong, X., D. T. Sandwell, and B. Smith-Konter (2013). "High-resolution interseismic velocity data along the San Andreas Fault from GPS and InSAR". *Journal of Geophysical Research: Solid Earth*. ISSN: 21699356. DOI: 10.1029/2012JB009442.

Tong, X., D. T. Sandwell, and Y. Fialko (2010). "Coseismic slip model of the 2008 Wenchuan earthquake derived from joint inversion of interferometric synthetic aperture radar, GPS, and field data". *Journal of Geophysical Research*. ISSN: 0148-0227. DOI: 10.1029/2009jb006625.

Toppozada, T. R. et al. (2002). "San Andreas Fault Zone, California: M 5.5 Earthquake History". *Bulletin of the Seismological Society of America* 92.7, pp. 2555–2601. ISSN: 0037-1106. DOI: 10.1785/0120000614.

Tormann, T, S Wiemer, and A Mignan (2014). "Systematic survey of high-resolution b value imaging along Californian faults: Inference on asperities". *Journal of Geophysical Research: Solid Earth* 119.3, pp. 2029–2054. ISSN: 2169-9313. DOI: https://doi.org/10.1002/2013JB010867.

Turner, R. C., R. M. Nadeau, and R Bürgmann (2013). "Aseismic slip and fault interaction from repeating earthquakes in the Loma Prieta aftershock zone". *Geophysical Research Letters* 40.6, pp. 1079–1083. ISSN: 1944-8007. DOI: 10.1002/grl.50212.

Turner, R. C. et al. (2015). "Slow and Go: Pulsing slip rates on the creeping section of the San Andreas Fault". *Journal of Geophysical Research: Solid Earth* 120.8, pp. 5940–5951. ISSN: 2169-9313. DOI: https://doi.org/10.1002/2015JB011998.

Tymofyeyeva, E. and Y. Fialko (2015). "Mitigation of atmospheric phase delays in InSAR data, with application to the eastern California shear zone". *Journal of Geophysical Research: Solid Earth* 120.8, pp. 5952–5963. ISSN: 21699356. DOI: 10.1002/2015JB011886.

Tymofyeyeva, E. et al. (2019). "Slow Slip Event On the Southern San Andreas Fault Triggered by the 2017 Mw8.2 Chiapas (Mexico) Earthquake". *Journal of Geophysical Research: Solid Earth* 124.9, pp. 9956–9975. ISSN: 21699356. DOI: 10.1029/2018JB016765.

Uchida, N. (2019). "Detection of repeating earthquakes and their application in characterizing slow fault slip". *Progress in Earth and Planetary Science* 6.1, p. 40. ISSN: 2197-4284. DOI: 10.1186/s40645-019-0284-z.

Uchida, N. and R. Bürgmann (2019). "Repeating Earthquakes". *Annual Review of Earth and Planetary Sciences* 47.1, pp. 305–332. ISSN: 0084-6597. DOI: 10.1146/annurev-earth-053018-060119.

Waldhauser, F. (2009). "Near-Real-Time Double-Difference Event Location Using Long-Term Seismic Archives, with Application to Northern California". *Bulletin of the Seismological Society of America* 99.5, pp. 2736–2748. ISSN: 0037-1106. DOI: 10.1785/0120080294.

Waldhauser, F. and D. P. Schaff (2008). "Large-scale relocation of two decades of Northern California seismicity using cross-correlation and double-difference methods". *Journal of Geophysical Research: Solid Earth* 113.B8. ISSN: 0148-0227. DOI: https://doi.org/10.1029/2007JB005479.

— (2021). "A Comprehensive Search for Repeating Earthquakes in Northern California: Implications for Fault Creep, Slip Rates, Slip Partitioning, and Transient Stress". *Journal of Geophysical Research: Solid Earth* 126.11. ISSN: 2169-9313. DOI: 10.1029/2021jb022495.

Wallace, R. E. (1990). *The San Andreas fault system, California*. Department of the Interior, US Geological Survey.

Walters, R. J. et al. (2013). "Rapid strain accumulation on the Ashkabad fault (Turkmenistan) from atmosphere-corrected InSAR". *Journal of Geophysical Research: Solid Earth* 118.7, pp. 3674–3690. DOI: https://doi.org/10.1002/jgrb.50236.

Wang, H., T. J. Wright, and J. Biggs (2009). "Interseismic slip rate of the northwestern Xianshuihe fault from InSAR data". *Geophysical Research Letters* 36.3, pp. 1–5. ISSN: 00948276. DOI: 10.1029/2008GL036560.

Wang, K. and R. Bürgmann (2020). "Probing fault frictional properties during afterslip up- and downdip of the 2017 Mw 7.3 Sarpol-e Zahab earthquake with space geodesy". *Journal of Geophysical Research: Solid Earth*. ISSN: 2169-9313. DOI: 10.1029/2020jb020319.

Wang, K. and Y. Fialko (2015). "Slip model of the 2015 Mw 7.8 Gorkha (Nepal) earthquake from inversions of ALOS-2 and GPS data". *Geophysical Research Letters*. ISSN: 19448007. DOI: 10.1002/2015GL065201.

Wang, M. and Z.-K. Shen (2020). "Present-Day Crustal Deformation of Continental China Derived From GPS and Its Tectonic Implications". *Journal of Geophysical Research: Solid Earth* 125.2, e2019JB018774. DOI: https://doi.org/10.1029/2019JB018774.

Wang, W., X. Qiao, and K. Ding (2021). "Present-Day Kinematics in Southeastern Tibet Inferred From GPS Measurements". *Journal of Geophysical Research: Solid Earth* 126.1, pp. 1–20. ISSN: 21699356. DOI: 10.1029/2020JB021305.

Wang, W. et al. (2017a). "Present-day velocity field and block kinematics of Tibetan Plateau from GPS measurements". *Geophysical Journal International* 208.2, pp. 1088–1102. ISSN: 1365246X. DOI: 10.1093/gji/ggw445.

Wang, Y., M. Wang, and Z. K. Shen (2017b). "Block-like versus distributed crustal deformation around the northeastern Tibetan plateau". *Journal of Asian Earth Sciences* 140, pp. 31–47. ISSN: 13679120. DOI: 10.1016/j.jseaes.2017.02.040.

Watt, J. T. et al. (2014). "Subsurface geometry of the San Andreas-Calaveras fault junction: Influence of serpentinite and the Coast Range Ophiolite". *Tectonics* 33.10, pp. 2025–2044. ISSN: 0278-7407. DOI: https://doi.org/10.1002/2014TC003561.

Wei, M., D. Sandwell, and Y. Fialko (2009). "A silent Mw 4.7 slip event of October 2006 on the Superstition Hills fault, southern California". *Journal of Geophysical Research: Solid Earth*. ISSN: 21699356. DOI: 10.1029/2008JB006135.

Wei, M. et al. (2011). "Slip on faults in the Imperial Valley triggered by the 4 April 2010 Mw 7.2 El Mayor-Cucapah earthquake revealed by InSAR". *Geophysical Research Letters* 38.1.

Wei, M. et al. (2013). "Episodic fault creep events in California controlled by shallow frictional heterogeneity". *Nature geoscience* 6.7, pp. 566–570.

Weiss, J. R. et al. (2020). "High-Resolution Surface Velocities and Strain for Anatolia From Sentinel-1 InSAR and GNSS Data". *Geophysical Research Letters* 47.17. e2020GL087376 2020GL087376, e2020GL087376. DOI: https://doi.org/10.1029/2020GL087376. eprint: https://agupubs.onlinelibrary.wiley.com/doi/pdf/10.1029/2020GL087376.

Wen, X. ze et al. (2008). "Historical pattern and behavior of earthquake ruptures along the eastern boundary of the Sichuan-Yunnan faulted-block, southwestern China". *Physics of the Earth and Planetary Interiors*. ISSN: 00319201. DOI: 10.1016/j.pepi.2008.04.013.

Wiemer, S. and M. Wyss (2000). "Minimum Magnitude of Completeness in Earthquake Catalogs: Examples from Alaska, the Western United States, and Japan". *Bulletin of*

the Seismological Society of America 90.4, pp. 859–869. ISSN: 0037-1106. DOI: 10.1785/0119990114.

Wilson, C. J. L. et al. (2004). "Active faulting and block movement associated with large earthquakes in the Min Shan and Longmen Mountains, northeastern Tibetan Plateau". *Journal of Geophysical Research: Solid Earth*. DOI: 10.1029/94jb02132.

Wimpenny, S., A. Copley, and T. Ingleby (2017). "Fault mechanics and post-seismic deformation at Bam, SE Iran". *Geophysical Journal International*. ISSN: 0956-540X. DOI: 10.1093/gji/ggx065.

Wright, T., B. Parsons, and E. Fielding (2001). "Measurement of interseismic strain accumulation across the North Anatolian Fault by satellite radar interferometry". *Geophysical Research Letters* 28.10, pp. 2117–2120. ISSN: 00948276. DOI: 10.1029/2000GL012850.

Wright, T. J. et al. (2004). "InSAR observations of low slip rates on the major faults of western Tibet". *Science* 305.5681, pp. 236–239. ISSN: 00368075. DOI: 10.1126/science.1096388.

Wu, Z., X. Zhang, and K. Sun (2019). "China Seismic Experiment Site: scientific challenges". *Acta Geologica Sinica - English Edition* 93.S1, pp. 273–273. DOI: https://doi.org/10.1111/1755-6724.14084. eprint: https://onlinelibrary.wiley.com/doi/pdf/10.1111/1755-6724.14084.

Xia, Y. et al. (2012). "Continental-scale water and energy flux analysis and validation for the North American Land Data Assimilation System project phase 2 (NLDAS-2): 1. Intercomparison and application of model products". *Journal of Geophysical Research: Atmospheres* 117.D3. ISSN: 0148-0227.

Xie, Z. et al. (2017). "An integrated analysis of source parameters, seismogenic structure, and seismic hazards related to the 2014 MS 6.3 Kangding earthquake, China". *Tectonophysics*. ISSN: 00401951. DOI: 10.1016/j.tecto.2017.04.030.

Xu, G. and P. J. Kamp (2000). "Tectonics and denudation adjacent to the Xianshuihe Fault, eastern Tibetan Plateau: Constraints from fission track thermochronology". *Journal of Geophysical Research: Solid Earth* 105.B8, pp. 19231–19251.

Xu, X. et al. (2016). "Refining the shallow slip deficit". *Geophysical Journal International*. ISSN: 1365246X. DOI: 10.1093/gji/ggv563.

Xu, X. et al. (2003). "Pattern of latest tectonic motion and its dynamics for active blocks in Sichuan-Yunnan region, China". *Science in China, Series D: Earth Sciences*. ISSN: 10069313. DOI: 10.1360/03yd9020.

Yi, G.-X. et al. (2017). "Focal mechanism solutions and seismogenic structure of the 8 August 2017 M7.0 Jiuzhaigou earthquake and its aftershocks, northern Sichuan". *Acta Geophysica Sinica*. ISSN: 00015733. DOI: 10.6038/cjg20171033.

Yi, G. (2005). "Study on faulting behavior and fault-segments for potential strong earthquake risk along the central-southern segment of Xianshuihe fault zone based on current seismicity". *Earthquake* 25, pp. 58–66.

Yu, C. et al. (2018). "Generic Atmospheric Correction Model for Interferometric Synthetic Aperture Radar Observations". *Journal of Geophysical Research: Solid Earth* 123.10,

pp. 9202–9222. DOI: https://doi.org/10.1029/2017JB015305. eprint: https://agupubs.onlinelibrary.wiley.com/doi/pdf/10.1029/2017JB015305.

Zaliapin, I. and Y. Ben-Zion (2013). "Earthquake clusters in southern California I: Identification and stability". *Journal of Geophysical Research: Solid Earth* 118.6, pp. 2847–2864. ISSN: 2169-9356. DOI: 10.1002/jgrb.50179.

Zhang, E. et al. (2018a). *Reexamination of the subsurface fault structure in the vicinity of the 1989 moment-magnitude-6.9 Loma Prieta earthquake, central California, using steep-reflection, earthquake, and magnetic data*. English. Tech. rep. Reston, VA. DOI: 10.3133/ofr20181093.

Zhang, J. et al. (2018b). "Surface creep and slip-behavior segmentation along the northwestern Xianshuihe fault zone of southwestern China determined from decades of fault-crossing short-baseline and short-level surveys". *Tectonophysics* 722.July 2017, pp. 356–372. ISSN: 00401951. DOI: 10.1016/j.tecto.2017.11.002.

Zhang, K. J. et al. (2012). *Late mesozoic tectonic evolution and growth of the tibetan plateau prior to the Indo-Asian collision*. DOI: 10.1016/j.earscirev.2012.06.002.

Zhang, L. et al. (2019). "Interseismic Fault Movement of Xianshuihe Fault Zone Based on Across-Fault Deformation Data and InSAR". *Pure and Applied Geophysics* 176.2, pp. 649–667. ISSN: 14209136. DOI: 10.1007/s00024-018-1989-4.

Zhang, L. et al. (2022). "Deep fault slip characteristics in the Xianshuihe-Anninghe-Daliangshan Fault junction region (eastern Tibet) revealed by repeating micro-earthquakes". *Journal of Asian Earth Sciences* 227, p. 105115. ISSN: 1367-9120. DOI: https://doi.org/10.1016/j.jseaes.2022.105115.

Zhang, P. Z. (2013). *A review on active tectonics and deep crustal processes of the Western Sichuan region, eastern margin of the Tibetan Plateau*. DOI: 10.1016/j.tecto.2012.02.021.

Zhang, Y. et al. (2018c). "Source Fault and Slip Distribution of the 2017 Mw 6.5 Jiuzhaigou, China, Earthquake and Its Tectonic Implications". *Seismological Research Letters*. ISSN: 0895-0695. DOI: 10.1785/0220170255.

Zhao, D. et al. (2018). "InSAR and GPS derived coseismic deformation and fault model of the 2017 Ms7.0 Jiuzhaigou earthquake in the Northeast Bayanhar block". *Tectonophysics*. ISSN: 00401951. DOI: 10.1016/j.tecto.2018.01.026.

Zheng, G. et al. (2017). "Crustal Deformation in the India-Eurasia Collision Zone From 25 Years of GPS Measurements". *Journal of Geophysical Research: Solid Earth*. ISSN: 21699356. DOI: 10.1002/2017JB014465.

Appendix A

Supporting information for: Evidence of Fault Immaturity from Shallow Slip Deficit and Lack of Postseismic Deformation of the 2017 Mw 6.5 Jiuzhaigou Earthquake

The chapter was adapted from the supplement of: Y. Li, R. Bürgmann, and B. Zhao (Jan. 2020). "Evidence of Fault Immaturity from Shallow Slip Deficit and Lack of Postseismic Deformation of the 2017 Mw 6.5 Jiuzhaigou Earthquake". *Bulletin of the Seismological Society of America* 110.1, pp. 154–165. ISSN: 0037-1106. DOI: 10.1785/0120190162

Institute	Magnitude (Mw)	Centroid Depth (km)	Location		Attitude*		
			Longitude(°)	Latitude(°)	Strike(°)	Dip(°)	Rake(°)
USGS	6.5	13.5	103.855	33.193	153	84	-33
GCMT	6.5	14.9	103.89	33.21	150	78	-13
CENC	6.5	11.0	103.82	33.20	326	62	-15
Han et al., 2018	6.5	14.0	103.82	33.20	156	65	9

Table A.1: Focal mechanisms of the Jiuzhaigou earthquake determined by different institutes. USGS, GCMT and CENC refer to U.S. Geological Survey, Global Centroid Moment Tensor and China Earthquake Network Center, respectively.
** Nodal plane aligned with aftershock distribution.*

	Single-segment model in this study	Two-segment model from Sun et al., 2018
RMS	1.06 cm	0.85 cm
AIC	-8987	-9172
BIC	-8292	-8128

Table A.2: Comparison of RMS, AIC and BIC for inversions using different coseismic model geometry.

Satellite	Orbit Direction	Track	Reference Date	Repeat Date	Time Interval	Perpendicular Baseline	Mean Coherence
S1A	Ascend	128	20170718	20170811	24 days	2.05 m	0.1995
S1A	Ascend	128	20170730*	20170811*	12 days	34.08 m	0.2346
S1A	Ascend	128	20170718	20170823	36 days	35.94 m	0.1426
S1A	Ascend	128	20170730	20170823	24 days	67.97 m	0.1625
S1A	Descend	62	20170725	20170818	24 days	15.73 m	0.1647
S1A	Descend	62	20170806*	20170818*	12 days	59.25 m	0.2178
S1A	Descend	62	20170725	20170830	36 days	14.60 m	0.1849
S1A	Descend	62	20170806	20170830	24 days	60.39 m	0.1443

Table A.3: Interferograms generated for coseismic study. Dates with *: Acquisition days of the interferograms selected for modeling.

Site	Lon (°)	Lat (°)	ue (mm)	un (mm)	se (mm)	sn (mm)	ue' (mm)	un' (mm)	Reference
J416	103.80	33.32	77.44	208.92	1.63	1.69	77.60	208.30	Zhao et al., 2018
JB33	103.89	33.28	21.89	97.62	1.41	1.48	17.82	103.08	Zhao et al., 2018
SCJZ	104.30	33.20	-9.80	3.30	2.10	1.20	-10.16	5.27	Li et al., 2018a
SCSP	103.58	32.65	-2.38	-9.27	1.53	1.50	-3.98	-9.39	Li et al., 2018a

Table A.4: Observed and modeled GPS displacements for coseismic study.

Site	Lon (°)	Lat (°)	ue (mm)	un (mm)	se (mm)	sn (mm)	ue' (mm)	un' (mm)	Reference
H019	104.40	33.79	0.42	7.85	2.11	2.07	2.48	4.62	This study
H020	103.73	33.94	-0.39	4.01	1.64	1.42	1.53	3.39	This study
H021	104.82	33.42	-3.89	0.97	2.40	1.74	-1.01	1.38	This study
H022	104.62	33.00	-6.33	4.37	1.72	1.78	-5.26	2.34	This study
H024	104.23	33.23	-8.20	4.12	2.19	2.10	-10.38	7.48	This study
H025	103.43	32.93	-7.26	-11.55	1.85	1.22	-6.26	-11.08	This study
H026	102.99	33.57	5.56	-0.84	1.30	1.25	5.08	-2.44	This study
H030	103.61	32.59	-3.01	-8.78	3.03	1.74	-3.36	-8.42	This study
H034	103.73	32.36	-1.95	0.72	4.17	1.51	-1.44	-4.19	This study
J416*	103.80	33.32	81.23	218.52	2.04	2.68	81.32	217.52	This study
J418	104.27	32.76	-3.90	5.01	2.30	2.42	-5.12	2.25	This study
JB33*	103.89	33.28	31.61	107.35	1.85	2.05	26.03	112.54	This study

Table A.5: Observed and modeled GPS displacements for co- and postseismic study.

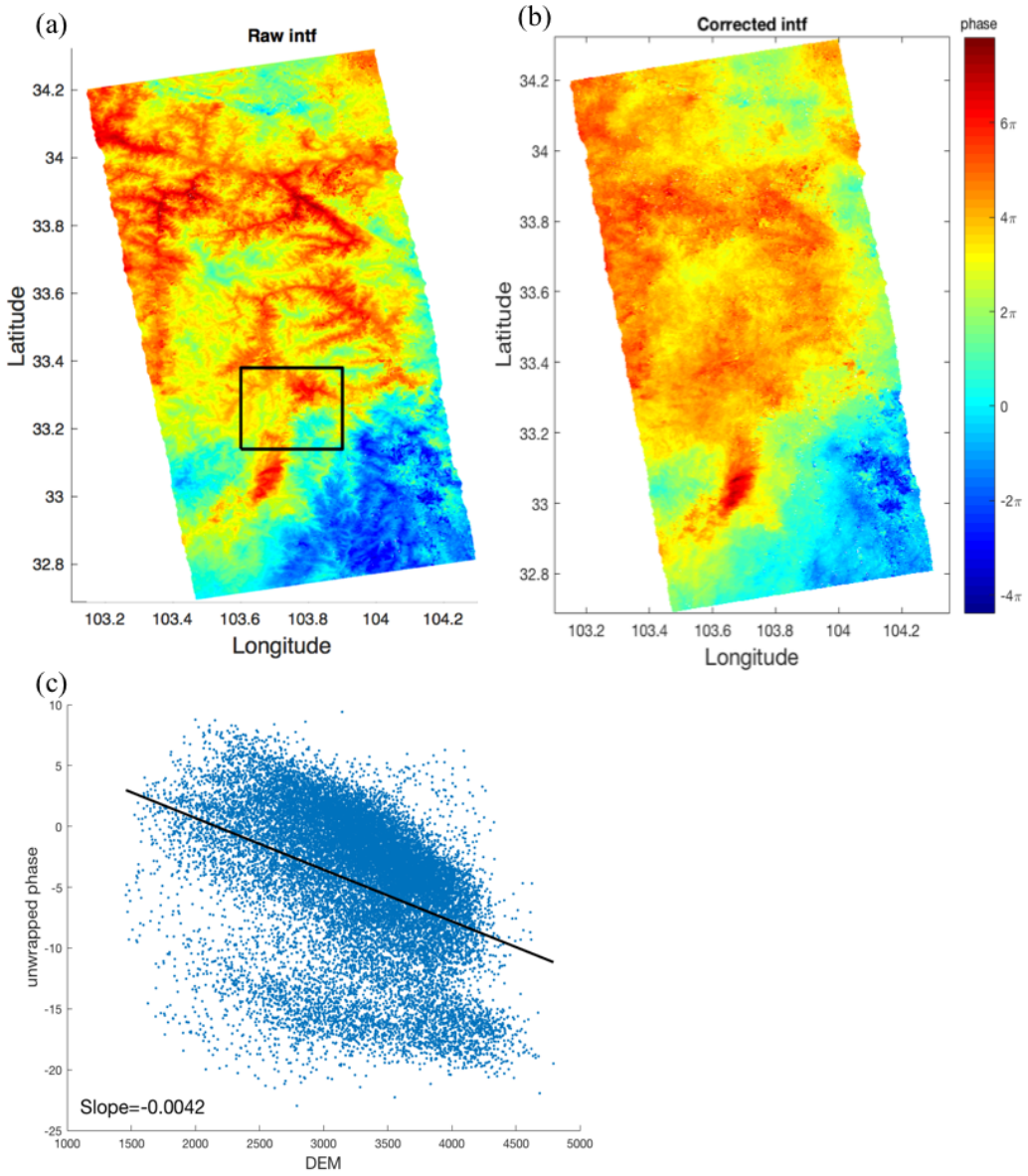


Figure A.1: Example demonstrating the correction of topography-correlated troposphere delay through linear regression. **(a)** raw ascending interferogram (20170811-20170823), and **(b)** corrected interferogram using slope derived from **(c)**. All interferograms used in this study are corrected. The coseismic deformation zone (shown by black rectangle in **(a)**) is masked when applying this method.

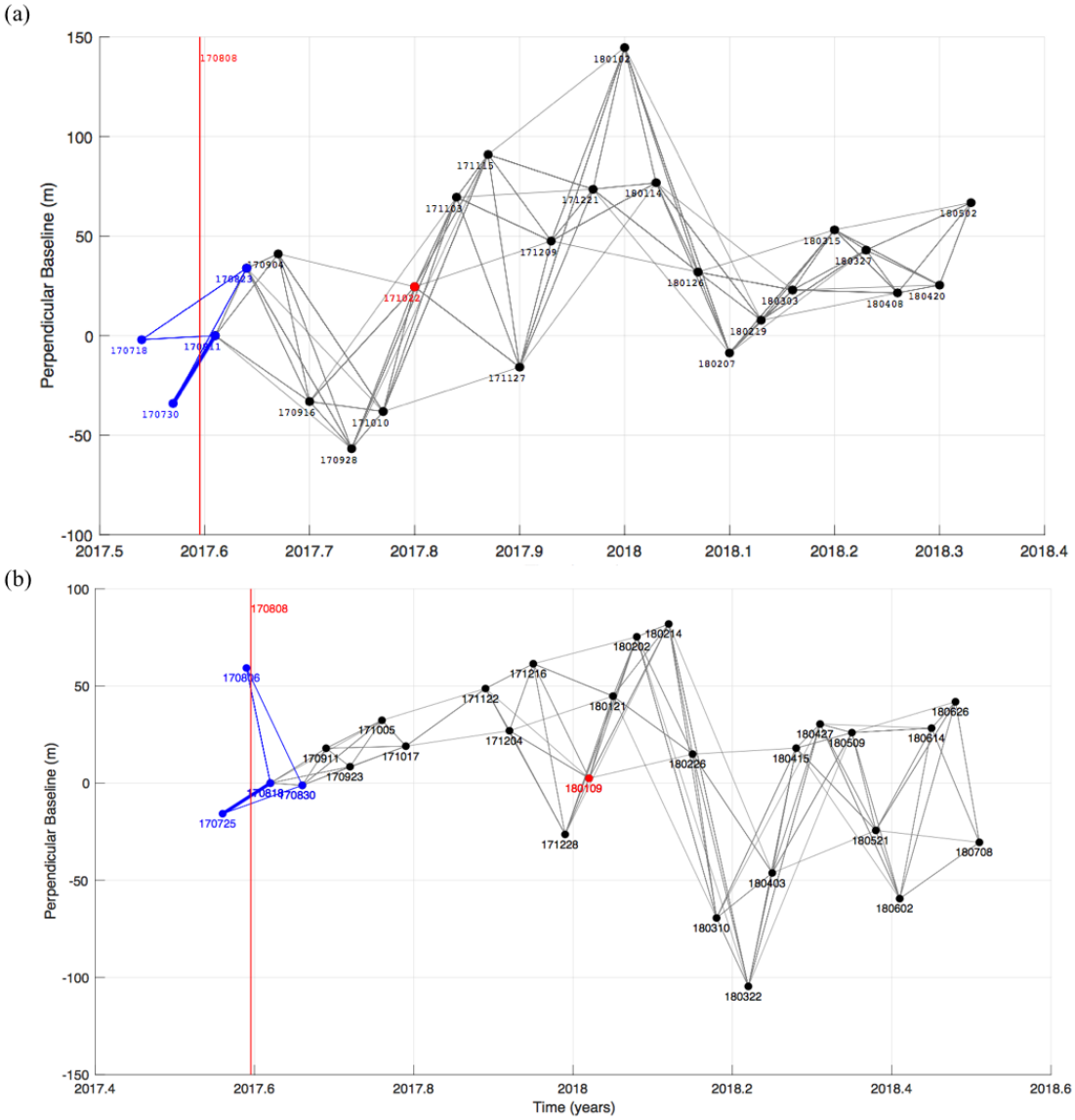


Figure A.2: **(a)** Baseline plot for the co- and postseismic analysis of ascending-orbit Sentinel-1 data from track T128. Coseismic SAR acquisitions are shown as blue dots and the interferogram we used is shown in bold. Postseismic acquisitions are shown as black dots labeled by their dates. The red dot indicates the supermaster. Gray lines indicate generated interferograms. The date of the 2017 Jiuzhaigou earthquake is marked by red lines. **(b)** Similar baseline plot for the descending-orbit Sentinel-1 data from track T62.

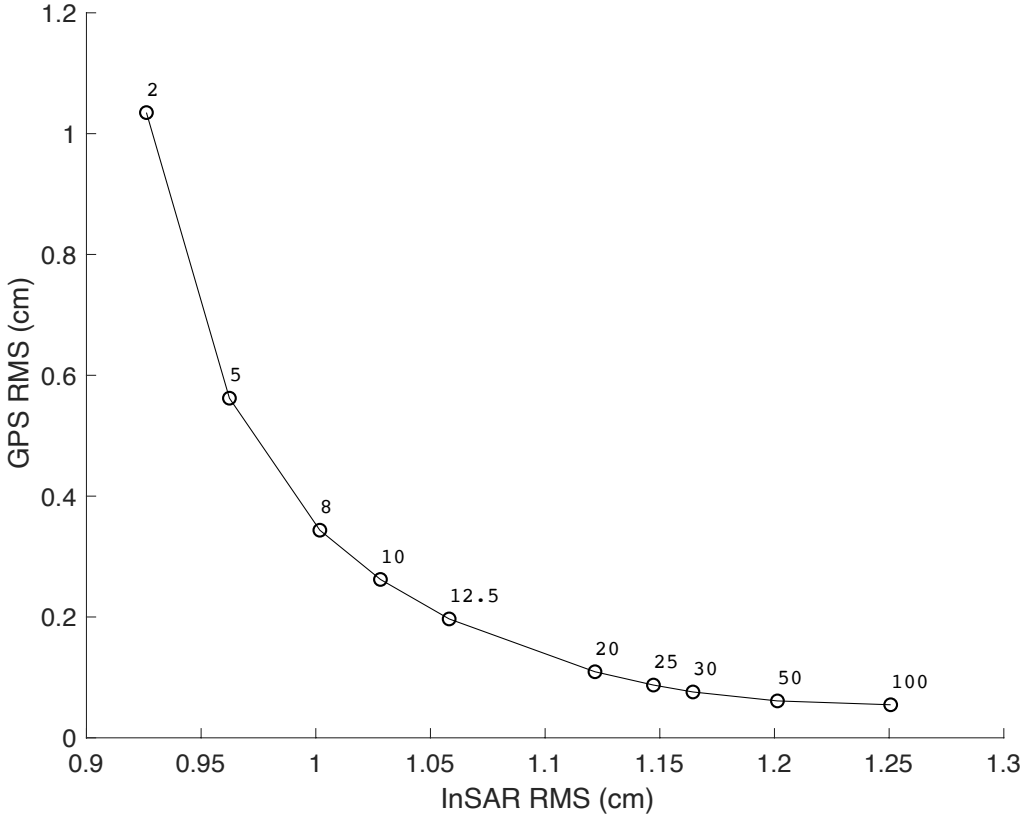


Figure A.3: The trade-off curve between InSAR residuals and GPS residuals with different weight. The number above each data point shows the weight ratio of GPS to InSAR data points.

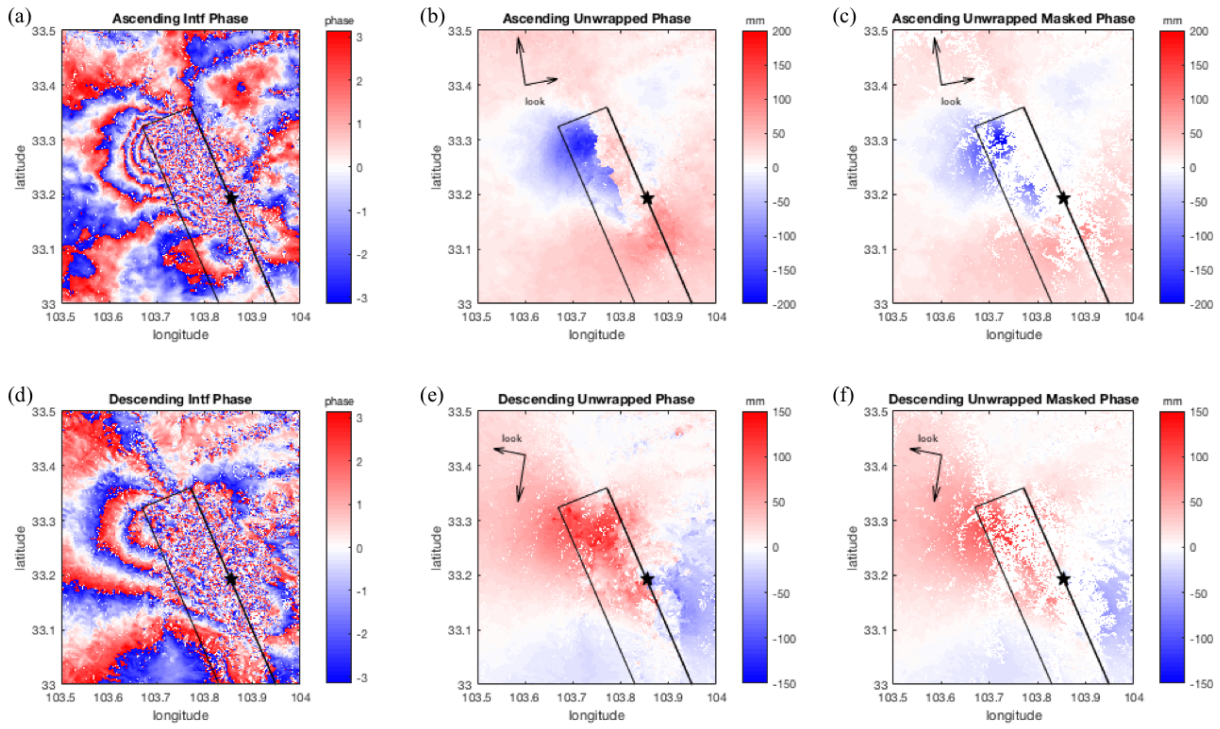


Figure A.4: A close-up view of wrapped, unwrapped and unwrapped masked (coherence<0.1) interferograms for ascending and descending orbits used in the coseismic modeling.

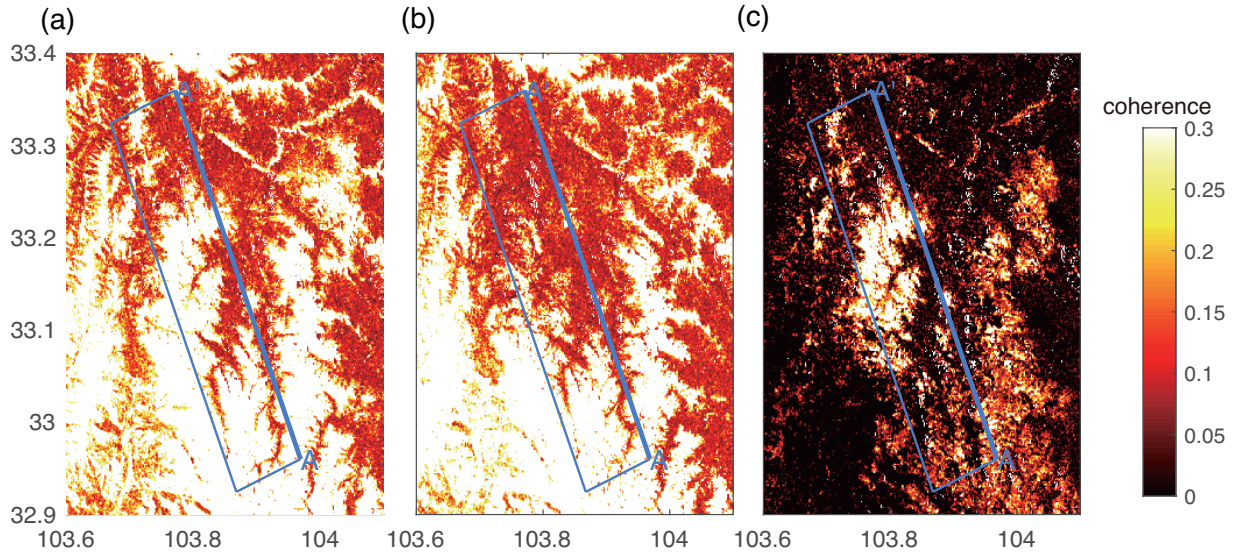


Figure A.5: Coherence maps of **(a)** preseismic (20170718-20170730), **(b)** coseismic (20170730-20170811) interferograms and **(c)** coseismic coherence loss (preseismic minus coseismic coherence) for ascending orbit T128. Coherence values larger than 0.3 are masked out to better visualize the decorrelation. The fault plane is drawn for reference and the upper edge is marked with AA'.

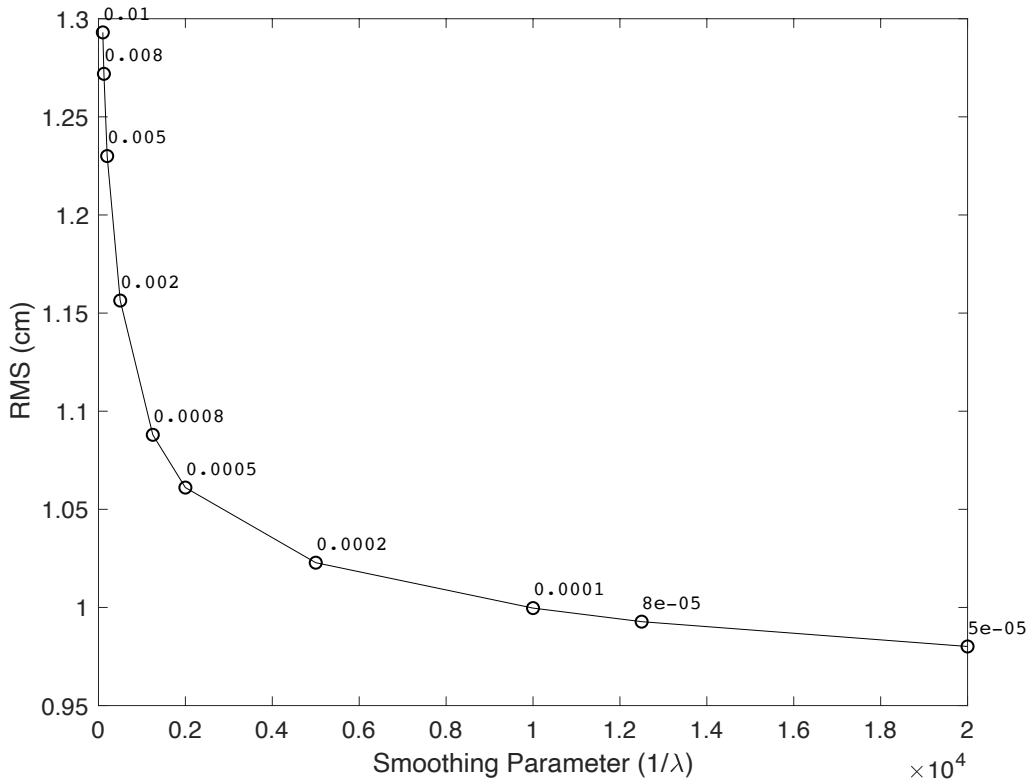


Figure A.6: The trade-off curve between smoothing parameter (λ) and InSAR and GPS combined RMS=RMS^2_{gps}+RMS^2_{sar}. Note that in the stage of determining smoothing parameter, no constraint was added on the coseismic slip distribution model.

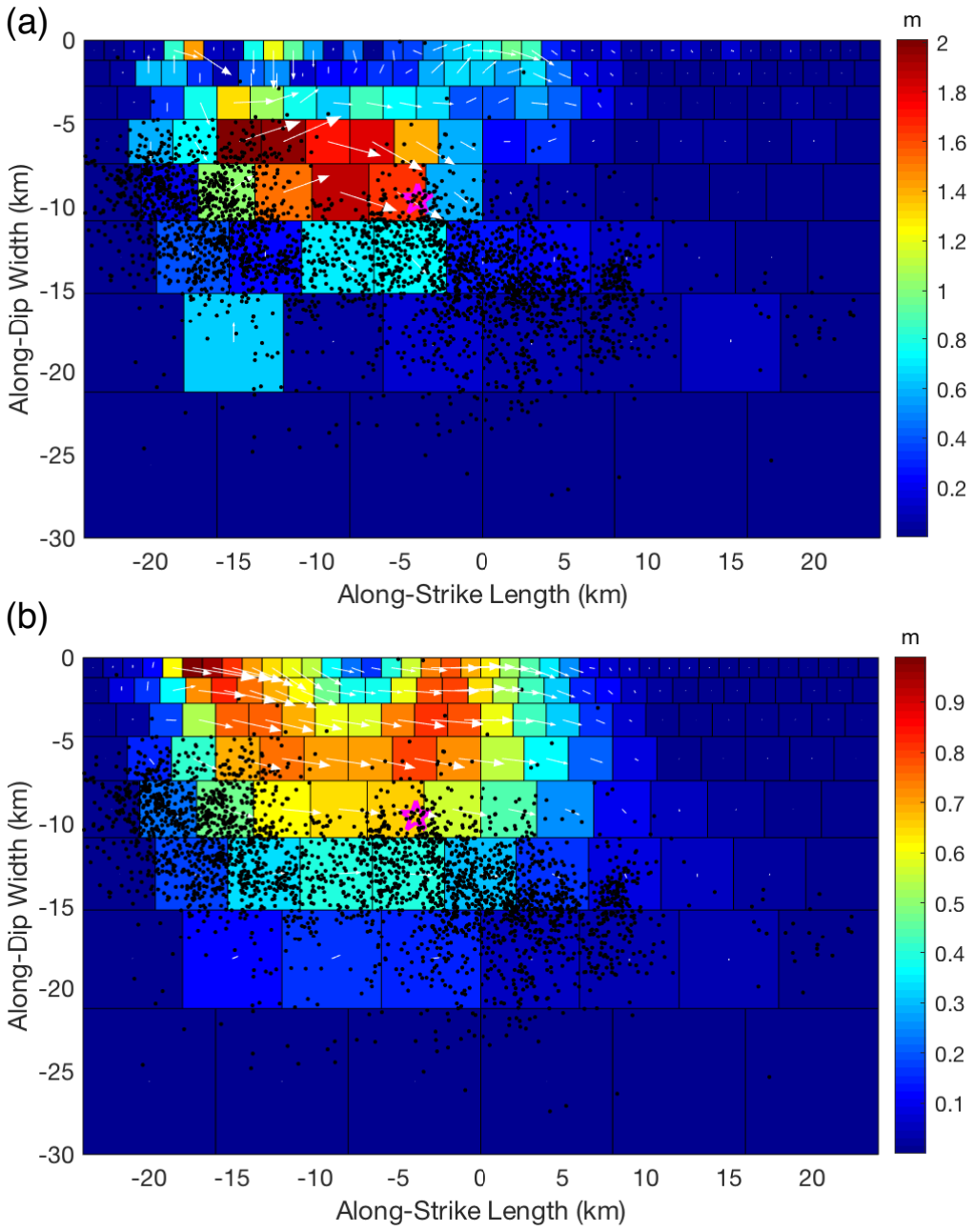


Figure A.7: An example of **(a)** an overly-rough slip model with λ=0.00005 (RMS_{gps}=0.258 cm, RMS_{sar}=0.945 cm) and **(b)** an overly-smooth model with λ=0.005 (RMS_{gps}=0.297 cm, RMS_{sar}=1.194 cm).

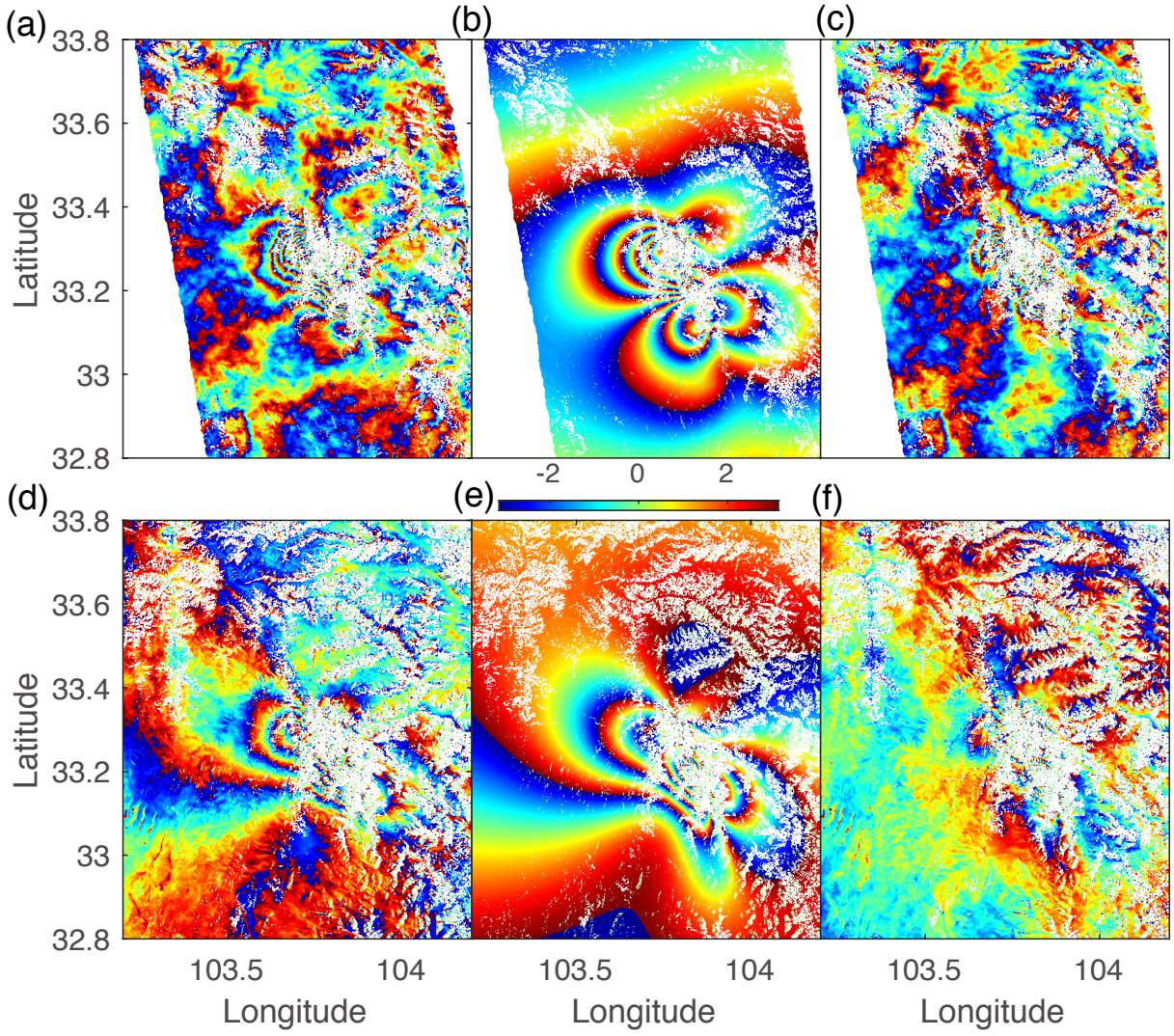


Figure A.8: Comparison of observed and modeled coseismic re-wrapped LOS displacements from both ascending and descending Sentinel-1A tracks. **(a-c)** are observation, model and observed minus modeled residual of plot for ascending orbit T128. **(d-f)** are corresponding plots for descending orbit T62.

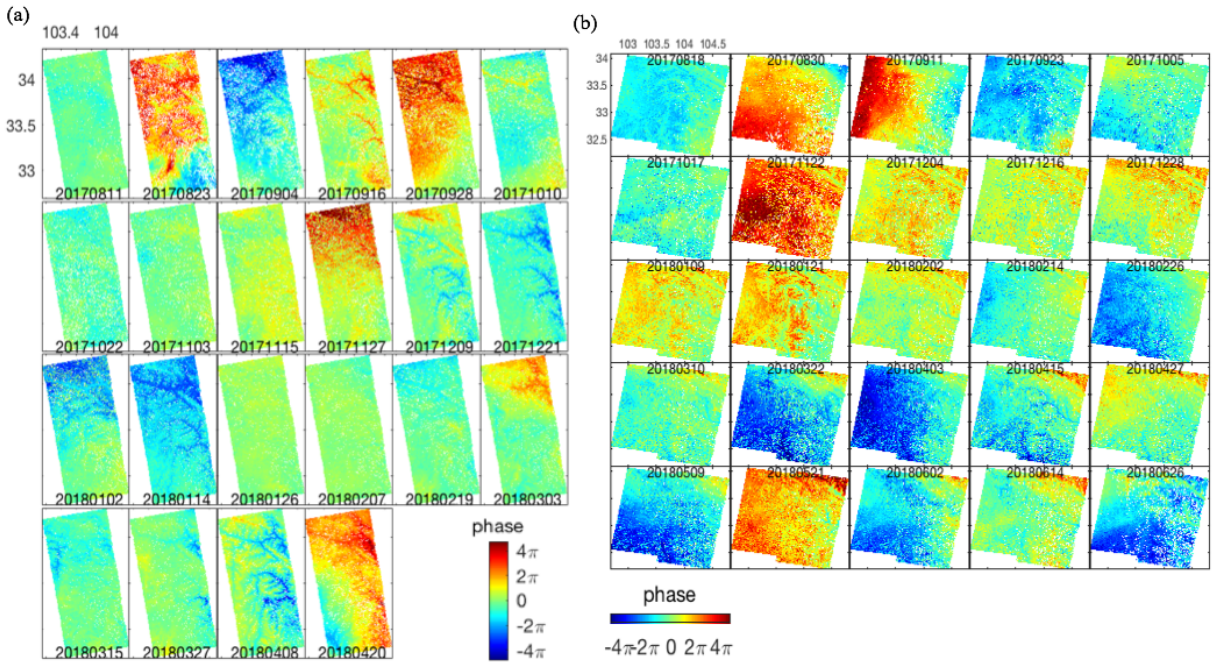


Figure A.9: **(a)** Atmospheric phase delay estimates of each selected scene from ascending orbit acquisitions estimated by the iteratively common point stacking method (Tymofyeyeva and Fialko, 2015). The horizontal axis indicates longitude and vertical axis indicates latitude. The scale for all images below is in phase (radians). **(b)** Atmospheric phase screen estimates for descending orbit.

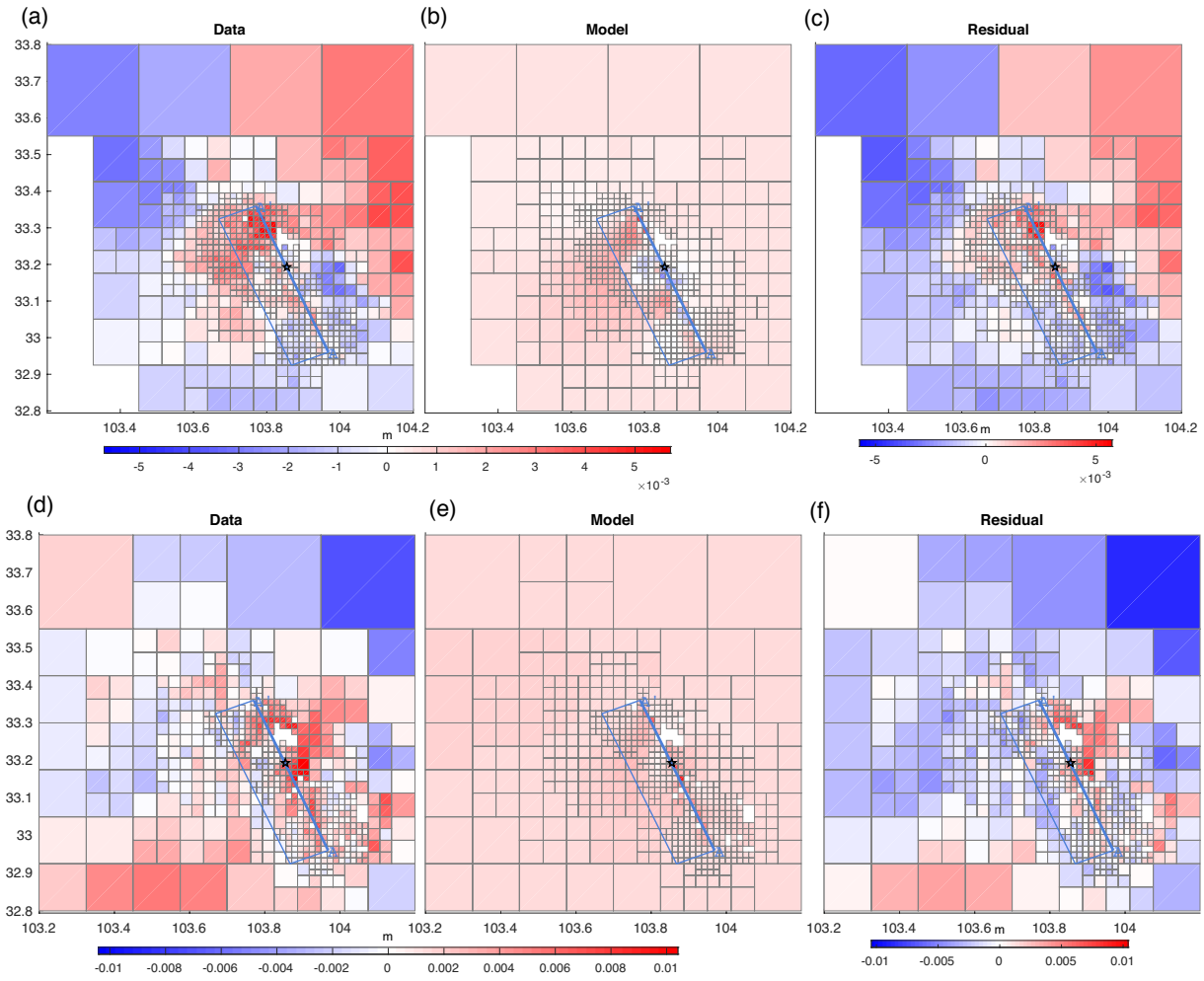


Figure A.10: Comparison of observed and modeled postseismic LOS displacements from both ascending and descending Sentinel-1A tracks. **(a-c)** are observation, model and observed minus modeled residual of plot for ascending orbit T128. **(d-f)** are corresponding plots for descending orbit T62. The fault plane is drawn as a reference and the upper edges are marked with AA'. The RMS are 0.18 cm and 0.24 cm for ascending data and its residuals, 0.30 cm and 0.18 cm for descending data and its residuals.

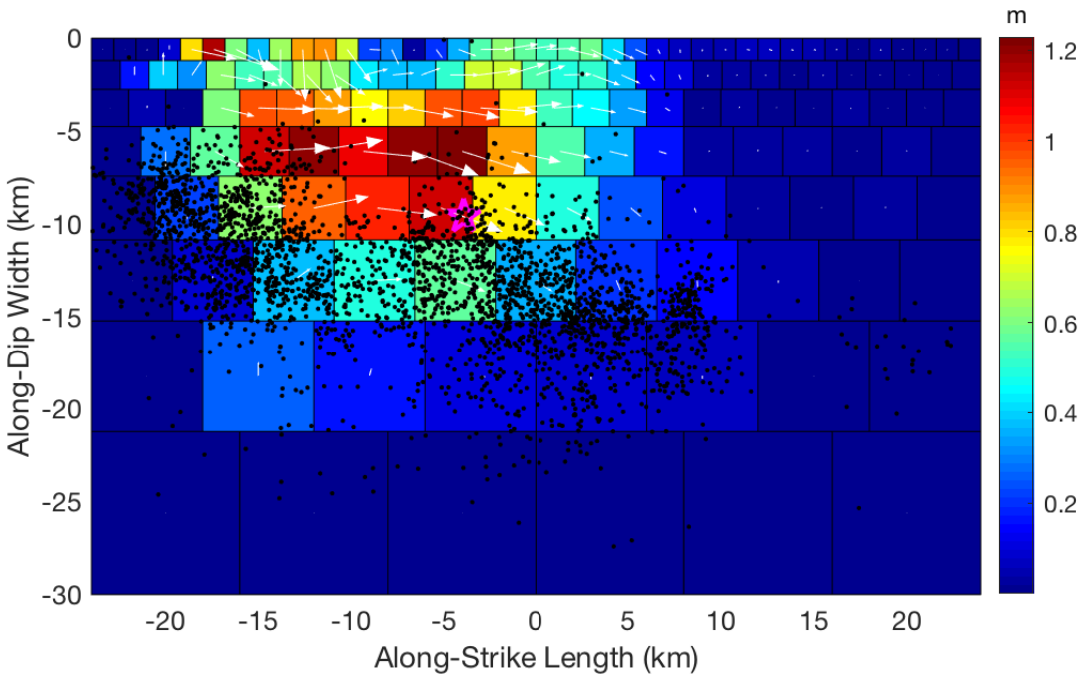


Figure A.11: Inverted co- and postseismic slip based on both InSAR and GPS data. (RMS_{gps}=0.246 cm, RMS_{sar}=1.109 cm).

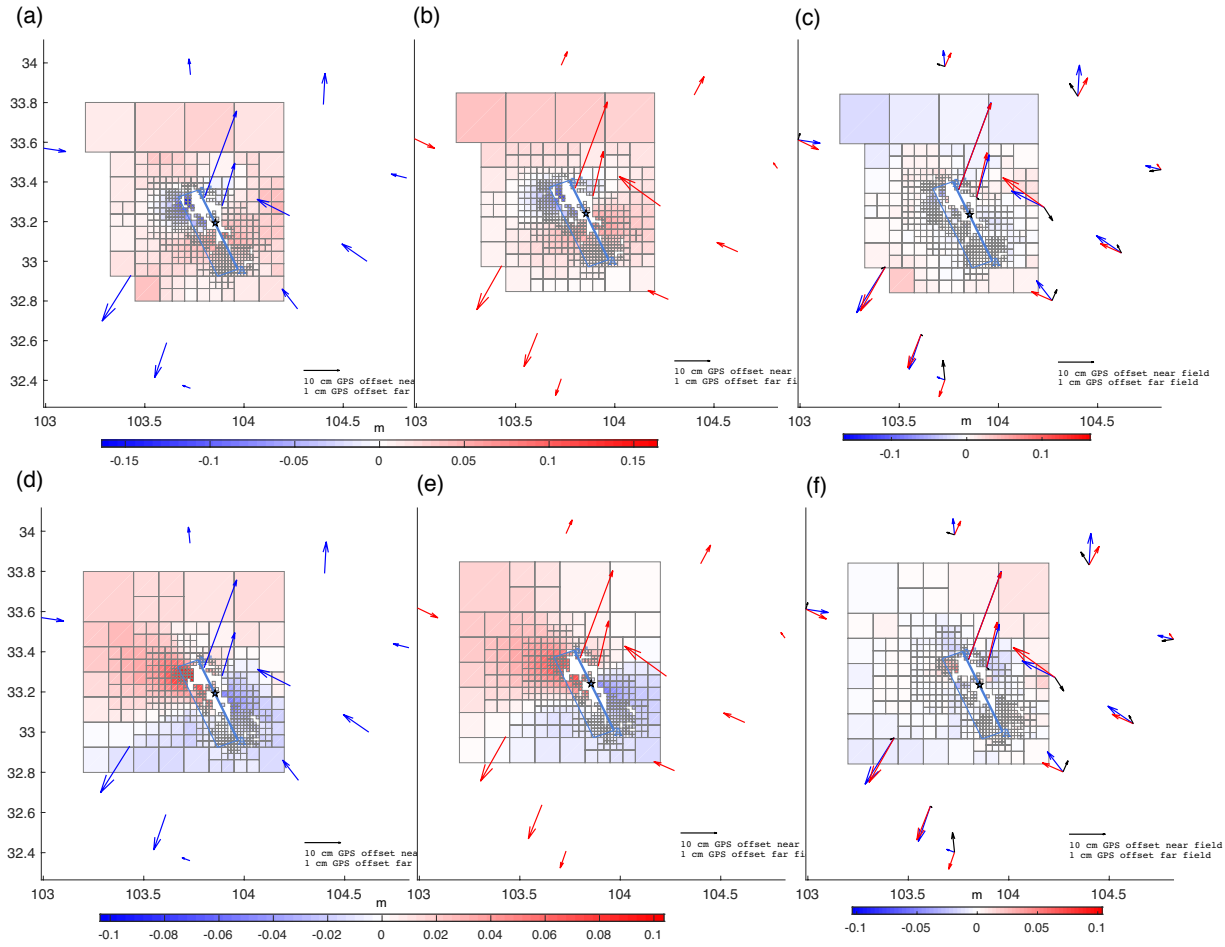


Figure A.12: Comparison of observed and modeled co+postseismic LOS displacements from both ascending and descending Sentinel-1A tracks and GPS offsets. **(a-c)** are observation, model and observed minus modeled residual of plot for ascending orbit T128. **(d-f)** are corresponding plots for descending orbit T62. Blue and red arrows show observed and modeled GPS displacements. J416 and JB33 are considered as near field stations. Note the different scale for near- and far-field motions. The fault plane is drawn as a reference and the upper edges are marked with AA'.

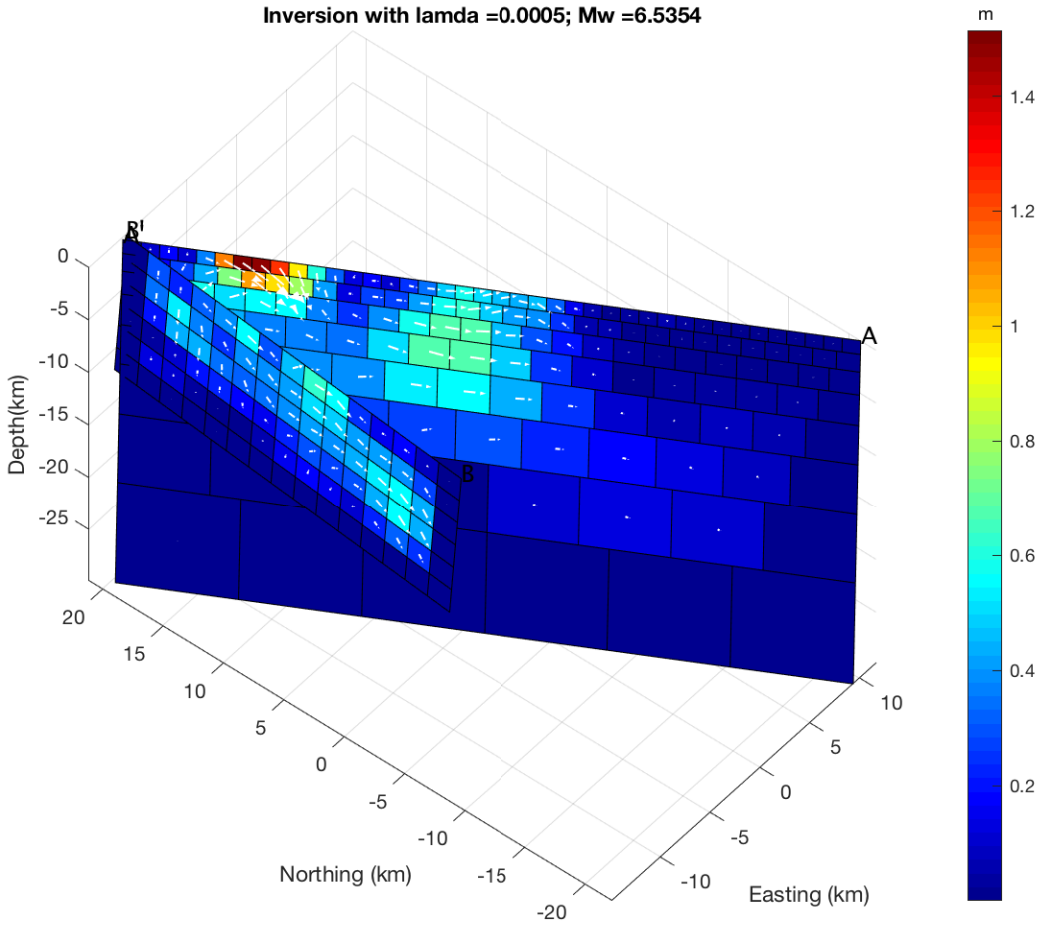


Figure A.13: The inverted slip model with a secondary fault with RMS_{gps}=0.13 cm and RMS_{sar}=0.84 cm, respectively.

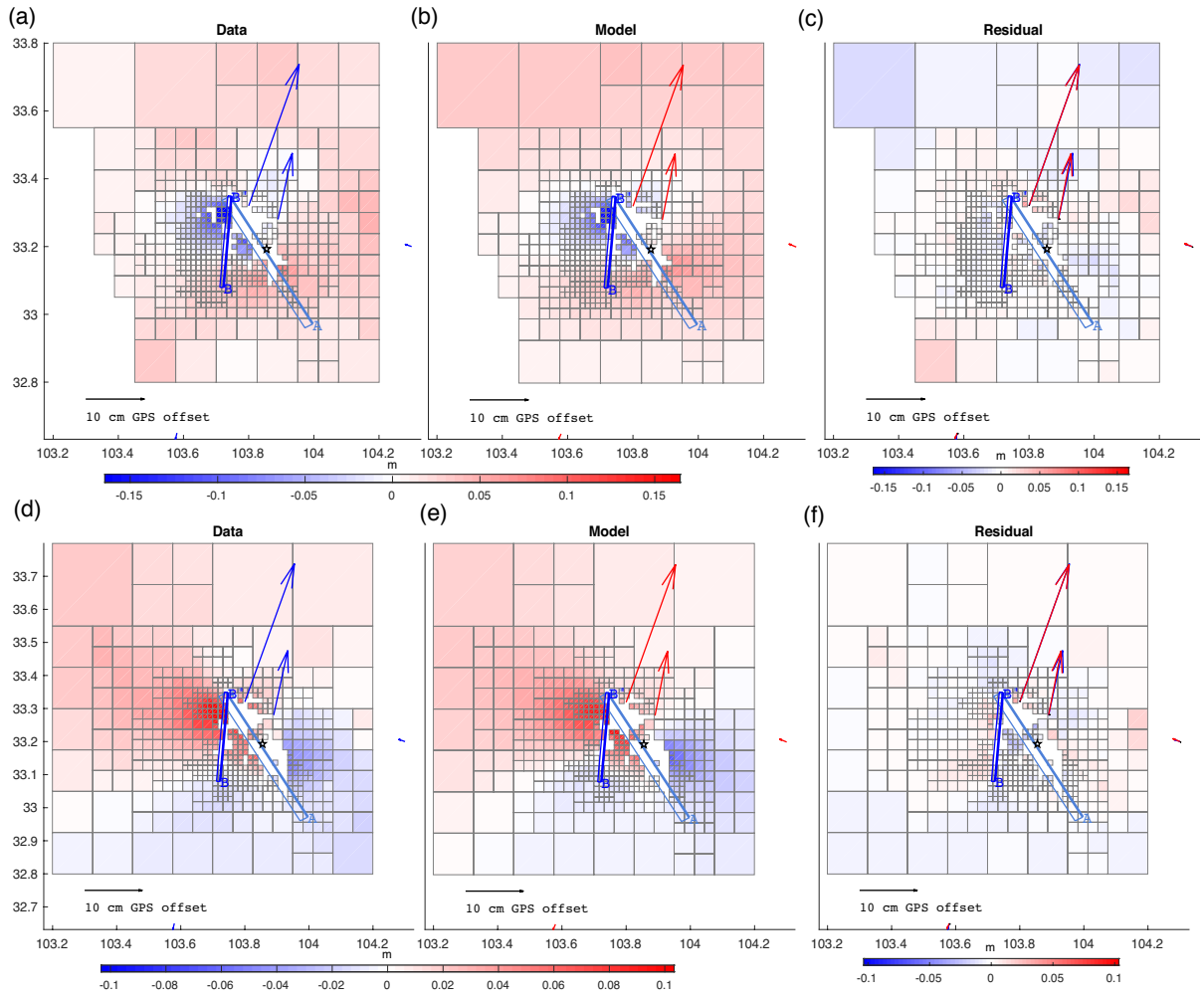


Figure A.14: Comparison of observed and modeled LOS displacements from both ascending and descending Sentinel-1A tracks with GPS for a secondary fault. **(a-c)** are observation, model and observed minus modeled residual of plot for ascending orbit T128. **(d-f)** are corresponding plots for descending orbit T62. The fault plane is drawn as a reference and the upper edges are marked with AA' and BB'.

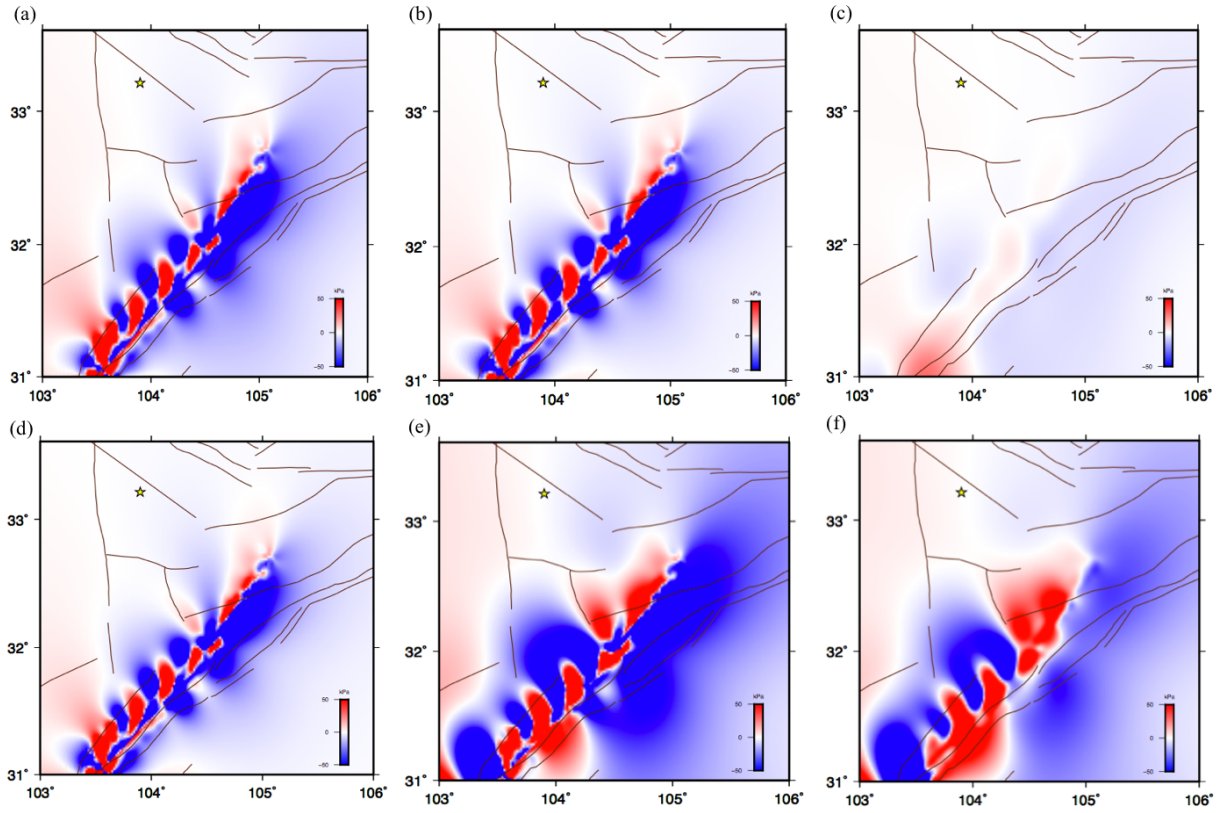


Figure A.15: **(a)** Calculated Coulomb stress change (assuming μ= 0.6), **(b)** Cumulative coseismic elastic and postseismic viscoelastic Coulomb stress change of the 2008 Wenchuan earthquake, and **(c)** Contribution of viscoelastic stress change only caused by the 2008 Wenchuan earthquake at the time of the 2017 Jiuzhaigou earthquake using Diao et al. (2018)'s rheology model. Both co- and postseismic calculations indicate a negative stress change of - 1.004 kPa and -0.772 kPa, respectively, at the mainshock hypocenter. **(d)-(f)** shows similar results with a 15-km-thick elastic upper crust and 10^{17} Pa lower crust viscosity in the Tibetan Plateau, representing a likely upper limit of the effect of the viscoelastic relaxation. Co- and postseismic calculations indicate a negative stress change of -1.116 kPa and -0.605 kPa. All stress changes are projected onto the 2017 Jiuzhaigou earthquake fault plane obtained in this study. The yellow star denotes the epicenter of the 2017 Jiuzhaigou earthquake.

Appendix B

Supporting information for: Partial Coupling and Earthquake Potential along the Xianshuihe Fault, China

The chapter was adapted from the supplement of: Y. Li and R. Bürgmann (2021). "Partial Coupling and Earthquake Potential Along the Xianshuihe Fault, China". *Journal of Geophysical Research: Solid Earth* 126.7. ISSN: 2169-9313. DOI: 10.1029/2020jb021406

B.1 Uncertainty quantification for the velocity maps

The average LOS velocity map is formed by summing the LOS range change and dividing by the total time span. As the number of interferograms used in stacking is quite small (<25 interferograms), and some interferograms are not independent, we use a bootstrapping method to estimate the pixel-by-pixel standard deviation of the stack. The implementation is briefly described below. On each iteration of bootstrapping, we randomly take N samples of the interferograms with replacement (i.e., samples can be selected multiple times), and form a velocity V using Eq 3.2, where N is the number of interferograms that are used in the stacking. After 100 bootstrapping runs, V has been estimated 100 times. We take the standard deviation of the estimated velocities V as the uncertainties of our velocity map products.

The pixel-by-pixel standard deviation of the velocity maps is shown in Figure B.1, where the average standard deviations are 0.63, 0.62, 0.76 mm/yr for D135, D33 and A26.

To further assess the uncertainties of the velocity map, we calculate the velocity difference between D33 and D135 in their overlapping region (Figure B.2). The velocity differences have a standard deviation of 1.17 mm/yr. As the acquisitions from two descending tracks are independent measurements, the standard deviation of the velocity differences is about

$\sqrt{2}$ times of the individual velocity maps (e.g., Walters et al., 2013). Therefore, the mean standard deviation of D33 and D135 is approximately 0.8 mm/yr, close to the values we estimated by bootstrapping.

The uncertainties of the LOS velocity maps can be further used to estimate uncertainties in fault-parallel (u) and vertical motions (w). From Eq 3.3, we can explicitly write out u and w as a function of V_{los_asc} and V_{los_des} (Eq B.1,B.2).

$$\begin{cases} u = \frac{-V_{los\_asc}B' + V_{los\_des}B}{A'B + B'A} \\ w = \frac{V_{los\_asc}A' + V_{los\_des}A}{A'B + B'A} \end{cases} \tag{B.1}$$

$$\begin{cases} \sigma_u = \sqrt{\left(\frac{B'}{A'B+B'A}\right)^2 {\sigma_{v\_asc}}^2 + \left(\frac{B}{A'B+B'A}\right)^2 {\sigma_{v\_\mathrm{des}}}^2} \\ \sigma_w = \sqrt{\left(\frac{A'}{A'B+B'A}\right)^2 {\sigma_{v\_asc}}^2 + \left(\frac{A}{A'B+B'A}\right)^2 {\sigma_{v\_\mathrm{des}}}^2} \end{cases} \tag{B.2}$$

where $A = look_{E\_asc}\sin\theta + look_{N\_asc}\cos\theta$, $B = look_{Z\_asc}$,
$A' = look_{E\_des}\sin\theta + look_{N\_des}\cos\theta$, and $B' = look_{Z\_des}$.

B.2 The influence of profile length and fitting method choices for surface creep rate estimation

The estimated surface creep rate depends on a number of choices. One of the important factors is the choice of the profile section on each side of the fault that is used in the cross-fault offset estimate, including how much data we mask out near the fault trace and the total length of the velocity profile. We explored multiple choices of profile settings varying the mask width and profile-line length from 0.5-1 km, 0.5-1.5 km, 0.5-2 km, 1-2 km, to 1-3 km. The inverted surface creep rates along the XSF using the listed settings are shown in Figure B.3 (a), with selected fitting examples shown in Figure B.3 (b). The result of all profile length choices shows a similar overall along-strike pattern. The choice of how wide a zone to mask out near the fault significantly influences the creep rate estimation. By changing the mask width from 0.5 km to 1 km, the creep rate increases by as much as 50% at ∼175 km along-strike distance. On the other hand, the change of total length of the profile lines does not alter the result that much. This is not surprising because we mainly care about the near fault velocity differences and based on our method stated in the main text, near-fault pixels would have more influence on the creep rate estimate.

Another factor that could affect the estimated creep rate is how the potential step is determined across the fault. We compared two different ways in our study and show the corresponding results in Figure B.3 (c). The first scheme is to conduct a linear regression

of the selected length on each side of the fault, and take the modeled velocity difference at the line-segment tips (solid lines in Figure B.3 (c); e.g., x=±0.5km). The second scheme is simply averaging the velocities of the near-fault data patches and then taking the difference (dashed lines in Figure B.3 (c)). Distributions of the along-strike creep rate estimated by the two schemes have a systematic shift of ∼1 mm/yr.

We ultimately adopted the 0.5-1.5km profile length and the linear-fitting method as our preferred choice, which keeps a balance between the signal to noise ratio, creep rate estimation bias, and possible location ambiguities of the fault trace.

Tracks	Interferogram	Coherence	STD (radians)
T135	20141213_20161220	0.19	1.94
	20150106_20190121	0.13	3.21
	20150130_20190121	0.14	2.62
	20150412_20170308	0.13	2.63
	20150412_20181216	0.11	2.36
	20150506_20181029	0.12	2.01
	20150506_20181122	0.11	2.43
	20150506_20190226	0.11	2.63
	20150506_20190310	0.10	2.24
	20160921_20190521	0.12	4.46
	20161102_20181110	0.15	1.58
	20161220_20181228	0.15	1.82
	20170113_20181204	0.15	1.71
T33	20150111_20170325	0.12	1.59
	20150111_20171202	0.11	2.28
	20150111_20171214	0.11	2.22
	20150111_20181103	0.10	2.26
	20150111_20190102	0.10	2.75
	20150920_20180519	0.11	3.40
	20151201_20170325	0.14	1.46
	20151201_20171202	0.12	2.18
	20151201_20181221	0.10	3.33
	20151201_20190102	0.10	2.66
	20151201_20190126	0.10	2.01
	20160330_20180224	0.11	2.42
	20160610_20180519	0.12	2.21
	20161014_20181010	0.11	2.29
	20141206_20161231	0.17	3.72
	20141206_20170205	0.16	4.06
	20141206_20170217	0.15	4.47
	20141206_20180212	0.12	3.86

	20150216_20180107	0.14	3.50
	20150216_20180119	0.14	4.24
	20150216_20180212	0.13	3.94
	20150511_20190114	0.11	6.35
	20150511_20190303	0.11	5.90
	20151026_20170301	0.12	3.72
	20151119_20190126	0.12	2.09
	20160106_20180308	0.12	1.86
	20160130_20161113	0.15	2.08
	20160130_20181127	0.12	1.58
	20160130_20190102	0.12	1.56
	20160318_20190126	0.11	3.29
	20160318_20190303	0.11	2.73
	20161231_20190114	0.14	2.29
	20171226_20190102	0.16	1.45
	20180308_20181127	0.14	1.98
	20180308_20181209	0.14	2.65

Table B.1: Selected interferograms used to form the average velocity maps.
** Coherence: Average coherence of the whole interferogram.*
** STD: Standard deviation of unwrapped interferogram for the whole image.*

τ (days)	0-1 km swath	1-2 km swath	2-3 km swath	**1-3 km swath**	3-5 km swath
Northern Segment	>5000	2500	1500	**2500**	1500
Central Segment	100	150	250	**200**	500
Southern Segment	100	150	150	**150**	200

Table B.2: Best-fitting characteristic decay times for time series differences taken from multiple swaths at variable distances from the fault.

ID	Year	Magnitude	Center Location (Lat/Lon)	Rupture Length (km)	Reference
1*	1700	>M 6.5	(30.36, 101.79)	35?	[1]
2*	1725	M 7	(30.16, 101.83)	50	[1]
3	1747	M 6.75	(31.23, 100.85)	>30	[1]
4	1748	M 6.5	(30.33, 101.62)	35	[1]
5*	1786	M 7.75	(29.87, 102.04)	90	[1]
6	1792	M 6.75	(31.06, 101.00)	>25	[1]
7	1793	>M 6	(30.75, 101.33)	Limited	[1]
8*	1811	M 6.75	(30.61, 100.15)	15	[1]
9	1816	M 7.5	(31.29, 100.75)	>60	[1]
10	1893	M 7	(30.70, 101.37)	70	[1]
11	1904	M 7	(31.06, 101.00)	55	[1]
12	1923	M 7.3	(31.17, 100.90)	60	[1]
13	1955	M 7.5	(30.03, 101.84)	35	[1]
14*	1967	M 6.8	(31.62, 100.20)	18	[1]
15	1973	M 7.6	(31.50, 100.52)	90	[1]
16	1981	M 6.9	(30.95, 101.15)	45	[1]
17	2011	Ms5.4	(31.20, 100.80)	Limited	[2], this study
18	2014	Mw5.9	(30.29, 101.68)	18	[2], this study
19	2014	Mw5.6	(30.20, 101.75)	9	[2], this study

Table B.3: List of historical (M>6) and recent (M>5 since 2010) earthquakes along the XSF. Note: References for earthquake magnitude, rupture extent and rupture center locations are [1] Wen et al. (2008) and [2] Chinese Earthquake Networks Center (CENC, http://www.ceic.ac.cn/). The rupture lengths for ID 17∼19 are estimated in this study.
** Earthquakes occurred on fault segments that are not included in our model and are therefore not included in Figure 3.8a.*

Asperity ID	Dataset	Reference
A0	Historical EQ	Wen et al., 2008
A1	InSAR*, GPS, viscoelastic modeling	Jiang et al., 2015a
A2	InSAR*, GPS, viscoelastic modeling	Jiang et al., 2015a
A3	InSAR*, GPS, viscoelastic modeling	Jiang et al., 2015a
A4	Microseismicity	Yi, 2005
A5	Microseismicity	Zhang et al., 2018b
A6	Microseismicity	Zhang et al., 2018b
S1	Historical EQ, InSAR	This study
S2	Historical EQ, InSAR	This study

Table B.4: List of identified asperities along the XSF. Note the InSAR data used in Jiang et al., 2015a was taken from Wang et al., 2009, which covers only the NW section of XSF.

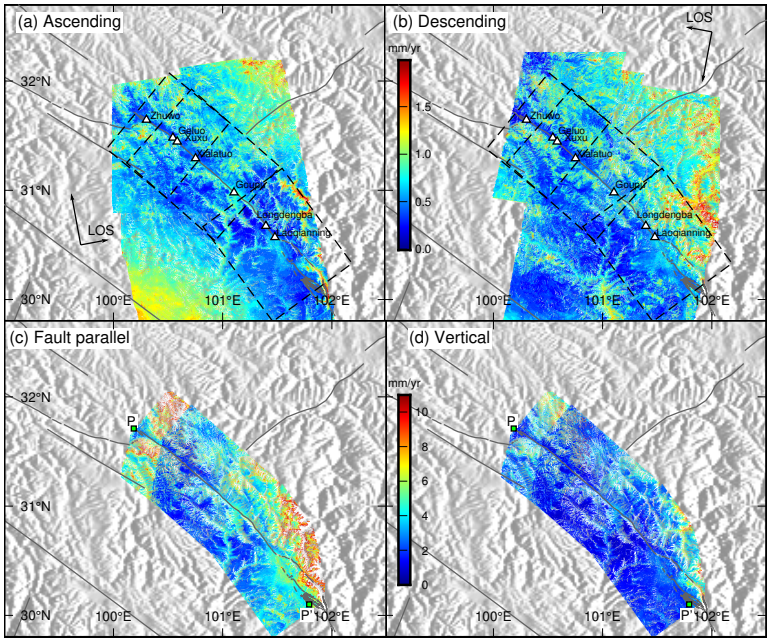


Figure B.1: Estimated uncertainties of the velocity maps for **(a)** ascending track 26, **(b)** descending tracks 33 and 135, **(c)** derived fault-parallel, and **(d)** vertical velocity fields along the XSF region. The bootstrapping methodology to derive the uncertainties is described in Section B.1.

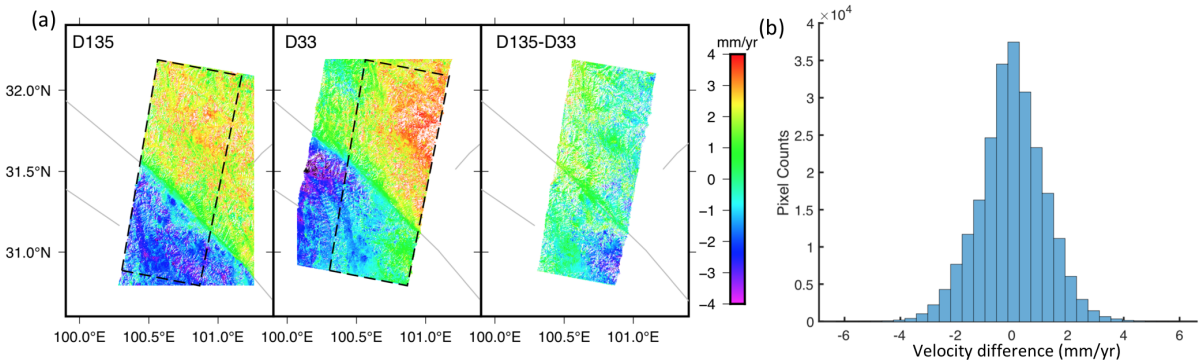


Figure B.2: **(a)** Comparison of the velocity maps in the overlapping region of descending tracks 33 and 135. **(b)** Histogram of the velocity differences in the overlapping region (σ=1.17 mm/yr).

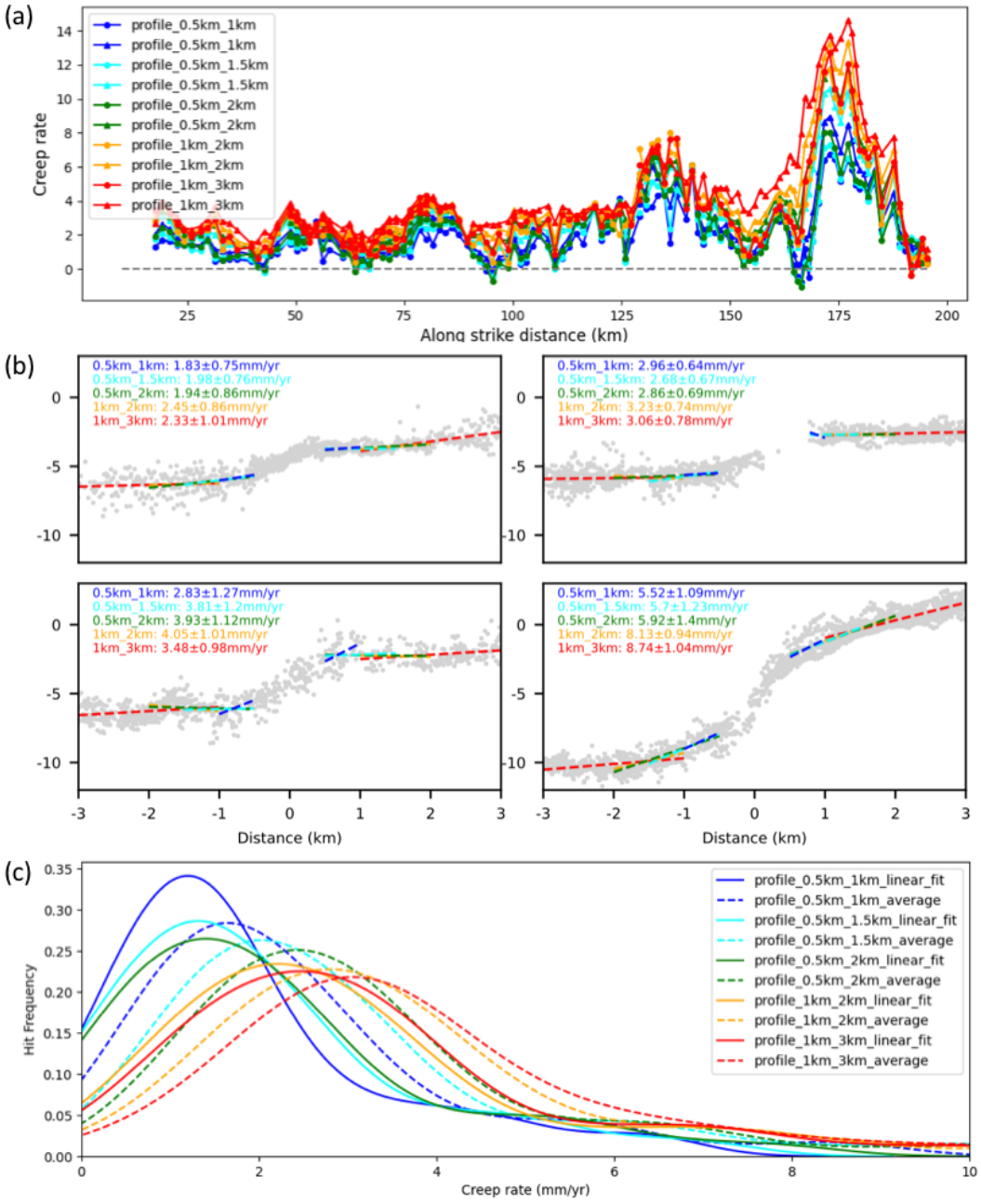


Figure B.3: **(a)** Comparisons of surface creep rates along the XSF estimated by multiple profile settings. **(b)** Examples of fault-perpendicular velocity profiles and their fittings for different profile lengths. **(c)** Distributions of the along-strike surface creep rate estimated by either averaging or linear fitting of the profile sections for each profile length.

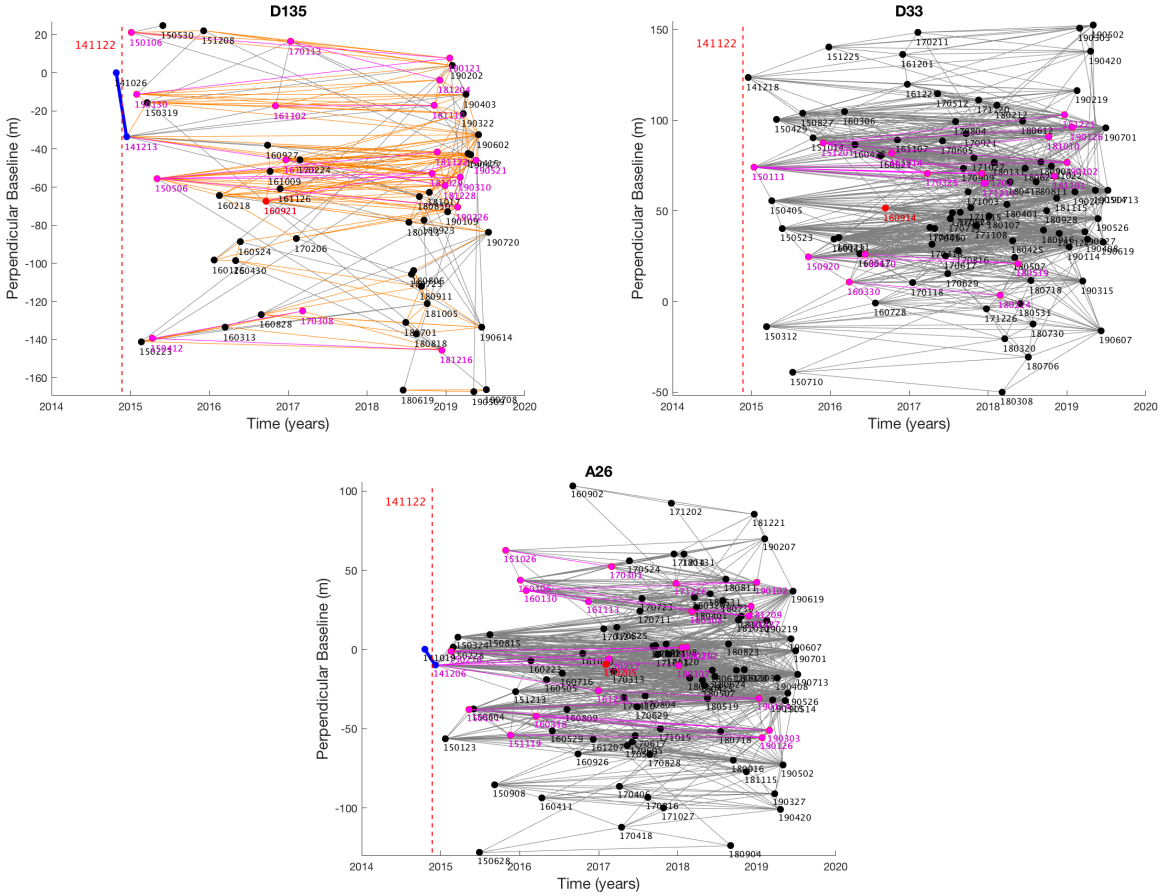


Figure B.4: **(a)-(c)** Interferogram network for tracks D33, D135 and A26 for co- and post-seismic deformation used in this study. Each acquired scene is marked as a solid circle and all interferograms generated in this study are marked as lines. For each track, all scenes are aligned to a single super-reference image that is colored in red. The selected interferograms for the velocity map formation (Figure 3.4) are colored in magenta. For D135, interferograms with STD<3 that are used in the time series analysis are colored in orange. The coseismic interferograms are shown by bold blue lines. The date of the Mw5.9 Kangding earthquake is marked by red dashed line.

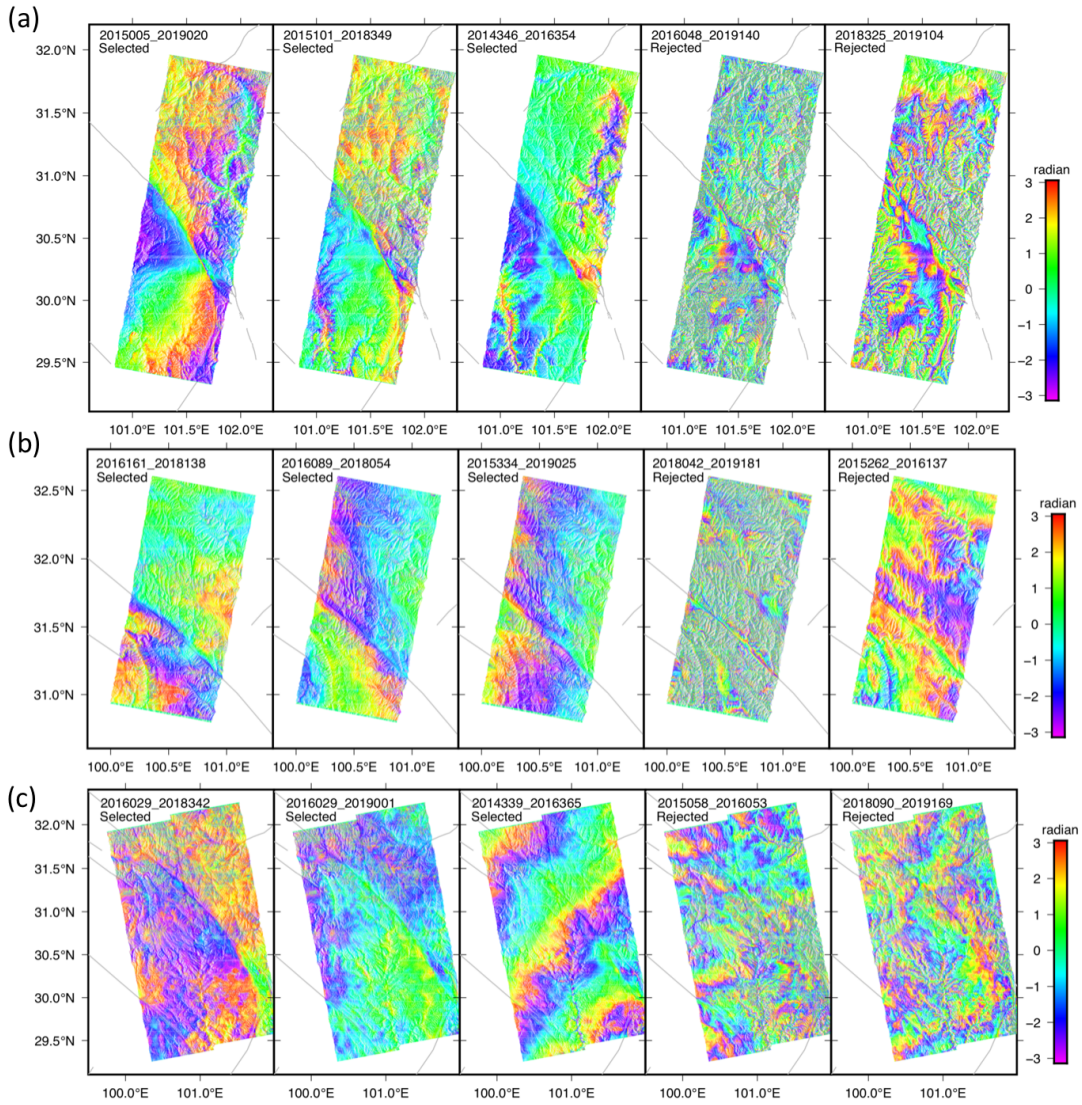


Figure B.5: Examples of selected and rejected interferograms for **(a)** descending track T135F2, **(b)** descending track T33, and **(c)** ascending track T26. Dates used to form the interferograms are shown at the top of each panel.

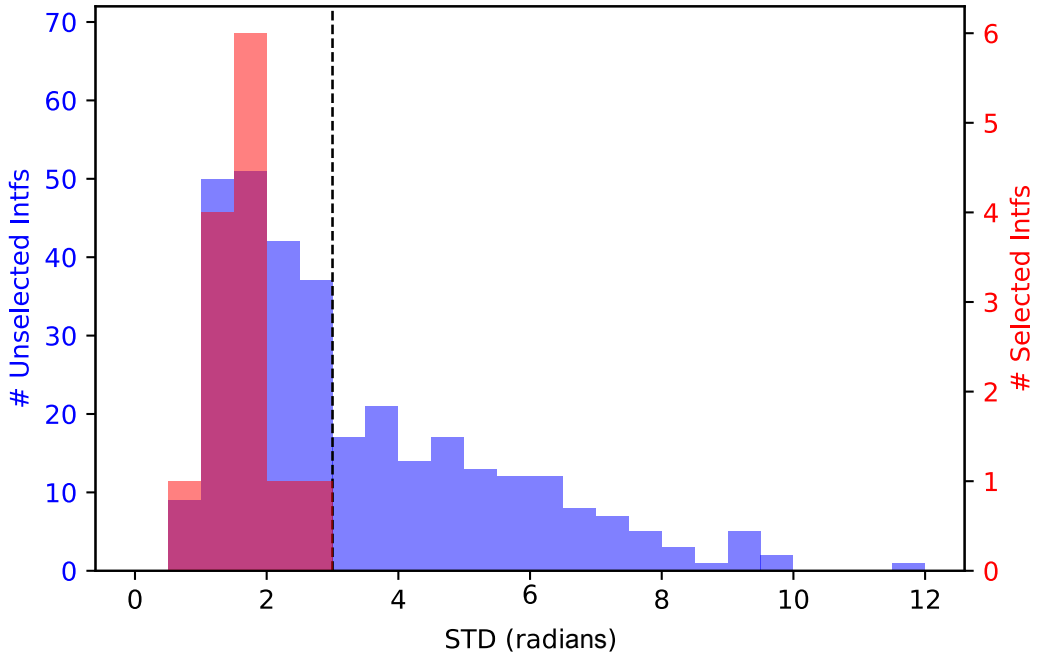


Figure B.6: Histogram of the standard deviation (STD) of selected and rejected unwrapped interferograms for D135F2.

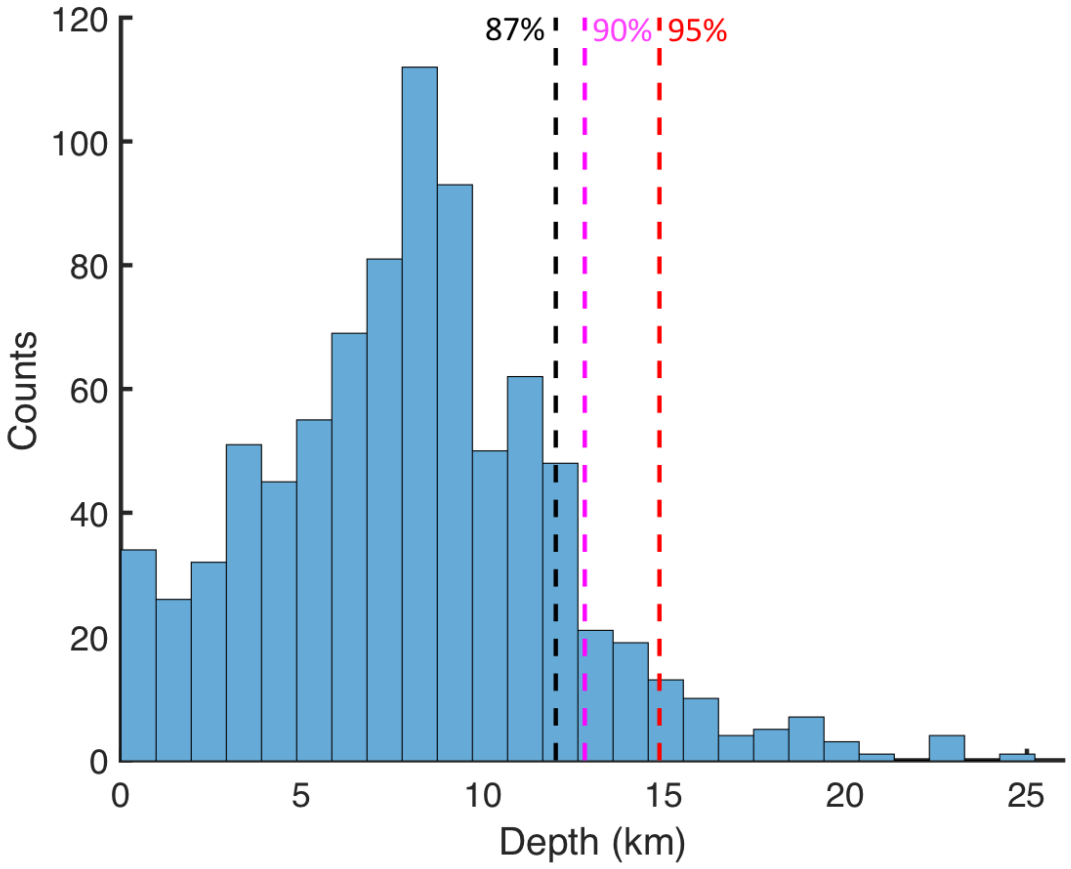


Figure B.7: Histogram of hypocenter depths of M≥1.5 earthquakes within 10 km of the XSF from China Seismic Experiment (2009-2019; Wu et al., 2019. Black, magenta and red dashed lines show the 87%, 90% and 95% seismicity cut-off depths, respectively.

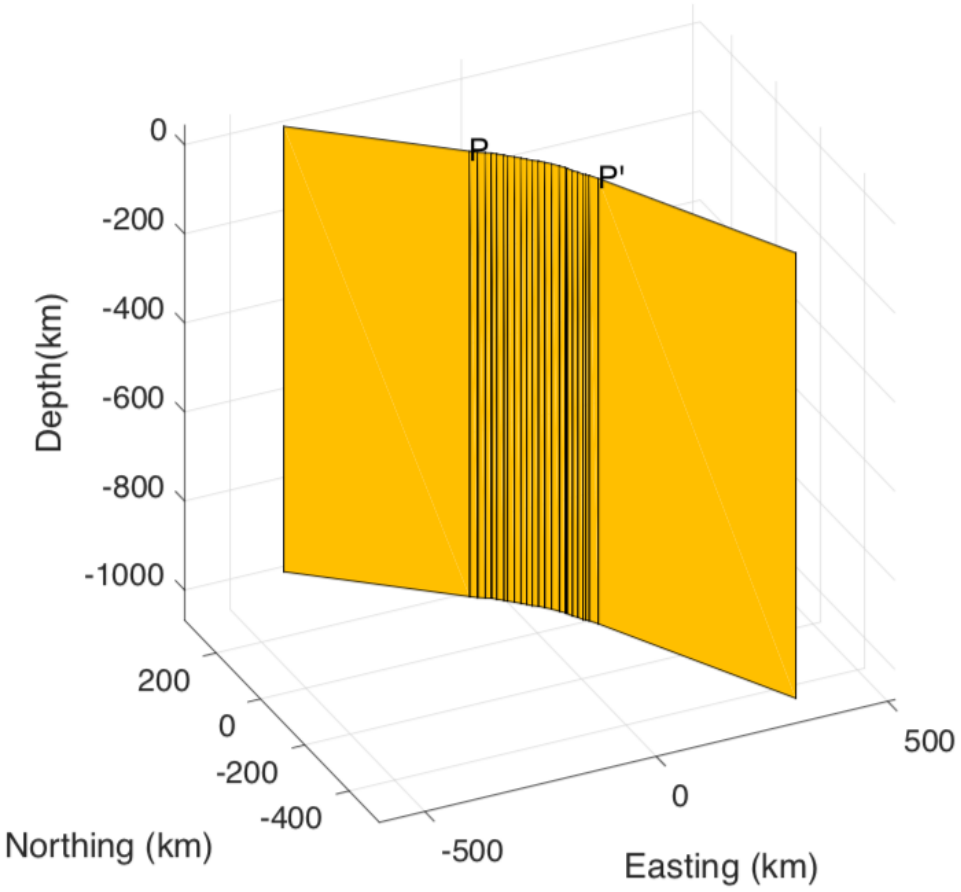


Figure B.8: Geometry of the deep dislocation model. PP' indicates the extent of the shallow slip model. The deep dislocation model consists of a series of 1000-km-wide dislocations slipping at 12.1 mm/yr below 12 km along the XSF, with lateral extensions that go far beyond the fault tips.

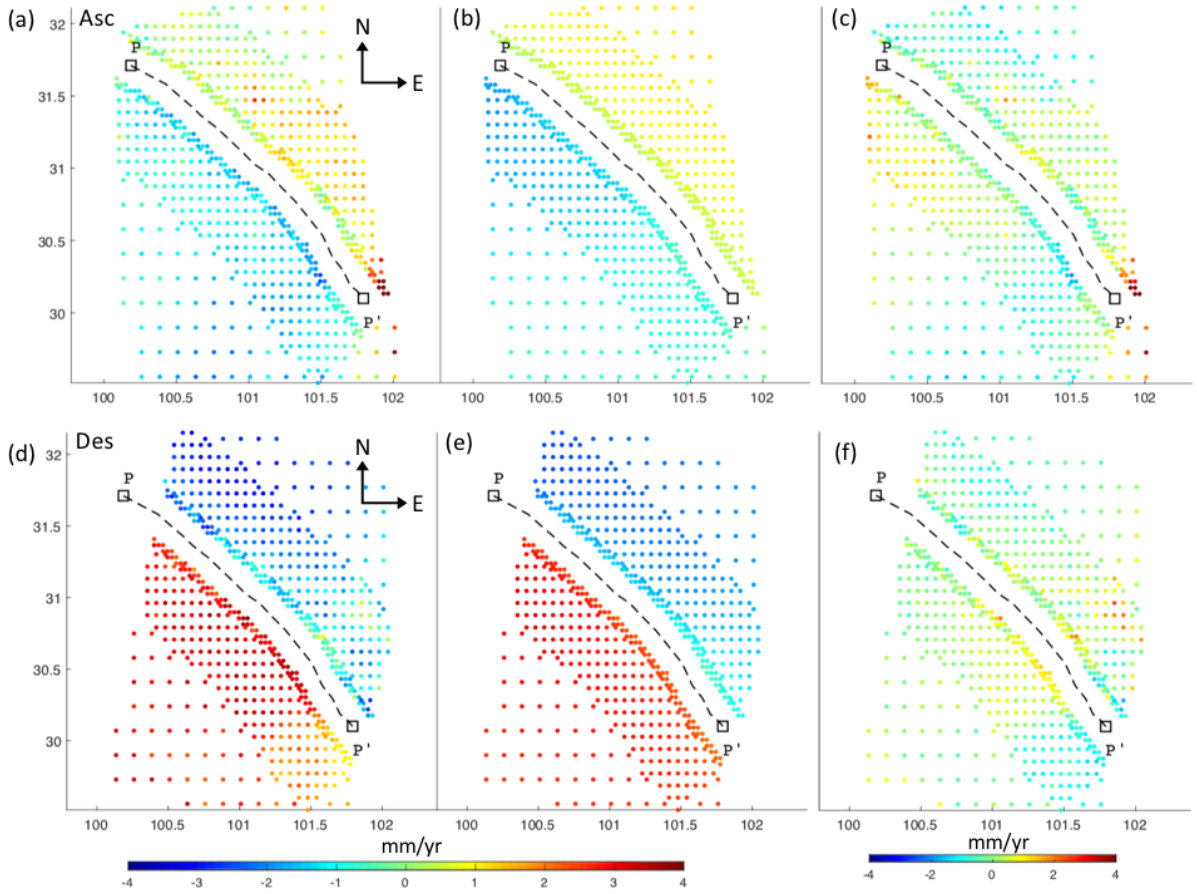


Figure B.9: Comparison of downsampled observed and modeled long-wavelength LOS velocities from ascending and descending Sentinel-1 viewing geometries. The deep-dislocation model geometry is shown in Figure B.8. **(a-c)** are observed, modeled, and observed-minus-modeled residuals for ascending track 26. **(d-f)** are corresponding maps for descending orbit 135. Note that near-fault data within 15 km of the XSF are masked out when inverting for the deep slip rate of 12.1 $\pm$ 0.7 mm/yr.

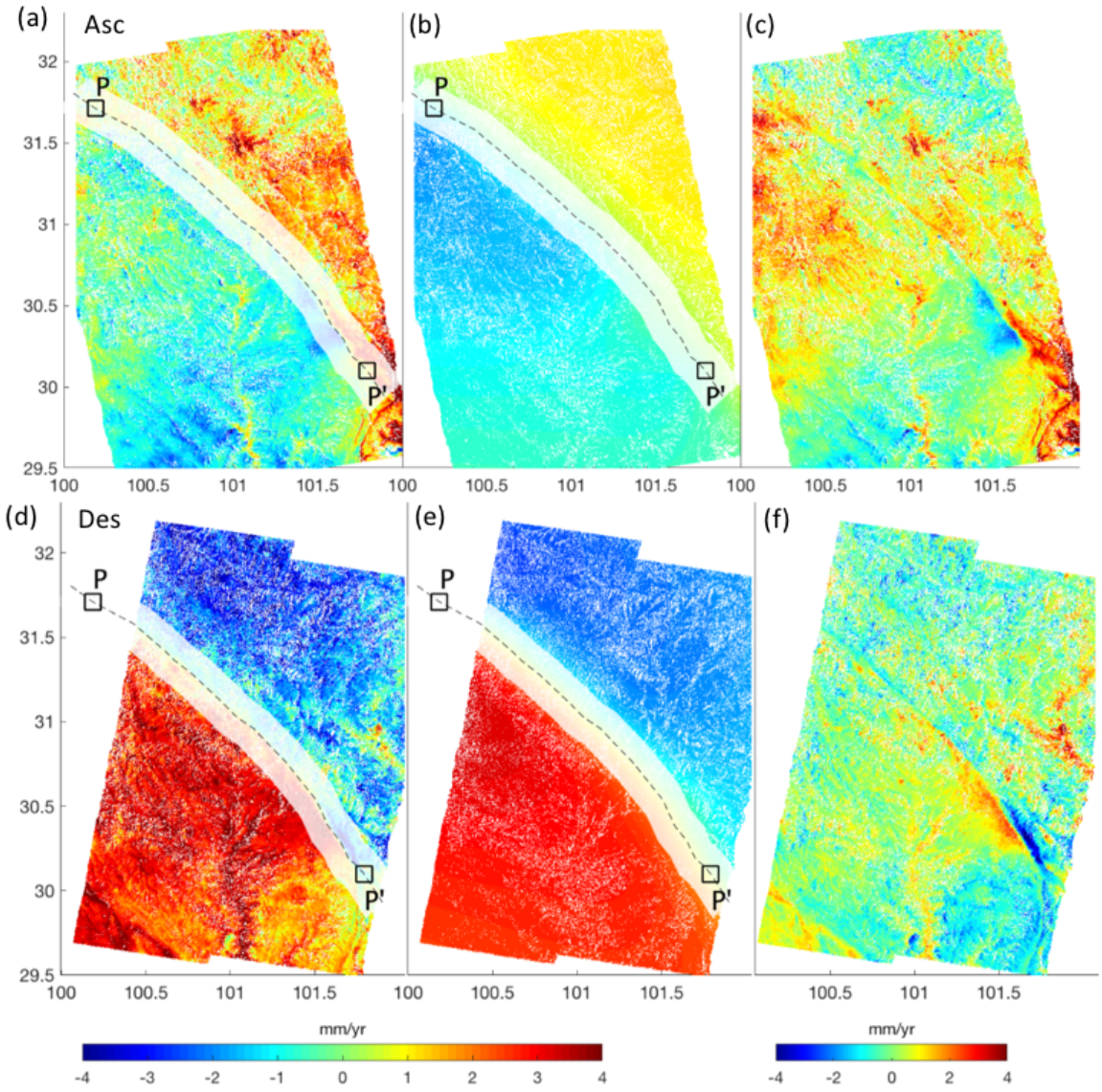


Figure B.10: Deep dislocation model and residual maps. **(a-c)** are observed, modeled, and residuals for ascending track 26 (same as in Figure B.9 but shown without downsampling used in the model inversion). **(d-f)** are corresponding maps for descending orbit 135. Note that data from within 15 km of the fault are masked out when inverting for the deep slip rate but are shown in the residual maps. The residual velocities shown in **(c)** and **(f)** are used to invert for the aseismic slip distribution above 12 km (Figures 3.7 and 3.8).

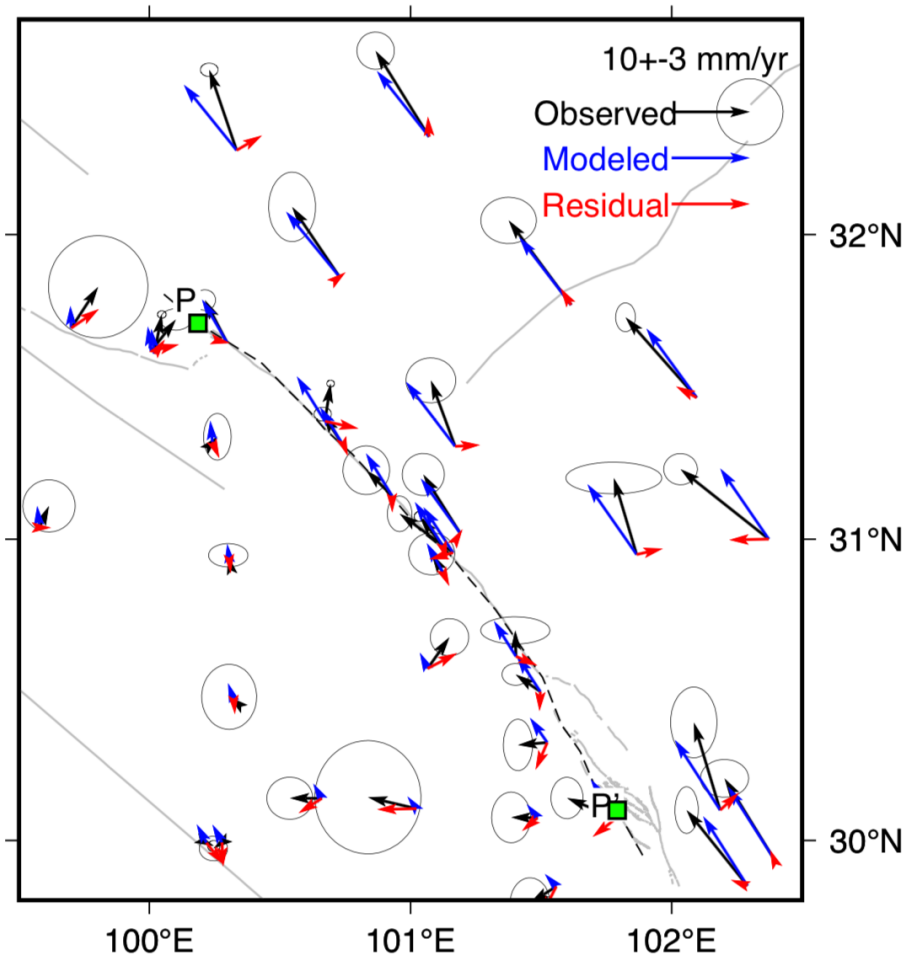


Figure B.11: Comparisons of observed and modeled GPS velocities using the derived deep dislocation model. Black, blue and red vectors show the observed, modeled, and observed-minus-modeled residual velocities, respectively. GPS velocities are relative to Yajiang sub-block and tipped with 95% confidence ellipses (Zheng et al., 2017). The modeled fault trace is shown in black dashed lines.

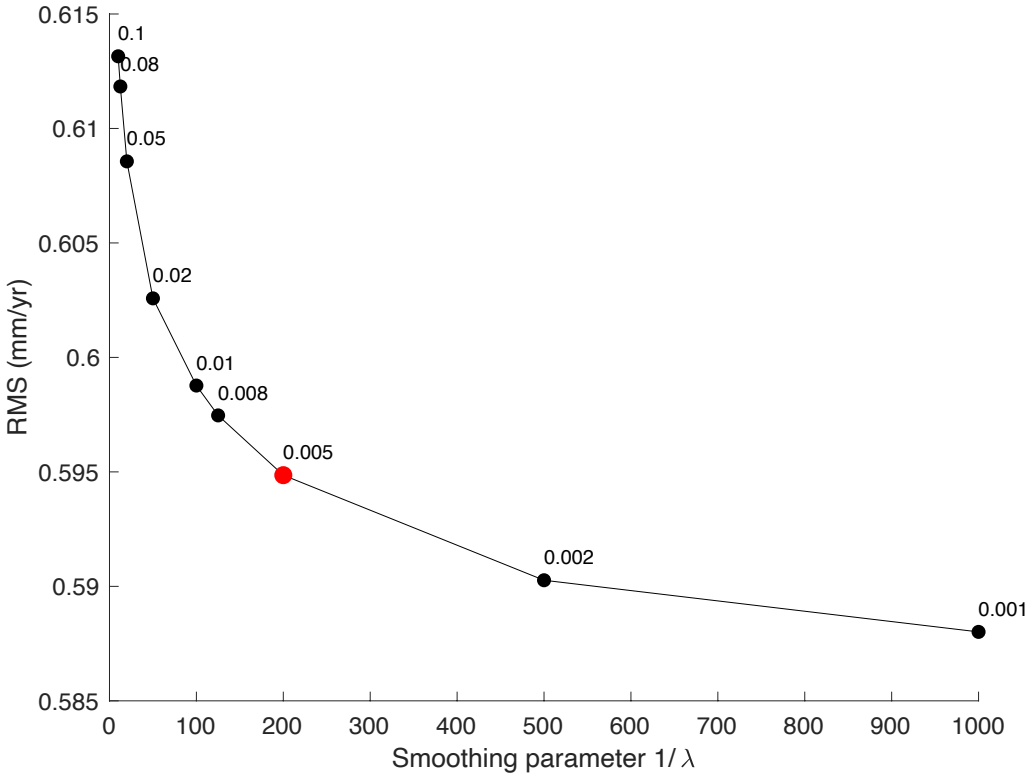


Figure B.12: Trade-off curve for smoothing parameters of the shallow slip inversion. We use 0.005 as our preferred smoothing parameter in the inversion.

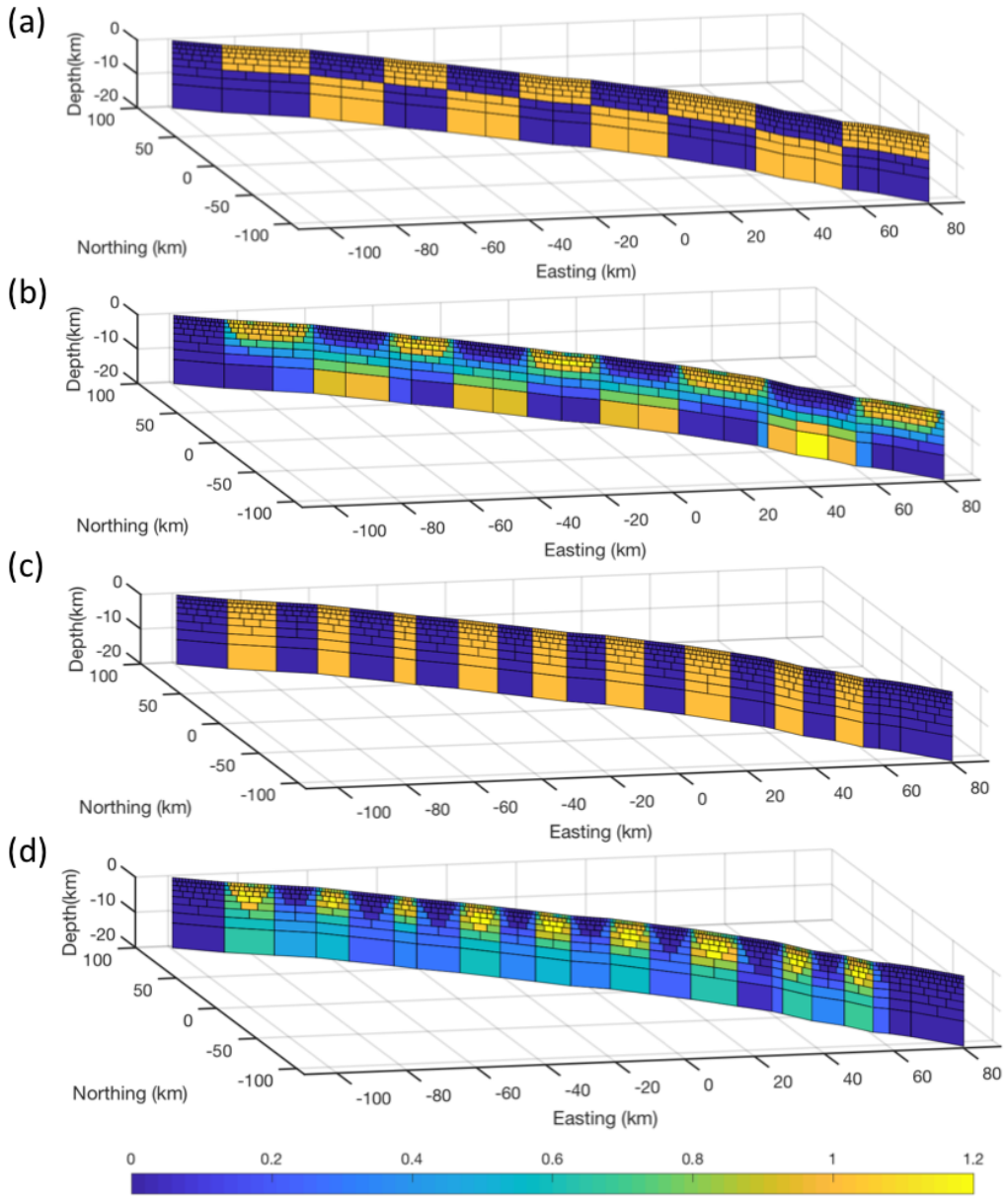


Figure B.13: Checkerboard tests for the model resolution using the preferred smoothing parameter of 0.005. **(a)**, **(c)** show input unit slip patterns, and **(b)**, **(d)** show the output slip patterns for **(a)**, **(c)**, respectively.

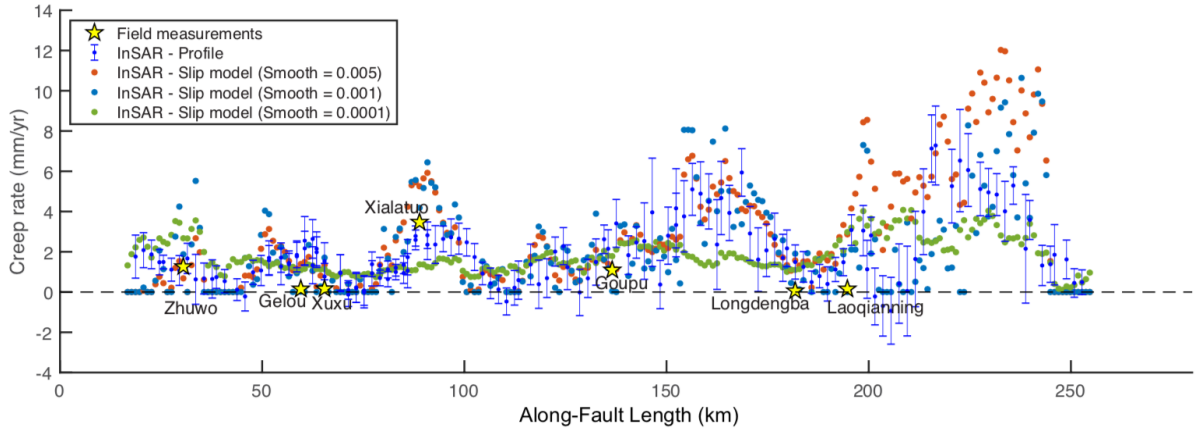


Figure B.14: Comparisons of surface creep rate derived from the distributed-creep model by varying the smoothing parameters in the inversion.

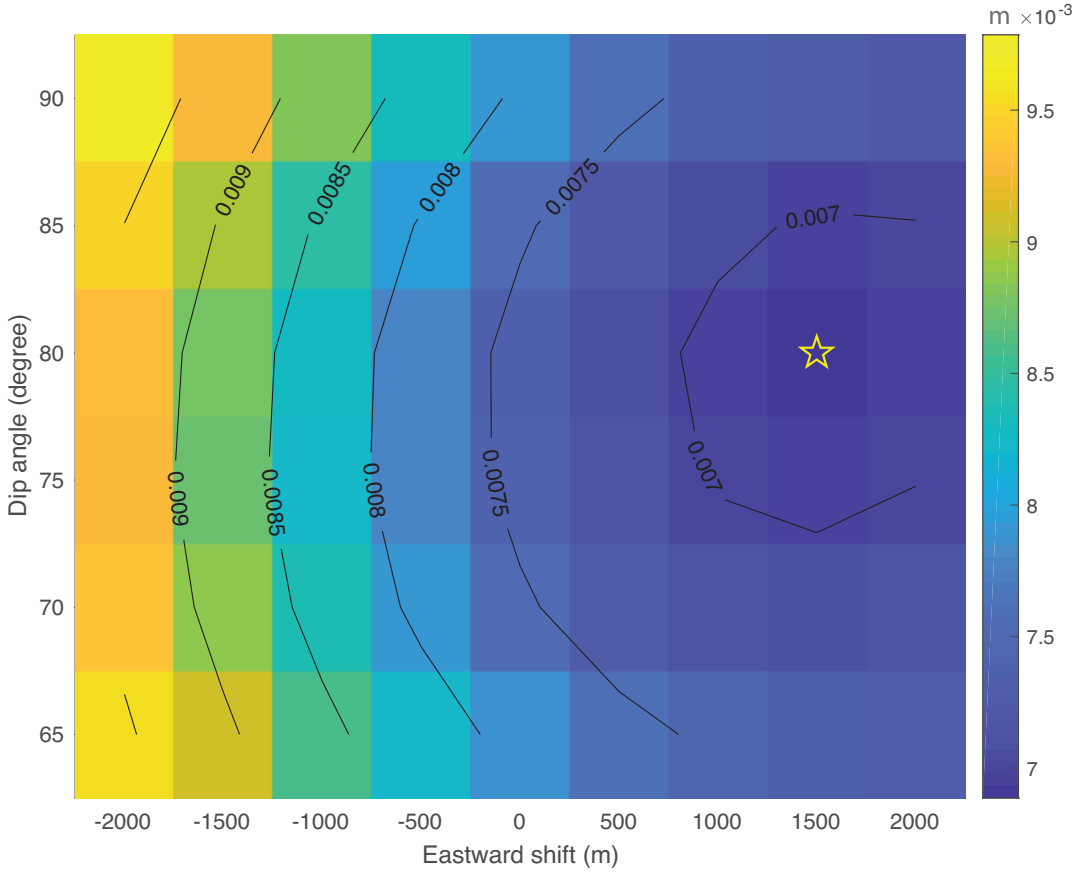


Figure B.15: Residual (RMS) plot for the coseismic slip model for ranges of locations of the surface trace and variable dip angles of the Mw5.9 rupture plane.

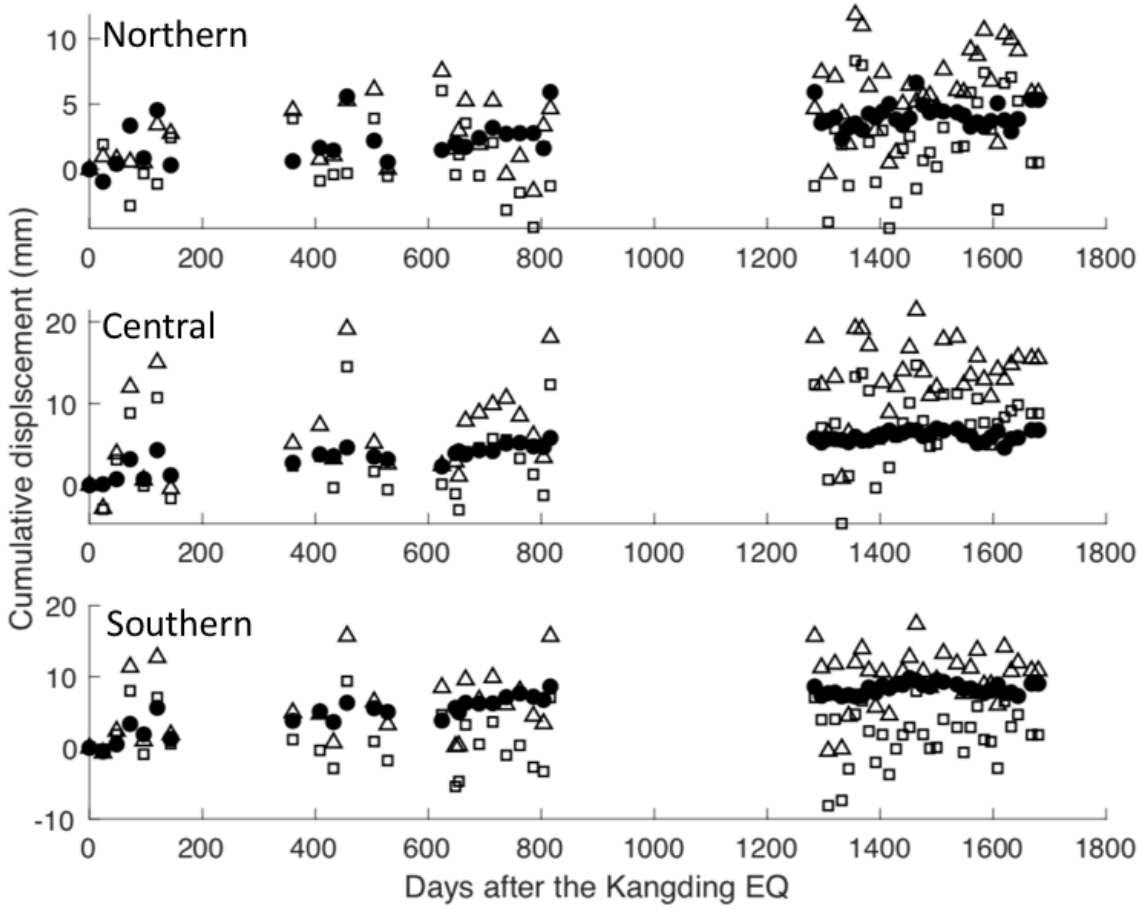


Figure B.16: Stacked averaged LOS time series and the cross-fault time series differences for descending track 135 along the northern, central and southern fault sections. Black triangles and squares show the averaged cumulative displacement at patches west and east of the fault, respectively. Black solid circles show their cross-fault differences. Note the data gap between ∼800-1300 days is due to lack of Sentinel-1 acquisitions of descending track 135.

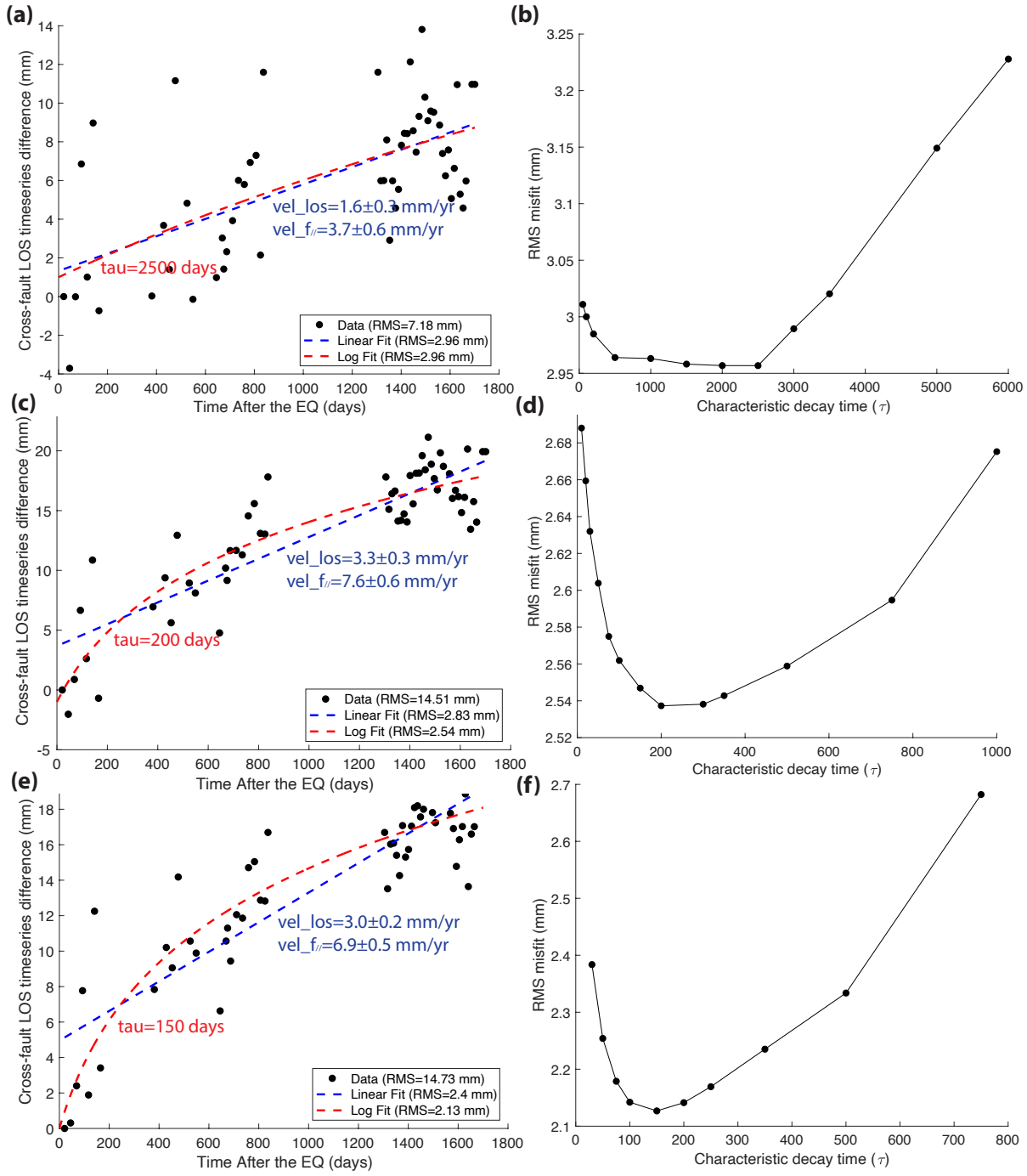


Figure B.17: Stacked averaged LOS cross-fault time series differences (see Figure B.16S) along the **(a)** northern, **(c)** central and **(e)** southern fault sections with the linear and log-decay fittings that minimize the RMS misfit. Relationship between the RMS misfit and chosen characteristic decay time (τ) for the corresponding segments are shown in **(b)**, **(d)** and **(f)**.

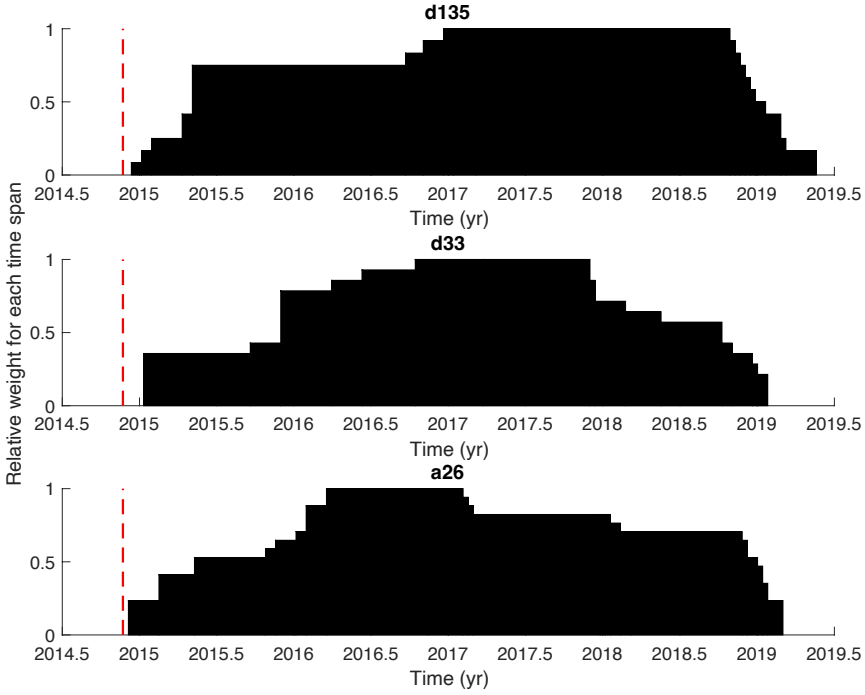


Figure B.18: The normalized weight of time-spans that are used in the average velocity map formation for **(a)** descending track 135, **(b)** descending track 33, and **(c)** ascending track 26.

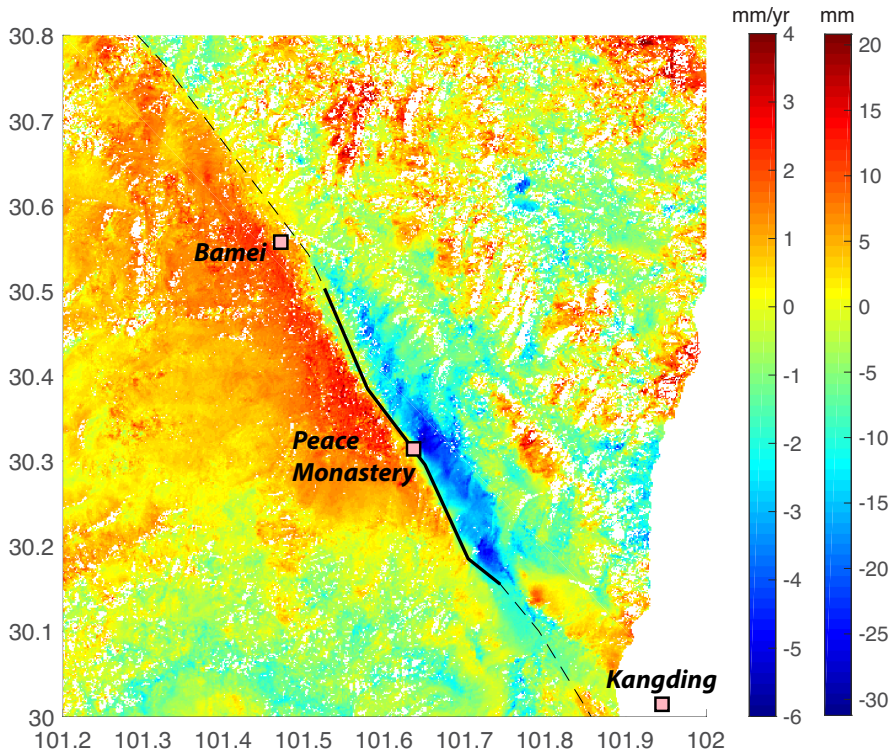


Figure B.19: A zoom-in map of the average velocity map of descending track 135. Positive values indicate LOS motions towards the satellite, and vice versa. The data and region are outlined in Figure 3.7d. Colorbar to the left shows the LOS velocity and colorbar to the right shows the reconstructed cumulative displacement map from the average velocity map by multiplying the average velocity map with a scaling factor of 5.20.

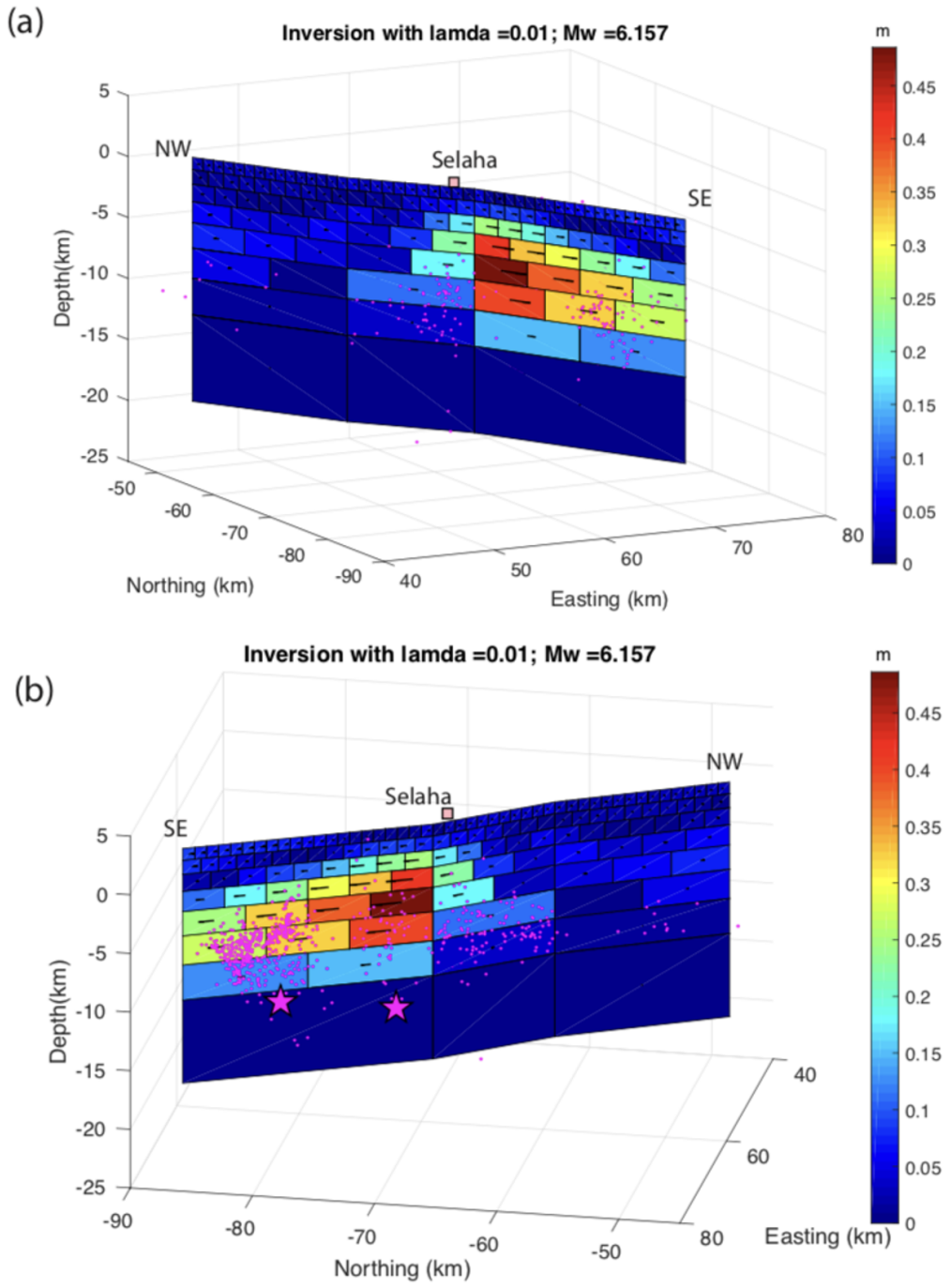


Figure B.20: Simplified coseismic slip model using the fault geometry of the SE section of the coupling model. Magenta stars show the hypocenters of the two largest events and magenta dots show the first 24 days of relocated aftershocks of the 2014 Kangding earthquake sequence (Fang et al., 2015). The location of Selaha B. is 101.64°E, 30.31°N.

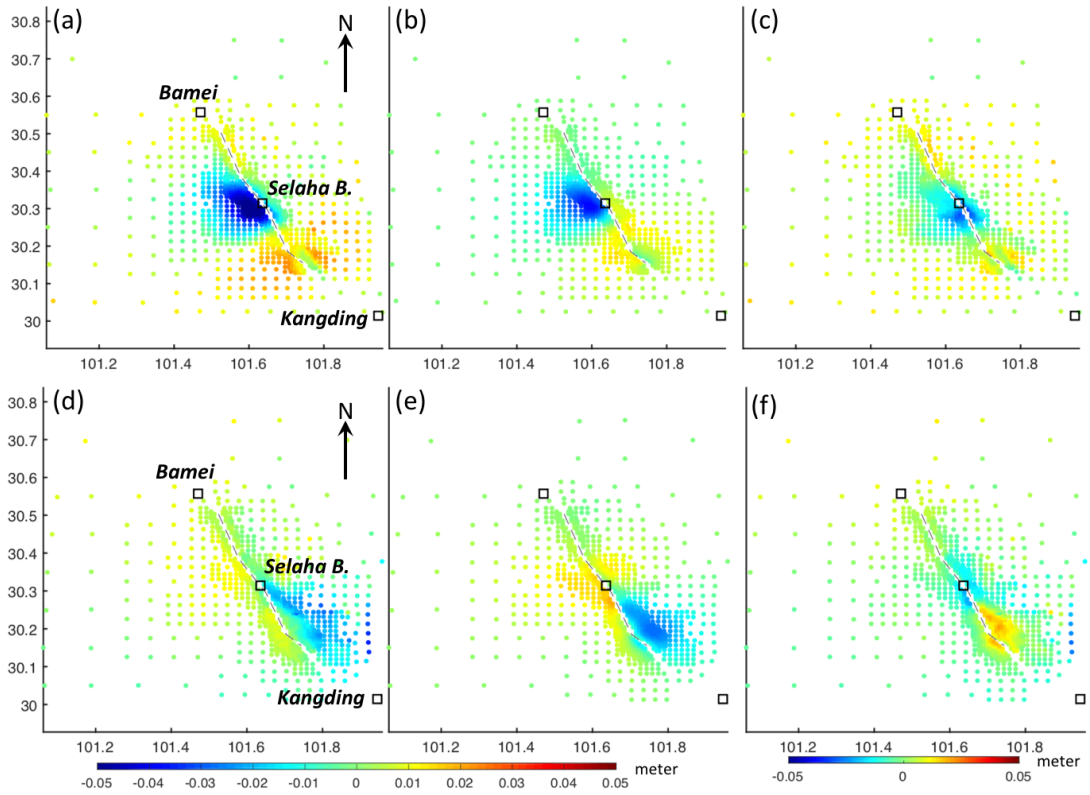


Figure B.21: Comparison of observed and modeled coseismic deformation of Kangding earthquake from both ascending and descending Sentinel-1 geometries using the fault geometry of the SE section of the coupling model. Positive values indicate LOS motions towards the satellite, and vice versa. **(a-c)** are observed, modeled, and observed-minus-modeled residuals for ascending track 26. **(d-f)** are corresponding maps for descending orbit 135. Black dashed lines indicate surface traces of the fault rupture model in Figure B.20. The location of Selaha B. is 101.64°E, 30.31°N.

Appendix C

Supporting information for: Spatiotemporal variations of surface deformation, shallow creep rate, and slip partitioning between the San Andreas and southern Calaveras Fault

The chapter was adapted from the supplement of: Y.Li, R. Bürgmann and T. Taira (2022). "Spatiotemporal variations of surface deformation, shallow creep rate, and slip partitioning between the San Andreas and southern Calaveras Fault". doi: https://doi.org/10.1002/essoar.10512336.1. *(Under review at Journal of Geophysical Research: Solid Earth)*

Fault Name	Longitude (°)	Latitude (°)	InSAR LOS Rate (mm/yr)	Dextral Rate (mm/yr)	Dextral Uncertainty (mm/yr)
SAF	-121.033	36.448	9.399	18.832	5.410
SAF	-121.046	36.461	8.551	17.099	4.659
SAF	-121.059	36.474	6.381	12.738	4.092
SAF	-121.072	36.486	6.972	13.892	3.387
SAF	-121.085	36.499	8.768	17.085	3.566
SAF	-121.098	36.512	8.303	16.105	4.209
SAF	-121.112	36.525	8.743	16.926	4.298
SAF	-121.126	36.538	7.695	14.869	3.768

SAF	-121.140	36.550	5.914	11.406	1.813
SAF	-121.154	36.563	6.370	12.201	3.486
SAF	-121.168	36.576	5.456	10.173	2.852
SAF	-121.183	36.589	6.586	12.253	3.647
SAF	-121.199	36.602	6.828	12.691	3.513
SAF	-121.214	36.614	7.058	13.133	3.051
SAF	-121.229	36.627	6.042	11.220	3.305
SAF	-121.244	36.640	6.469	11.989	2.446
SAF	-121.259	36.653	6.679	12.353	2.589
SAF	-121.274	36.666	6.544	12.080	2.511
SAF	-121.289	36.678	6.248	11.512	3.814
SAF	-121.304	36.691	6.957	12.375	4.909
SAF	-121.322	36.704	7.734	13.650	4.553
SAF	-121.339	36.717	6.231	10.973	4.315
SAF	-121.357	36.730	6.953	12.091	3.982
SAF	-121.375	36.742	4.143	7.003	3.246
SAF	-121.396	36.755	3.580	6.036	4.081
SAF	-121.417	36.768	4.174	7.021	4.659
SAF	-121.438	36.781	nan	nan	3.574
SAF	-121.480	36.806	3.472	5.948	4.420
SAF	-121.498	36.819	2.555	4.367	3.180
SAF	-121.517	36.832	4.176	7.179	4.057
SAF	-121.534	36.845	3.246	5.581	3.817
SAF	-121.552	36.858	1.453	2.493	3.878
SAF	-121.570	36.870	0.685	1.173	3.613
SAF	-121.587	36.883	1.646	2.814	3.862
SAF	-121.605	36.896	-0.621	-1.043	6.472
SAF	-121.624	36.909	0.360	0.590	3.882
SAF	-121.645	36.922	0.785	1.287	4.952
SAF	-121.666	36.934	1.649	2.880	6.443
SAF	-121.681	36.947	0.660	1.151	6.938
SAF	-121.896	37.101	-0.438	-0.736	6.707
SAF	-121.914	37.114	0.320	0.537	6.762
SAF	-121.932	37.126	nan	nan	5.846
CF	-121.510	37.062	-0.475	-1.103	5.180
CF	-121.518	37.075	1.840	4.271	5.755
CF	-121.525	37.088	1.258	2.749	5.200
CF	-121.534	37.101	1.275	2.618	3.243
CF	-121.544	37.114	2.806	5.752	3.485

CF	-121.555	37.126	1.737	3.363	3.136
CF	-121.566	37.139	2.791	5.110	2.856
CF	-121.580	37.152	1.893	3.460	2.888
CF	-121.594	37.165	3.772	7.004	3.138
CF	-121.607	37.178	2.372	4.554	3.647
CF	-121.618	37.190	1.255	2.406	3.566
CF	-121.630	37.203	2.284	4.372	2.508
CF	-121.642	37.216	2.657	5.079	2.619
CF	-121.654	37.229	2.798	6.454	3.068
CF	-121.661	37.242	3.217	9.400	5.435
CF	-121.666	37.254	1.300	3.796	5.051
CF	-121.671	37.267	1.684	4.913	4.698
CF	-121.676	37.280	-0.038	-0.112	4.404
CF	-121.688	37.306	0.122	0.276	3.306
CF	-121.696	37.318	0.722	1.485	3.477
CF	-121.706	37.331	0.314	0.644	3.001
CF	-121.715	37.344	1.075	2.208	3.244
CF	-121.725	37.357	0.918	1.882	2.584
CF	-121.735	37.370	0.181	0.360	2.810
CF	-121.745	37.382	0.624	1.214	3.149
CF	-121.756	37.395	0.943	1.690	3.082
CF	-121.770	37.408	1.957	3.447	2.853
CF	-121.784	37.421	2.023	3.636	2.175
CF	-121.798	37.434	nan	nan	2.958
CF	-120.983	36.435	0.226	0.471	1.478
CF	-120.994	36.448	2.747	5.706	2.181
CF	-121.006	36.461	2.564	5.318	1.991
CF	-121.018	36.474	0.622	1.288	1.635
CF	-121.030	36.486	2.557	5.283	2.087
CF	-121.042	36.499	2.163	4.462	2.269
CF	-121.054	36.512	3.266	6.603	2.669
CF	-121.066	36.525	3.595	6.819	2.333
CF	-121.081	36.538	3.245	6.141	2.422
CF	-121.096	36.550	5.082	9.598	3.135
CF	-121.111	36.563	2.237	4.217	2.620
CF	-121.126	36.576	4.193	8.014	2.905
CF	-121.141	36.589	5.225	10.000	2.813
CF	-121.155	36.602	5.001	9.553	3.324
CF	-121.169	36.614	4.567	8.707	2.269

CF	-121.183	36.627	3.345	6.365	3.178
CF	-121.197	36.640	3.372	6.404	1.785
CF	-121.211	36.653	4.195	7.952	2.730
CF	-121.226	36.666	4.947	9.360	4.579
CF	-121.240	36.678	4.467	8.796	2.757
CF	-121.252	36.691	4.765	9.617	2.503
CF	-121.264	36.704	3.787	7.632	2.398
CF	-121.276	36.717	3.797	7.639	2.877
CF	-121.287	36.730	4.214	8.137	2.665
CF	-121.300	36.742	2.317	4.170	2.682
CF	-121.316	36.755	3.369	6.052	1.527
CF	-121.333	36.768	3.769	6.756	2.510
CF	-121.349	36.781	2.983	5.878	2.187
CF	-121.361	36.794	3.320	7.098	2.565
CF	-121.371	36.806	2.923	6.240	2.818
CF	-121.381	36.819	1.501	3.201	1.194
CF	-121.390	36.832	1.619	3.734	2.606
CF	-121.399	36.845	1.567	4.230	1.727
CF	-121.405	36.858	2.238	6.036	3.452
CF	-121.411	36.870	3.081	8.300	3.826
CF	-121.417	36.883	2.623	7.046	4.083
CF	-121.423	36.896	3.205	8.510	6.797
CF	-121.429	36.909	6.051	16.052	5.439
CF	-121.436	36.922	3.978	10.545	5.195
CF	-121.442	36.934	6.754	17.887	4.396
CF	-121.448	36.947	5.910	15.638	4.049
CF	-121.454	36.960	5.369	13.801	5.115
CF	-121.461	36.973	4.524	11.310	5.500
CF	-121.468	36.986	3.524	8.803	5.421
CF	-121.475	36.998	2.330	5.816	3.345
CF	-121.482	37.011	-0.102	-0.254	5.386
CF	-121.488	37.024	2.075	5.170	6.552
CF	-121.495	37.037	nan	nan	5.302
SF	-121.444	36.883	0.189	0.300	2.146
SF	-121.477	36.896	0.067	0.106	2.059
SF	-121.509	36.909	2.596	4.208	3.112
SF	-121.534	36.922	1.767	2.947	3.370
SF	-121.554	36.934	1.095	1.823	3.495
SF	-121.574	36.947	0.850	1.411	2.906

SF	-121.595	36.960	0.839	1.390	2.154
SF	-121.615	36.973	-0.376	-0.614	3.345
SF	-121.636	36.986	-2.423	-3.897	4.279
SF	-121.660	36.998	-1.308	-2.110	4.437
SF	-121.683	37.011	-0.889	-1.507	4.729
SF	-121.700	37.024	-0.283	-0.479	4.703
SF	-121.717	37.037	-1.201	-2.028	5.403
SF	-121.798	37.088	-1.166	-1.772	7.037
SF	-121.833	37.101	-1.689	-2.550	5.043
SF	-121.870	37.114	nan	nan	6.121
QSF	-121.207	36.755	-1.765	-3.567	2.466
QSF	-121.219	36.768	-0.616	-1.243	2.079
QSF	-121.231	36.781	-1.242	-2.504	2.197
QSF	-121.243	36.794	-0.654	-1.316	2.153
QSF	-121.254	36.806	-1.206	-2.456	2.790
QSF	-121.266	36.819	0.913	1.868	2.232
QSF	-121.277	36.832	0.701	1.432	3.108
QSF	-121.288	36.845	1.738	3.518	2.632
QSF	-121.299	36.858	0.989	1.904	3.658
QSF	-121.312	36.870	0.419	0.805	1.883
QSF	-121.325	36.883	0.442	0.854	1.351
QSF	-121.338	36.896	1.392	2.763	3.414
QSF	-121.349	36.909	nan	nan	2.259

Table C.3: Fault creep rates derived from Sentinel-1 InSAR timeseries (2015-2020). *SAF: San Andreas Fault, CF: Calaveras Fault, SF: Sargent Fault, QSF: Quien Sabe Fault.*

Fault	Type	Longitude (°)	Latitude (°)	Time Period	Dextral Rate (mm/yr)	Uncer--tainty (mm/yr)	Reference
SAF	AA	-121.6483	36.9267	1967-1972	0.8	/	Burford & Harsh, 1980
SAF	AA	-121.5200	36.8367	1968-1977	14.0	/	Burford & Harsh, 1980
SAF	AA	-121.3467	36.7200	1972-1977	13.5	/	Burford & Harsh, 1980
SAF	AA	-121.2717	36.6583	1973-1977	14.0	/	Burford & Harsh, 1980
SAF	AA	-121.2017	36.6050	1972-1977	19.9	/	Burford & Harsh, 1980

SAF	AA	-121.1850	36.5950	1972-1977	22.7	/	Burford & Harsh, 1980
SAF	AA	-121.1845	36.5933	1967-1978	22.9	/	Burford & Harsh, 1980
SAF	AA	-121.1635	36.5740	1970-1973	23.1	/	Burford & Harsh, 1980
SAF	AA	-121.1350	36.5433	1972-1977	23.1	/	Burford & Harsh, 1980
SAF	AA	-121.0626	36.4762	1967-1974	21.9	/	Burford & Harsh, 1980
SAF	AA	-121.1850	36.5950	1967-2004	20.2	/	Titus et al., 2006
SAF	AA	-120.9693	36.3833	1967-2003	26.2	/	Titus et al., 2006
SAF	AA	-121.5728	36.8745	2015-2020	5.6	/	McFarland et al, 2017
SAF	AA	-121.5217	36.8350	2015-2020	5.8	/	McFarland et al, 2017
CF	AA	-121.7139	37.3417	1977-1984	9.4	0.4	Oppenheimer et al.,1990
CF	AA	-121.5242	37.0699	1968-2001	14.0	2.0	Galehouse & Lienkaemper, 2003
CF	AA	-121.4826	37.0096	1972-1979	13.0	2.0	Lisowski & Prescott., 1981
CF	AA	-121.4128	36.8699	1979-1989	12.2	0.2	Galehouse & Lienkaemper, 2003
CF	AA	-121.4053	36.8496	1979-1989	6.4	0.2	Galehouse & Lienkaemper, 2003
CF	AA	-121.3736	36.8050	1975-1979	5	3	Lisowski & Prescott., 1981
CF	AA	-121.3233	36.7617	1973-1986	6.2	0.1	Harsh & Pavoni, 1978; Wilmesher & Baker, 1987
CF	AA	-121.1425	36.5932	1975-1979	10	3	Lisowski & Prescott., 1981
CF	AA	-121.4063	36.8495	2015-2020	7.6	/	McFarland et al, 2017

CF	AA	-121.4138	36.8698	2015-2020	9.8	/	McFarland et al, 2017
CF	AA	-121.5252	37.0698	2015-2020	11.3	/	McFarland et al, 2017
CF	AA	-121.6494	37.2220	2015-2020	1.6	/	McFarland et al, 2017
SF	AA	-121.6462	36.9763	1970-1975	2.9	0.7	Prescott & Burford, 1976
SAF	CM	-121.5200	36.8370	1985-1989	4.5	/	XSJ2, USGS
SAF	CM	-121.5200	36.8370	1989-2000	11.5	/	XSJ2, USGS
SAF	CM	-121.5200	36.8370	2007-2015	10.1	/	XSJ3, USGS
SAF	CM	-121.5200	36.8370	2015-2017	6.9	/	XSJ3, USGS
SAF	CM	-121.4220	36.7720	1985-1989	11.5	/	XHR2, USGS
SAF	CM	-121.4220	36.7720	1989-2000	14.5	/	XHR2, USGS
SAF	CM	-121.4220	36.7720	2009-2015	11.4	/	XHR3, USGS
SAF	CM	-121.4220	36.7720	2015-2020	10.3	/	XHR3, USGS
SAF	CM	-121.3850	36.7500	1985-1989	11.4	/	CWC3, USGS
SAF	CM	-121.3850	36.7500	1989-2000	12.7	/	CWC3, USGS
SAF	CM	-121.3850	36.7500	1985-1989	9.4	/	CWN1, USGS
SAF	CM	-121.3850	36.7500	1989-2000	16.0	/	CWN1, USGS
SAF	CM	-121.3850	36.7500	2000-2015	13.4	/	CWN1, USGS
SAF	CM	-121.3850	36.7500	2015-2020	11.9	/	CWN1, USGS
SAF	CM	-121.1870	36.5950	1985-1989	17.3	/	XMR1, USGS
SAF	CM	-121.1870	36.5950	1989-2000	16.5	/	XMR1, USGS
SAF	CM	-121.1870	36.5950	2000-2015	16.3	/	XMR1, USGS
SAF	CM	-121.1870	36.5950	2015-2020	16.0	/	XMR1, USGS
CF	CM	-121.4450	36.9430	1985-1989	10.5	/	XSH1, USGS
CF	CM	-121.4450	36.9430	1989-2000	6.5	/	XSH1, USGS
CF	CM	-121.4450	36.9430	2000-2015	10.3	/	XSH1, USGS
CF	CM	-121.4450	36.9430	1985-1989	9.0	/	SHR2, USGS
CF	CM	-121.4450	36.9430	1989-1999	3.9	/	SHR2, USGS
CF	CM	-121.4050	36.8570	1985-1989	6.6	/	HLC1, USGS
CF	CM	-121.4050	36.8570	1989-2000	0.9	/	HLC1, USGS
CF	CM	-121.4050	36.8570	2000-2009	2.4	/	HLC1, USGS
CF	CM	-121.4030	36.8420	1985-1989	3.3	/	HLD1, USGS
CF	CM	-121.4030	36.8420	1989-2000	0.0	/	HLD1, USGS
CF	CM	-121.4030	36.8420	2000-2015	2.4	/	HLD1, USGS

Table C.4: Creep rates derived from alignment array and creepmeter measurements.
Fault names: SAF: San Andreas Fault, CF: Calaveras Fault, SF: Sargent Fault
Type of measurements: AA: Alignment arrays, CM: Creepmeter
** Creepmeter timeseries are downloaded from*
https://earthquake.usgs.gov/monitoring/deformation/data/download.php

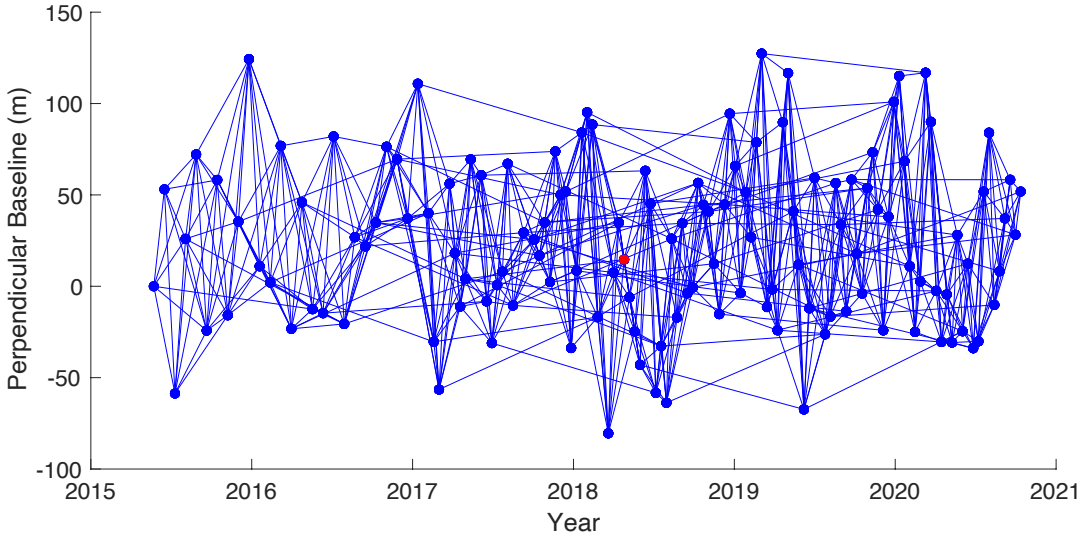


Figure C.1: SBAS network used in this study. Each dot represents an acquired SAR image and each line represents an interferogram. All SAR images are co-registered to the reference image acquired on April 26^{th} 2018, that colored in red.

Network	# Intfs	min/max/mean # of links	Rate STD (mm/yr)	Avg Timeseries STD (mm)
60, 200	450	2/8/6.7	2.66	5.55
60, 200 + 1 year	539	3/12/8.1	1.87	4.74
Nearest 3	393	3/6/5.9	3.31	6.64
Nearest 5	650	5/10/9.7	1.95; 1.86 (ramp)	4.63
Nearest 5 + 1 year	739	6/14/11.1	1.69; 1.39 (ramp) 1.56 (w/o CSS)	4.16; 4.09 (ramp) 13.52 (w/o CSS)

Table C.1: Effect of the selection of temporal-baseline networks on the statistics of InSAR velocity products.
** ERA5 and CSS corrections are applied to all InSAR timeseries unless otherwise noted.*
** Rate STD: Standard deviation of the velocity difference between InSAR and GPS velocities on 66 GPS sites.*
** Avg Timeseries STD: Standard deviation of the difference between InSAR and GPS timeseries averaged on 66 GPS sites.*

#	Station ID	Longitude (°)	Latitude (°)	InSAR LOS Rate (mm/yr)	3D GPS LOS Rate (mm/yr)	2D GPS LOS Rate (mm/yr)
1	CHOW	-120.21	37.08	-63.67	-61.99	5.70
2	MULN	-120.10	36.56	-32.99	-45.99	7.40
3	TRAN	-120.25	36.65	-43.33	-38.12	5.94
4	P307	-120.06	36.95	-30.61	-37.99	4.56
5	CALB	-120.71	37.10	-24.45	-25.15	6.27
6	P303	-120.71	37.05	-22.98	-21.47	6.70
7	ALTH	-120.67	36.89	-7.54	-2.77	5.02
8	OXMT	-122.42	37.50	3.20	-17.30	-2.86
9	P277	-122.37	37.19	-3.78	-6.33	-6.38

Table C.2: List of GPS stations that are excluded in the InSAR-GPS rate comparison.
** We exclude 7 stations (#1-#7) within the Central Valley experiencing severe subsidence and 2 stations (#8-#9) in coastal areas with extremely poor InSAR coherence.*

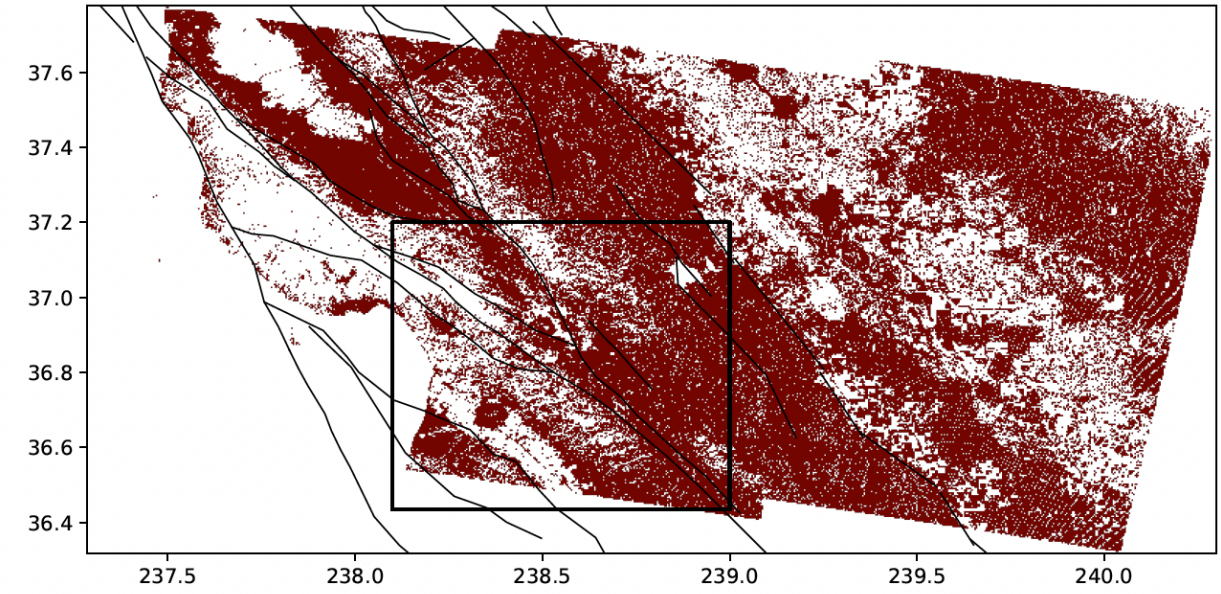


Figure C.2: Coherence mask applied in unwrapping process with an average (temporal) coherence threshold of 0.2. Pixels with average coherence lower than 0.2 (white) are masked.

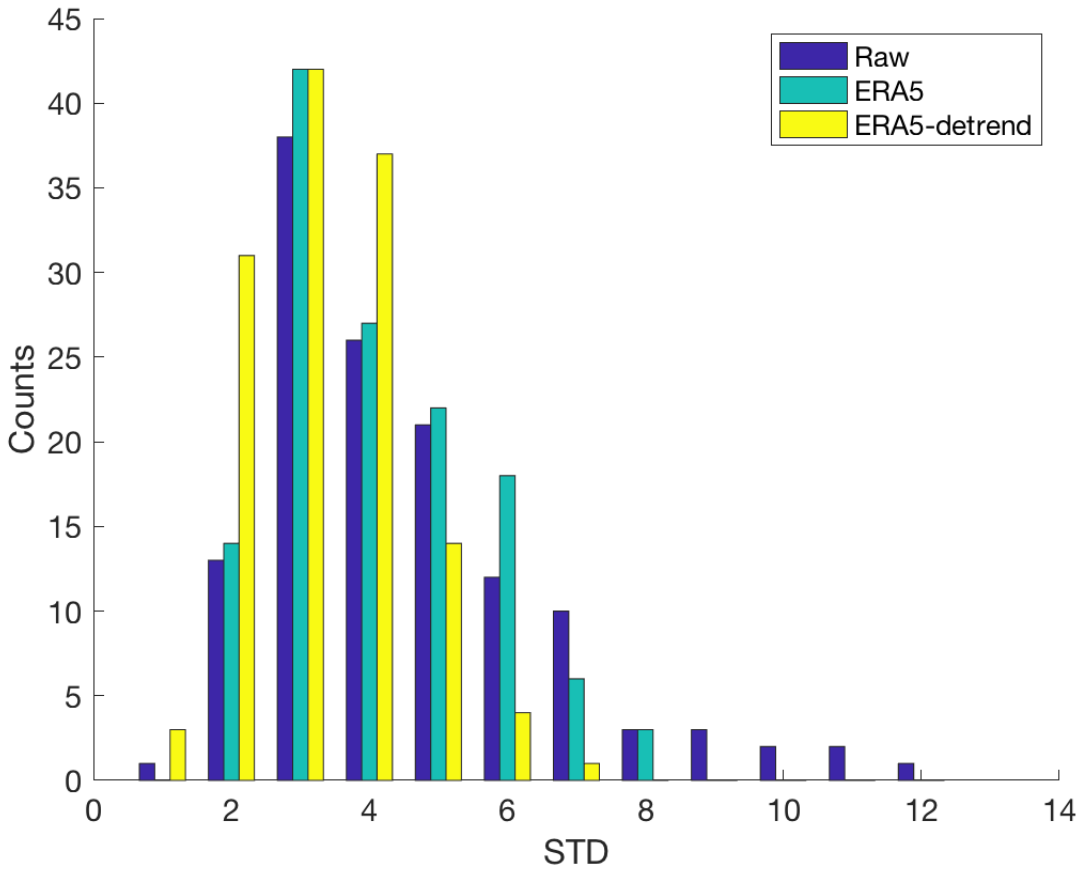


Figure C.3: Histogram of the variance of the sequential interferograms (standard deviation in radians) before and after ERA5 correction.

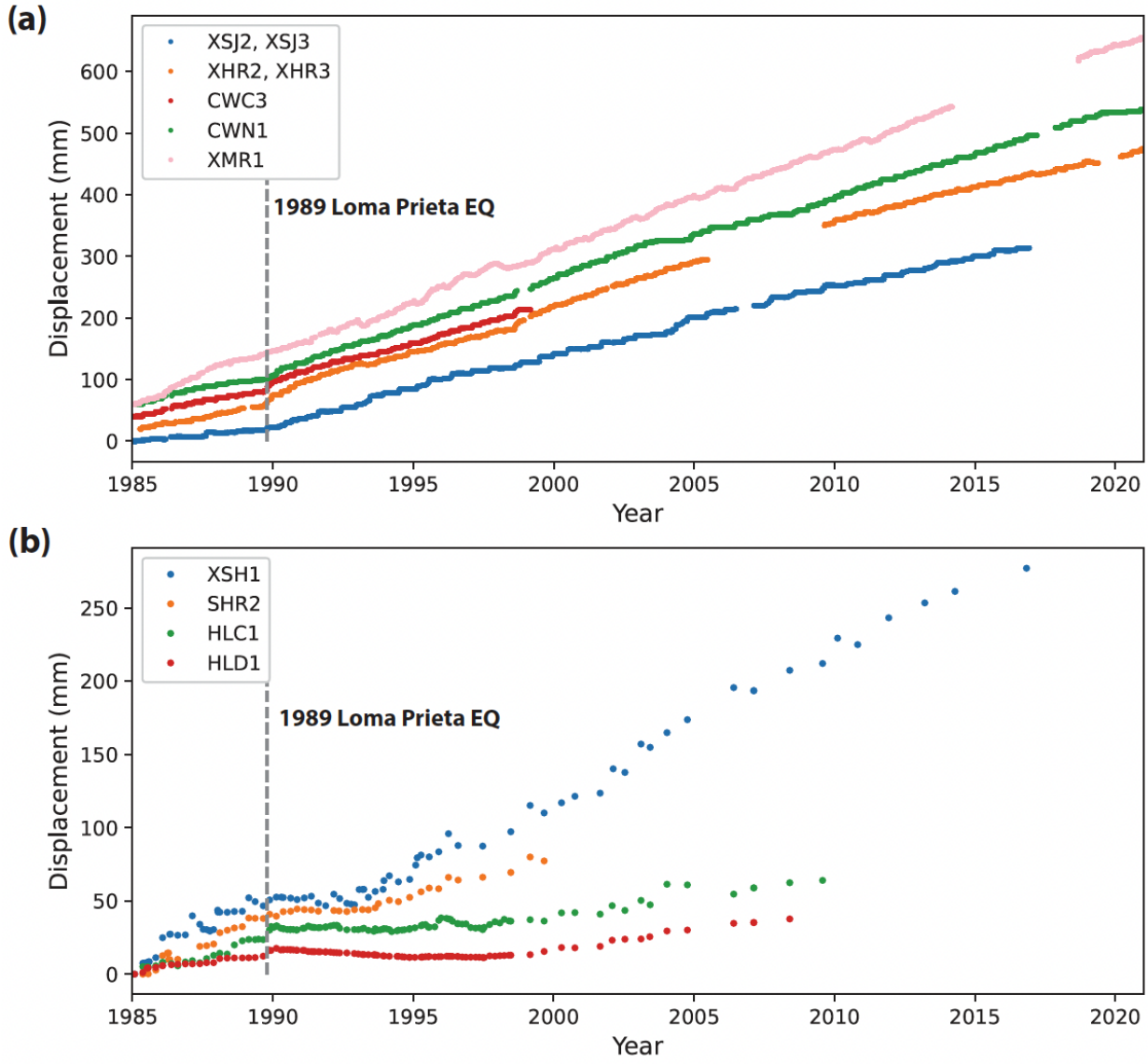


Figure C.4: Creepmeter timeseries measurements on the **(a)** SAF and **(b)** CF, respectively. The time of the 1989 M6.9 Loma Prieta earthquake is indicated by gray dashed lines. Creep rates on the SAF (XSJ2, XHR2, CWC3, CWN1) increased immediately after the 1989 Loma Prieta earthquake, while creep rates on the CF decreased and the slowdown lasted for ∼10 years.

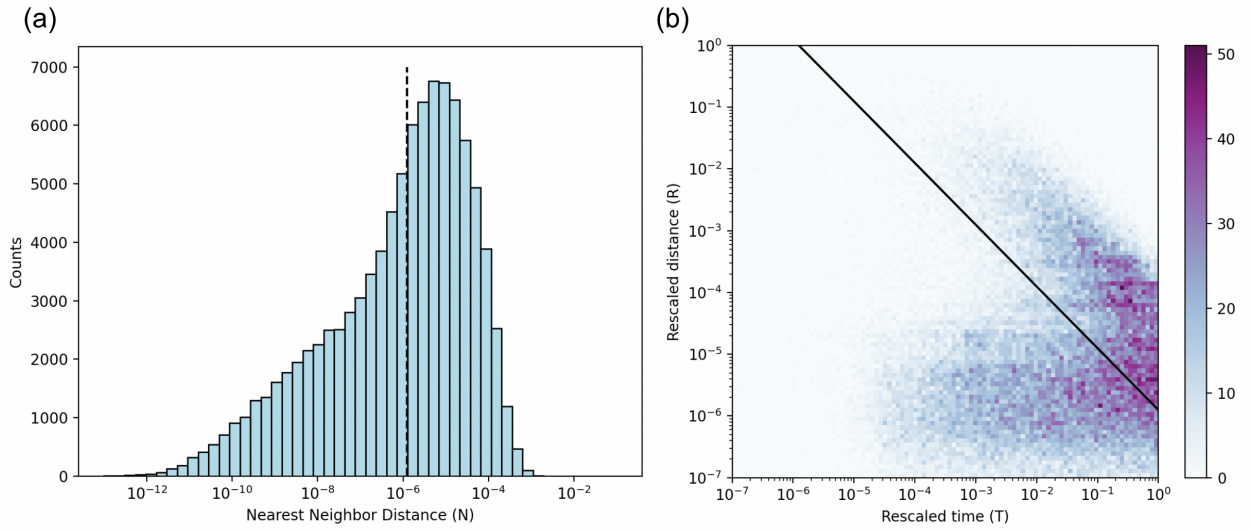


Figure C.5: **(a)** Distribution of nearest-neighbor distances for all events in the double-difference relocated NCEDC catalog in log scale. Black dashed line corresponds to $\eta = 1.25 \times 10^{-6}$. **(b)** Nearest-neighbor rescaled-time and rescaled-distance plot for all events in the NCEDC catalog. The color shows the number of events at each bin. Black line corresponds to $\log T + \log R = \log \eta$, where $\eta = 1.25 \times 10^{-6}$.

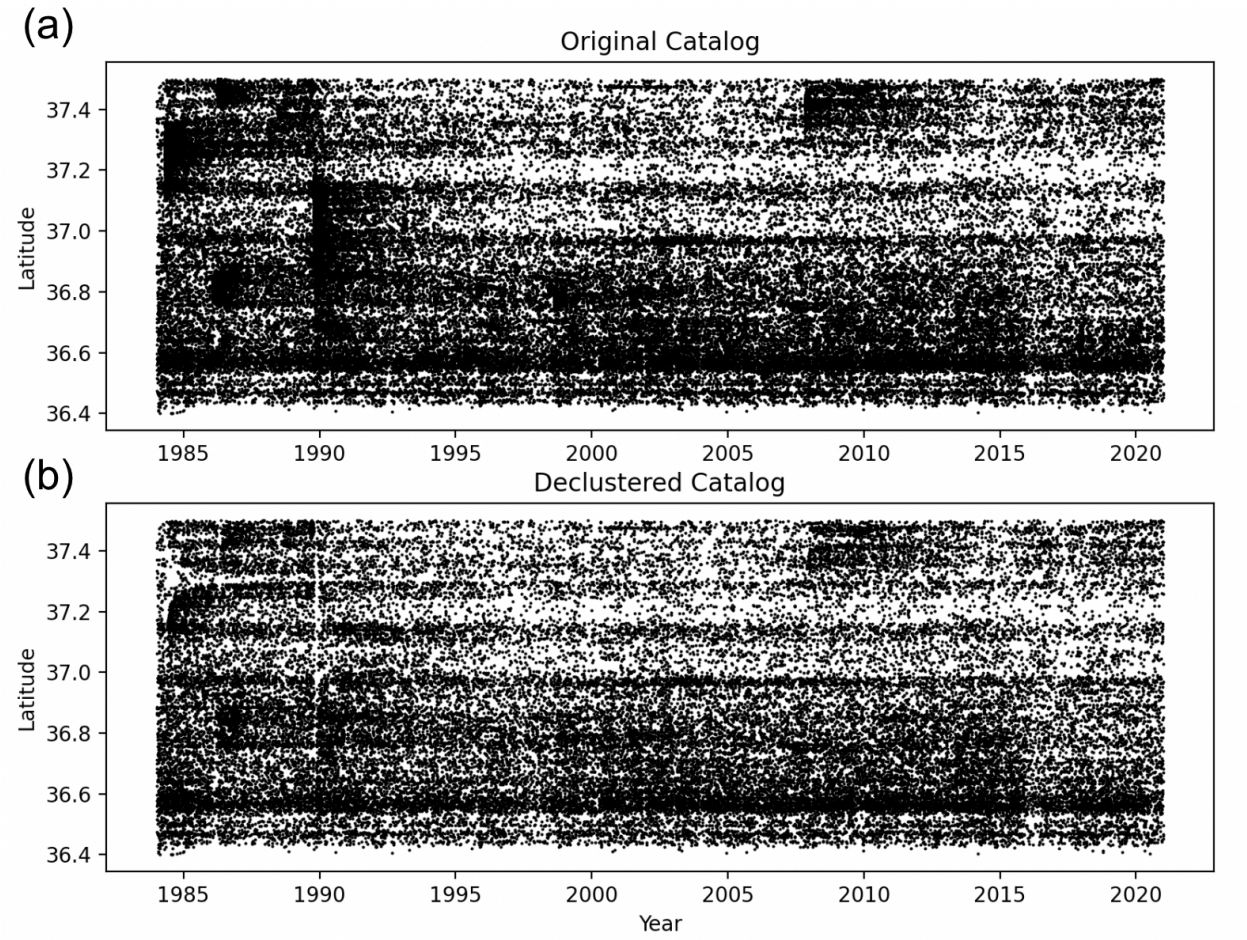


Figure C.6: Time-latitude plot of the **(a)** original and **(b)** declustered catalog using nearest-neighbor approach with $\eta = 1.25 \times 10^{-6}$.

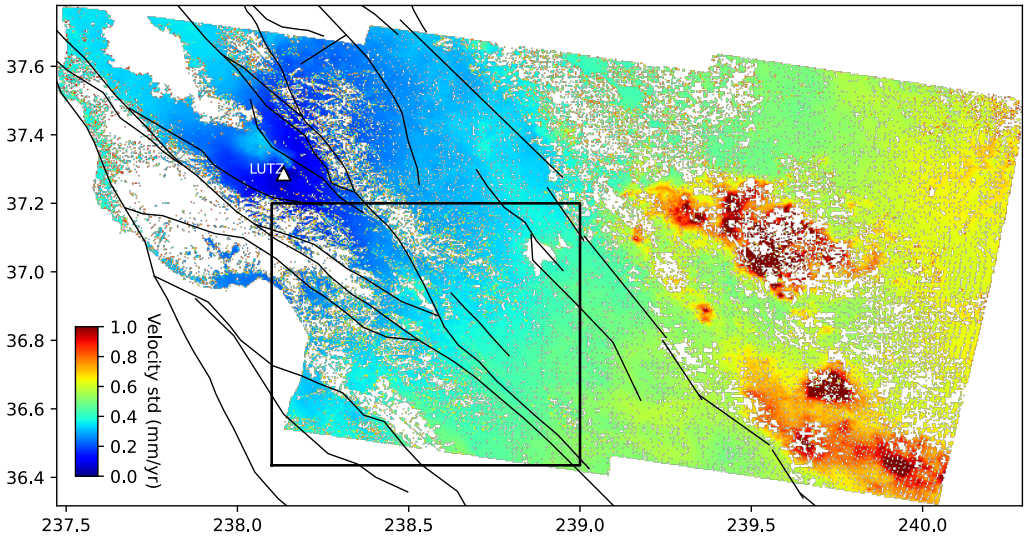


Figure C.7: Standard deviation of the InSAR LOS velocity when solving for a linear trend of the InSAR timeseries. The velocity standard deviation increases with distance away from the reference station LUTZ as well as in areas that experience time-dependent (seasonal) hydrological deformation and in areas with low InSAR coherence (Figure 4.4b).

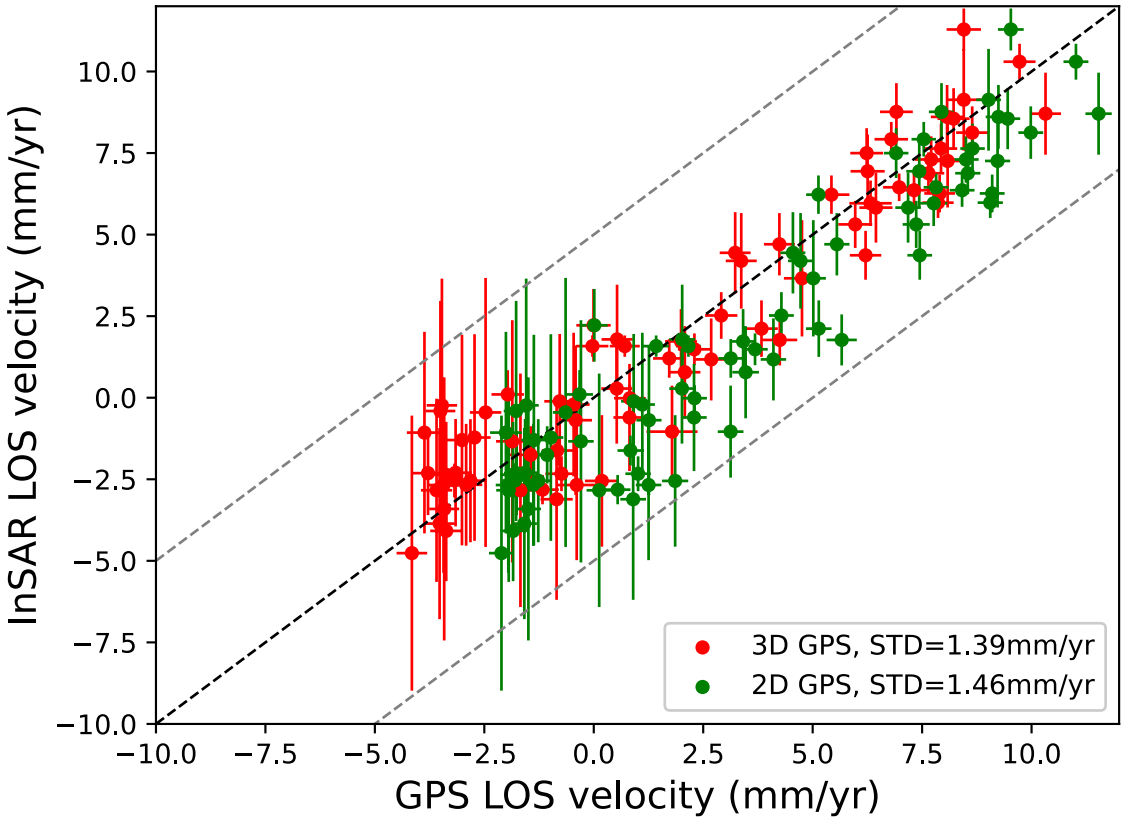


Figure C.8: Comparison of the InSAR LOS velocity with 3D and 2D GPS velocities projected into LOS, respectively. Stations experiencing rapid land subsidence are excluded (Table C.2).

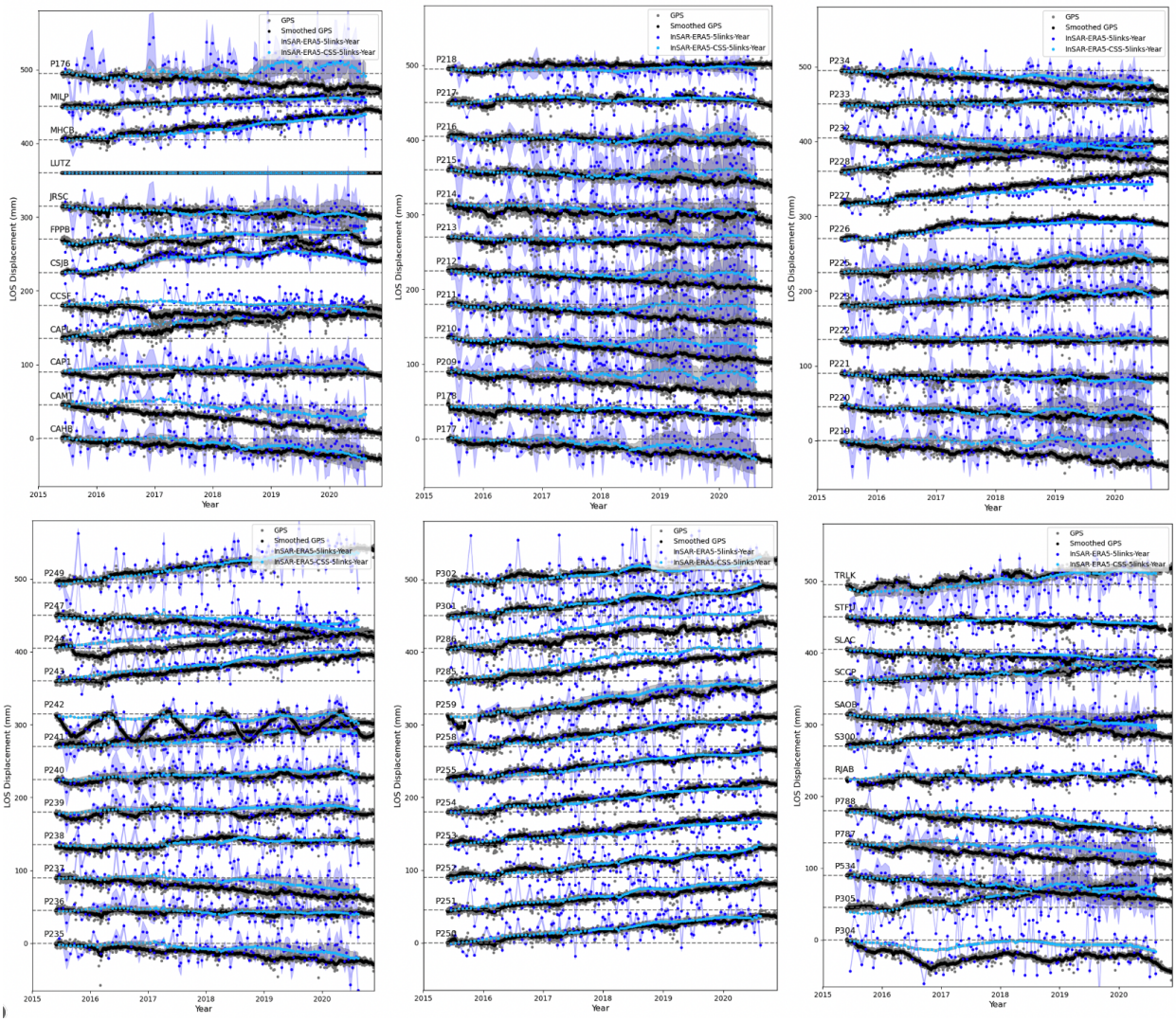


Figure C.9: Comparison of GPS and InSAR timeseries at GPS sites relative to LUTZ (Central Valley stations excluded). Gray dots show the raw GPS timeseries, black dots show the smoothed GPS timeseries using a 14-day moving average, blue dots show the InSAR timeseries with ERA5 weather model correction, and cyan dots show the InSAR timeseries corrected with both the ERA5 weather model and common scene stacking method (Tymofyeyeva and Fialko, 2015). Note that the seasonal patterns are smoothed out by CSS method (e.g., P242).

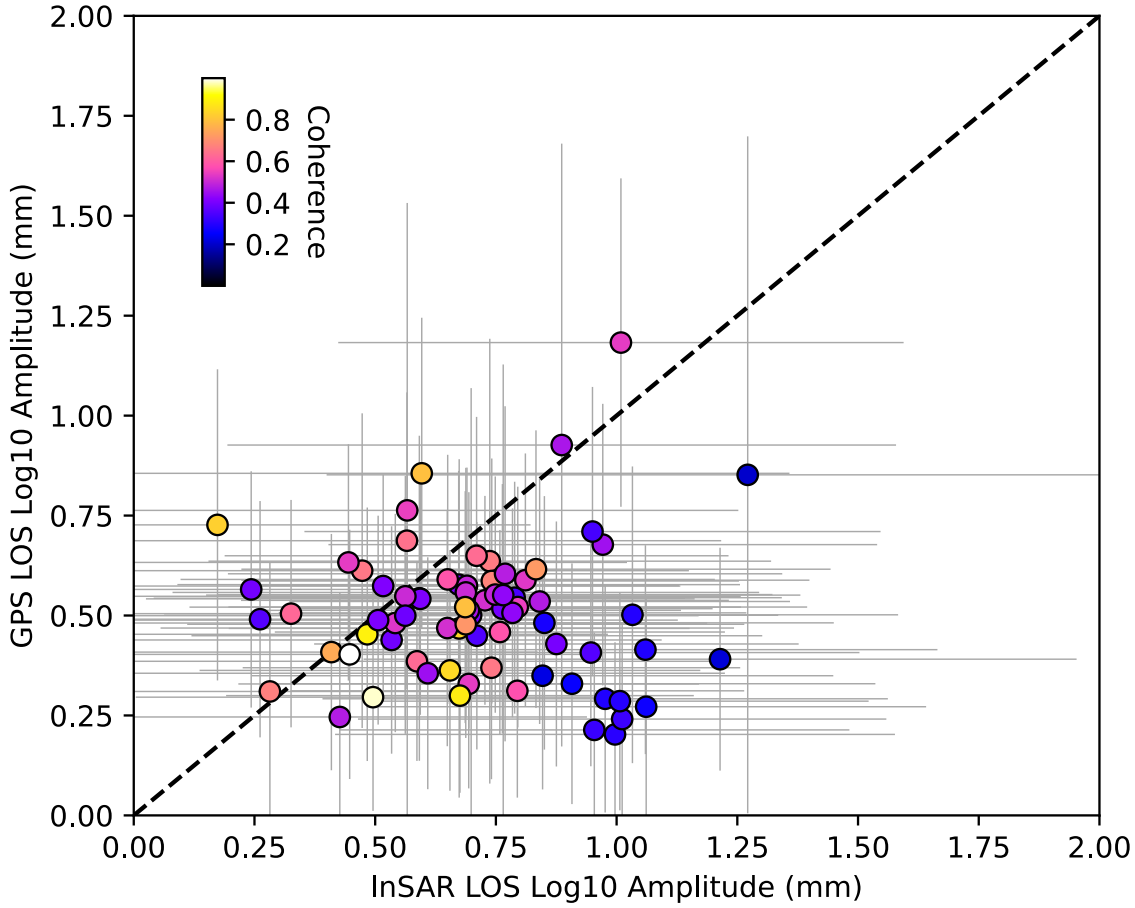


Figure C.10: Comparison of the amplitudes of seasonal deformation from InSAR and GPS timeseries. Each dot is colored with the average coherence from InSAR.

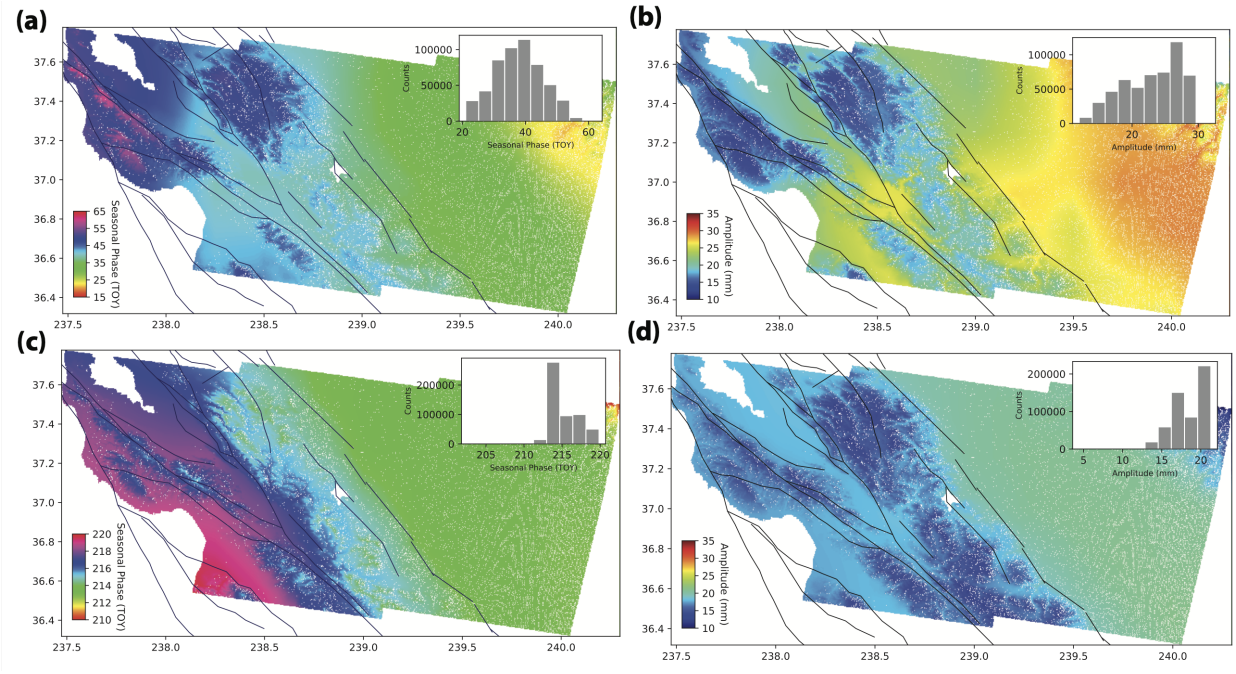


Figure C.11: Seasonal effects of the atmospheric phase delay estimated from ERA5 weather model timeseries. **(a)** Seasonal phase and **(b)** amplitude of the zenith wet delay (ZWD). **(c)** Seasonal phase and **(d)** amplitude of the zenith hydrostatic delay (ZHD).

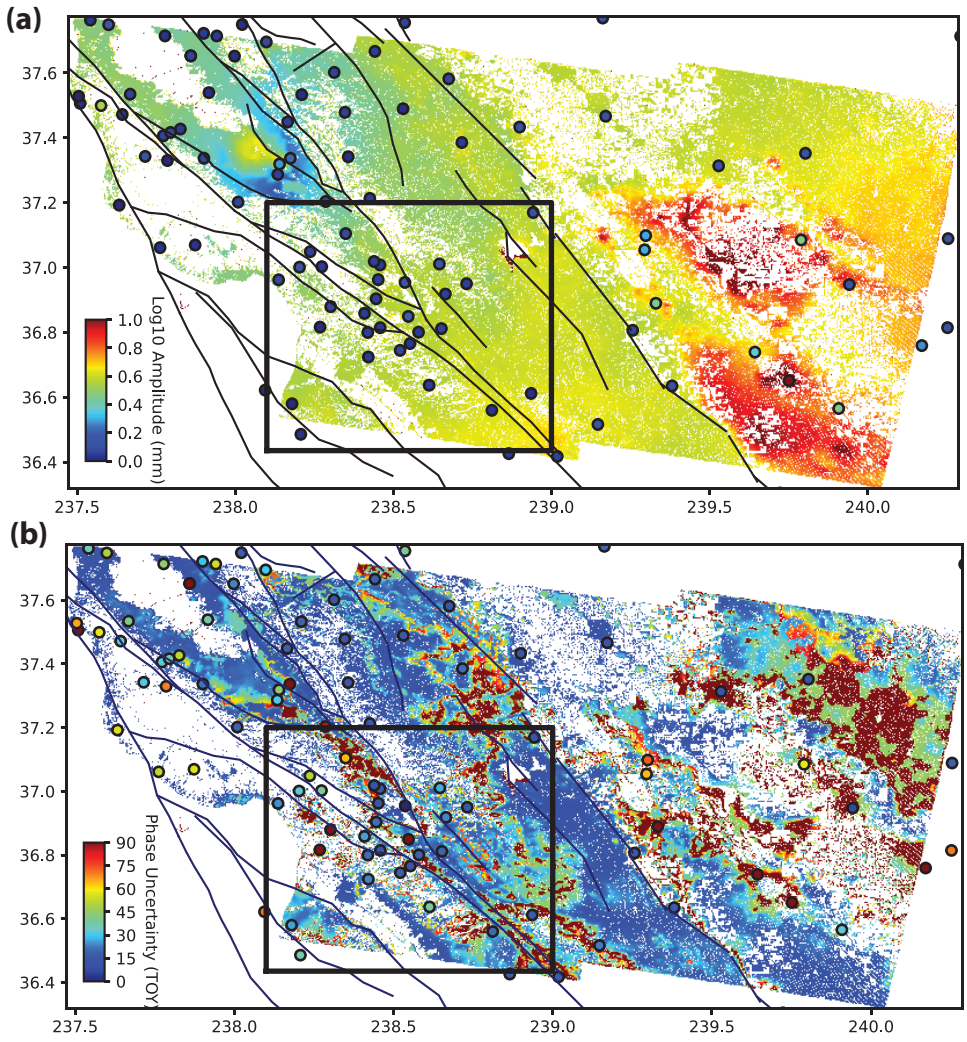


Figure C.12: Uncertainty of the **(a)** amplitude and **(b)** timing of peak seasonal uplift (phase) from InSAR and GPS timeseries. Timeseries with seasonal phase >90 days are unreliable.

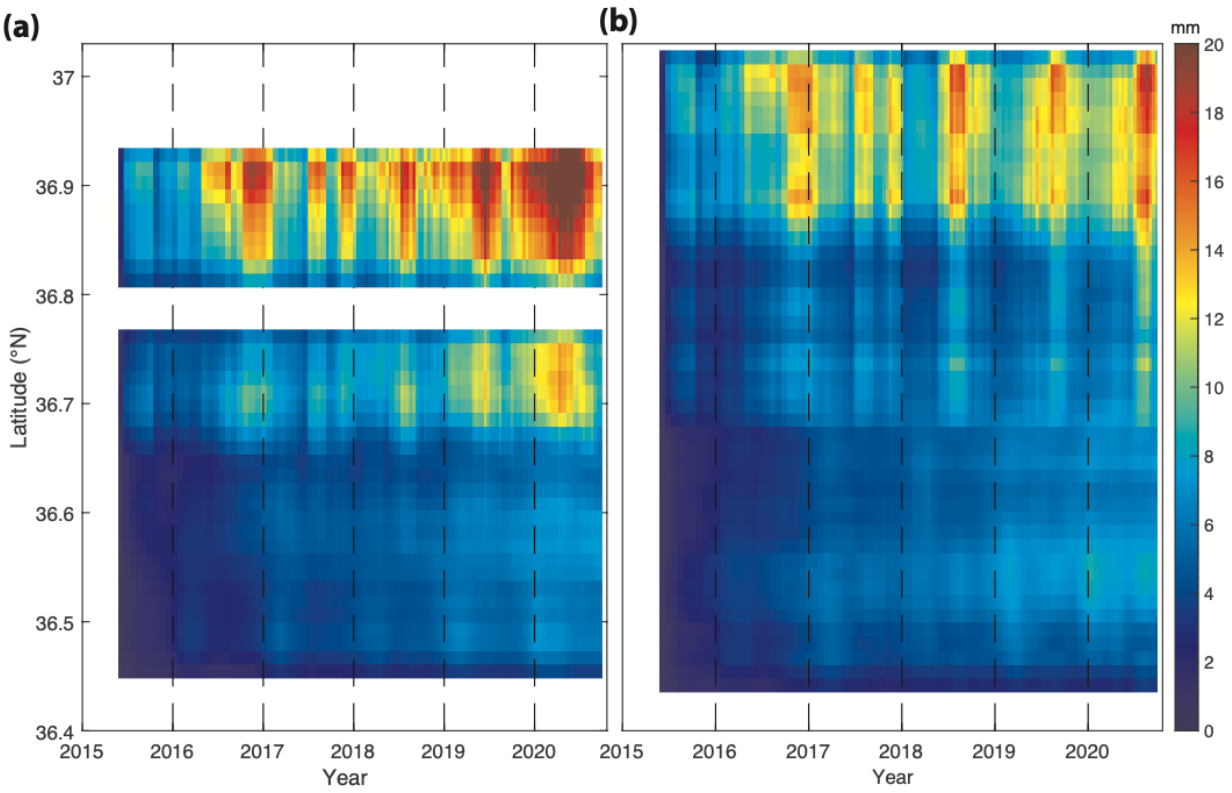


Figure C.13: Uncertainty (standard deviation) of the InSAR LOS cross-fault timeseries along the **(a)** SAF and **(b)** CF.

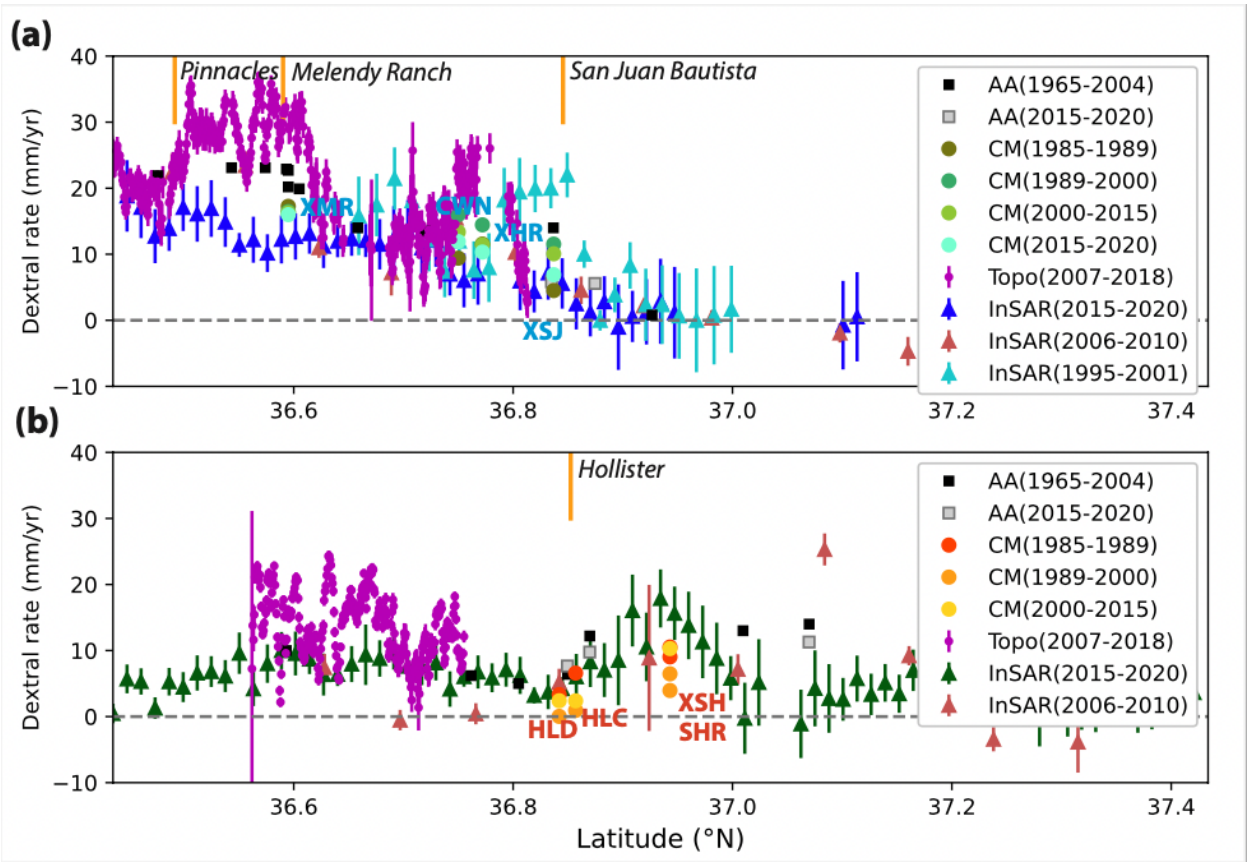


Figure C.14: Comparison of spatial distributions of average right-lateral creep rates along the **(a)** SAF and **(b)** CF with topographic differencing measurements (purple dots, 2007-2018, Scott et al., 2020). Refer to Figure 4.6 for more information.

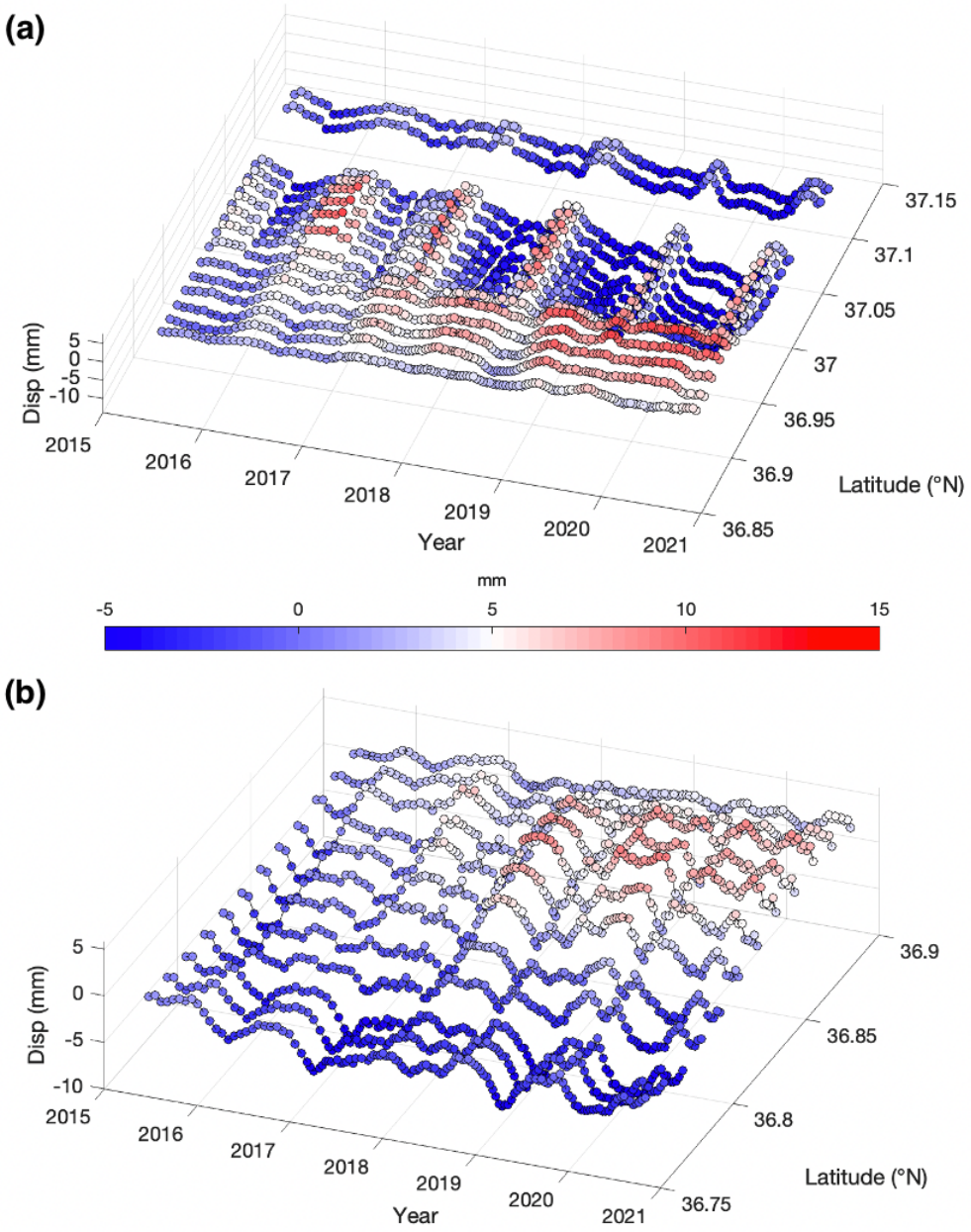


Figure C.15: InSAR LOS cross-fault timeseries differences along the **(a)** Sargent Fault and **(b)** Quien Sabe Fault. The cross-fault timeseries are calculated by differencing the InSAR timeseries averaged from 1-km-wide, 1-km-long boxes 0.5 km to 1.5 km on each side of the fault (Figure 4.3).

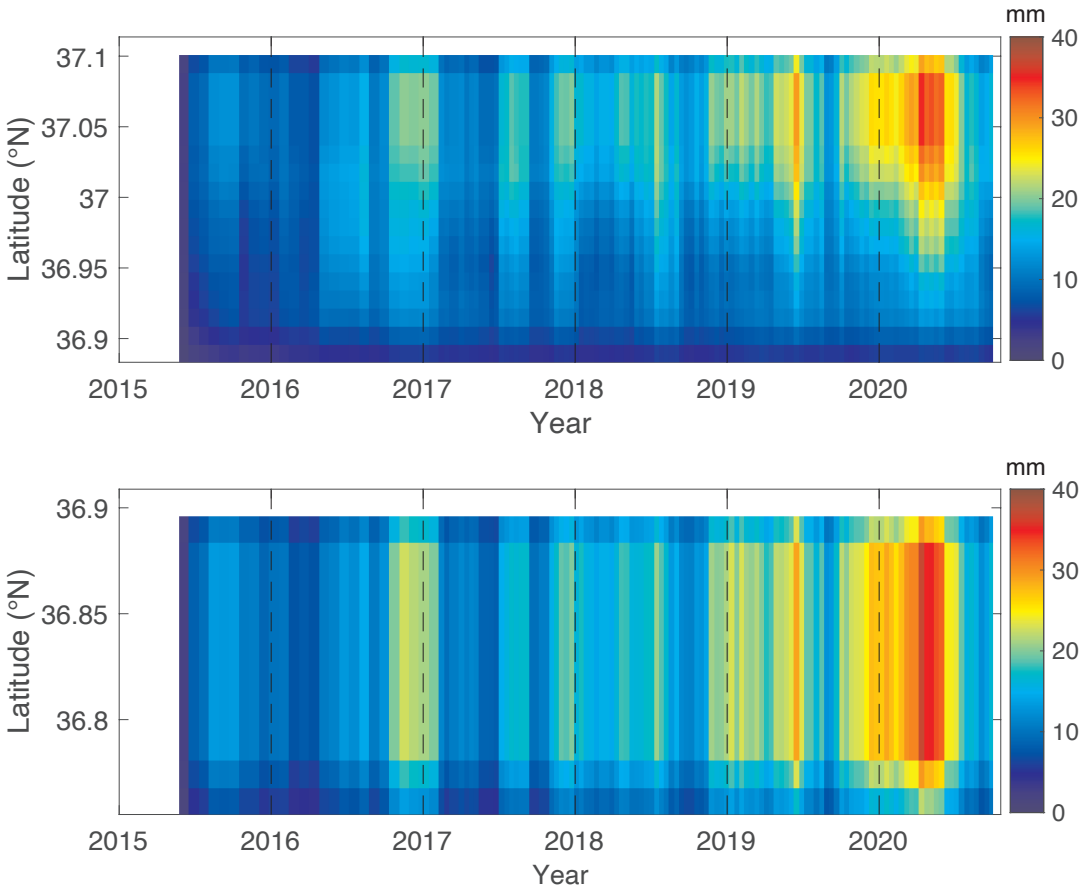


Figure C.16: Uncertainty (standard deviation) of the InSAR LOS cross-fault timeseries along **(a)** the Sargent Fault and **(b)** the Quien Sabe Fault.

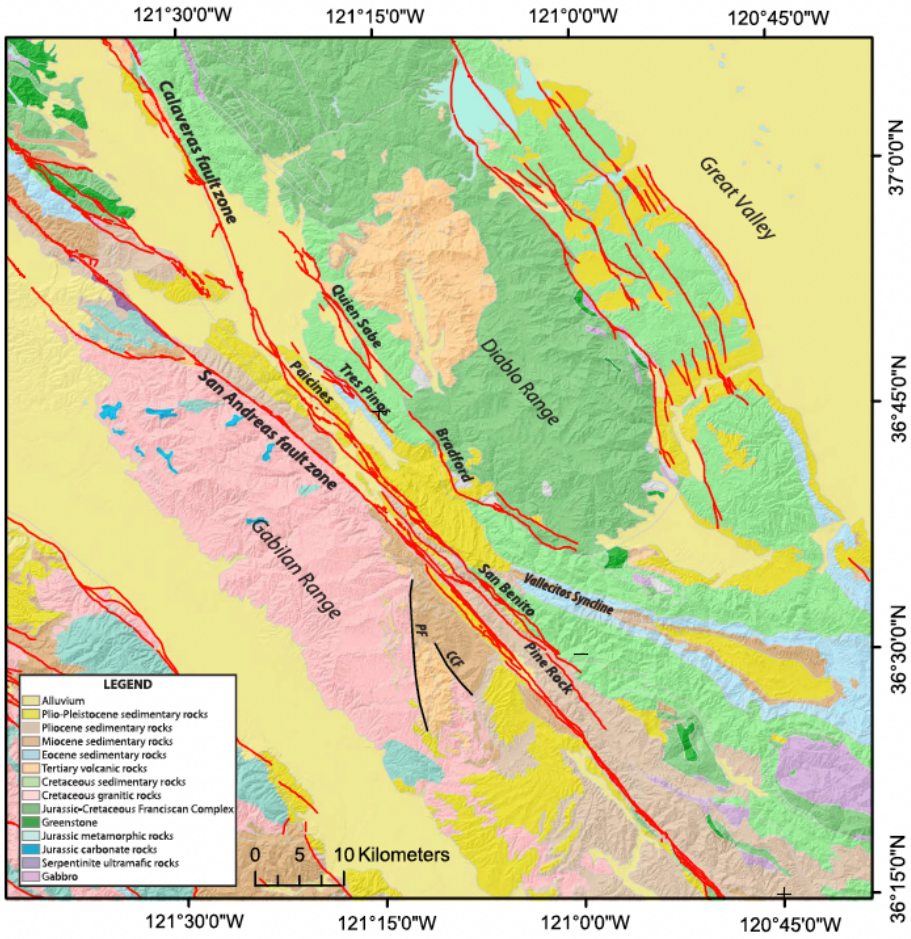


Figure C.17: Simplified geologic map of the SAF-CF junction adapted from Figure 2 in Watt et al. (2014).

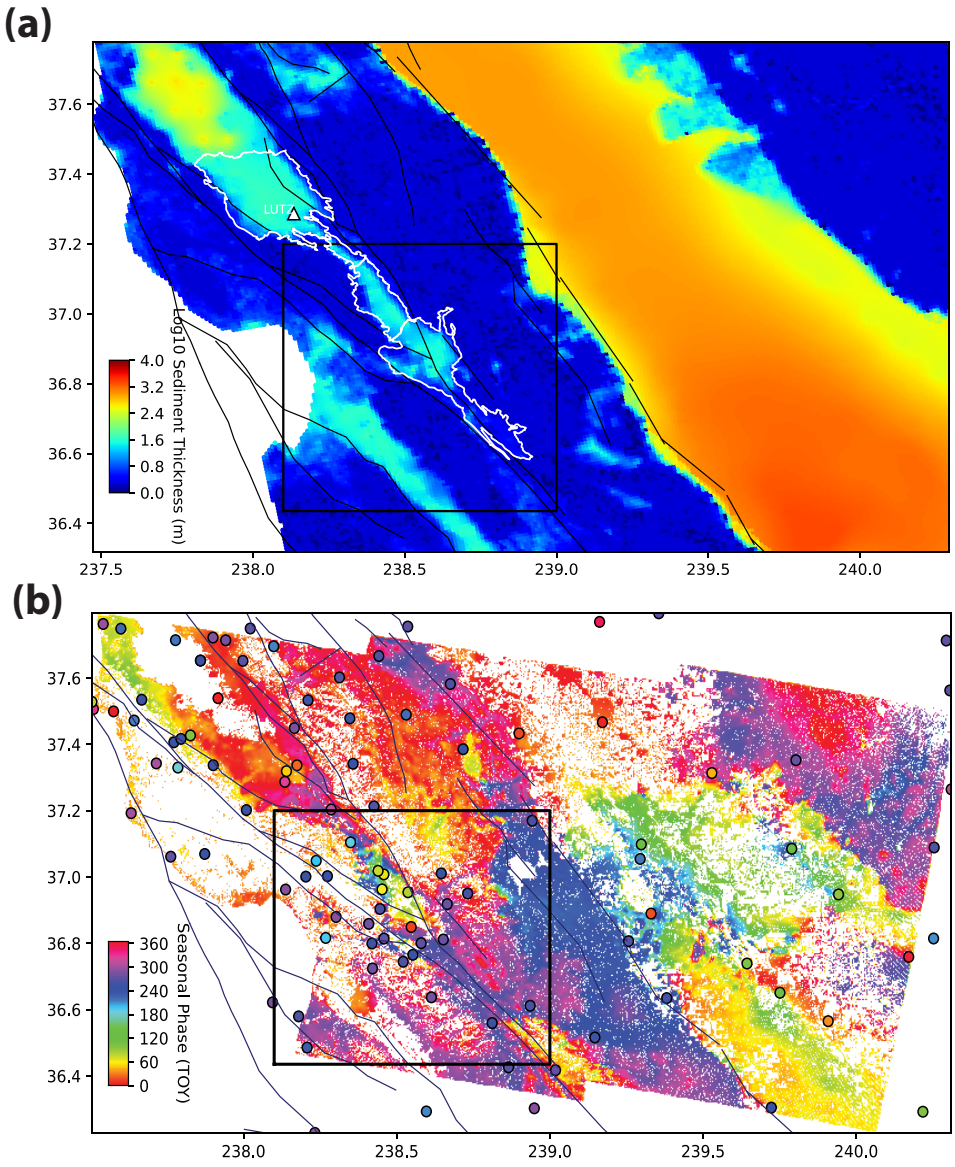


Figure C.18: **(a)** Sedimentary thickness map with basin outline over the study region (Shah and Boyd, 2018). **(b)** Timing of peak seasonal uplift (phase) map obtained from InSAR and GPS timeseries (same as Figure 4.4c).

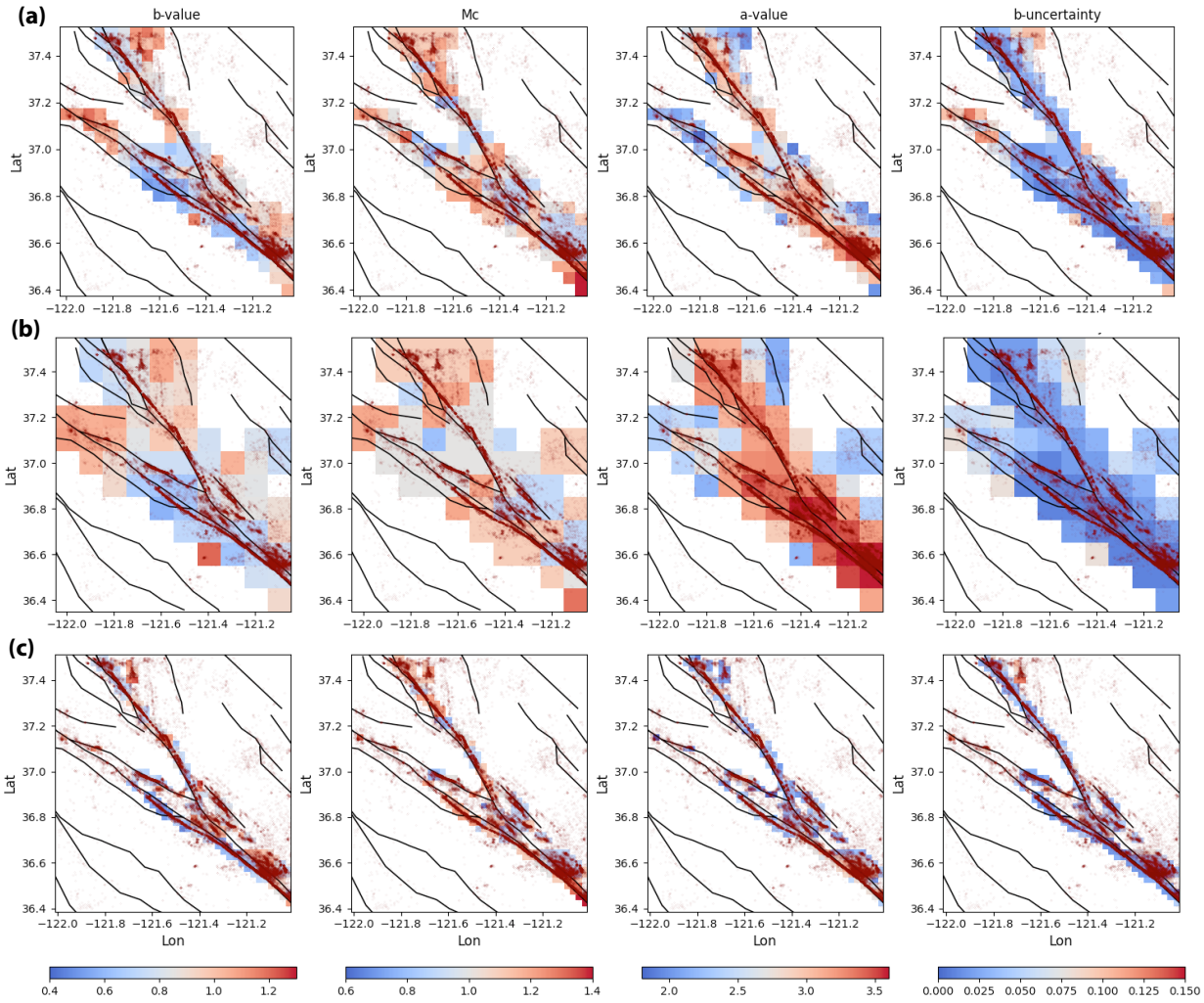


Figure C.19: Spatial distribution of the b-value, M_c, a-value and b-value uncertainties in each grid cell with grid size of **(a)** 0.05°, **(b)** 0.1°, and **(c)** 0.025°. We only estimate b-values on grid cells with N>200 events.

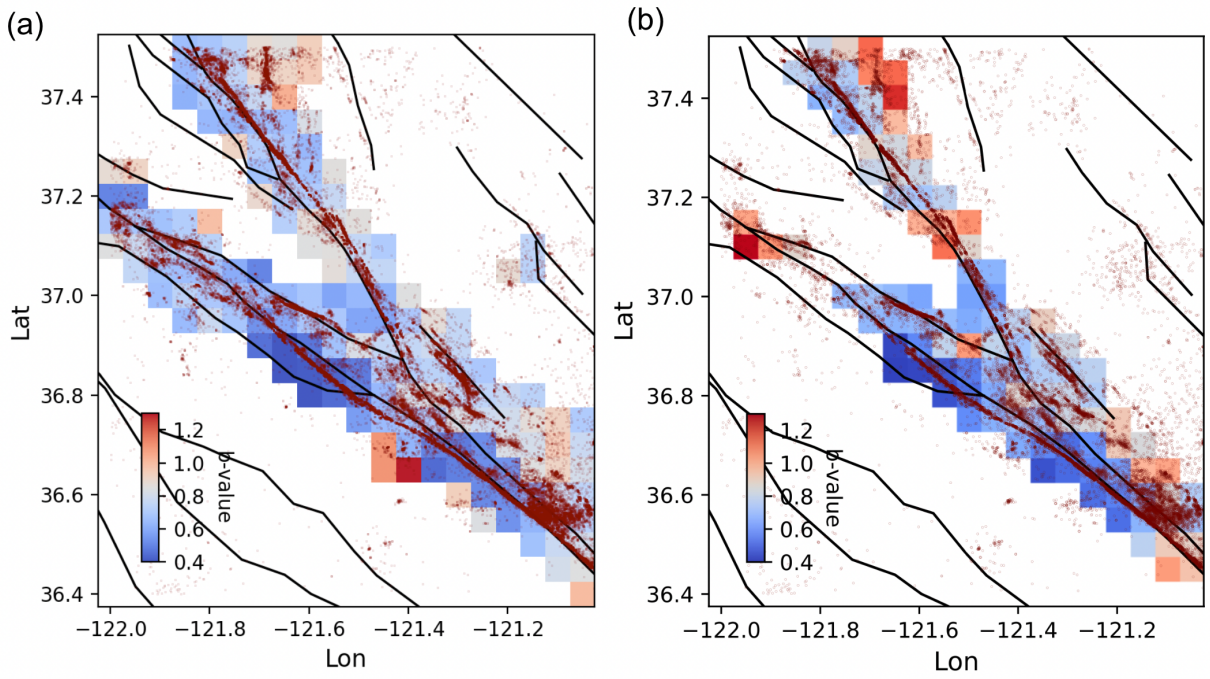


Figure C.20: Spatial distribution of the microseismicity and b-values using the **(a)** original and **(b)** declustered catalogs.

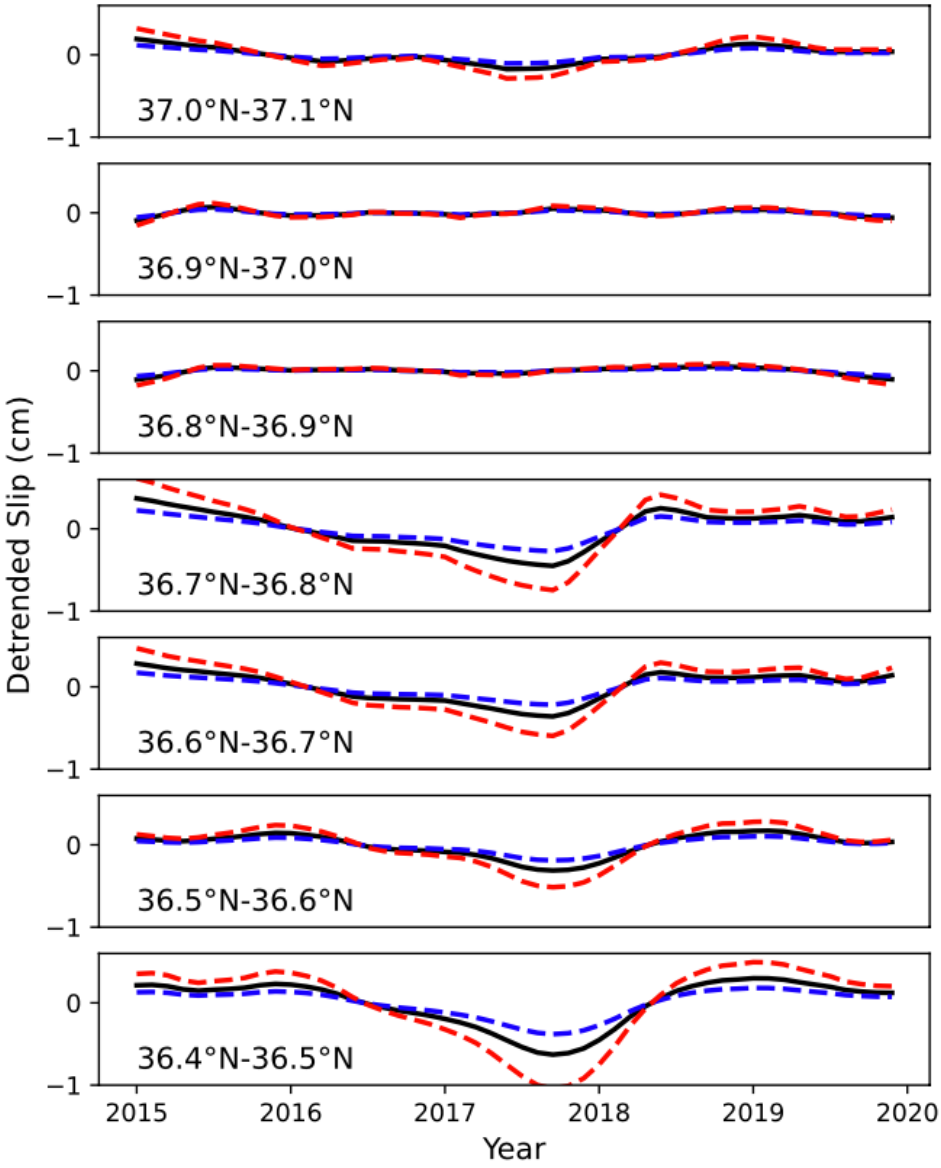


Figure C.21: Spatiotemporal variation of the residual CRE-inferred slip timeseries after the removal of a linear trend along the SAF that are binned by latitude. Black curve are derived using the empirical relationship from Nadeau and Johnson (1998). Red and blue dash lines show the upper- and -bound of the slip amplitude estimation, which is based on the uncertainties of the scaling parameters of the empirical relationship.

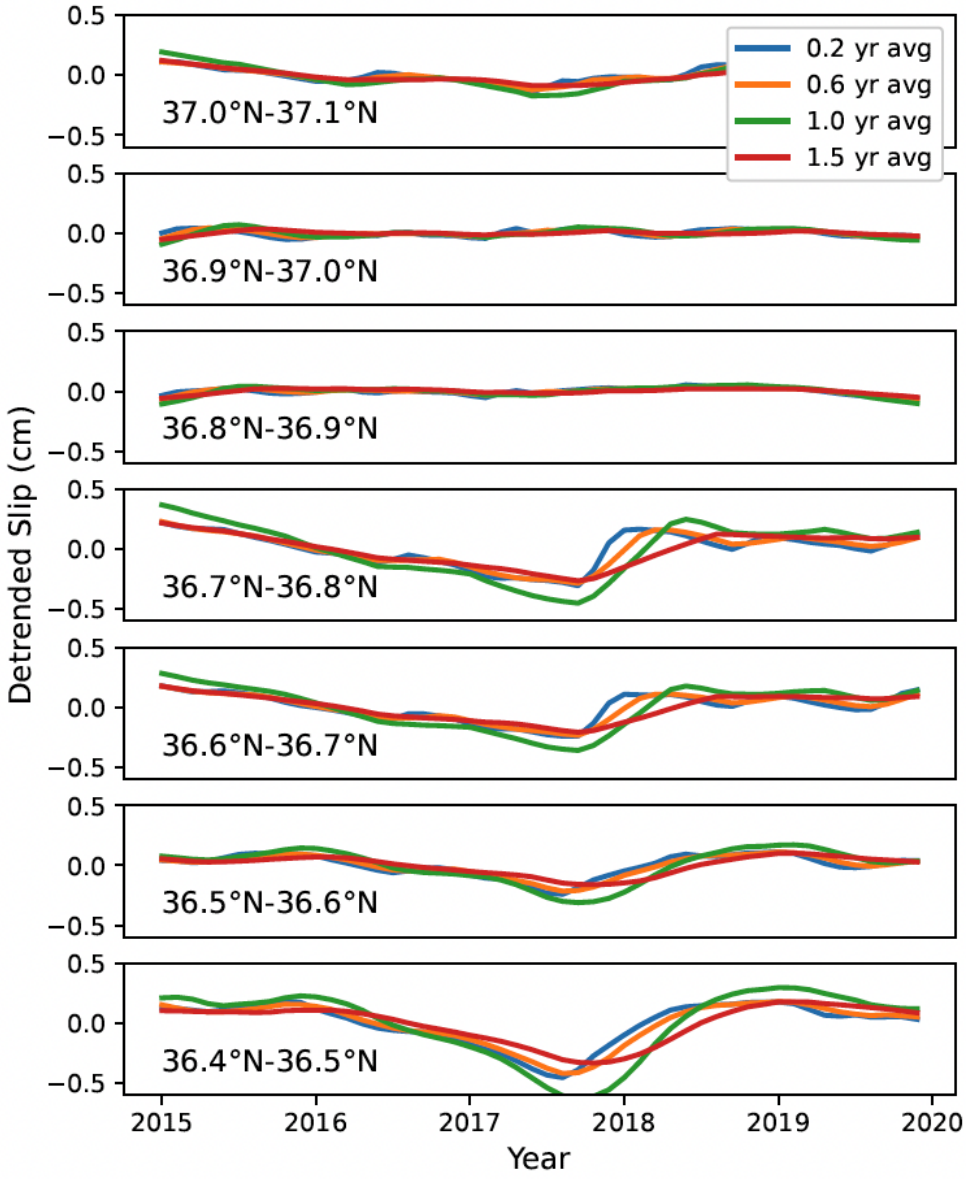


Figure C.22: Spatiotemporal variation of the residual CRE-inferred slip timeseries after the removal of a linear trend along the SAF that are binned by latitude. Timeseries with different moving average window are shown in different colors, respectively.

Appendix D

Supporting information for: Detecting Creep Transients in InSAR Timeseries Using Deep Neural Networks

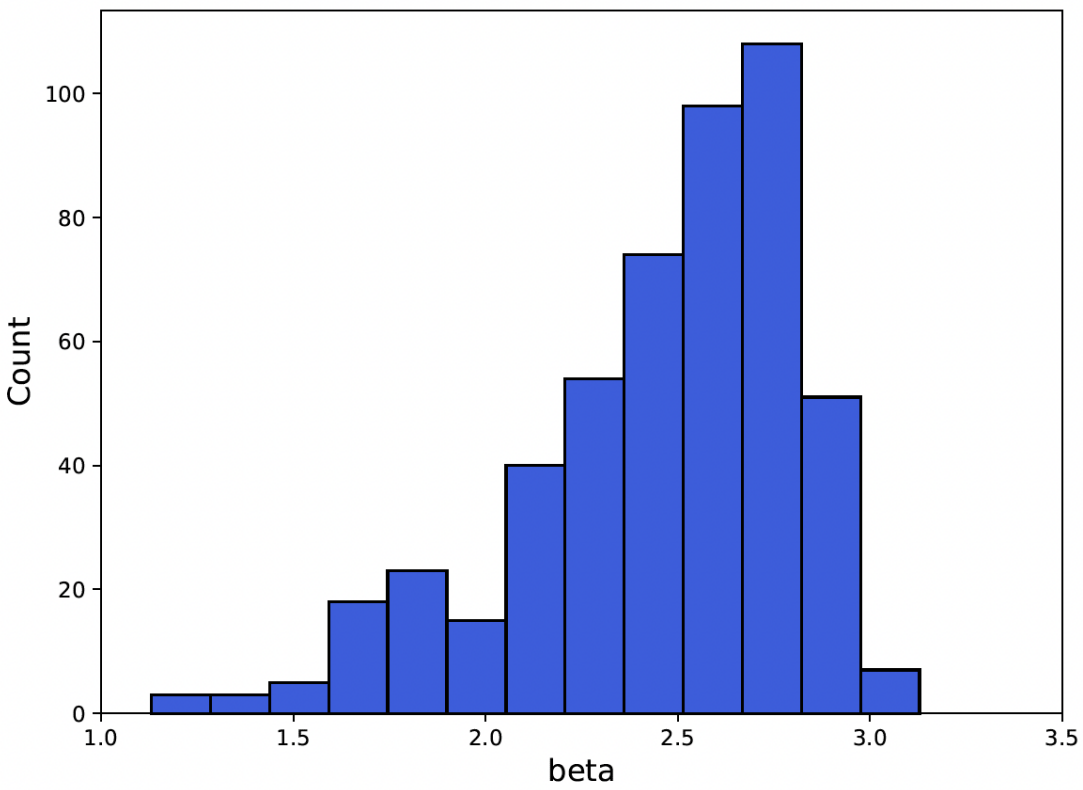


Figure D.1: Histogram of the power-law exponent (β) calculated from 500 randomly sampled land-based DEMs around the world (Brengman and Barnhart, 2021).

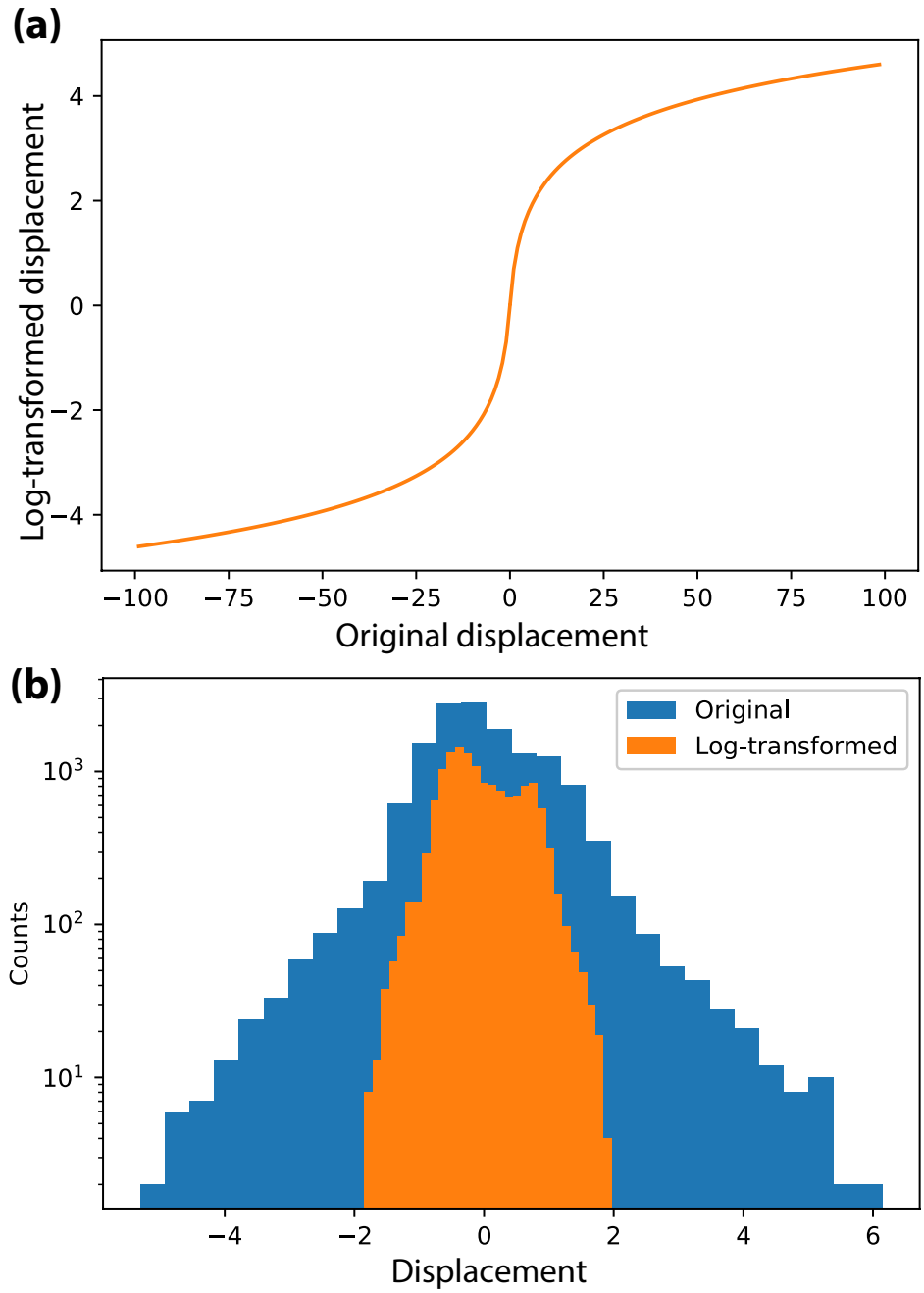


Figure D.2: **(a)** Demonstration of the log-transform on the InSAR displacement. **(b)** Histogram of the LOS displacements from synthetic InSAR timeseries before and after log-transformation.

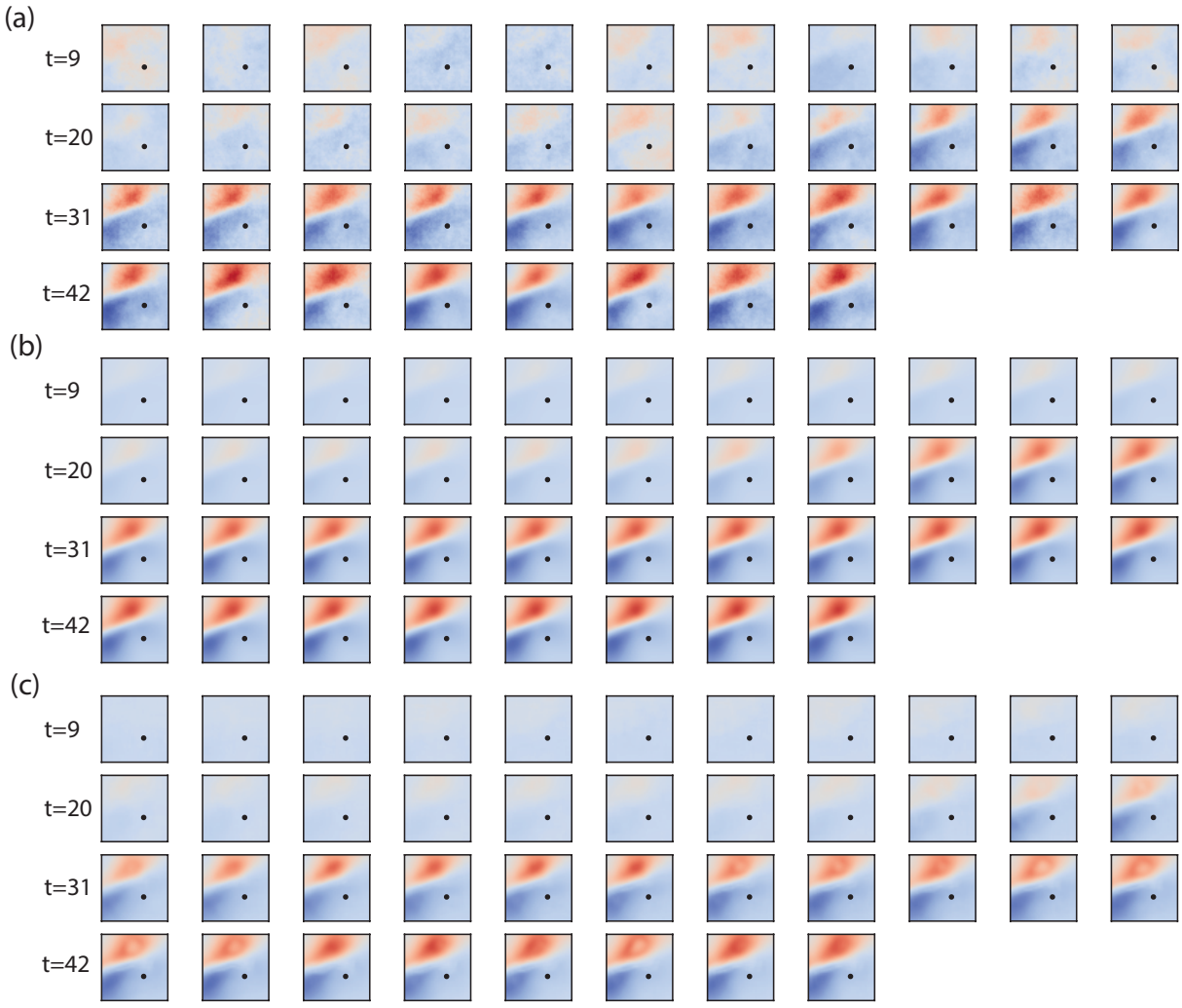


Figure D.3: Cumulative displacement of the noisy, DAE recovered, and clean InSAR time-series with a single creep transient episode. The black dot shows the location where the temporal pattern in Figure 5.11a is extracted.

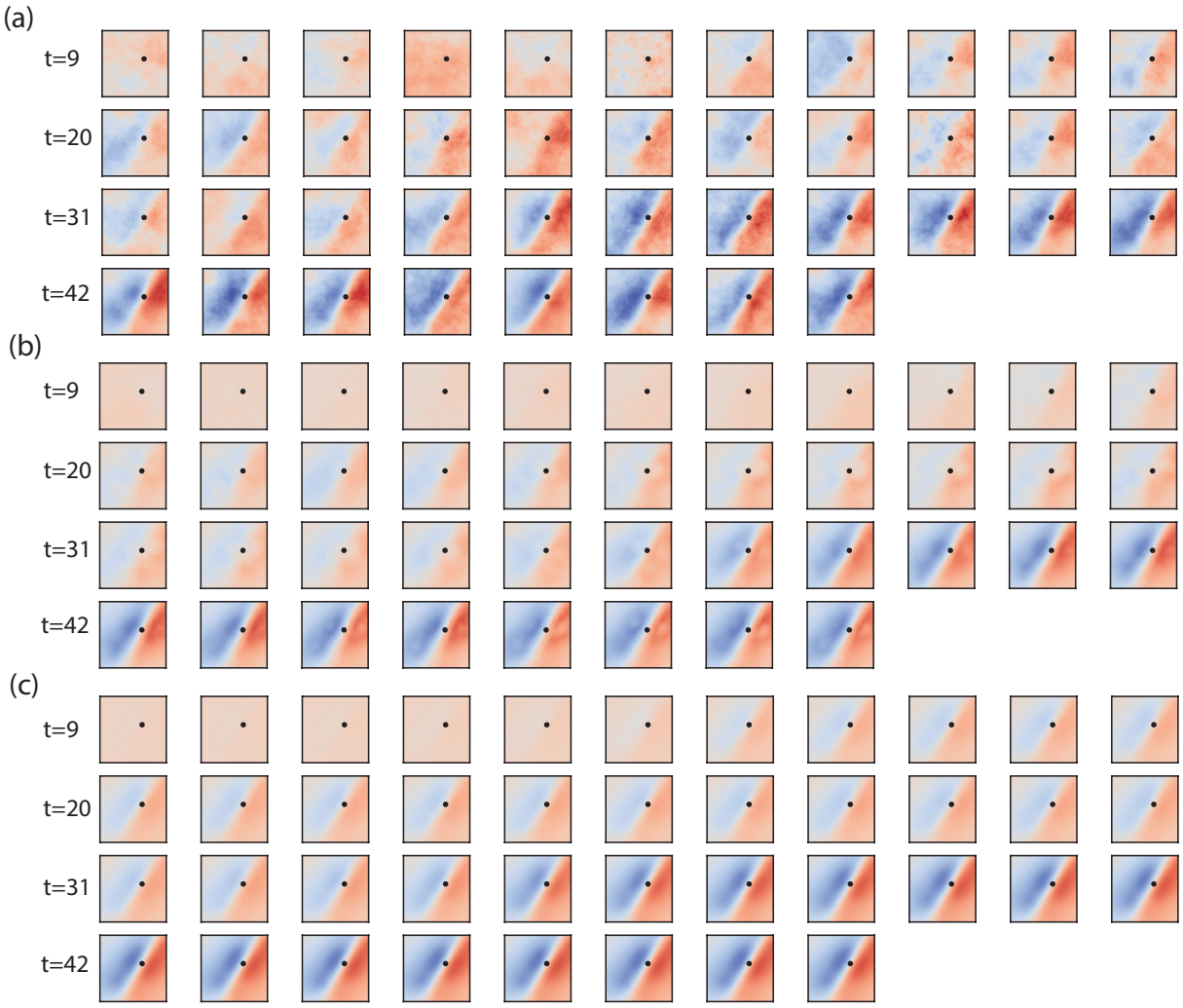


Figure D.4: Cumulative displacement of the noisy, DAE recovered, and clean InSAR time-series with multiple creep transient episodes. The black dot shows the location where the temporal pattern in Figure 5.11b is extracted.